# Seismic Characterization of A Possible Buried Impact Structure near Bow City in Southern Alberta

by

Wei Xie

A thesis submitted in partial fulfillment of the requirements for the degree of

Master of Science

in
Geophysics

Department of Physics
University of Alberta

# Abstract

Impact cratering has been accepted as a major process that significantly affects the geological and biological histories on earth. In fact, there have been a number of impact craters detected in western Canada since the 1970's. Following this tradition, a possible buried impact structure near Bow City in Southern Alberta was discovered in 2010 by careful near-surface structural mapping. The motivation of this study is to examine the impact origin of this abnormal structure, which could provide valuable information for the impact research and the geological development of the Western Canada Sedimentary Basin. The work is carried out with integrated legacy and new seismic reflection images, seismic travel time inversion, and structural modeling. This evidence shows distinct listric faulting at the structure's edge and a more central uplift zone that is highly faulted; this structural evidence is similar to that seen in other craters and supports interpretation of the structure as an impact crater. Final definitive confirmation, however, still requires that evidence of shock metamorphism be found.

# Preface

Chapter 4 of this thesis has been published in Glombick, P., D. R. Schmitt, W. Xie, T. Bown, B. Hathway, and C. Banks (2014), " The Bow City structure, southern Alberta, Canada: The deep roots of a complex impact structure? ", *Meteoritics & Planetary Science*. I was primarily responsible for the analyses of the seismic data with the assistance of my supervisor Dr. Douglas R. Schmitt. Dr. Glombick P. was mainly responsible for the geologic interpretation and mapping with helping in the manuscript preparation and edits. T. Bown contributed to the preliminary data preparation and analysis. B. Hathway and C. Banks helped the geologic outcrop reconnaissance and modeling. Chapters 5 through 7 are all completely original work carried out by the author.

# Acknowledgement

I would like to thank my supervisor, Dr. Doug Schmitt for providing me the opportunity to work on this impact crater study, which makes us so famous! He is knowledgeable, helpful and dedicated, though he is not available all the time. He respects my opinions and inspires me to be brave and independent. He guides me through my entire graduate school, not only in technical study, but also in moral cultivation. I was very much enjoyed the field experience at Milk River and Bow City with so many hard work and unexpectedness. I also got the chance to present the academic progress in various conferences with his support and encouragement. Thank you very much, Doug!

This project was funded by Department of Physics teaching assistantships from University of Alberta, NSERC and Dr. Schmitt's Canada Research Chair in Rock Physics. It was also strongly supported by various oil and gas companies for kindly donating the seismic dataset, which includes Canadian Forest Oil, Canadian Natural Resources Ltd., Husky Ltd., Penn West Ltd. and ConocoPhillips Ltd. For the software support, I acknowledge Schlumberger for providing Petrel® software, GEDCO for the VISTA 2D/3D seismic data processing package, and IHS for AccuMap® and Petra®.

More importantly, the author was assisted by many individuals to accomplish this project. Thank you to Paul Globick for guiding me through the regional geology and sharing the valuable stratigraphic information. Thank you to Judith Chan who helped me learn multiple pieces of software. Also, many thanks to Gautier Njiekak and Randolf Kofman for their patient descriptions on the geological outcropping. I would also like to thank Drs. Ben Hanthway and Christopher Banks for providing their photographs from their field reconnaissance. Furthermore, seismic data acquisition was greatly facilitated with the assistance of

the members from Experimental Geophysics Group including R. Kofman, M. Novakovic, M. Morin, B. Snow, T. Mohammed, X.W. Chen, S. Vermorel, P. Milan, V. Vragov and G. Njiekak. Thank you, folks! I am also grateful to all my friends, for their company, their support and all the time we spent together.

Last but not the least, I would like to give my special thanks to my Mom and Dad. Thanks for supporting and encouraging me through every little steps in my life!

# Table of Contents

# List of Tables

# List of Figures

# List of Symbols and Abbreviations

| | |
|---|---|
| 2D | Two-dimensional |
| 3D | Three-dimensional |
| $\lambda$ | Elastic modulus |
| $\lambda$ | Wavelength of the seismic wvelet |
| $\mu$ | Shear modulus |
| $\rho$ | Density |
| $\Delta t_{NMO}$ | Time shift of the NMO correction |
| $\Delta t_i$ | Travel time in the *i*th layer at zero offset |
| $\Delta t$ | Spatial sampling interval (the distance between each station) |
| $\Delta t$ | Travel time residual vector, the time increment |
| $\Delta m$ | Model parameter adjustment vector (either a velocity node or boundary node) |
| $\sigma_v$ | Uncertainty of the velocity nodes |
| $\sigma_z$ | Uncertainty of the boundary nodes |
| $\theta_1$ | Angle of incidence |
| $\theta_2$ | Angle of refraction |

| | |
|---|---|
| $A$ | Partial derivative matrix |
| AGC | Auto gain control |
| AI | Acoustic impedance |
| API | American Petroleum Institute |
| a.s.l | Above sea level |
| BIA | Bow Island Arch |
| CMP | Common midpoint |
| CAL | Caliper |
| CSG | Common shot gather |
| CVS | Constant velocity stack |
| D | Damping factor |
| $D$ | Diameter |
| $d_a$ | Apparent depth |
| $d_t$ | True depth |
| DT | Sonic log |
| e(t) | Earth reflectivity |
| ERT | Electrical resistivity tomography |
| $f$ | Frequency |

| | |
|---|---|
| FFT | Fast Fourier transform |
| FD | Finite difference |
| F-K | Frequency-wavenumber |
| FX | Frequency offset |
| GLI | General linearize inversion method |
| GPS | Global positioning satellites |
| GR | Gamma ray |
| IFFT | Inverse Fast Fourier transform |
| k | Wavenumber |
| KB | Kelly bushing |
| KS | Kevin Sunburst |
| MD | Measured depth |
| $m_j$ | $j$th model parameter |
| NMO | Normal moveout |
| Ma | Million years |
| MSC | Multichannel seismic reflection |
| NPOR | Neutron porosity |
| n(t) | Random ambient noise |

| | |
|---|---|
| OBHs | Ocean-Bottom-Hydrophones |
| p | Horizontal slowness or the ray parameter |
| PDFs | Planer deforemations |
| R | Radius of the waverfront |
| PRA | Peach River Arch |
| QC | Quality control |
| $R_f$ | Radius of the first Fresnel zone |
| RES | Resistivity |
| RC | Reflect coefficient |
| RHO | Density log |
| RT | Radial trace |
| SH | Horizontal-polarized shear waves |
| S/N | Signal to noise ratio |
| SP | Spontaneous Potential |
| $t_i$ | *i*th observed travel time |
| $t_0$ | Travel time at zero-offset |
| $T_{RMS}$ | Travel-time residual |
| V | Velocity of the seismic wave |

| | |
|---|---|
| $v_i$ | Interval velocity of the *i*th layer |
| $V_p$ | P-waves or primary waves |
| $v_{rms}$ | Rms velocity |
| $V_s$ | S-waves or secondary waves |
| $v_x$ | Partial derivatives of the velocity in terms of x axis |
| $v_z$ | Partial derivatives of the velocity in terms of z axis |
| $x$ | Offset between source and receiver |
| $X^2$ | Nominal misfit parameter |
| x-t | Space-time |
| x(t) | Seismic recorded trace |
| WCSB | West Canadian Sedimentary Basin |
| w(t) | Source wavelet |
| $Z$ | Contrast of the acoustic impedance |

# Chapter 1 Overview

The motivation of the work presented here is to examine the impact origin of the deep roots of a possible impact crater near Bow City by means of geophysical subsurface imaging techniques. Currently, looking at the deep portion of an impact crater is quite unique in impact studies and such analysis would provide valuable data for the planetary research to get a better understanding of the cratering process. In addition, the research adds to our general knowledge of the geologic history of western Canada.

Although the earliest record of the abnormal faults existing in the outcrop along the Bow River was pointed out by Stewart [1943], the potential impact origin of this unique structure buried under the ground was not noticed until 2010, when it was pointed out by the staff in Alberta Geological Survey (AGS) [*Glombick*, 2010]. In an area of uniform and slightly dipping stratigraphic units, a semi-circular outline was observed in the structure maps generated with the geologic units. Folded and faulted beds are also visible with locally missing and duplicated strata. Hence, collaborative work was conducted with the University of Alberta to use seismic techniques to examine the structural genesis. The first seismic datasets obtained were donated by a number of oil and gas companies. They are comprised of seven 2D profiles, all of which were acquired for the deeper hydrocarbon targets. The newest dataset we acquired was a high-resolution survey consisting of two short 2D profiles. This survey was carried out in 2013 by the research group of Dr. Schmitt and significant improvements were achieved. Utilizing this dataset, I present the comprehensive geophysical characterization of this structure, separated into eight chapters.

This first chapter is the overview of this thesis and it introduces the project motivation, the working dataset, and a general description of each chapter.

The second chapter presents the background information for this study. It starts with the introduction to the study area and points out the availability of datasets to carry out the geophysical characterizations. The chapter begins with a detailed geoscience introduction of the impact crater research, and a series of earlier seismic studies over possible or confirmed impact craters are included. Such seismic studies are selected from the conformed impact craters that have similar sizes and were developed under the analogous circumstance as the Western Canada Sedimentary Basin (WCSB). These reviews provide important information on how seismic techniques have been successfully employed in distinguishing impact architectures. More importantly, it points out clues and directions on how to apply the seismic method on Bow City structure.

The third chapter describes the geological background of the study region to further assist the geophysical data interpretations. The regional geological setting and tectonics of Southern Alberta plain are first discussed. Detailed bedrock descriptions focused on the shallow Cretaceous units are introduced. In addition, a sub-section on the eroded strata is presented due to the fact that the studied structure is highly eroded and buried. The first geological mapping carried out by Stewart [1943] is described to introduce the historical record of the Bow City structure. In addition, the structure mapping conducted in 2010 by the staff in Alberta Geological Survey (AGS) is introduced to show the semi-circular outline. To the end, another field reconnaissance is presented to exhibit more abnormal and diagnostic faulting and dipping beds observed in the field in 2013.

The fourth chapter introduces the geophysical study that was carried out with the early legacy dataset. Portions of this chapter have been published in the journal Meteoritics and Planetary Science [1] . In order to provide a general background on the seismic methodology, a section that introduces the methodology of the seismic reflection technique is presented first. Detailed descriptions on the multiple dataset are performed thereafter. After carefully calibration and checking the

seismic profiles with the synthetic seismograms, the analysis of the seismic images is carried out on different surveys. In addition, structure mapping with the tracked horizons are produced to display the feature of the structure patterns from map views. This chapter provides the preliminary analysis on the Bow City structure and points out the clue for the later tomographic study and new seismic acquisition that are the central parts of this thesis.

The travel time inversion technique is discussed in the Chapter 5 to further detect the velocity anomaly existing in the Bow City structure. It is worthwhile to mention that impact damage and induced fracturing processes can significantly affect the distribution of the velocity field within the impact crater. Thus, RayInvr, a ray tracing method conducted with forward modeling and inversion programs, is utilized to display the velocity circumstance. First arrivals picked on Profile 86251 are selected as the input of the model. Detailed discussions on the methodology of the technique, the application of the method, and the interpretation of the resulted model are made. To better correlate the inverted model with the information provided by seismic reflection imaging and well log data, a comparison is described between all of these results.

In order to gain a better understanding of the structural patterns observed in the early 2D seismic profiles, Chapter 6 works with the application of the new high-resolution seismic reflection profiles collected in 2013. It begins with a thorough overview on the data acquisition, and follows with the detailed descriptions on the processing workflows. Finally, the stacked images are produced and careful analysis is made with the assistance of the sonic and density logs. It is important to notice that, through the entire working flow, more attention is applied on the

[1].This chapter has been published:Glombick, P., D. R. Schmitt, W. Xie, T. Bown, B. Hathway, and C. Banks (2014), The Bow City structure, southern Alberta, Canada: The deep roots of a complex impact structure?, *Meteoritics & Planetary Science*.

near-surface signals due to the fact that the target surfaces are within the upper 500 m. As a result, additional evidence that supports the impact hypothesis of Bow City structure is obtained.

Chapter 7 deals with the joint interpretation and modeling of the methods discussed above. The time-to-depth conversion of the seismic profiles is conducted by employing the velocity model generated with well logs and the regional structure maps. A 3D model showing the structure patterns is created and the isopach maps are generated to display the thickness variations of the geological units. The systematic discussions are pointed out in the end to introduce the other possible origins of the structure such as volcanic caldera, dolines and haloknesis. However, such scenarios do not completely reproduce the structure features observed in Bow City structure. In the end, different scaling relationships described by Melosh [2011] are performed to calculate the structure development and the final age of the structure.

The last chapter of the thesis (Chapter 8) concludes all of the discoveries observed in the aforementioned techniques. The final assessment of the genesis of the Bow City structure is pointed out. In addition, future work that might provide more unique structural details is mentioned.

The Appendix in this thesis includes the photo of the vibrator utilized to acquire the seismic data and a series of the seismic profiles in depth scale. Although structure patterns show similar feature as the time scales images discussed in Chapter 4, such profiles provide more geological meaning with a measurement in depth.

# Chapter 2 Introduction

This chapter provides the background information on the study of the extraterrestrial impact structures. Such studies present an essential basis for understanding the impact process and further assist in the characterization of the Bow City structure. Starting with a detailed description of the target area and the project data set, the geoscience studies on the impact craters including the transition of the physical condition and structural pattern will be followed. At last, a detailed literature review of the geological and geophysical observations on similar impact craters will be illustrated. These case studies are focused on the application of the seismic techniques within the sedimentary basin similar to the Western Canada Sedimentary Basin.

## 2.1 Location and Study Area

The structure of interest is located on the west bank of Bow River, Alberta and is centered at approximately 50.45° N and 111.91° W (UTM N5589320 E435710 Zone 12N). In Alberta Township System (ATS), the structure is estimated to cross the Range 16 to 17 in Township 17, west of the 4$^{th}$ Meridian (Figure 2.1).

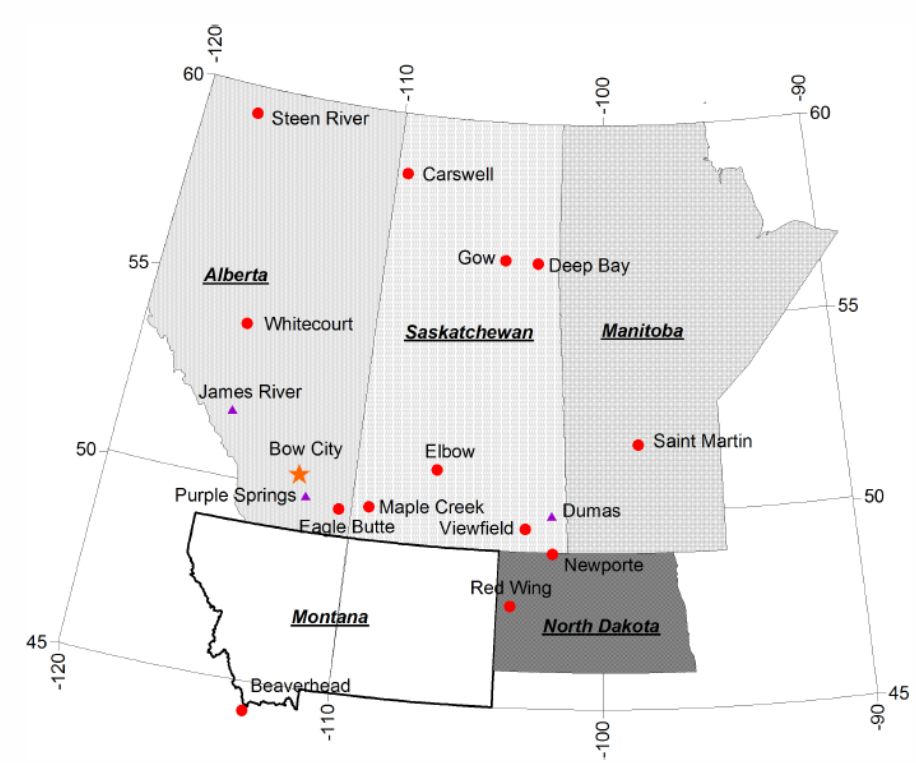


Figure 2.1 Location map of the Bow City structure and similar impact structures nearby. Red circles present the impact craters listed from Spray and Ellis [2013] and purple triangles show the possible impact structures. Figure modified from Schmitt et al [2013].

The first discovery of these unique faults along the west bank of Bow River was recorded in Stewart's 1943 regional mapping report [*Stewart*, 1943]. However, to our knowledge, no impact origin of this anomalous structure was suggested, likely as this predated the understanding that impacts are a geological process on the earth's surface. As such, no further investigations were carried out. Attention to the structure was delayed for more than half a century until the distinctive structures in the shallow sub-surface were noticed during the detailed near-surface mapping with geophysical well logs in 2010 [*Glombick*, 2010]. In this area, more than 2000 wells have been drilled since 1927, due to the high production of the underlying hydrocarbon reservoirs. This further gives the possibility of

conducting a geologic reconnaissance with well log data. Other techniques such as seismic reflection and refraction are applied to characterize the structure as well. Figure 2.2 shows the regional map covering the Bow City structure that exhibits the locations of wells, seismic surveys, and refraction profile. Currently, five individual seismic surveys have been obtained that are closely positioned across the estimated structures. In addition, velocity tomography modeling has been carried out on Line 86251 and a 3D structural model has been created to describe the abnormal structural pattern in the subsurface.

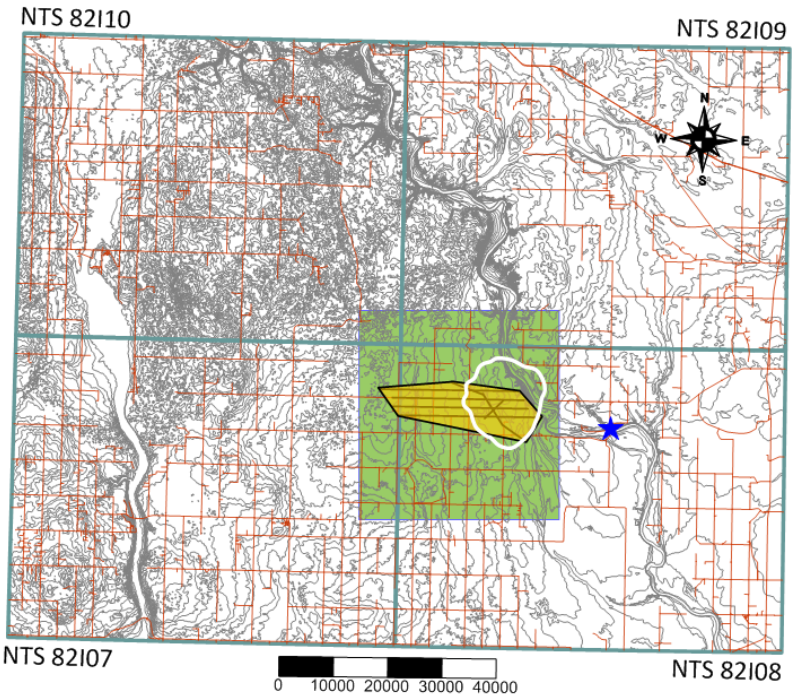


Figure 2.2 Regional map of the vicinity area of Bow City structure over NTS Zones 82I07- 82I10. The green colored area shows where the structure maps have been generated with well logs. The yellow colored area represents where horizon maps have been produced with seismic lines (black lines). Red lines and gray polygons designate roads and topographic contours, respectively [*CANVEC*, 2007] Figure is modified from *Schmitt et al.* [2013]. The blue star indicates the location of the village of Bow City.

## 2.2 Impact Geosciences

In the last four decades, meteorite impact studies have been well developed and are considered as one of the key factors that affect the biological and geological history of the earth [*French*, 1998]. By utilizing a combination of geosciences techniques, including geophysical subsurface imaging, geological structural mapping, and geochemistry analysis, increasing numbers of features have been characterized. In this section, background information on impact studies is introduced, followed by a general description of the formation and classification of the impact craters.

### 2.2.1 Overview

Impact craters are formed by extraterrestrial projectiles that are large enough (>20 m) to both survive entering the earth's atmosphere and retain sufficient speed to impact the surface with sufficient kinetic energy. Such bodies appear to be traveling at a velocity faster than 11 km/s [*French*, 1998], thus the rapid release of the velocity, pressure, stress and energy would significantly destroy the contact surface. Under these extreme situations, the impact and the target rocks are vaporized, melted, deformed, shattered, and excavated to form the eventually unique impact structures.

Extraterrestrial impacts have been accounted by scientists as a significant factor affecting the Earth's surface, crust, and geological history in recent decades [*French*, 1998; *French and Koeberl*, 2010]. Indeed, this process is a ubiquitous geologic activity that shaped the surfaces of all the planetary objects. Generally, a circular morphology on the target surface is presented at first. This bowl-shape cavity might collapse and modify into complex structure if the size is sufficiently large enough. However, it is important to note that other endogenous geologic processes including earthquakes, dissolution of salt or carbonates, or volcanic

explosions can also result in similar circular structures. Thus, it is difficult to confirm the impact origin based on the structures morphology alone without considering the regional geological history and, in particular, finding evidence for shock metamorphism [1] [*French*, 1998; *French and Koeberl*, 2010]. Table 2.1 lists the distinctive stages of the shock metamorphism in terms of the pressure change.

Table 2.1 Classifications of the shock-metamorphic stages of the nonporous crystalline rocks. Table is modified from *French* [1998].

| Approximate Shock Pressure (GPa) | Effects |
|---|---|
| < 2 | Fracturing and brecciation (no unique shock features). |
| > 2 to <30? * | Shatter cones. |
| >8 to <25 | Microscopic planar deformation features (PDFs) in minerals, particularly feldspar and quartz. |
| >25 to <40 | Metamorphism of specific minerals to diaplectic glasses accompanied with development of the high-pressure mineral polymorphs (no melting). |
| >35 to <60 | Individual partial melting, especially in feldspars. |
| >60 to <100 | Complete melting of the entire minerals and a superheated rock melt formed. |
| >100 | Full vaporization of all the minerals. No rock preserved. |

*French (1998)

(?) = uncertain

Although the impact event and the endogenous earthbound processes share numerous features in common, quite a few characteristics have been detected to differentiate these two events. The special characteristics of an impact event include (1) the extreme physical conditions including high-pressure, high-temperature and high-strain (e.g., the maximum pressure can reach to 100 GPa or

[1] Shock metamorphism is a metamorphism of rocks and minerals due to the high heat and pressures resulted from the shock wave compression and decompression. Diagnostic deformations can be obtained such as planer deformation features and shatter cones.

more, which is well above the pressures attained by even the most devastating earthbound geological processes (i.e. volcanic explosions) cannot such attain such pressures) [*Boslough*, 1990]; (2) the instantaneous nature of the deformation (e.g., a 1-km-diameter crater forms in a few seconds and even a large crater having a 200-km diameter forms in less than 10 minutes); (3) the concentrated energy is released at a single point; (4) the unique shock-metamorphic structures (e.g., the transient shock waves result in the special deformations of the target rocks and mineral grains where they pass through. These shocked deformed rocks include shatter cones, planar deformation features (PDFs), and shock metamorphism) [*French*, 1998; *Osinski*, 2004].

Currently, there are more than 185 impact craters formally accepted on the earth (Earth Impact Data Base maintained at the University of New Brunswick [*Spray and Elliot*, 2013]) and numerous possible impact craters have been detected recently by the geophysical tools including airborne, spaceborne, seismic imaging and gravity, magnetic surveying [*Pilkington and Grieve*, 1992; *Stewart*, 2003; 2011]. Most of the impact structures formed over the history of the Earth have not been found. For example, according to the cratering statistics, it is expected that about 500 impact craters alone greater than 1 km in diameter within the Western Canada Sedimentary Basin (WCSB) formed during the past 600 Ma [*Mazur et al.*, 2000].

It is likely that most of the impact structures are still buried underneath and remain to be discovered [*Stewart*, 2011]. Due to the availability of the high-resolution seismic data in Alberta, more possible impact structures have been found to be deeply buried by the sedimentary deposits. However, confirming the existence of appropriately shocked geological materials is one of the key features need to confirm the impact nature of these newly discovered structures. Similar to such potential impact craters, Bow City structure is awaiting for the conclusive

indicators (e.g., shocked metamorphism and shatter cones) to definitively prove its impact genesis.

### 2.2.2 Formation of Impact Crater

Prior to conducting the detailed examination of the Bow City structure, a general introduction of current impact catering physis is necessary. Based on the variation of the impact mechanism, the development of a complex crater is separated into three different temporal regimes [*Ahrens and O'Keefe*, 1987; *French*, 1998], though, the propagation of the shock wave is continuous and many of these stages are taking placing at the same time (Figure 2.3). The three regimes are described respectively as followed:

i) Contact/Compression Stage: an initial stage takes place immediately as the high-velocity projectile makes contact with the target surface. Shortly after, a cavity about 1 or 2 times of its diameter is formed on the solid striking surface. With the kinetic energy transmitting into the target rocks, the energy releases rapidly as the wave front expands radially through a growing hemispherical volume. Additional heating, melting and deformations of the target material attenuate the shock front. As a result, the peak pressure of the shock wave drops significantly with distance from the impact point and consequently the shock damage varies. At the contact point, a shock pressure higher than 100 GPa leads to the complete melting or vaporization of the surrounding target rocks and projectiles. Moving outwards, shock pressures between 10 - 50 GPa still remain for many kilometers and the corresponding distinctive shock metamorphic features are generated within this range [*French*, 1998]. With continued propagation, conventional elastic waves or seismic waves at 1 - 2 GPa dominate the zone in which no distinctive damage occurs except the process of fracturing and brecciating. When the shock waves that reflected

back from the projectile/target surface reach the wave front of the projectile, it is considered to be the end of the contact/compression stage. The total duration of this period is usually less than a second.

ii) Excavation Stage: In this relatively longer period, a transient cavity is created on the target surface and the intense energy is released from shock waves and release waves. The morphology of this hemispherical cavity is recognized as a critical element in characterizing the impact crater as it defines the original diameter of the impact crater and consequently the energy of the impact event, the size and incoming velocity of the projectile, the shape of the final crater and the distribution of the shock front pressures. The transient crater is distinguished by the direction of the excavation flows that includes an upper zone dominated by the upward and outward shock waves, and a deeper zone created by tensional stresses from the release waves. The bowl-shaped crater continues to grow and open up with the uplifted transit rim and downwards expanding depth. This continues to the moment that the shock and the release energy are not sufficient enough to displace and eject the target rocks; at this point, the excavation stage ceases and the transient crater reaches its maximum size. The depth of this structure is estimated to be one third of its final diameter. The transient crater is developed within several minutes [*Melosh*, 1989]. Particular to our study, this relationship provides a useful information to describe the Bow City structure since the structure is highly eroded with only deep roots remaining.

iii) Modification Stage: The development of this final stage is mainly dependent on the size of the transient crater and the material of the target rocks [*Melosh*, 1989]. The crater is modified by the normal elastic waves and is gradually shaped by the gravity and conventional rock strength. Indeed, there is no clear end of this stage and the final impact structure is

classified as simple crater, complex crater and multi-ring basin according to the different morphologies.

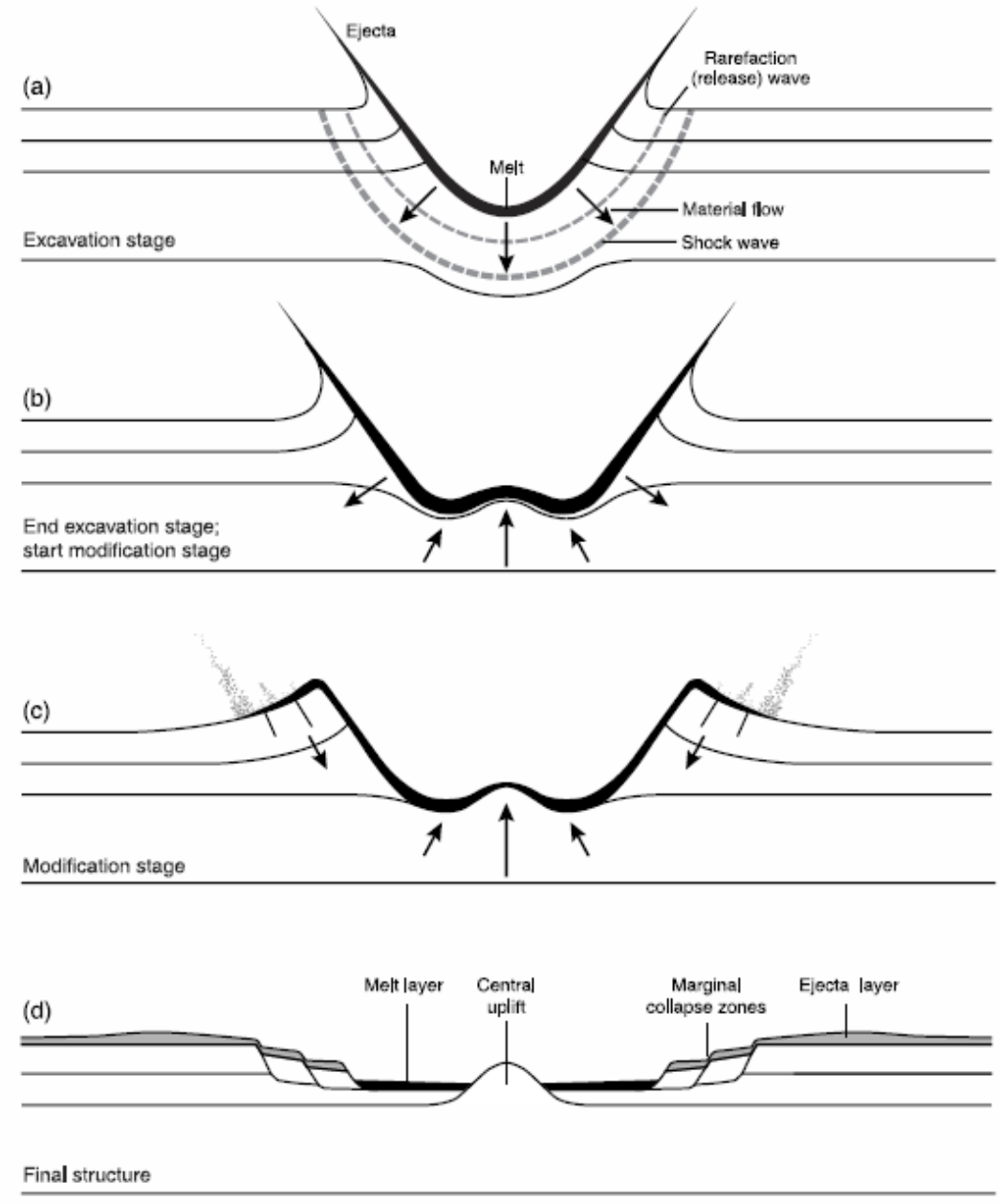


Figure 2.3 A schematic image shows the formation of a complex impact crater on earth. Figure from *French* [1998].

### 2.2.3 Classification of Impact Crater

Impact craters are classified as simple or complex based on their size and morphology. A simple crater (Figure 2.4) is less than a few kilometers wide and displays an elegant bowl-shaped concave cavity that is similar to the transient cavity. Slightly modified by the steep wall collapsing and rim ejecta refilling, the initial transit crater is well preserved in the modification stage. The filling materials, officially named as breccia, are comprised of numerous rocks masses, both shocked and unshocked rock pieces and impact melt. Indeed, the diameter of the final crater ($D$) might be 20% bigger than the original transient crater, while its apparent depth ($d_a$) might be 50% shallower than the true depth ($d_t$). The depth to diameter ratio ($d_a/D$) for simple impact is usually between 1:7 and 1:5.

As the size of the impact craters increases a more complicated structure, called a complex crater, is formed. A complex crater is significantly altered during the modification stage (Figure 2.5). This complex structure is characterized by a central uplifted peak, a sub-horizontal annular terrace, and an inward collapsing rim. However, the apparent vertical depth ($d_a$) of the final complex craters is much shallower than those of simple craters. Indeed, the depth to diameter ($d_a/D$) ratio for a complex crater is usually between 1:10 and 1:20. With increasing diameter of the structure, the single central peak might transition into multi-ring peaks. For structures on the Earth, the limit of the diameter between simple and complex craters is taken to be about 2 km in sedimentary, and 4 km in crystalline rock masses, respectively. It is necessary to point out that this transition boundary varies evidently from planet to planet since the gravitational acceleration in the host planet has a major influence on the formation of the crater.

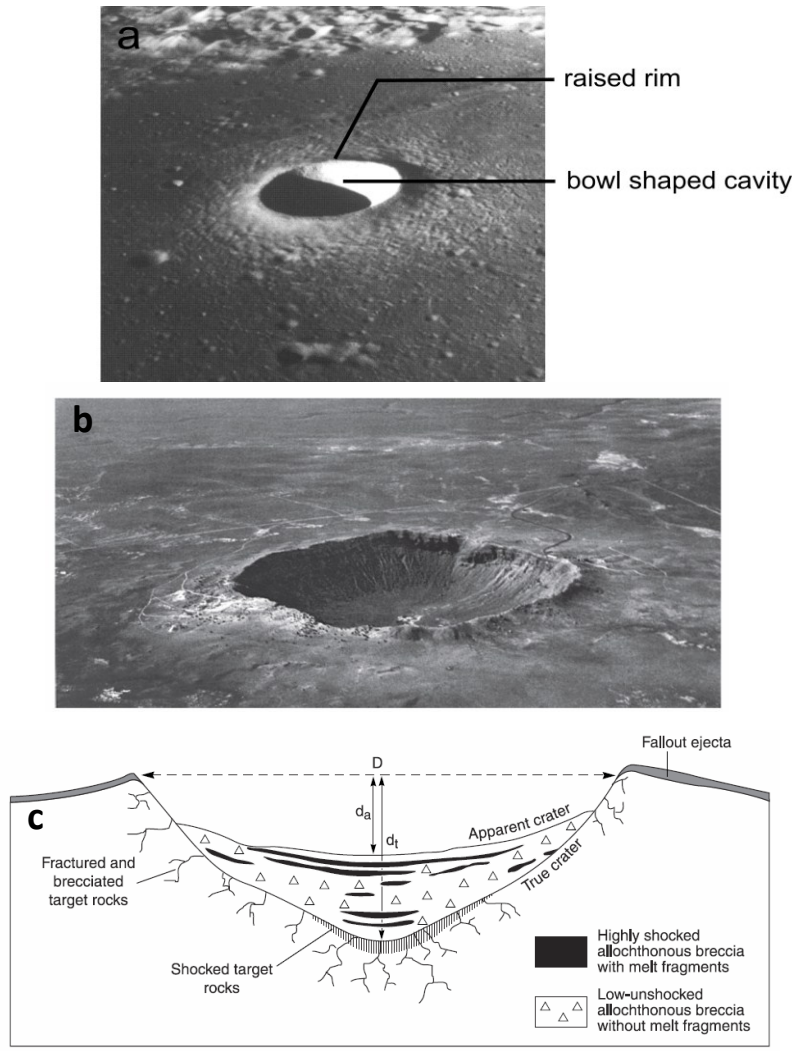


Figure 2.4 Examples of a) a simple crater on moon: Moltke Crater, ~7 km (from [*French*, 1998], figure 3.7); b) a simple crater on earth in Arizona: Barringer Crater, ~1.2 km (from *French* [1998], Photograph by David Roddy, United States Geological Survey); c) schematic section of a simple terrestrial impact structure, <2-4 km (from *French* [1998] ).

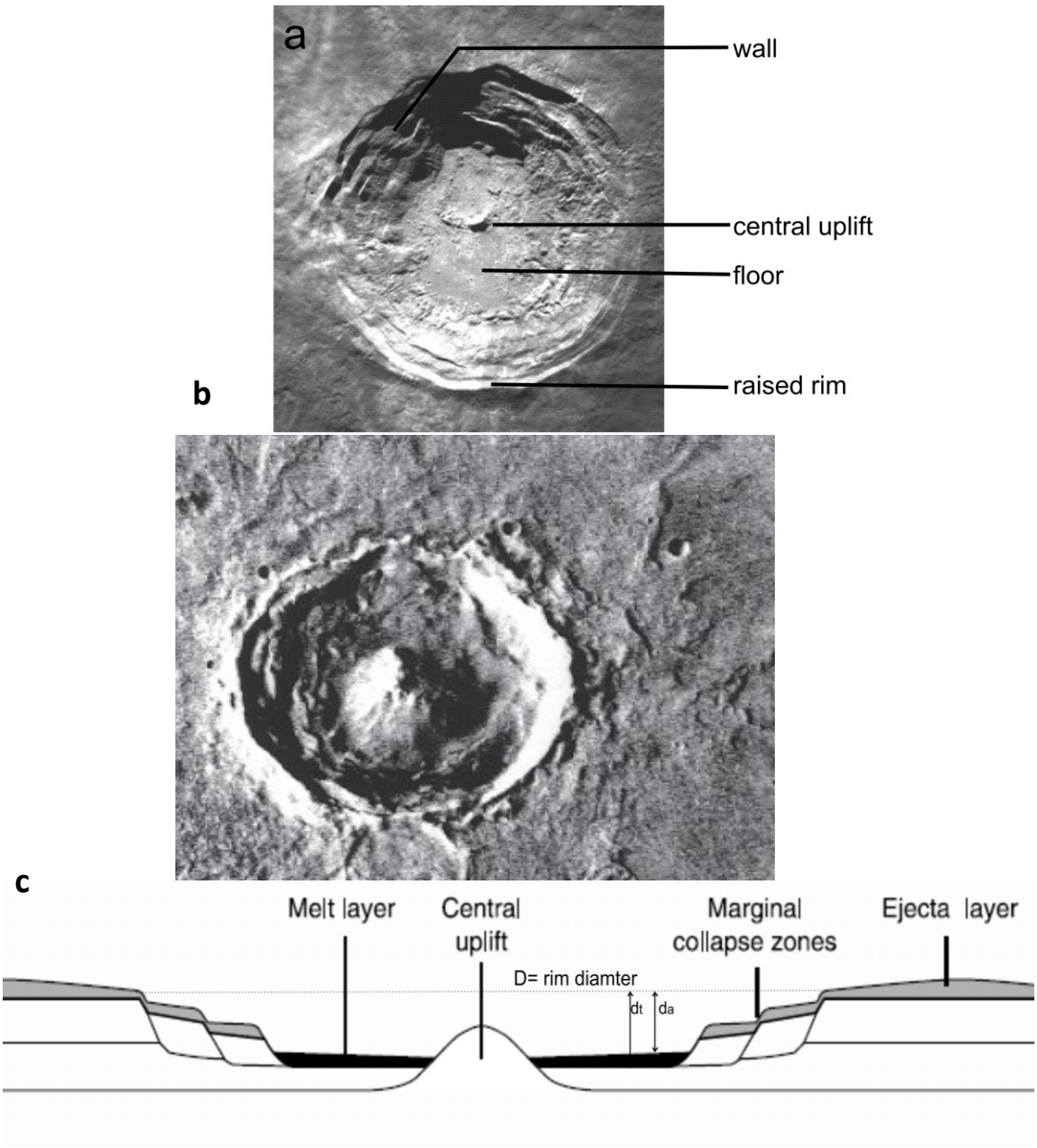


Figure 2.5 Examples of a) a complex crater on the Moon, Aristarchus Crater (from *Collins et al* [2002] figure 3); b) a different view of the complex crater on the Mars (Viking Orbiter image 003A07, from *French [1998]*).; c) schematic section of a complex territorial impact structure (modified from *French* [1998]).

One of the most distinctive features observed in a complex crater is the appearance of the central uplifted area. A converging material trajectory field is created by the inward and upward moving materials [*Milton et al.*, 1996; *Wilshire and Howard,* 1968] in the later stages of the modification period. These large rebounding surface movements are taking place in the center of the structure as the outer rim is collapsing downward and inwards to fill the crater. As a result, the crater is likely to have a bigger size with an obvious central high uplift. The relationship between the central raised amount and the crater rim-to-rim diameter is approximately one over ten based on the detailed study of the complex impact craters *[French,* 1998].

Moving outwards, an annular terrace filled by numerous impactites is observed. As noted by *Stöffler and Grieve* [1994,1996], impactites are deformed target rocks. They can be separated into three categories of i) shocked rocks, ii) impact melt rocks, and iii) impact breccias. The impact melt material is richer on the top and the center, and might even cover the entire crater as a cap. Beneath this melt sheet, the sintered suevite breccia, which is strong enough to be used as the construction stone, are visible *[Shoemaker and Chao, 1961]*. The other area between the central peak and the rim is filled with lithic breccia consisting of less melted materials.

In the outmost region, the fault-bounded trough is produced with the collapsing rim wall. As described by *Osinski and Lee* [2005], during their geological structural mapping of the Haughton impact crater, a series of key features in the fault system have been summarized that consist of i) radial and concentric faults created during the early excavation stage, ii) the reverse thrusting faults developed during the late excavation stage, iii) the rose-petal faults within the highly disrupted region generated during early modification stage and, iv) the roll-over anticline formed in the modification stage (Figure 2.6).

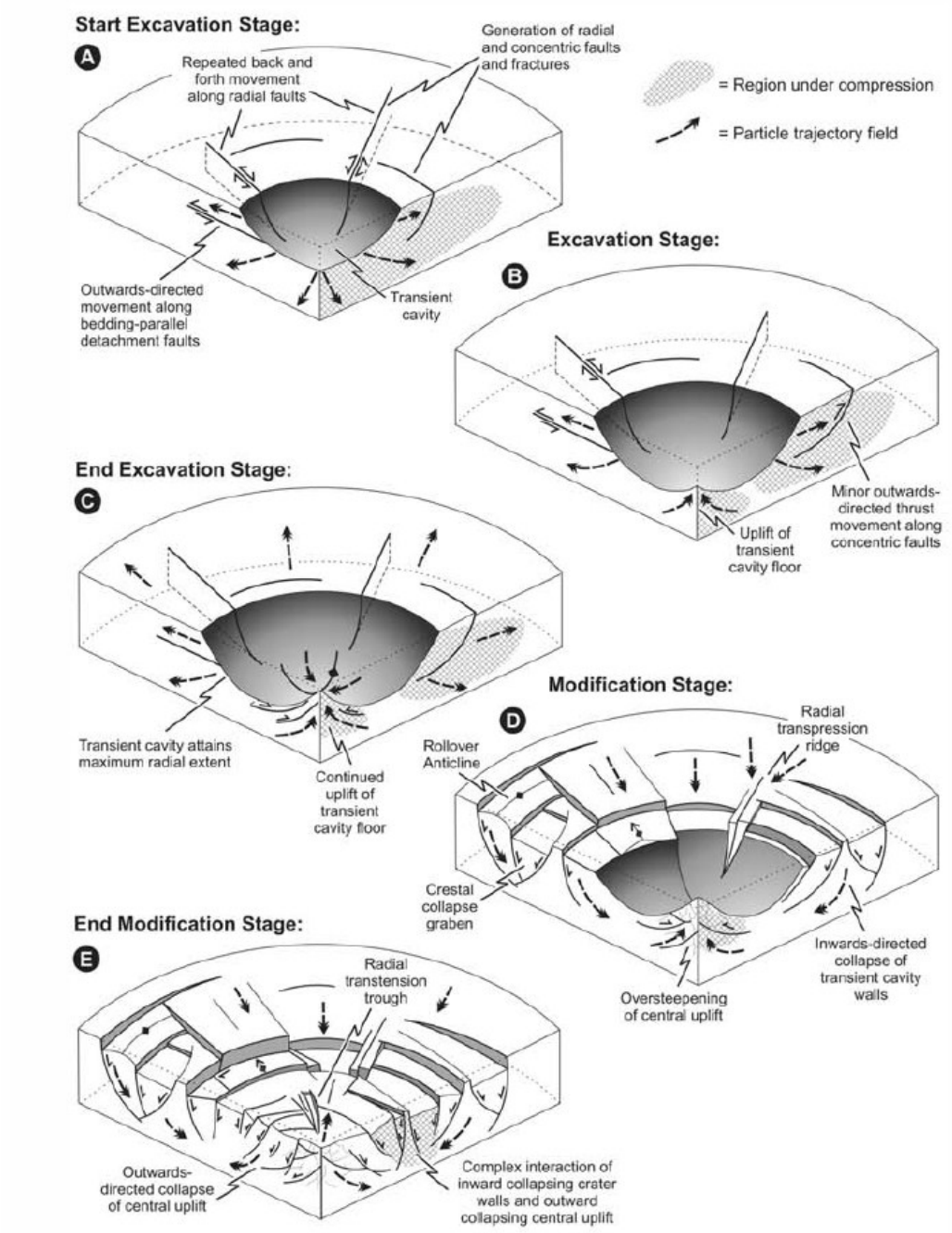


Figure 2.6 Schematic diagrams displaying the numerous types of faults generated during the formation of a complex impact crater. a) Early excavation stage, a transient bowl-shape cavity is formed with the propagation of the downward and outward waves; concentric, radial and horizontal detached faults along are

produced. b) Excavation stage, the transit crater keeps expanding and a central uplift is created by the rebounded waves. c) End excavation stage, the transit cavity approaches its maximum while the central uplift continues to raise up. d) Modification stage, the central peak still keeps growing; the rim walls start collapsing inwards along the faults; the radial transpression ridges appear with significant displacements. e) End modification stage, central peak collapses outwards due to gravitational force, a complex faults pattern is produced by the interaction collapsing inwards and outwards *Osinski and Spray* [2005].

## 2.3 Geophysical Study of Impact Structures

An extraterrestrial impact event is a process occurring on the near surface of the target area, thus over long time periods the resulting cavity might be significantly eroded or erased by filling with younger sediments. To our knowledge, no large impact event has occurred during the recorded human history. Moreover, almost one-third of the discovered impact craters on the earth are buried below the surface. As a result, geophysical subsurface imaging and drilling techniques play important roles in detecting impact structures.

Before presenting the detailed impact features discovered from the Bow City structure, it is necessary to describe the geological and geophysical character of similar impact craters, some of which are certainly confirmed by associated observations of shock damage, as a reference. The impact structures discussed as followed are primarily focusing on the complex craters found in the sedimentary basins which are analogous to Western Canada Sedimentary Basin (WCSB). In addition, seismic imaging was utilized to identify structural features in these example craters. In these studies, a series of distinctive features are exhibited including circular morphology, central uplift, disruptive rock masses, and a faulted out rim.

### 2.3.1 Bosumtwi impact crater, West Africa

The Bosumtwi impact structure is one of the youngest and best-preserved complex craters. It is located at 6°30 N and 1°25 W in Ghana, West Africa. It has a rim-to-rim diameter of 10.5 km and was formed 1.07 Ma ago *[Karp et al*., 2002]. Due to its relative young age and the top water layer from Lake Bosumtwi, more impact features are preserved and the central uplift is highly distinguished under the layer of the post-impact sediments on seismic image (Figure 2.7). As such, geophysical tools are recognized as the best methods to delineate the buried structure [*Karp et al., 2002; Schmitt et al.,* 2007].

In the seismic reflection study carried out by *Scholz et al.* [2002], eight 2D profiles from the multichannel seismic reflection (MCS) data were employed to image the subsurface structure. The representative profile in figure 2.7(a) displays two pronounced central peaks sitting below the post-impact lacustrine rocks. Further structural mappings of the geologic units below the brecciated layer in figure 2.7(b) present an evident bowl-shaped cavity with the central uplifted region.

Another highly recognized effect of the impact event is the severe fracturing and damaging on the target rocks. Consequently, the speed of the propagating seismic waves would be significantly affected in these disruptive zones. The refraction study [*Karp et al.*, 2002] conducted with wide angle Ocean-Bottom-Hydrophones (OBHs) were conducted to provide the velocity information of the estimated central uplift and the disturbed strata. An average velocity of 3.00 $km/s$ in the brecciated rocks and 3.8 $km/s$ in the fractured crater floor were obtained which displayed a much lower velocity response than the normal speed of 5 $km/s$ in the unaffected rocks (Figure 2.7(c)). Such velocity anomalies might be suggestive of a highly fractured region due to the significant damage of the impact process. Further in-situ seismic examination in borehole LB-08A [*Schmitt et al.*, 2007]

yielded an agreement with these abnormal low velocities and the obvious velocity variation over small confining pressures proved the highly fractured conditions in the central uplift.

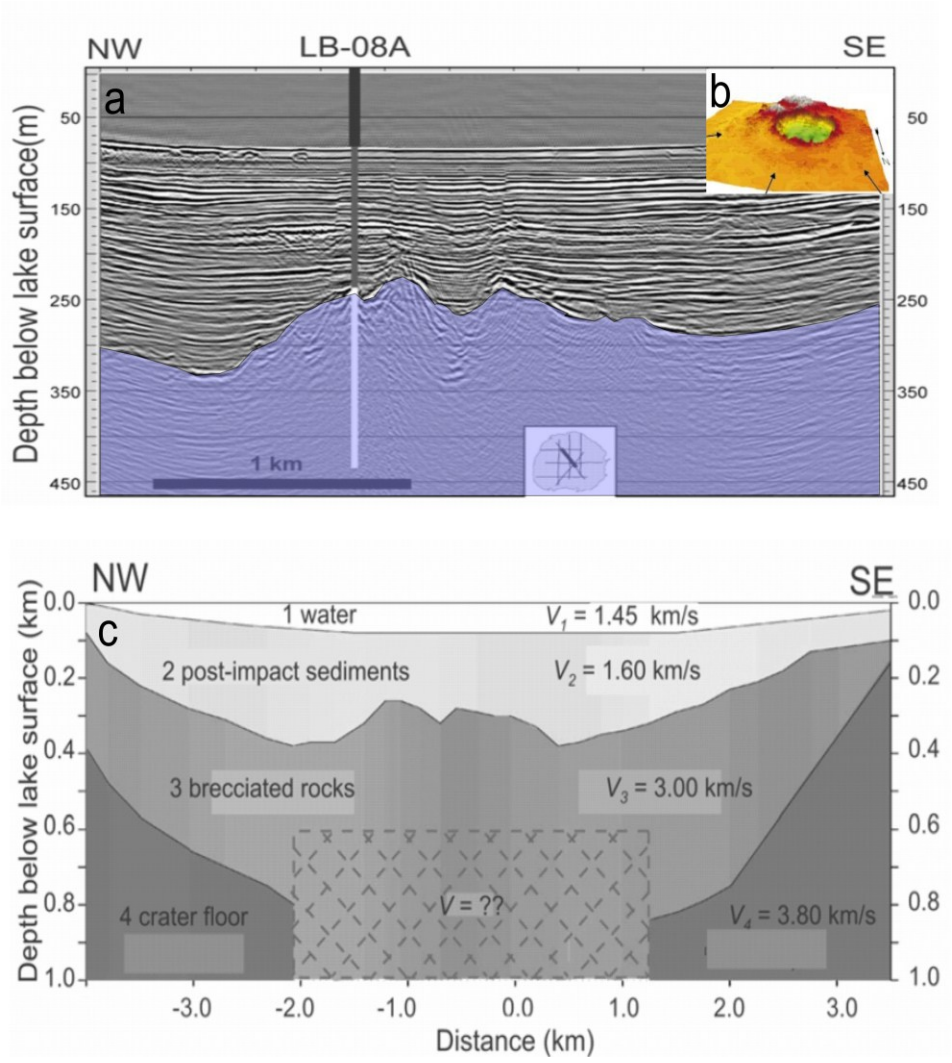


Figure 2.7 Seismic study conducted near Lake Bosumtwi. a) 2D seismic reflection section showing the lower strata with the central uplift (Colored by purple). LB-08A represents the location of the drill hole. b) Horizon map from the interpreted seismic reflectors showing the uplifted rim and central uplift. c) Velocity model generated with the refraction data which exhibits the central abnormal velocity structure. Image from *Karp et al* [2002] and *Schmitt et al* [2007].

### 2.3.2 Haughton Impact structure, Canada

The Haughton Impact crater, situated in the western part of Devon Island in Canadian Arctic Archipelago, is about 20 km wide from rim to rim [*Osinski and Lee*, 2005]. Based on the exposed Paleozoic carbonate rocks, the structure is estimated to have been created in the Eocene (~39 Ma). Numerous shocked features detected on the outcropping rocks include shatter cones, the existence of coesite (a high pressure form of quartz), and diaplectic glass, all of which are definitively indicative of an impact origin [*Robertson and Sweeney*, 1983]. In addition, geologic and geophysical studies reveal concentric ring-like structure, a pattern of complex faults, and impact-induced fractures in this structure. [*Frisch and Thorsteinsson*, 1978; *Osinski et al.*, 2005; *Robertson and Sweeney*, 1983; *Singleton et al.*, 2011].

It is important to review this structure because distinctive impact features including the numerous faults and the highly damaged central core were exhibited on a 10 km 2D seismic profile that covered the western side of the structure. This survey was conducted by the team from University of Saskatchewan in 1988 and careful examinations and interpretations were performed afterwards (Figure 2.8). On the stacked seismic image, a series of criteria were utilized in identifying these structural faults such as the appearance of the significant variations in amplitude, the existence of discontinuous seismic reflectors, and the observations of diffraction patterns and abnormal waves [*Hajnal et al.*, 1988]. The disrupted chaotic central area on the interpreted profile is similar with the central peak feature seen in the Bosumtwi Crater. Furthermore, the extreme velocity contrast found between the shallow strata and the deeper carbonates are indicative of the pronounced fracturing zone induced by impact event. The wave speeds of 3280 m/s and 3780-3860 m/s were observed in the lacustrine sediments and the underlying breccia layer respectively, while a uniform high velocity of 5020 m/s is found in the deep undisturbed strata.

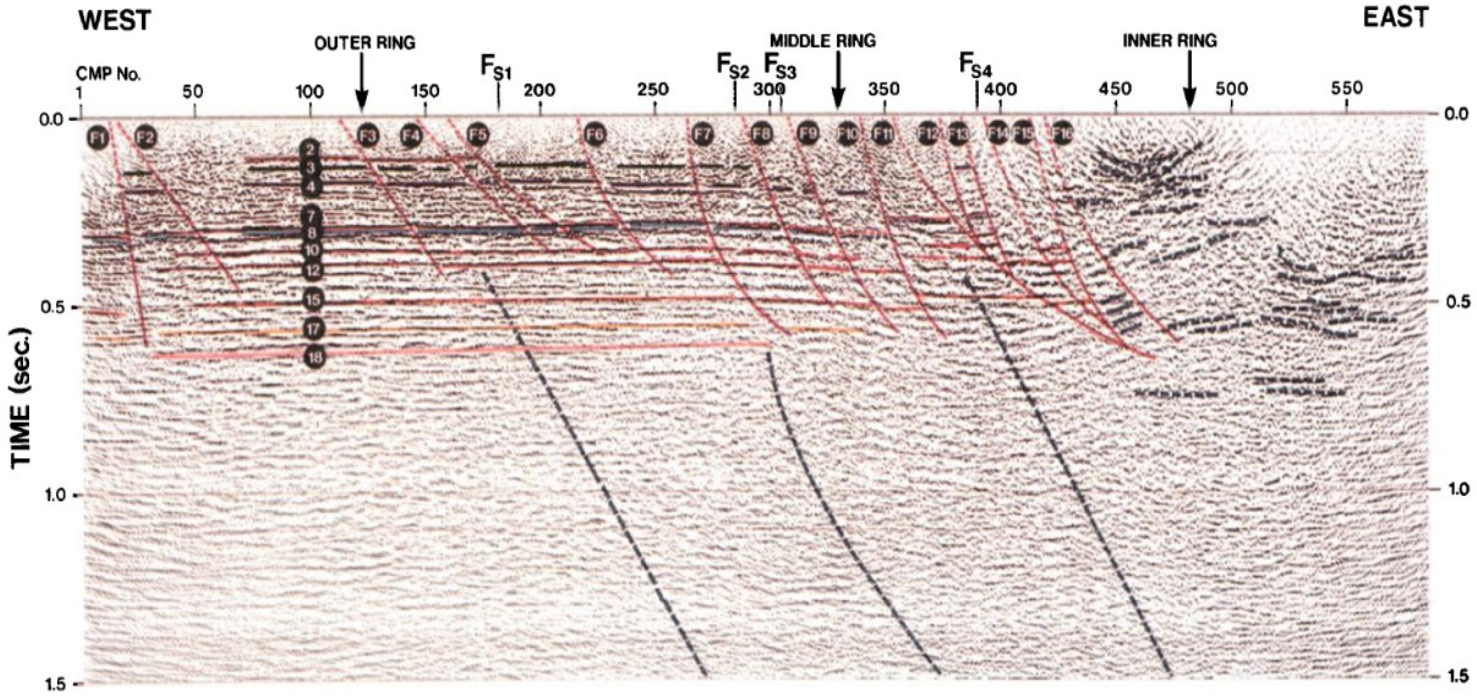


Figure 2.8 2D seismic profile presenting the various faults patterns and central disrupted zone across the western part of the Haughton crater. The numbers in the black circle indicate the picked horizons. F1 to F16 represent the interpreted faults according to the interpreted seismic horizons. The discontinuous dash lines in the east end of the profile show the disturbed features in the central core. Image from *Hajnal et al* [1988].

### 2.3.3 Cloud Creek structure, USA

The Cloud Creek impact structure is located in central Wyoming, USA. The rim-to-rim diameter is estimated to be about 7 km. Overlain by 1200 m sedimentary rocks in Mesozoic, the crater has an approximate age between 170 - 210 Ma. Indicated by the abnormal circular morphology and central raised area discovered on the seismic profiles, the impact origin of Cloud Creek structure was first proposed by Dr. Stone in 1999 [*Stone*, 1999]. Later discovery of the shock-metamorphic features of the planar deformations (PDFs) in the thin section of the drilling cores conformed its impact origin [*Stone and Therriault*, 2003]. The commonality of this impact crater to the Bow City structure is its similar size, the pronounced erosion history, and the analogous buried geological environment.

On the seismic profile, a number of structural elements are visible to identify this complex crater, such as the central raised zone, the faulted rim with anticlinal horizon, and the ring-like trough [*Stone and Therriault*, 2003]. However, the relative coherent seismic events in the central peak of the Cloud Creek structure reveal a different response compared to the chaotic and disordered events in the Bosumtwi impact crater and the Haughton impact crater. This uniqueness might be suggestive of the existence of the significant erosion, and that what we observe now are the remaining roots of the impact structure. In addition, the Triassic-Jurassic (TR-J) unconformity displayed on the borehole well logs and the severely fractured zone below the unconformity provide the evidence of erosion. Furthermore, based on the scaling relationship pointed out by Melosh [*Melosh*, 1989], for a crater which is 7 km wide, the central peak is supposed to be 700 m instead of the currently observed 520 m. This evident removal of estimated 200 m strata might be another hint of active erosion events during the deposit environments.

### 2.3.4 Newporte Impact Crater, USA

The Newporte impact structure is located in the North Dakota, just to the south of the border between USA and Canada. The structure is deeply buried under the thick sedimentary strata (~3 km) in the Williston basin and is recognized to have an age between the Late Cambrian and the Early Ordovician (523 Ma - 478Ma) [*Clement and Mayhew*, 1979; *Forsman et al.*, 1996; *Gerlach*, 1994]. The particular importance of this simple impact structure (3.2 km wide) is that the economic hydrocarbon targets were preserved within the crater of the Precambrian basement.

The distinctive features of this impact crater were first noticed during petroleum exploration in 1979 [*Clement and Mayhew*, 1979]. The impact nature was not confirmed until the detection of the microscopic shock metamorphic features in 1995 [*Koeberl and Reimold*, 1995]. Based on the geophysical evidence from the seismic, well-log and core data, the impact origin of the structure has been further reinforced by *Forsman et al.* [1996]. Due to the unavailability of the seismic data, only the contour map showing bowl-shape cavity and uplifted rims are shown in Figure 2.9.

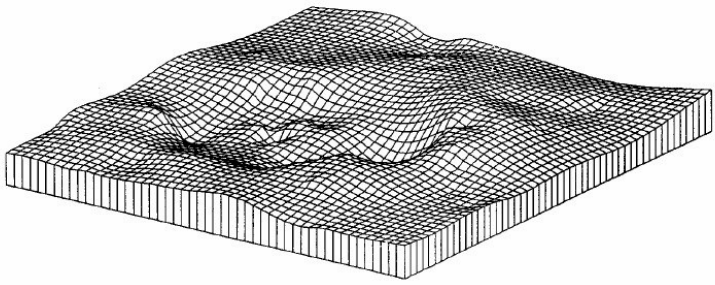

Figure 2.9 Structure maps generated from the interpreted basement horizon in Newporte Crater. The evident concave shape and uplifted rim are visible. A vertical exaggeration of 2.5 was utilized. Image from *Forsman et al* [1996].

### 2.3.5 Red Wing Creek, USA

The Red Wing Creek impact structure, located in North Dakota, is another confirmed petroleum producing impact craters within the Williston basin [*Barton et al.*, 2009; *Koeberl et al.*, 1996; *Sawatzky*, 1975; 1977]. This complex crater is buried under 2 km of sedimentary rocks and the rim-to-rim diameter is about 9 km. The abnormal structural patterns visible on the seismic profiles motivated Shell Ltd. to drill the first of two wells in the 1960s [*Barton et al.*, 2009]. Although these two wells were not prolific, the detection of the unexpected thick units of Mississippian and Pennsylvanian formation on the core samples led to another drilling test in 1972 that found a highly productive 870 m thick oil column [*Barton et al.*, 2009; *Brenan et al.*, 1975]. Facilitated by the detailed mapping with the modern 3D seismic dataset acquired in 2001, 26 wells have been drilled in the central peak and 22 of which continue producing. This impact crater is recognized as one of the most prolific impact structures in Western Canada Sedimentary Basin (WCSB) with the hydrocarbon production.

In 2010, *Herber* [2010] analyzed the 3D seismic cube and numerous structural features similar to those observed in the Haughton structure [*Osinski and Lee*, 2005] were interpreted. Figure 2.10 shows one of the representative 2D seismic profiles extracted from the 3D volume that crosses the entire crater from north to south. Outside the disrupted central zone, the area was severely faulted and the nonsymmetrical radially faulted patterns were displayed. The deeper strata above the Bakken unit on the northern section are mostly normal faulted, in contrast, the thrusting faults patterns are seen on the southern side. More complex structure patterns are visible in the severely damaged central peak. Another interesting structure noted by *Herber* [2010] is that the significant uplifted unit in the central raised area might be an artifact of the seismic ‘pull up’ which results from the central velocity high.

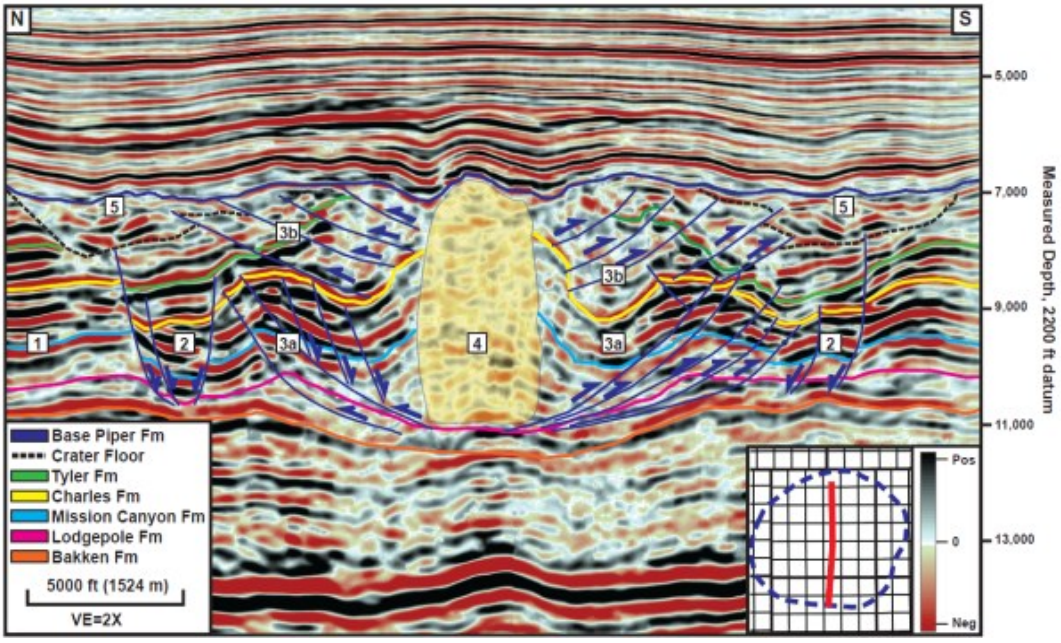


Figure 2.10 2D seismic image across the entire impact crater from south to north. Numbers represent the different zones including 1) outer rim 2) annular trough 3a) lower thrust zone 3b) upper thrust zone 4) central core 5) crater floor. Figure from *Herber* [2010].

### 2.3.6 Viewfield Impact structure, Canada

The Viewfield crater is a simple impact structure with a diameter of 2.5 km in southeast Saskatchewan, and is recognized to have developed during Jurassic-Triassic time (~200 Ma) [*Grieve et al.*, 1998; *Sawatzky*, 1972; 1977]. The impact origin was first proposed by Sawatzky [*Sawatzky*, 1972] due to the detection of the bowl-shape cavity and the out rim in hydrocarbon exploration. It was proved by the shock metamorphism observed in the drilling core [*Grieve et al.*, 1998]. In the anticlinal structure rim, the petroliferous Mississippian carbonate breccia amid the Watrous Red strata and the oil-bearing Griffin beds below the unconformity were discovered [*Donofrio*, 1981]. This discovery further indicates that impact craters could be a good place for hydrocarbon storage.

Although the structure is relatively small, a complex history including the hypervelocity impact event and the subsequent dissolution was pointed out by *Sawatzky* [1972]. The seismic profile in figure 2.11 shows the interpreted horizons in Jurassic and Triassic period. Compared with the flat Second White Speckled Shale and the top Blairmore horizons, significant cavity structure could be seen from the lower units [*Sawatzky*, 1977; *Westbroek and Stewart*, 1996]. An infill of the basal Jurassic horizon might also be interpreted, which is ascribed from post-impact salt collapse and solution.

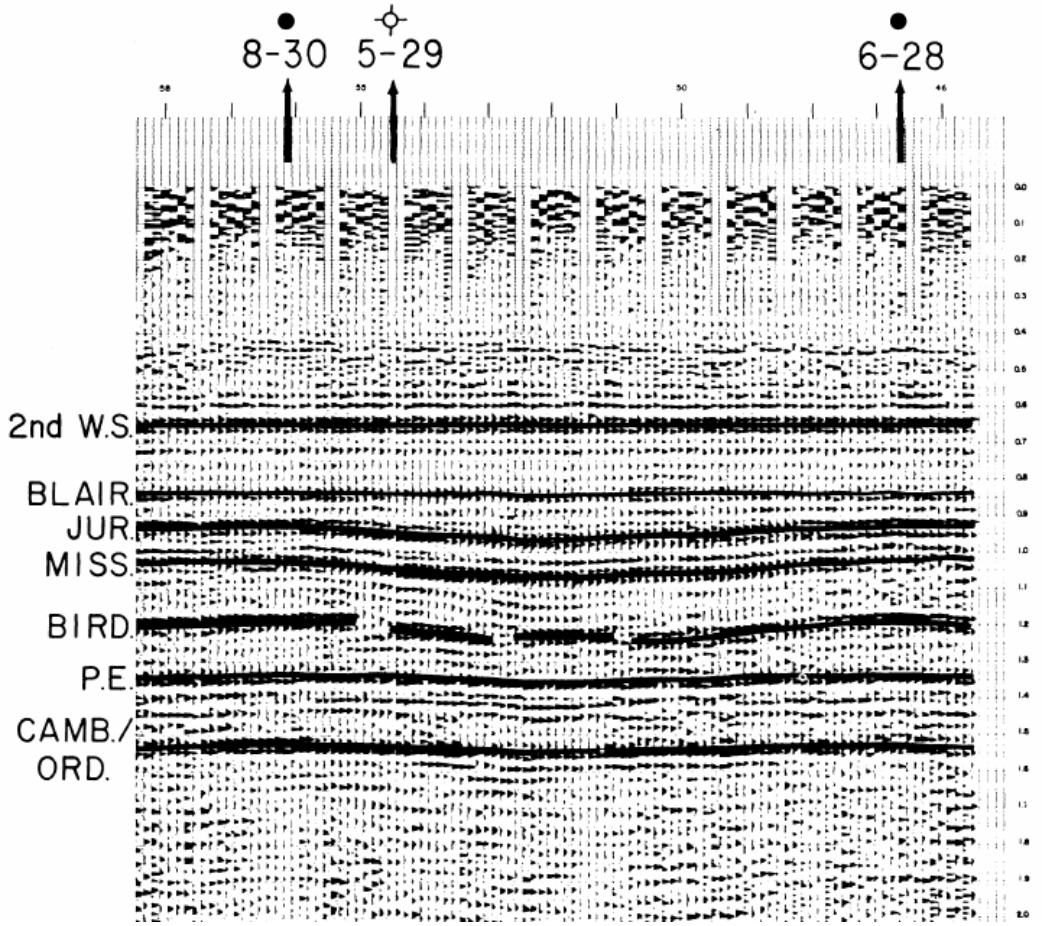


Figure 2.11 2D seismic section over the Viewfield impact structure representing the displaced subsurface horizons, Jurraic (JUR), Missiipion (MISS) and Birdbear (BIRD). Image from *Sawtazky* [1972].

### 2.3.7 Elbow, Canada

The Elbow complex structure is centered at 106°45' W and 49°51'N in west Saskatchewan. The rim-to-rim diameter is approximately 8 km with a central uplift surrounded by an annular depression on the seismic profiles [*Grieve et al.*, 1998; *Sawatzky*, 1977]. These structural anomalies were first noticed by *DeMille* [1960] from the seismic images, and the impact origin was not emphasized until 1998 when the PDFs were detected in the well cuttings. However, only limited materials are currently available to discuss the impact origin of the structure.

### 2.3.8 Maple Creek (White Valley), Canada

The Maple Creek structure, also known as the White Valley structure, is discovered in the Cypress Hills region of southwestern Saskatchewan (49°48'N, 109°06'W). The abnormal outcropped tilting strata [*Whitaker*, 1976] and the repeated section of Eastend and Bearpaw formations [*Gent et al.*, 1992] inspired a detailed field reconnaissance and seismic examination in 1997 [*Westbroek and Stewart*, 1996]. Numerous impact features were exhibited in this 7.5 km wide complex structures and an age of 60 Ma was estimated [*Westbroek*, 1997; *Westbroek and Stewart*, 1996]. Figure 2.12 describes the significant features including a 620 m central uplift, annular trough and faulted rim. The discovery of PDFs in the well cuttings confirmed its impact origin [*Grieve et al.*, 1998].

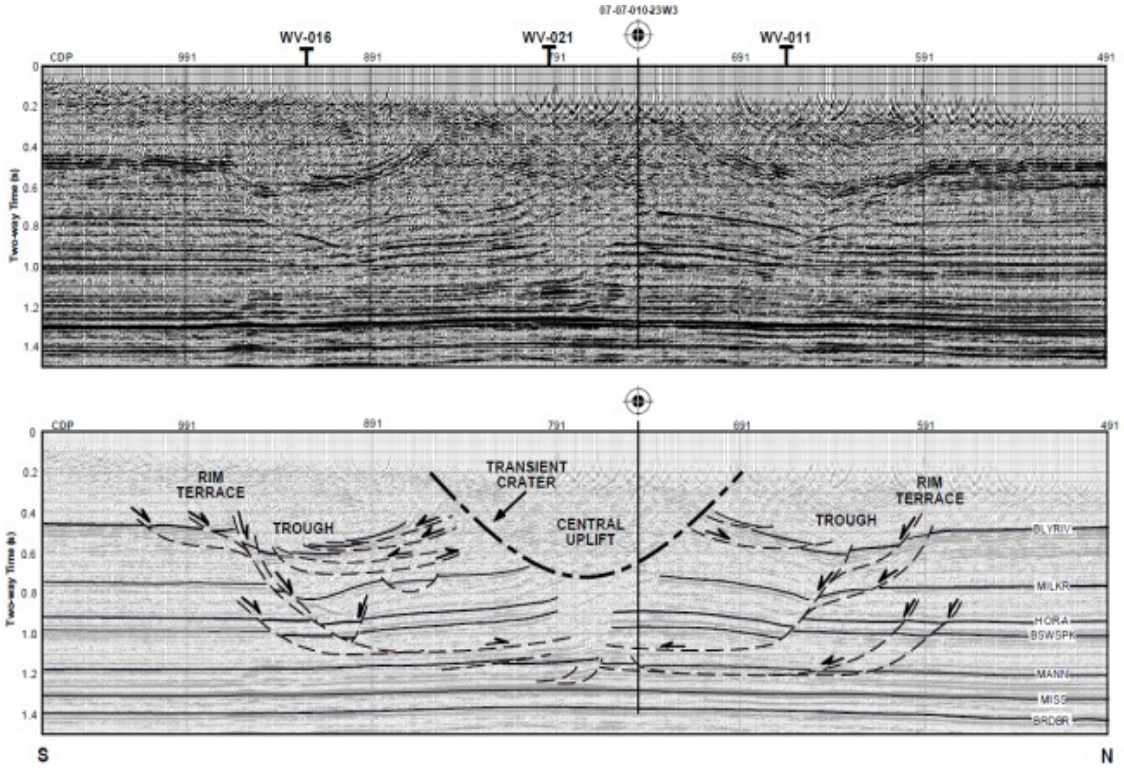


Figure 2.12 Uninterpreted (top) and interpreted (bottom) seismic profiles showing the distinctive impact features. Raised central peak, faulted out rim and ring-like trough can be characterized in the disturbed seismic horizons. Images from *Westbroek and Stewart*[1996].

### 2.3.9 James River, Canada

The James River impact structure, located in the southeast Alberta plain, is a deeply buried circular structure with a rim-to-rim diameter of 4.8 km. The complex structural features observed on the 3D seismic data set, which included the raised central peak, annular synforms and rim faulted strata, have been well studied by *Isaac and Stewart* [1993]. Beneath the 4500 m thick strata, the top of the anomaly structure was detected on top of the Cambrian units and the structure is estimated to form between the Late Cambrian and Middle Devonian time. Figure 2.13 shows the synclinal features and a raised zone that performs the apparent erosion. However, due to the deep burial and lack of economic potential, no well has yet penetrated the target layer and as such there are no materials that could provide evidence of shock metamorphism. Thus, the impact essence of this potential impact structure is still waiting to be confirmed.

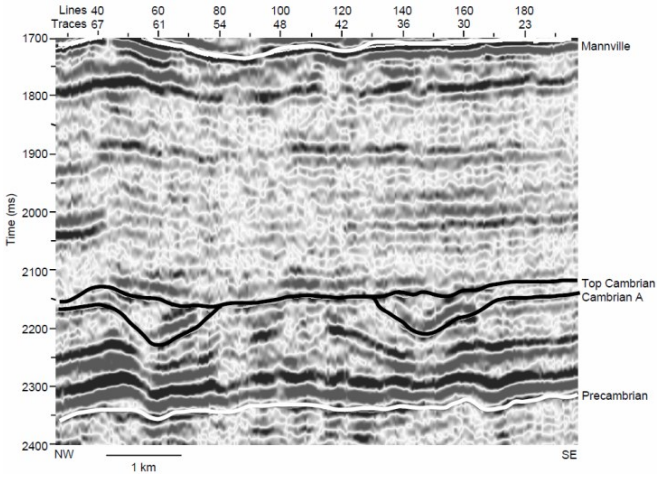


Figure 2.13 2D seismic profile intercepted the James River structure, displaying almost symmetric synclines surround the eroded central peak. Image from *Isaac and Stewart* [1993].

## 2.3.10. Eagle Butte, Canada

The Eagle Butte impact structure is located in southern Alberta with a ~15 km diameter of the circular outline. The unknown faulting pattern on the surface was first noticed by *Haites and Van Hees* [1962] and the impact origin was only confirmed recently by the discovery of shatter cones near the central uplift [*Hanova et al.*, 2005]. Of all the impact structures found within the Western Canada Sedimentary Basin (WCSB), the Eagle Butte crater is one of the best studied with a combination of information from outcrop exposure, 2D and 3D seismic imaging, and well log mapping [*Hanova et al.*, 2005; *Sawatzky*, 1976]. On the representative seismic image (Figure 2.14), significant impact features are displayed including a central raised core, a severely faulted annular syncline, listric normal faults[2], and structural thinning and thickening. Based on the displacements of a target bed in the Cretaceous, the structure is estimated to have formed between the Cretaceous and the Lower Tertiary.

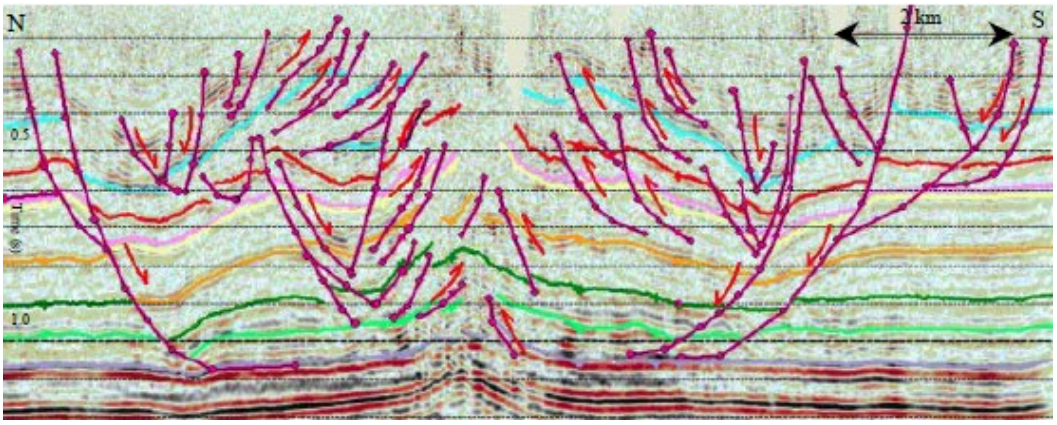


Figure 2.14 2D seismic profile across Eagle Butte crater showing a central raised area, disturbed horizons with apparent displacements and multiple faults pattern. Image from *Hanova* [2005].

[2] Listric faults: can be defined as bent normal faults with a concave upwards fault surface. Such faults usually develop in extensional regimes.

## 2.4 Conclusion

It has been widely acknowledged that the extraterrestrial impact events are still an ongoing process and play an important role in shaping the Earth's surface. Following this tradition, the Bow City structure, a potential impact crater, was discovered and characterized by a series of geologic and geophysical techniques. In this chapter, detailed background information was described to build a basis for conducting the geosciences characterization in the followed chapters. Beginning with the presentation of the study area and dataset, an overview of the impact geosciences including the mechanics, formation and classification of the impacts were present. This introduction provides the essential ideas to initiate the impact studies with geophysical seismic subsurface imaging and geologic mapping. Further, 10 confirmed and possible impact craters developed in analogous Western Canada Sedimentary Basin (WCSB) were reviewed, particularly focusing on the application of the geophysical seismic techniques.

# Chapter 3 Geological Framework

This chapter describes the geological setting of the Bow City study area. This review begins with a brief introduction of the regional geology followed by detailed description of the bedrock stratigraphy with most focus on the Cretaceous strata that is significantly deformed by the impact. The relationships to the geophysical well logs will be explained as well. Furthermore, early recorded bedrock mapping and field observations will be presented to better image the structure. This geology study provides the necessary background to understand the structure's origin and correlate with the geophysical seismic study.

## 3.1 Regional Geological Setting

The Bow City structure is centered at 50.45°N and 111.91°W in southern Alberta (Figure 3.1). The regional Phanerozoic structure is controlled by the Bow Island Arch (BIA). The BIA is a broad Paleocene flexure that extends north-eastward and joins the northern part of the northwest trending Sweetgrass Arch at the Kevin-Sunburst dome [*Wright et al.*, 1994]. It acts as a saddle between the Alberta and the Williston basins, which together comprise the southern area of the Western Canada Sedimentary Basin (WCSB) [*Williams and Burk*, 1964]. The study area is situated in the northwest flank of the BIA.

According to the result of bedrock mapping, the underlying strata gently dips toward the northwest (0.2° towards 310°). Due to the erosion and glaciation of the surface, there is little topographic character visible on the map generated with LiDAR data (Figure 3.2).


Figure 3.1 Regional geology of Alberta. The study area is marked by a red star. Figure was modified from the Alberta Geological Survey (AGS) website with authorization under Non-Commercial Reproduction policy of AGS.

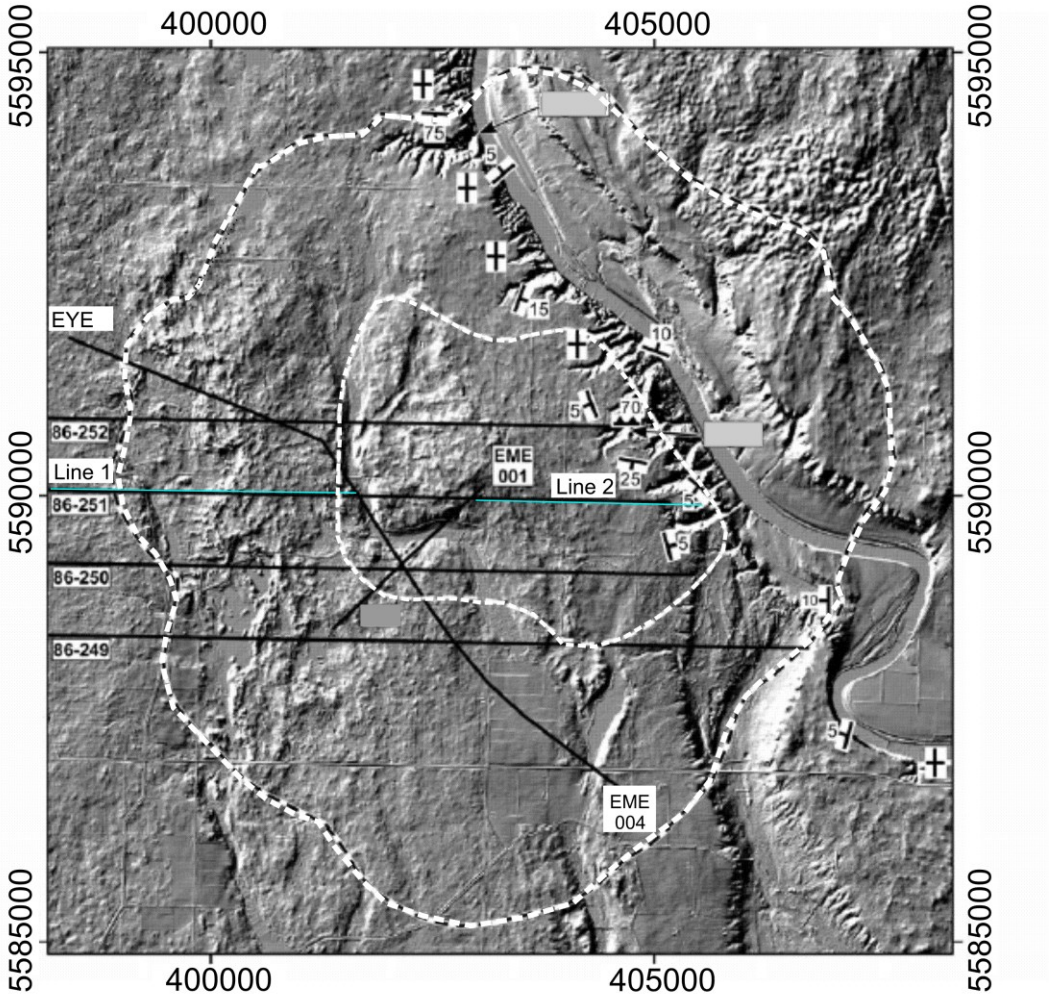


Figure 3.2 Topographic LiDAR map displaying the estimated outline of Bow City structure (highlighted by dashed line) and the structure measurements from outcrop. Donated legacy seismic lines are shown by the solid black lines. The blue lines represent the new high resolutions surveys conducted in 2013 by the University of Alberta. Coordinates are in UTM 12N, NAD 83. Modified from *Glombick et al*.[2014].

The Alberta basin is a northwest-trending trough in front of the Cordilleran Fold and Thrust Belt. This basin extends eastward to the Canadian Shield [*Wright et al.*, 1994]. Two major positive subsurface topographic anomalies, which can be

observed in the Phanerozoic wedge are the Peace River Arch (PRA) and the aforementioned BIA (Figure3.1) [*Kent*, 1987; *Wright et al.*, 1994].

The PRA is an east-northeasterly trending uplift in northwestern Alberta and northeastern British Columbia. It transformed from an arch in the Early Paleozoic, to a basin in late Paleozoic and Mesozoic, and at present exists as a subtle arch [*Podruski*, 1988]. The significantly disturbed Phanerozoic strata indicates the intense tectonic activities during these transitions [*O'Connell*, 1994].

In the southern Alberta plains, the stable platform changed into a lowland foreland basin due to sudden subsidence in the Triassic and the Jurassic. Later orogeny events moved the peripheral bulge eastward with periodically arrested by overlying anomaly structures, which might, in part, comprise the Bow Island Arch (BIA) [*Wright et al.*, 1994]. The BIA, which is recognized as the eastern bulge of the foreland basin, is a subtle, mildly positive structural element. It became more well developed in post-Jurassic times and was not a positive structure until the Laramie Orogeny [*Christopher*, 1984; *Kent*, 1987; *Wright et al.*, 1994; *Wu*, 1991]. The only feature that reveals the ancestry of the arch is the contour map of Jurassic strata. Later, during the Cretaceous there is little evidence of obvious tectonic events; there is no major deposition, erosional thinning, or erosional thickening of the Cretaceous sediments [*Podruski*, 1988]. The sediments were eroded and deposited under post-Laramide Orogeny and Tertiary tectonic relaxation during the late Cretaceous and Tertiary [*Bustin*, 1992; *Nurkowski*, 1984]. In the Late Tertiary (~52 Ma), the thick sedimentary sequences were eroded as a result of the regional tectonic uplift and isotactic rebound [*Dawson et al.*, 1994].

## 3.2 Bedrock Deposition

The sediments in southern Alberta plain are capped with Cretaceous period (~ 110 Ma) silicilastics and underlain by the thick strata from the Paleozoic (Figure 3.3). On the surface of the study area (Figure 3.4), a thin Quaternary glacial drift covers most of the area with slightly higher elevations towards the east side.

Based on the different lithologies, the underlying strata in Cretaceous period are subdivided into seven groups. On the bottom of the Cretaceous strata, the Mannville sandstone lies on the unconformity of the Paleozoic carbonates (~ 245Ma) resulting from the high erosion in the Late Cretaceous-Cenozoic Laramide Orogeny. The overlying stratigraphic intervals within Upper Cretaceous include the Colorado Group shale, the Milk River sandstone, the Pakowki shale, and the Belly River Group sandstone (Figure 3.5). The youngest rocks outcropping collected within the study structure are from the Horseshoe Canyon Formation deposited during the Late Campanian (~ 73 Ma). Of particular interest to this study, the stratigraphic interval of interest is bounded at the bottom by the strata of the Early Cretaceous Mannville Group and at the top by the Late Cretaceous Horseshoe Canyon Formation. Milk River sandstone is recognized as the deepest layer that significantly disturbed by any hypothesized impact event at least to the extent that can be detecteded in the seismic images.

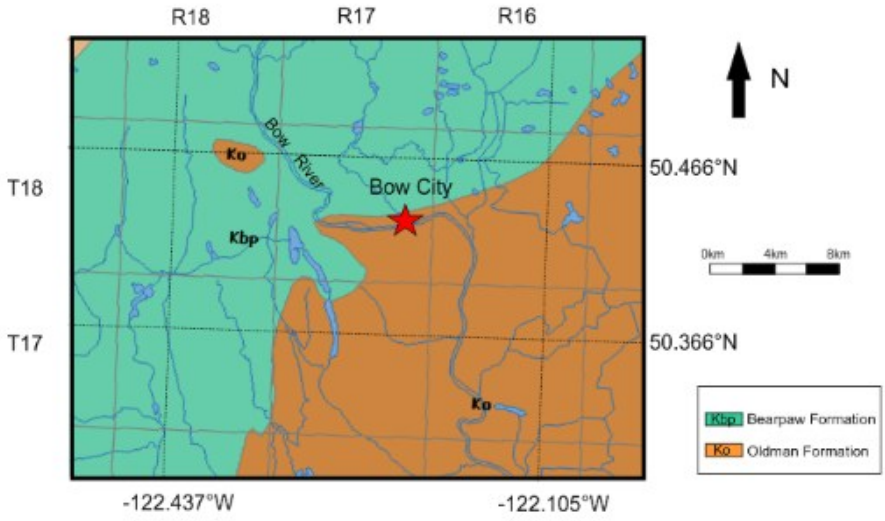


Figure 3.3 Bedrock geology of the Bow City area. Coordinates are given in ATS and lat/long coordinates. Figure was reprinted with authorization under the Non-Commercial Reproduction policy of the AGS.

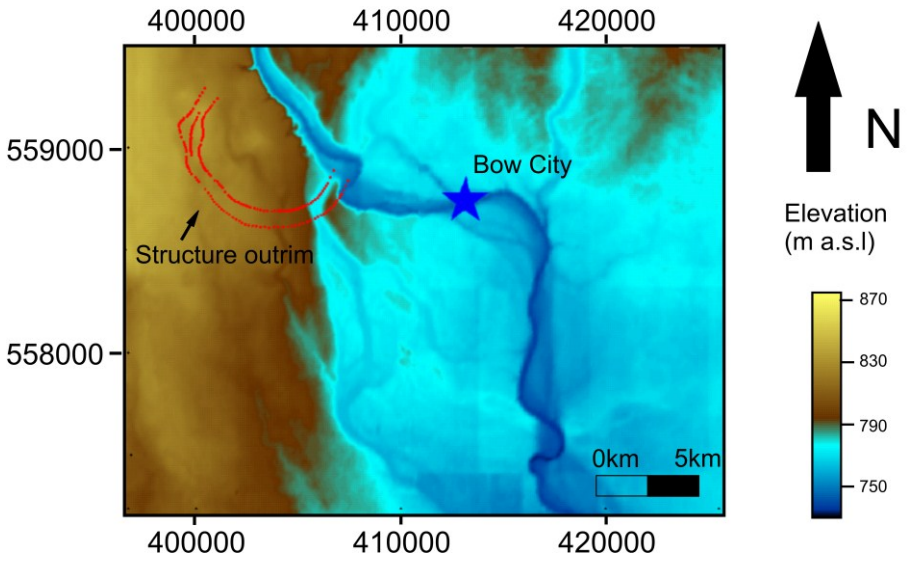


Figure 3.4 Surface topography of the Bow City area. Coordinates are given in UTM Zone 12N NAD83 (data provided by the Centre for Topographic Information).

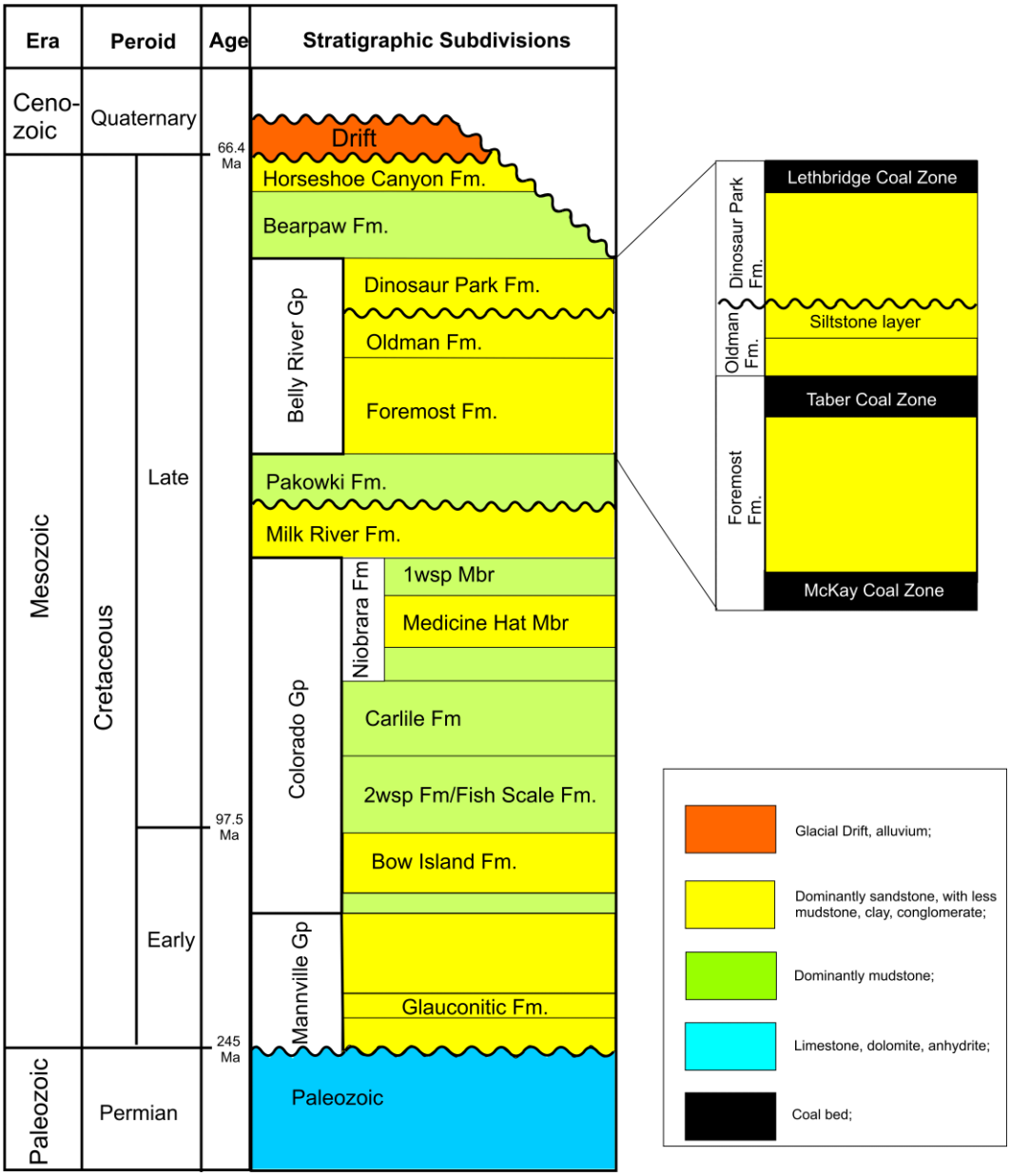


Figure 3.5 Stratigraphic table of the study area. Figure modified from *Glombick et al.* [2014].

### 3.2.1 Mannville Group

At the bottom of the Cretaceous bedrocks, the northwestwards dipping clastic layer of the Mannville Group lies immediately on the Paleozoic carbonates. [*Cant and Stockmal*, 1989; *Smith*, 1994]. An unconformity surface truncating the strata from lowermost Cretaceous to Paleozoic was developed due to the erosion from the major drop of sea level in the Jurassic which results in the loss of 140 Ma of strata [*Smith*, 1994]. The Mannville Group is the oldest basin-wide Cretaceous rock and the strata are complex and heterogeneous across the WCSB. Based on the lithology variations, it is divided into lower and upper groups. The lower group is a thin and sandstone-dominated layer that is rich in quartz and cherts, whereas the upper interval contains more volcanic and feldspathic materials [*Christopher*, 1974; *Glaister*, 1959; *Mellon*, 1967; *Williams*, 1963]. In southern Alberta, the lower Mannville strata are generally continental and dated to be of Aptian age (~ 125 Ma). The depositional environment was strongly influenced by huge valley systems and Cordilleran tectonic activities during late Aptian time [*Christopher*, 1984; *Smith*, 1994]. The rock is rich with quartz and cherts and does not contain much igneous detritus, indicating Cordilleran source rocks [*Hayes et al.*, 1994]. The Glauconitic sandstone formation lies on the bottom of Upper Mannville strata and records the maximum transgression of the Moosebar/Clearwater Sea; this layer is capped with fluvial and estuarine facies [*Farshori*, 1983; *Hopkins*, 1987; *Hopkins et al.*, 1982]. The overlying sediments in the Upper Mannville Group are complex and heterogeneous due to the unstable depositional environment including tidal reworking undulations, valley incisions, and Cordilleran tectonic events during the Albian time (~ 113 Ma) [*Hayes et al.*, 1994; *Wood and Hopkins*, 1989].

### 3.2.2 Colorado Group

During Middle to Late Albian time (100-107 Ma), the shaly Colorado units started deposition on the top of the sandy Mannville rocks [*Smith*, 1994]. This interval is dominated by marine mudstone interspersed with thin sandstone and conglomerates [*Leckie et al.*, 1994]. As mentioned by Podruski [1988] and Porter [1992], it is one of the richest strata and contains nearly 14 percent of the total western Canada hydrocarbon reserves. The Colorado Group is divided into upper and lower subgroups that are separated by the organic-rich Fish Scale Formation [*Rudkin*, 1964]. The basal Colorado unit is a thin sheet-like sandstone layer overlying the non-marine Mannville Group [*Banerjee*, 1989]. The upper units within Lower Colorado Group are composed of the sandy Bow Island Formation and the shaly Westgate Formation [*Leckie et al.*, 1994]. In the Upper Colorado Group, the Fish Scales, the Second White Specks, the Carlile and the Niobrara Formations were deposited in a predominantly marine environment. During Late Turonian and Late Santonia time (~ 90Ma), several regressive periods result from the global sea-level drop, which led to the coarse clastic wedges of Cardium and Medicine Hat sandstones that settled on the thick upper group marine shale [*Leckie et al.*, 1994].

### 3.2.3 Milk River Formation

The early Campanian Milk River Formation is a typical sandy clastic sediment in southern Alberta [*Dawson et al.*, 1994]. It is considered to represent the first significant marine regression in the active marine environments during the Late Cretaceous [*Payenberg et al.*, 2001]. On the sonic and resistivity well logs, it shows an obvious shoulder-like transition and has been applied as a major marker to identify the stratigraphic sequence boundary [*Leckie et al.*, 1994]. In southern Alberta, the Milk River Formation is exposed along Milk River due to the erosion dominated in Quaternary period, and it mainly consists of medium grained

sandstones interbedded with siltstones of the Virgelle and Alderson Members. As documented by *McNeil and Caldwell* [1981], there are nearly 150 billion $m^3$ of recoverable gas reserves in the "Milk River" gas pool, which formed from late Santonian to early Campanian [*Sweet and Braman*, 1990]. Following the deposition of this sandstone layer, an obvious marine regressive event removed the capping strata on the surface and resulted in a basin-wide unconformity contact [*Rosenthal and Walker*, 1987]. This unconformity is characterized by chert-pebbles that separate the Milk River strata from the overlying Pakowki marine shale [*Braman and Hills*, 1990].

### 3.2.4 Pakowki Formation

The Pakowki Formation is a thin marine shaly layer overlying the sandy Milk River formation. This fine sediment indicates a distinctive marine transgression in the Late Campanian (~75 Ma) [*Dawson et al.*, 1994]. It mainly consists of dark gray to brown mudstone and siltstone, and the base contact is an unconformity with chert and pebble lag [*Rosenthal et al.*, 1984]. During the Campanian period (~ 83Ma), the transgression of the Pakowki Sea and the uplift of the Bow Island Arch were the major events that affected the local deposition. As a result, the layer was thicker eastwards with a gradational top attached with the Belly River interval. The time of this period was proved to be short-lived in southern Alberta, and is associated with the rapid fall of the sea-level [*Dawson et al.*, 1994].

### 3.2.5 Belly River Group

Above the marine shaly layer of the Pakowki Formation, the coarsening clastics of the Belly River wedge deposited in a continental environment during the Late Campanian [*Dawson et al.*, 1994; *McLean*, 1971]. Sediments, which mainly have a fluvial origin, consist of light gray to buff, medium- to fine- grained sandstone and siltstone [*Jerzykiewicz*, 1985]. In most areas of southern Alberta, the Belly

River Group is comprised of three units. From oldest to youngest, these are the Foremost, Oldman, and Dinosaur Park Formations [*Koster*, 1984].

The Foremost Formation is the lowest interval deposited under the transitional environment from coastal to shallow-marine. The lower contact is characterized as the boundary of the first coarsening-upward cycle which is made up of the incised valley deposits [*Dawson et al.*, 1994; *McLean*, 1971]. The overlying strata in the Foremost Formation contain a series of marine sandstones, mudstones, and siltstones; two thin coal beds are recognized as bounding its top and bottom surfaces. These are named the Taber and the McKay coal zones, respectively.

Above the Foremost Formation, an interval comprising a 'siltstone unit' and a sandstone unit is recognized as the Oldman Formation. The top of this 'siltstone unit' is considered as the regional discontinuity that separates the overlying Dinosaur Park Formation from the Oldman Formation, which primarily comprised of pale-colored, thin noncalcareous mudstone and fine sandstone [*Glombick*, 2010; *Hamblin*, 1997]. On the top of the Belly River Group, another thin coal seam called the Lethbridge coal zone is found in the Dinosaur Park Formation. An interbedded bentonite and carbonaceous mudstone is locally observed where the coal bed is absent. [*Glombick*, 2010; *Russell and Landes*, 1940].

### 3.2.6 Bearpaw Formation

During the latest Campanian time (~72 Ma), the fine-grained Bearpaw Formation was deposited over the coarse-grained sandstones of the Belly River Group. In many areas, the Bearpaw shale or mudstone layer directly overlies the Lethbridge coal beds, while in other areas, a thin oyster bed, chert-pebble conglomerate of around 1-3 m thickness can be observed between the Bearpaw Formation and underlying Lethbridge coal beds [*Glombick*, 2010; *Russell and Landes*, 1940].

The Bearpaw Formation is mainly comprised of laminated shale and siltstone, with some sandstone beds and claystone [*Habib*, 1981; *Macdonald et al.*, 1987]. The Bearpaw-Belly River contact is sharp and notable, hence it provides a good stratigraphic marker due to the apparent transition from heterogeneous rocks to homogeneous sequence.

### 3.2.7 Horseshoe Canyon Formation

The Horseshoe Canyon Formation is the youngest outcropping bedrock within the study area [*Glombick*, 2010]. It settled on the top of the Bearpaw shale during the drop of the sea-level and mainly consists of interbedded sandstone, siltstone, and mudstone with extremely rich coal beds [*Dawson et al.*, 1994]. This Formation is the shallowest layer within the study interest due to the high erosion in Tertiary period.

### 3.2.8 Eroded strata

It is important to notice that, in WCSB, significant erosion removed massive strata of Upper Cretacesous to lower Paleocene sediments due to the end of thrusting in the thrust-fold belt in the Early Eocene (~47 Ma - 56 Ma) [*Glombick et al.*, 2014]. According to the diagnostic moisture feature of the coal beds, *Nurkowski* [1984] suggested that around 900 -1900 m of overlying sedimentary rock has been removed due to post-orognic uplift and erosion. He also pointed out that almost 1500 m of sedimentary strata have been eroded near Bow City. In addition, more evidence of the substantial erosion was observed on the stratigraphic section by *England and Bustin* [1986]. They deducted an erosion of 1450-1500 m overburden has occurred since Oligocene time (~ 28 Ma). Later studies carried out on authigenic clays indicated an erosion of 1500 m of the strata in Upper Cretaceous and Paleocene [*Khidir and Catuneanu*, 2009].

### 3.2.9 Bedrock Signature on Geophysical Logs

In the vicinity of the study area, more than 1000 wells were examined by Dr. *Glombick* [2010] and significant stratigraphic intervals were divided for geological mapping [*Glombick*, 2010]. As such, two representative wells (00/08-28-017-18W4/0 and 00/22-10-017-18W4/0 shown in Figures 3.6 and 3.7) are selected to display the log signatures of the stratigraphic units. Wellbore 00/08-28-017-18W4/0 was drilled vertically from 831.5m above sea level (a.s.l) datum to a total depth of 633.5 m in 2001. It shows the information from the Bearpaw Formation in Late Cretaceous to the Medicine Hat sandstone in Early Cretaceous. In this well, geophysical logs, including natural gamma ray (GR), spontaneous potential (SP), acoustic (DT) and density logs (RHO) are obtained to identify the different facies. Because it is not deep enough to penetrate the Colorado Group strata, another well is chosen to illustrate the lower strata from the Late Cretaceous to the Paleozoic Unconformity. Wellbore 00/22-10-017-18W4/0 is a vertical drilled gas well from 837.20m a.s.l datum to -377.80 m a.s.l. Due to the sufficient geophysical logs data, accurate well tops are identified with a combination of natural gamma ray (GR), spontaneous potential (SP), caliper (CAL), density (RHO), acoustic (DT), and resistivity (RES). The geological units can be picked from the shallow coal layer in the Foremost strata to the bottom of the Paleozoic unconformity.

The boundary between the Bearpaw Formation and Belly River Group is the uppermost visible stratigraphic interface in Wellbore 00/08-28-017-18W4/0. In general, the log responses of the heterogeneous Belly River sandstone succession are more spiky and serrated than the overlying shaly Bearpaw units. An abrupt transition from the mudstone-rich Bearpaw interval to the Lethbridge coal layer lying on the top of the Belly River Group is indicated by the low density and the high apparent neutron-porosity character. The increasing gamma ray, resistivity, and sonic values also exhibit the response of this coal layer. Beneath this coal bed,

the underlying siltstone layer in the Oldman Formation is marked most obviously by an increased gamma ray response. The following gamma ray decrease is suggestive of another sandstone unit in this unit. Correspondingly, the sonic log values turn from high to low because of a high velocity signature in sandstone. Marked by high neutron porosity and low density values, the Taber coal bed on the top of the sandy Foremost Formation is observed. A similar response is seen on the bottom of the Foremost Formation, which is interpreted as the McKay Coal Formation.

Below the sandy Foremost interval, a thin marine shale unit of the Pakowki Formation is easy to identify with a combination of gamma ray, spontaneous potential, and neutron-porosity logs. The corresponding high gamma ray, flat spontaneous potential, and high neutron-porosity signatures are presented. Going deeper, a second clear increase in both the sonic and resistivity logs is detected. This abrupt change, which shows as a shoulder-like structure, is considered to be an apparent marker of the Milk River sandstone layer.

Indicated by the high gamma ray response, the transition from the Milk River sandstone to the thick marine shale in the Colorado Group is easily distinguished. Within this shale/mudstone-dominated Colorado unit, three sandstone intervals could also be detected by the varied gamma ray, resistivity, and porosity logs. The first marker near the top of the group is the Medicine Hat Sandstone Formation. It is a transition contact from shale to sandstone units with a low gamma ray value and deflected spontaneous potential response. The next marker for the Second White Speckled Shale Formation is characterized by high radioactivity and hydrogen, which is represented by high gamma ray and high neutron-porosity on well logs. It is difficult to separate this formation from the underlying Fish Scale Zone, whereas the base of the Fish Scale Zone is easily indicated a by a sudden drop in the gamma ray response. The underlying marine sandstone of the Bow Island Formation is characterized by low but highly varying and heterogeneous

gamma ray values. The spiky and deflected spontaneous potential curve is suggestive of the sandstone interval as well.

Below the thick marine shale of the Colorado Group, decreasing gamma ray, deflected spontaneous potential, and increasing resistivity are seen on the log curves. These contrasts reveal the appearance of the Mannville sandstone. As this interval is sitting in the deep sediments that present less damaged features, only one marker, the Glauconitic sandstone, is interpreted from its low gamma ray, low neutron-porosity, and high resistivity values. The base contact between Mannville sandstone and Paleozoic carboniferous is readily detected a by a significant drop in the spontaneous potential, the density, and the neutron-porosity values.

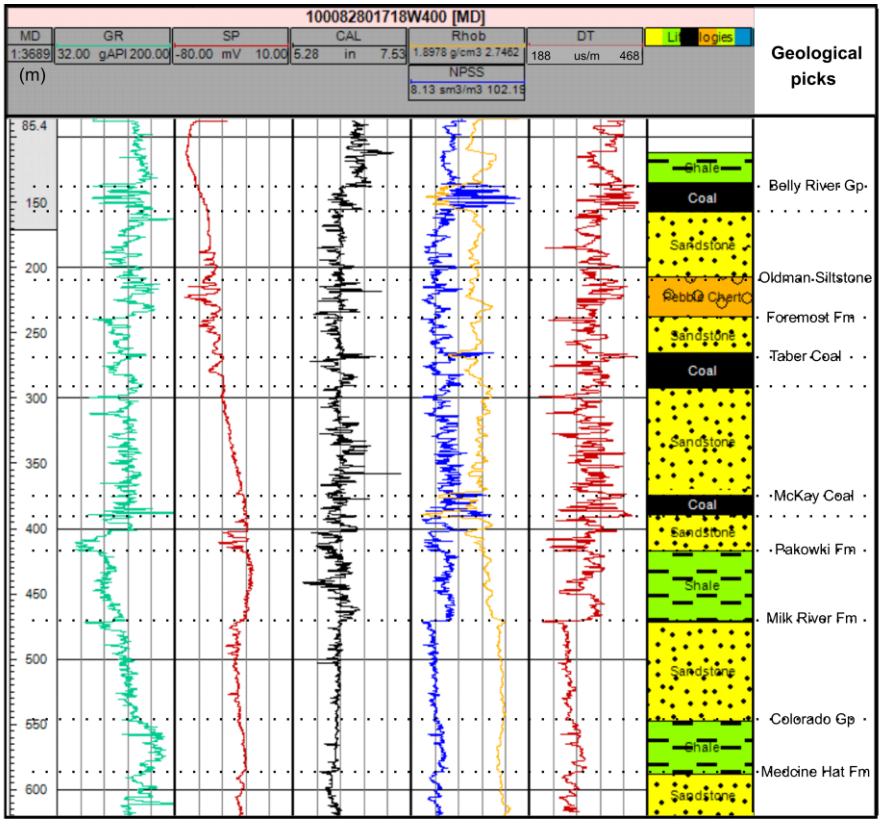


Figure 3.6 Geophysical well logs from well 00/08-28-017-18W4/0, showing detailed shallow Cretaceous stratigraphy mapped in the vicinity of the Bow City structure. Logs are shown in measure depth in meter from ground level 831.5 m a.s.l. From left to right, logs are gamma-ray (API), spontaneous potential (mv), Caliper (inch), neutron porosity (%, sandstone calibration), density and sonic (us/m). The last track in the right is the lithology of different units. Grey dotted lines mark the boundary between different formations [*Energy*, 2011].

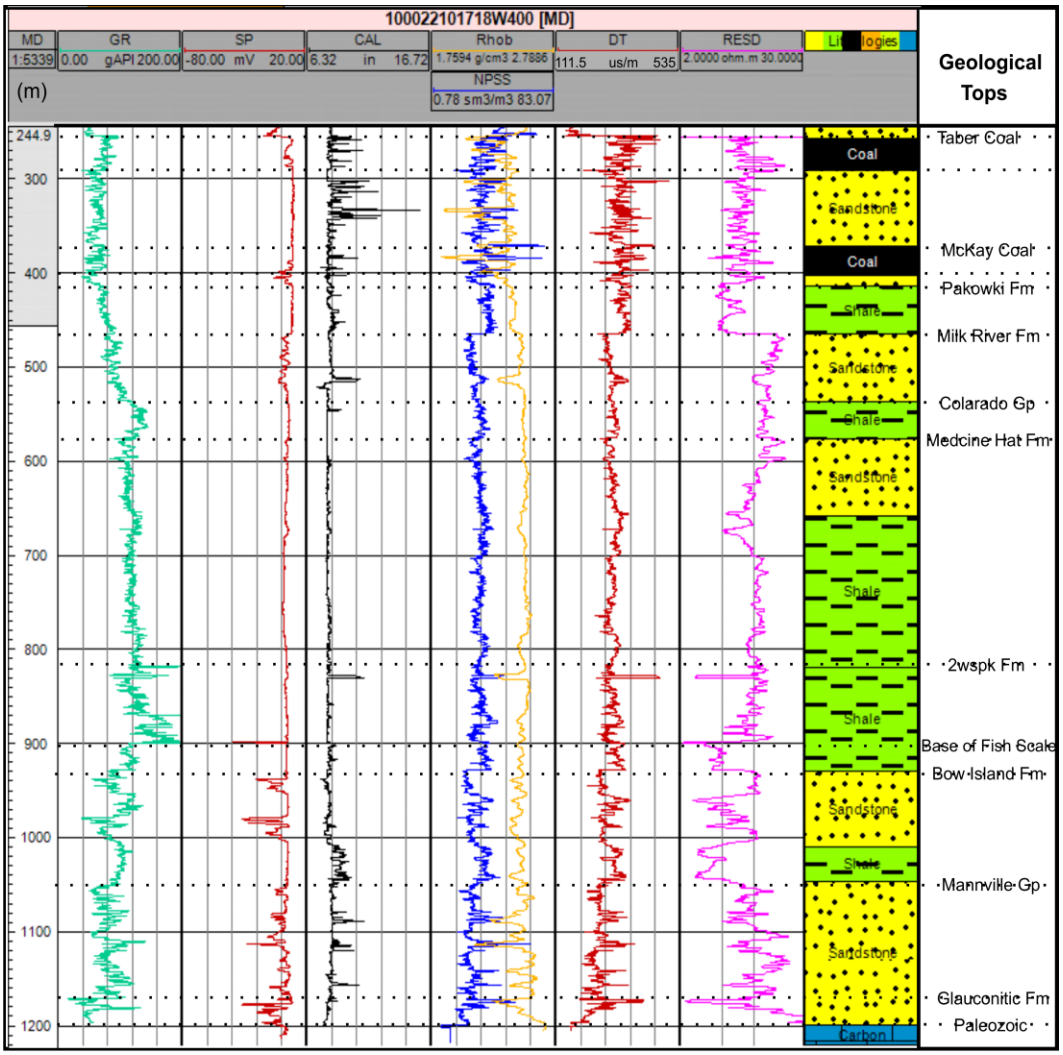


Figure 3.7 Geophysical well logs from well 00/22-10-017-18W4/0, showing detailed Cretaceous stratigraphy mapped in the vicinity of the Bow City structure. Logs are shown in measure depth in meter from ground level 837.2 m a.s.l. From left to right, logs are gamma-ray (API), spontaneous potential (mv), Caliper (inch), neutron porosity (%, sandstone calibration), density(g/cm$^3$), sonic (us/m) and resistivity. The last track in the right is the lithology of different units. Grey dotted line marks the boundary between different formations [*Energy*, 2011].

## 3.3 Early Mapping

To our knowledge there has been little discussion of the special geological features associated with the Bow City structure. This is in part likely due to the fact that there is only limited outcrop along the Bow River. That said, there are two historical pieces of information worth mentioning.

In 1929, two exploration wells (Hudson's Bay Oil and Gas, Eyemore) were drilled near the exposed Belly River Group rocks within the centre of the structure. There is no mention of why these wells were drilled at that time. It is likely that these rather early wells were drilled based on the nearby dipping structures seen in the outcrop on the Bow River.

The first mention in the literature that unusual structures existed occurred in the 1940's. *Stewart* [1942, 1943] reported the anomalous structures detected during surface bedrock mapping on the west bank of Bow River (Figure 3.8). This record is considered to be that discovery of the Bow City structure that is the subject of this thesis. In the report, Stewart wrote:

*"One group of faults is mapped on Bow River near Eyremore* (i.e. a school on the south bank of the Bow River). *There a downfaulted block of the Edmonton has a vertical stratigraphic displacement of about 300 feet. The strike of the individual faults could only be determined approximately."*

*"… located on a faulted inlier of the Oldman formation and on beds that, where exposed about a mile to the east of the well, show some steep dips".*

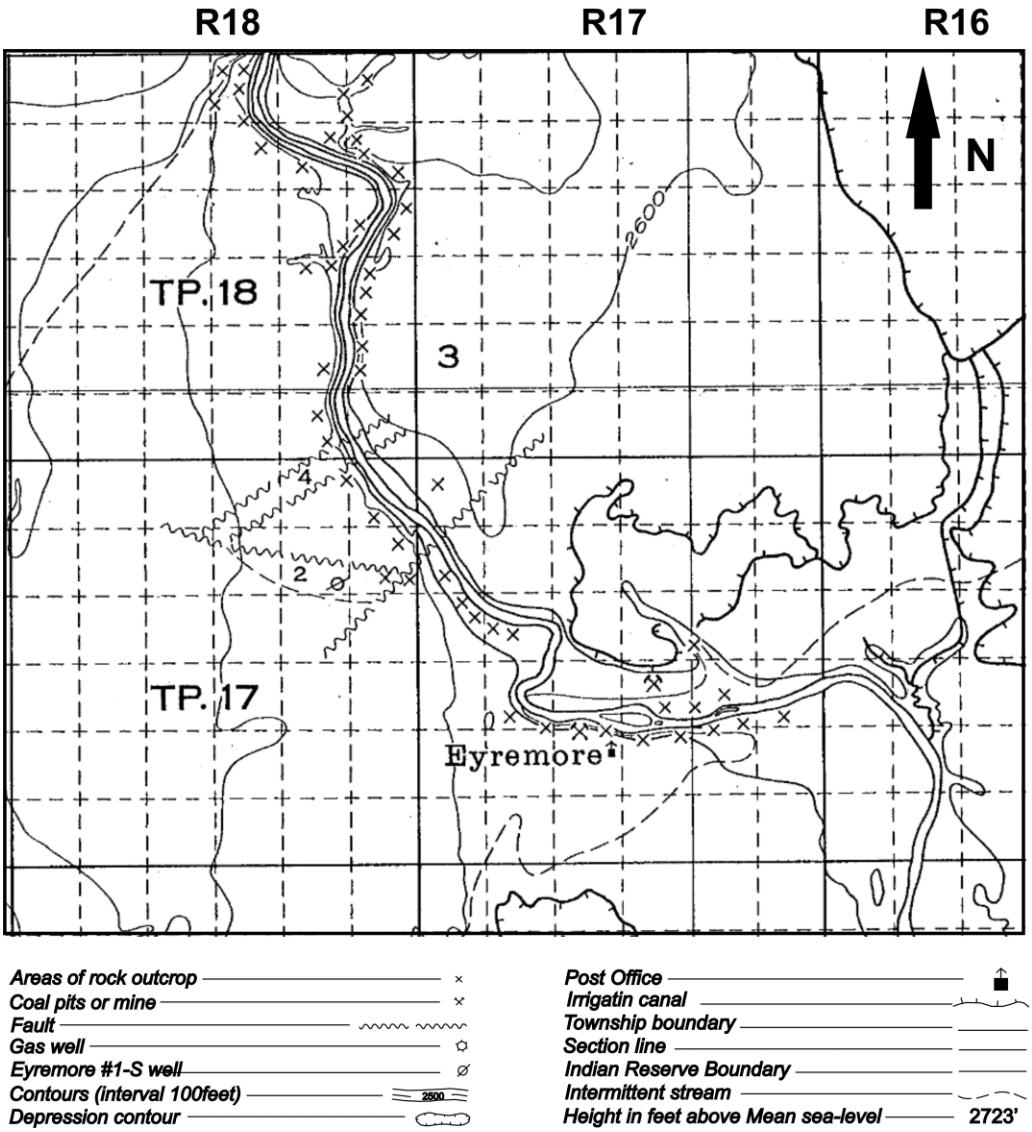


Figure 3.8 Geological map from *Stewart* [1943] showing the Township 17-18 from Range 16 to 18 west of the 4th Meridian.(2) Oldman Formation (now subdivided into Dinosaur Park and Oldman Formations).(3) Bearpaw Formation.(4) Edmonton Group (Horseshoe Canyon Formation). Figure is modified from *Stewart* [1943].

## 3.4 Structure mapping from well log data

In order to extract more information to characterize the structure features, a number of wells (1044) within the studied structure were examined (Figure 3.9). Apparent geological well tops in Cretaceous period were picked by Dr. Glombick [2010] to further generate the structure maps of the subsurface geological units. The log data were obtained from the IHS AccupMap® database and the geological well tops were marked using IHS Petra®. Based on the log signatures of different formations as discussed in the last section, most of the units can be identified confidently by a combination of the Gamma Ray, Spontaneous Potential, Sonic, Density, Neutron-porosity, and Resistivity logs.

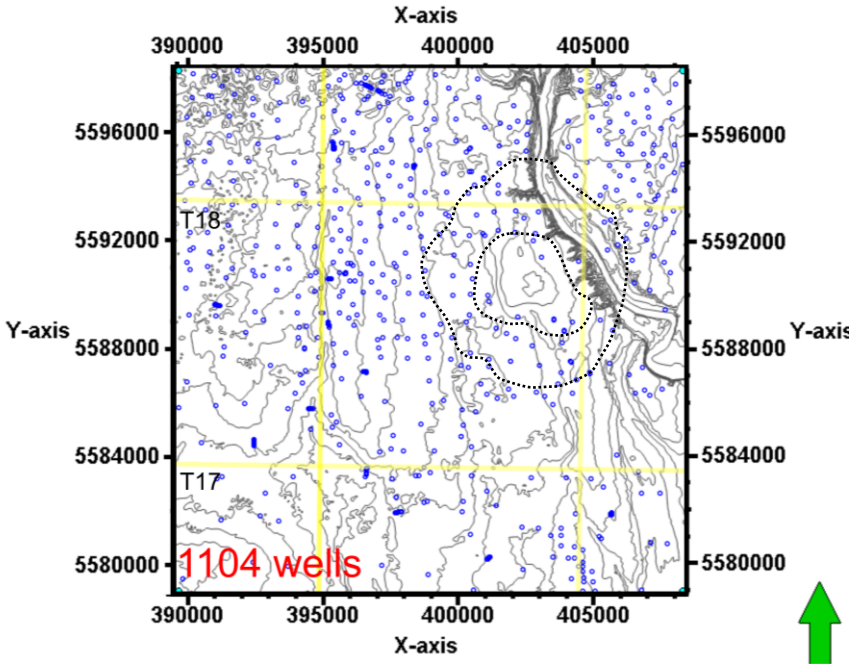


Figure 3.9 Location map of the wells utilized in this study. Coordinates are in 12N NAD83. Yellow lines show the township boundaries. Blue circles represent the wells. Dash lines show the estimated outline of the structure.

It is important to examine the structure maps to show the topographic features of near-surface geological units (Figure 3.10). Indeed, it is such data that shows us the first clue that identify this buried anomalous structure as a potential impact crater. Figure 3.10 shows the structure maps created from 10 distinctive geological tops from the uppermost Belly River Group (Dinosaur Park Formation) to the deepest Paleozoic Unconformity. These maps are generated with a convergent interpolation gridding algorithm where the gridding cell size is 50m x 50m. Some attention should be made during the interpretation since specific geological markers are missing in some wells because of the disruption, and the data density varied for different maps. Regardless, these contour maps are still geological meaningful and point out the abnormities of the buried structure, particularly with respect to the otherwise almost flat-lying layering.

The most obvious feature can be observed on the uppermost (a) Belly River Tops map, namely is the 'ring-like' depression. It displays an outline with a semi-circular depression and an apparent high uplift region in the central core. The elevation difference between the highest point within the central peak to the lowest point in the annulus region is almost 110 m. Moving into the deeper units, this 'ring-like' feature is still seen in (b) the Oldman and (c) the Foremost maps but it becomes less distinctive with a difference of 70m in elevation. At the depth of (e) the Milk River 'Shoulder', the 'ring-like' character is almost gone and only several irregular high spots are visible with a maximum difference of 40 m in central uplift. Instead, moving down to (f) the Colorado Group, the central raised zone transforms into a low depressed region and a clearer regional trend dipping westwards appears across the entire map. This low zone is still well-defined in the deeper (g) Medicine Hat sandstone interval, but gradually disappears in the Lower Colorado units of (h) the Bow Island and (i) the Mannville Group. On the bottom (j) Paleozoic Unconformity map, a flat and gently dipping surface is seen, which is expected as the normal geology feature. This means that any deformations associated with the structure could not be detected at this depth.

Examination of the thickness maps of geological formations are also important and necessary to bring up more detailed structure features. Figure 3.11 shows the isopach maps of the selected geological intervals. On (a) the Dinosaur Park Formation map, an apparent thickening zone is detected in the middle of the structure. This interesting and complex feature can also be observed on the map of (b) the Oldman Formation and appears most clearly as a ring-shape thinning on (c) the Foremost Formation. However, it gradually decays going deeper, and only the central thickening area is present at (d) the Milk River Formation. Much less evidence for any damage can be observed from deeper isopach map in (e) the First White Spectacled and (f) Mannville Group, except for localized thinning and thickening spots.

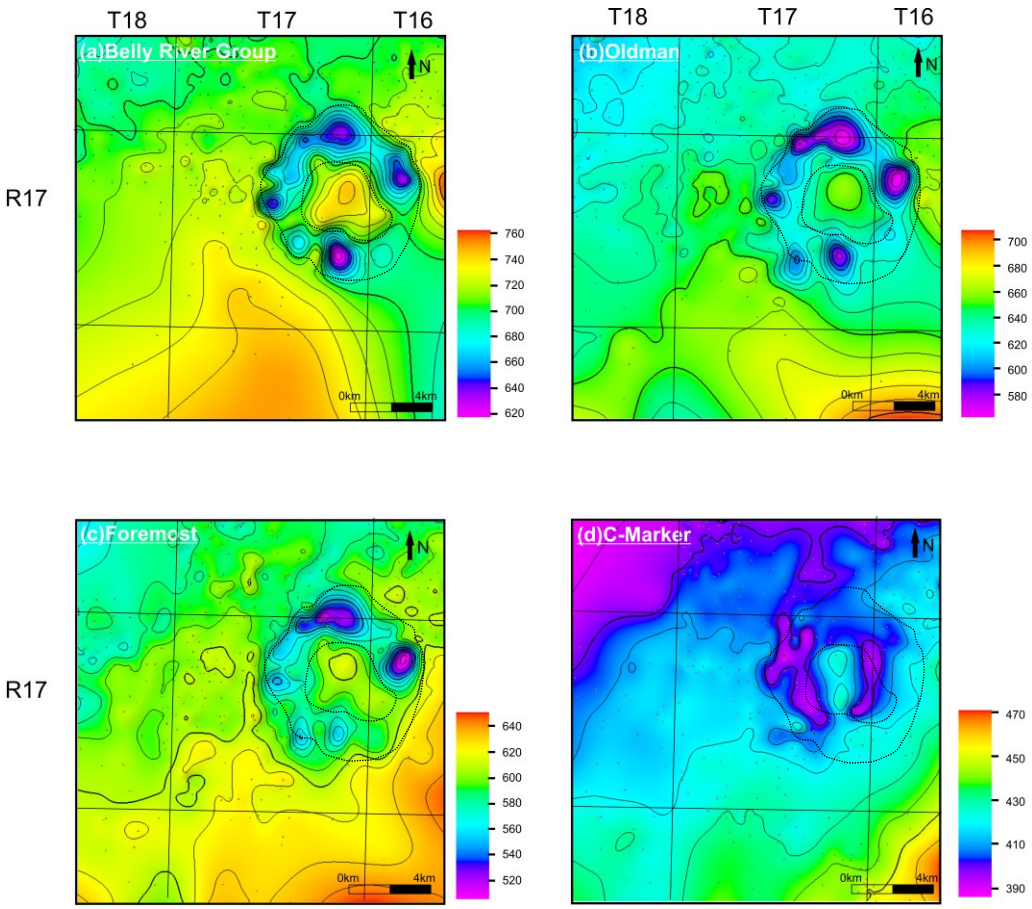

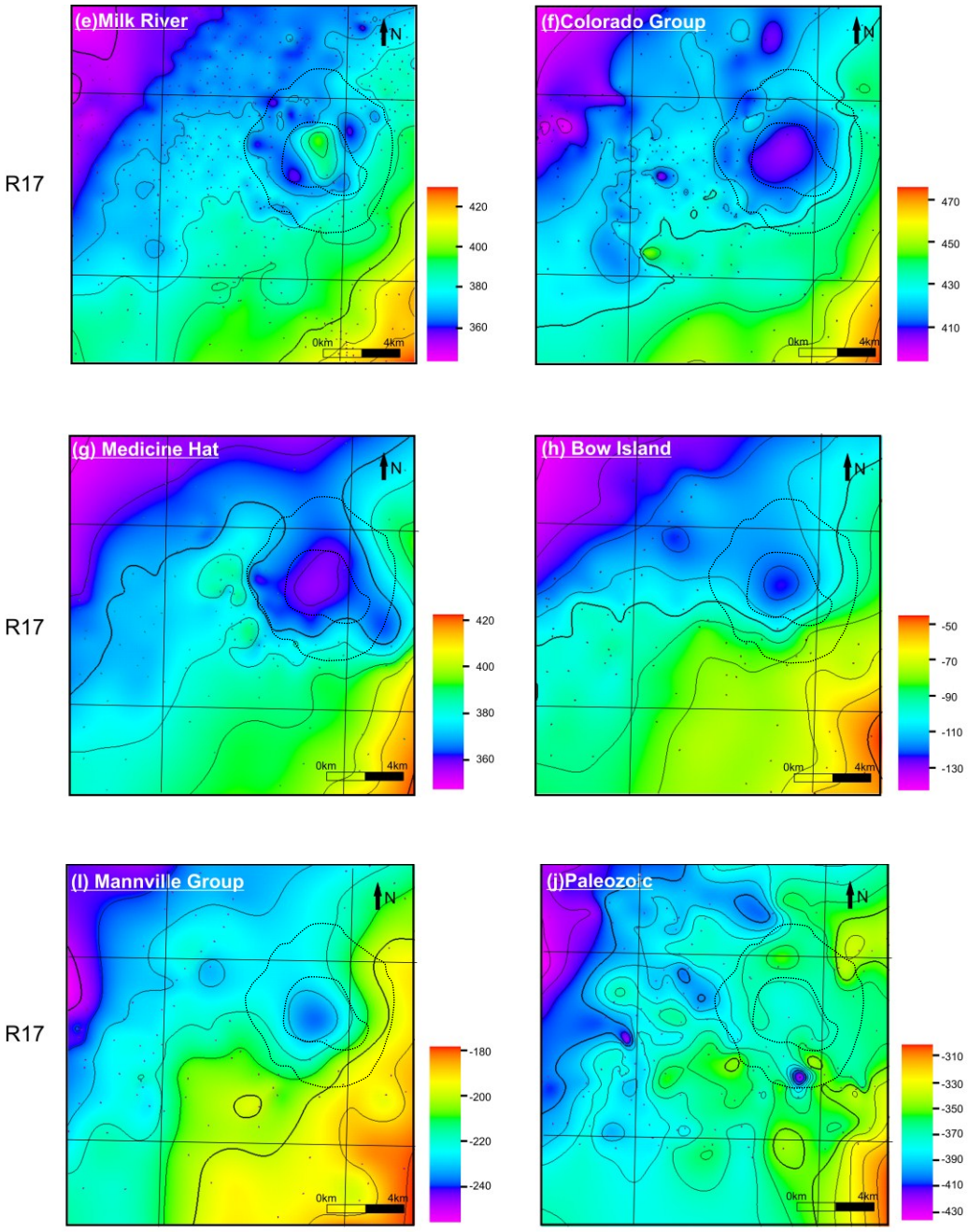


Figure 3.10 Structure maps of geological tops in the Cretaceous peroid procgessing from least shallow (a) the Belly River Goup to deepest (j) the Paleozoic. The black dotted curve is the estimated structure outrim and central high region from the elevation contrast. Data are obtained from Dr. Glombick.

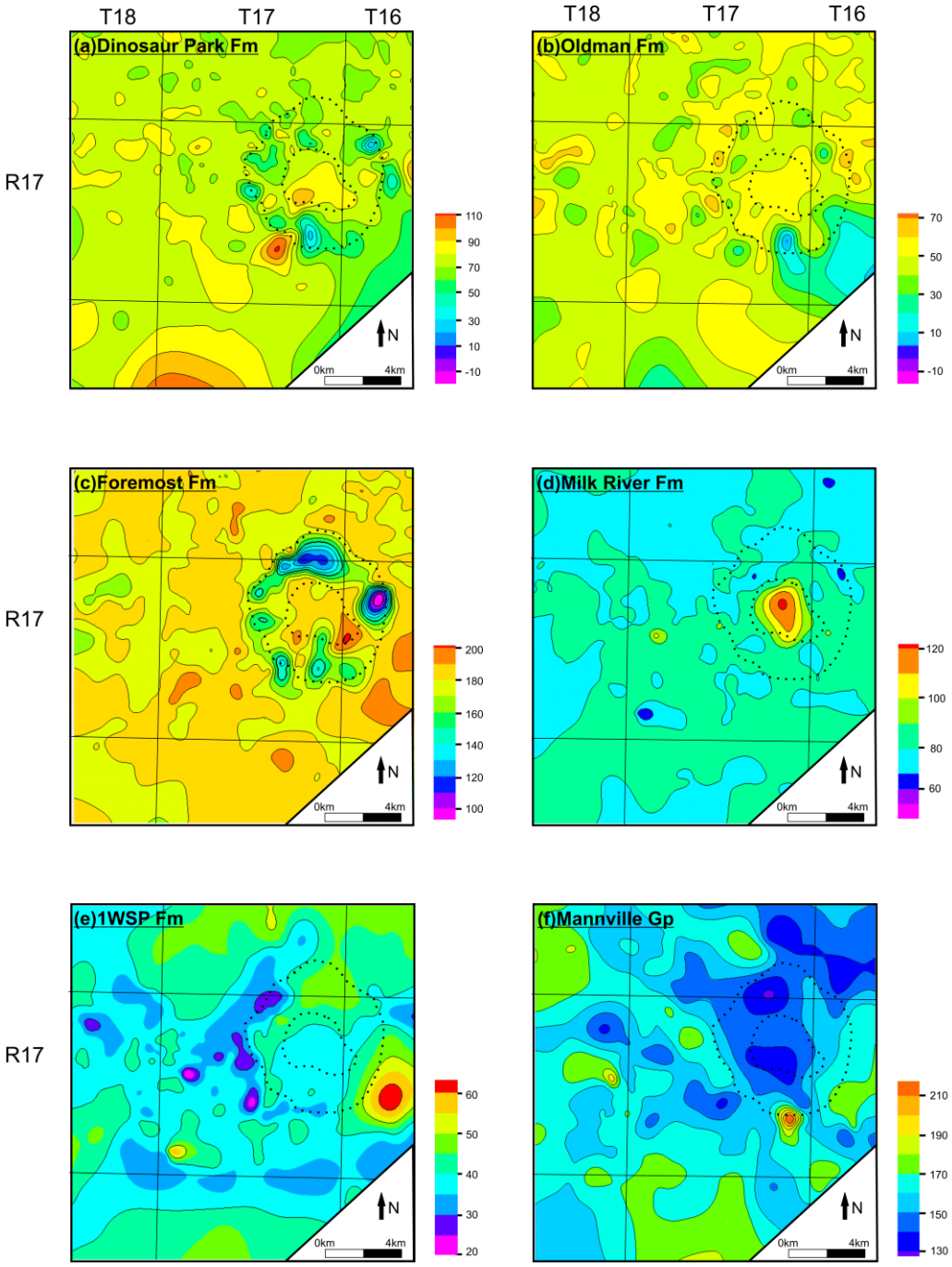


Figure 3.11 Isopach maps of selected geological intervals increasing with depth. The dotted black curves show the estimated structure outer rim and central peak. Data are obtained from Dr. Glombick.

## 3.5 Field Observation

Based on the previous abnormal faults identified by Stewart [1942, 1943] and the initial evidence noticed by Dr. Glombick [*Glombick*, 2010] during the subsurface bedrock mapping, Dr. Hathaway and Dr. Banks from AGS carried out a brief photographic reconnaissance in 2010 along the west bank of Bow River. Later in the summer of 2013, another geological reconnaissance conducted by Dr. Schmitt's group was able to collect more information to show the structure anomalies (Figure 3.12).

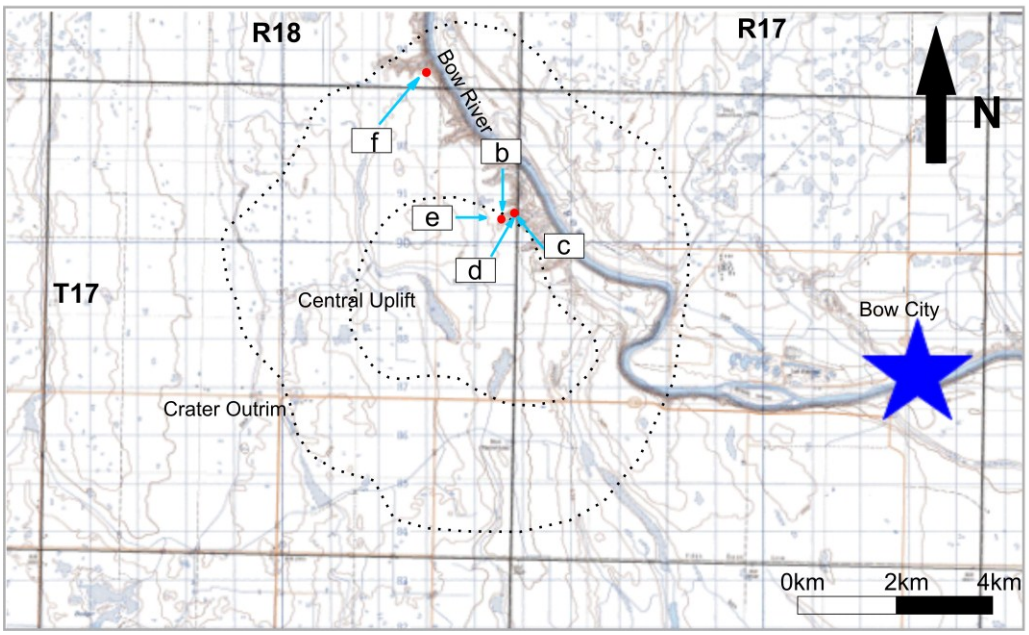


Figure 3.12 Location and photographs of the outcrop exposed along the west bank of Bow River. a) Location map of the pictures (shown as red dots). Letters with arrows indicate location where the photographs were taken. Black dot curves are the contours of the crater outer rim and central uplift region estimated by geological structure mapping. The red lines in each photograph draw attention to the individual features discussed below. b) Exposed outcrop of sub-horizontal Dinosaur Park Formation with normal listric faults and reverse thrusting faults. c)

Photograph of the Dinosaur Park Formation showing steeply-dipping beds of ironstone and coal overlying coaly shale. d) North side view showing the reappearing Dinosaur Park Formation with relatively steep dipping beds and high angles thrust faults. e) Close up view of the outcropped Dinosaur Park Formation rocks showing localized normal faults in sub-horizontal beds. Note nearly horizontal beds on left and relative steep strata on the right. f) Panoramic view showing the transition from the almost flat-lying Horseshoe Canyon Formation overlying on the steep dipping Bearpaw Formation. Photographs are taken by B. Hathway (AGS), C. Banks (AGS) and Randy Kofman (UofA).


c


d

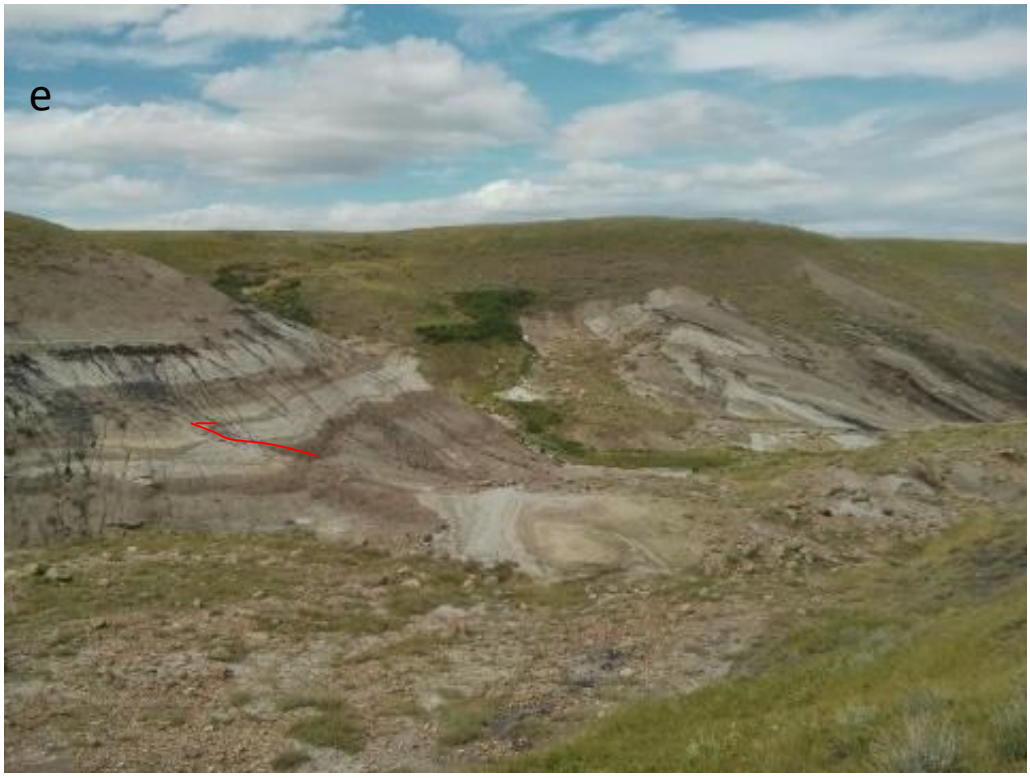
e


f

## 3.6 Summary

The geology of the Cretaceous bedrock in Bow City area has been reviewed in this chapter. Geophysical well log signatures and field mapping within the structure region have also been discussed. During the Cretaceous period, the tectonic events and regional geology in southern Alberta is relatively simple with several eustatic movements. Therefore, the Cretaceous strata laid uniformly on the Paleozoic carbonate with generally dipping towards the west. Though there are no obvious morphological characters to show the structure anomalies at the surface because of the glacial deposits and highly erosion during Quaternary period. It is important to notice that the unexpected structures including thrusting faults and normal faults were observed in this geological simple region. The youngest exposed disruptive rocks in Horseshoe Canyon Formation hints for the structures age as well. Furthermore, the geophysical seismic study was inspired to carry out to delineate more detailed features.

# Chapter 4 Regional Seismic Surveys[1]

The seismic reflection method has been widely recognized as one of the best techniques to study impact craters, particularly because, as noted in earlier, many impact structures are hidden within sedimentary basins [*Stewart*, 2011]. In this chapter, the reprocessing and interpretation of a number of legacy 2D reflection seismic profiles are discussed. These profiles were donated to the University of Alberta for use in this study by a number of petroleum companies (see the acknowledgements section) after the Alberta Geological Survey had asked for assistance. The primary goal of analyzing these seismic profiles was to obtain more detailed information on the geological structure than can be achieved by mapping of geological formation tops alone [*Glombick et al.*, 2010].

This Chapter begins with a brief overview of reflection seismic profiling to familiarize the reader with this method of imaging the subsurface. This is followed by the specific detailed geophysical analysis procedures beginning with data acquisition and processing methodologies, 'calibration' of the reflection seismic profile with data from geophysical logs, final interpretations, and mapping of the geological horizons. One of the most important procedures to ensure the success of the interpretation, seismic data (re)processing sequences, will be discussed in Chapter 6,while the data analysis will be mainly focused on here. Also, it is vital to note that these data sets provide important input for designing the acquisition of the new seismic lines that will be discussed in Chapter 6.

[1].Much of the material in this chapter has been published in Glombick, P., D. R. Schmitt, W. Xie, T. Bown, B. Hathway, and C. Banks (2014), The Bow City structure, southern Alberta, Canada: The deep roots of a complex impact structure?, *Meteoritics & Planetary Science*. The author was primarily responsible for the analyses of the seismic data.

## 4.1 Seismic Methodology

The seismic reflection method was first pointed out by Canadian scientist Fessenden [1917], and currently is widely used in imaging the Earth's interior structures. In conventional seismic reflection studies, reflected waves are recognized as the dominant signals due to their characteristics strong energy and high speed. Although theoretically there is no depth constraint in the reflection method, the data quality is highly affected by the seismic sources and the geological environments [*Duo*, 2011]. The elastic waves generated from a surface energy source travel radially into the Earth. Every time the wavefront reaches the interface between two different rock types with contrasting velocities and densities, an upward seismic reflection is produced. These reflections propagate back to the surface where they are detected by various kinds of receivers, usually particle-velocity sensitive geophones, but more lately micromechanical accelerometers. The responses recorded by the geophones are digitized form and archived for later seismic processing.

There are two types of seismic body waves of interest in reflection seismology: P, or primary waves, and S, or secondary waves. Other surface related waves such as Rayleigh waves and Love waves, which propagate along the surface, are also recorded by the surface receivers but these provide little signal useful for purposes of reflection imaging and are usually considered to be noise for practical purposes.

P-waves ($V_p$) are characterized by particle motions that are parallel with the propagation direction. They are also variously referred to in the literature as primary, compressional, or longitudinal waves. They are the fastest and consequently are always the first-arriving signal recorded by the geophones (e.g., [*Sheriff*, 2002; *Yilmaz*, 2001]). The speed of the P-wave depends on the Lamé elastic parameter $\lambda$, the shear modulus $\mu$, and the density ($\rho$) of the medium that the wave is propagating in. The P-wave velocity is expressed as:

$$V_{p=}\sqrt{\frac{\lambda+2u}{\rho}} \tag{4.1}$$

The second type of body wave is the S-wave ($V_s$), which has a particle motion perpendicular to its traveling direction. It propagates at a slower speed and is mainly affected by the shear modulus ($u$) and the density ($\rho$) of the material:

$$V_{s=}\sqrt{\frac{u}{\rho}} \tag{4.2}$$

Compared with the body waves, surface waves that travel along the surface or the interface between the solid bodies are slower. The Rayleigh wave, one kind of surface wave, consists of both longitudinal and transverse motions [*Sheriff*, 2002]. These elliptical particle motions propagate through a plane that is perpendicular to the surface, and the corresponding wave energy decreases exponentially with depth in the Earth. The velocity of Rayleigh waves predominantly depend on the elastic constants of the medium and are actually just slightly slower than the shear waves. In seismic exploration recording, Rayleigh waves, often referred to more colloquially as ground roll, can significantly obscure the seismic reflected signals.

A second type of surface wave is the Love wave (formed from interfering SH waves), distinguished by the horizontal transverse particle motions to the propagation direction. Love waves are produced from the interactions of different shear waves and they require that the subsurface be layered to exist. They propagate at a speed slower than P- and S- waves but faster than Rayleigh waves [*Sheriff*, 2002; *Yilmaz*, 2001]. Indeed, by analyzing the spectral dispersion of the Rayleigh and Love waves, the velocity of S-waves of the subsurface material can be indirectly obtained [*Beaty and Schmitt*, 2003; *Pelton*, 2005; *Safani et al.*, 2005]. Regardless, such methods are not applied in this study and P-waves are considered as the primary signals.

In order to characterize the seismic waves travelling though the Earth, the concepts of wave fronts and ray paths are introduced. A wave front is the instantaneous locus in 3D of all the points to which the wave has just arrived at a snapshot in time. There are different ways to construct the wavefront and its continued propagation but the most intuitive is to consider each point on the wavefront as acting as a new source point according to Huygen's principle [*Yilmaz*, 2001].

A ray path is the route that the wave energy takes between two points and its propagation follows Fermat's law of minimum time (e.g., [*Gadallah and Fisher*, 2005]). As the seismic waves travel through the earth, they are refracted or reflected between the boundaries. According to Snell's Law, the geometry of the ray path across the interface can be described by:

$$\frac{sin\theta_1}{v_1} = \frac{sin\theta_2}{v_2} = p \tag{4.3}$$

where $\theta_1$ is the angle of incidence, $\theta_2$ is the angle of refraction, $v_1, v_2$ are the velocities in the respective medium, and $p$ is the horizontal slowness or the ray parameter. The ray parameter remains constant throughout the ray path. Figure 4.1 illustrates this geometry of seismic reflections and refractions. Consequently, the paths of the refracted and reflected waves can be predicted and the corresponding travel time and depth are accurately determined.

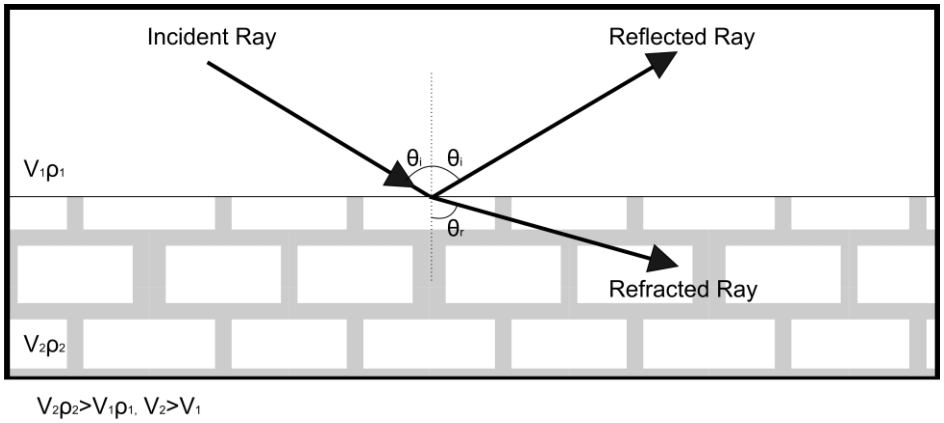


Figure 4.1 Diagram showing the reflection and refraction at an interface.

Besides, the amplitude of the reflected waves can be obtained from the reflection coefficient ($R$) which is defined as the contrast of the acoustic impedance ($Z$) between two media. The acoustic impedance ($Z$), a parameter measuring the physical property of the medium, is a product of medium density and seismic velocity. Hence, the reflection coefficient ($R$) for normal incidence reflections can be determined from

$$R = \frac{Z_2 - Z_1}{Z_1 + Z_2} = \frac{\rho_2 v_2 - \rho_1 v_1}{\rho_2 v_2 + \rho_1 v_1}, \tag{4.4}$$

where $R$ is the reflection coefficient between the two layers, and $\rho_1, \rho_2, v_1, v_2$ are the density and velocities of the two media respectively. The Zeoppritz equations are used if one wishes to examine the changes in the reflection co-efficient with angle of incidence [*Gadallah and Fisher*, 2005] although recently *Bouzidi and Schmitt* [2012] have questioned their validity when applied to interfaces with porous rocks.

In seismic survey, the seismic waves generated from the energy source are recorded by the geophones, which convert the ground motions to the electrical signals. The energy source is selected with the consideration of the local

environment, target depth, and economic cost. In most 2D seismic reflection surveys, either vibrators or explosives are the most common utilized source. As the energy is transmitting into the ground, the seismic waves are reflected on the different interfaces and a seismic shot record with a series of seismic traces is collected (Figure 4.2a). This record that consists of the traces produced from the same source location is called the common-source gather (CSG). In fact, the seismic refracted waves are obtained inevitably during the reflections survey and are recognized as the first arrivals on the shot gather. The travel times of reflected signals from the same interface vary with the distance (offset) between the source and the surface geophone as a hyperbolic curve. This is referred to as a hyperbolic *moveout*. In contrast, the refracted waves exhibit a linear moveout (Figure 4.2b).

A key geometrical factor that determines the propagation of the seismic waves is the midpoint, which simply marks the surface point that is equal-distant between the source and receiver. Indeed, sorting, flattening, and stacking the traces into a common-midpoint gather (CMP) that is comprised of the traces reflected at the same midpoint can better boost the signal-to-noise ratio (S/N) and display the subsurface structural pattern (Figure 4.3). Detailed CMP staking methods will be discussed in Chapter 6.

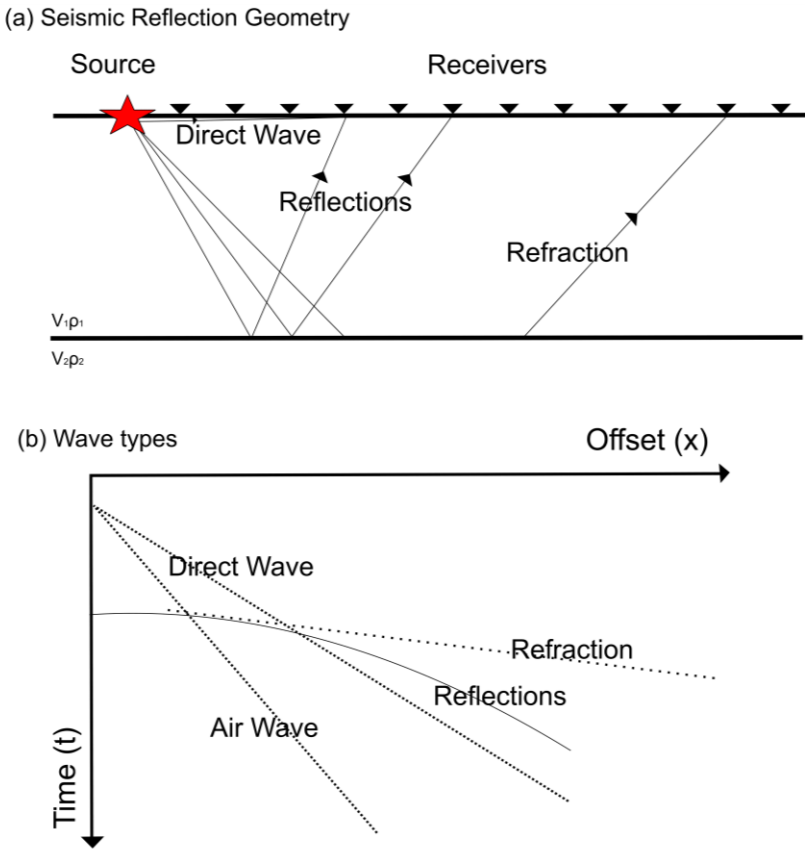


Figure 4.2 Illustration of the (a) Seismic reflection geometry and (b) the travel time versus offset curves (moveout) for differing seismic arrivals. Figure modified from *Duo* [2011].

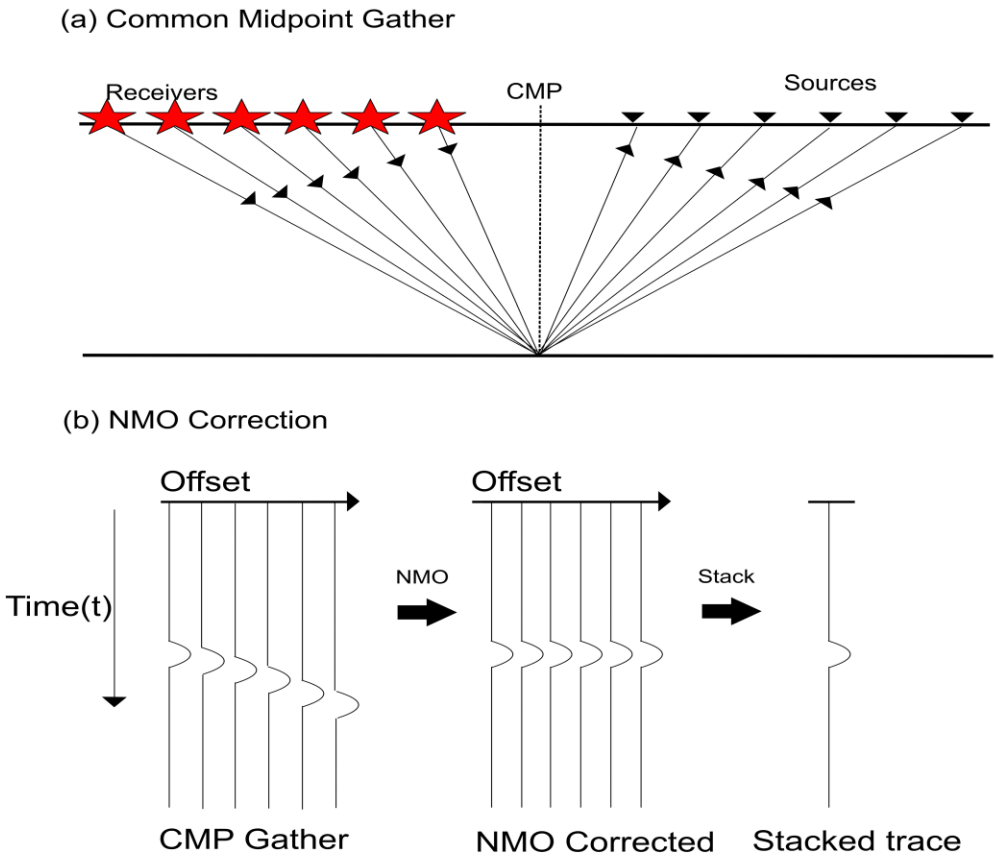


Figure 4.3 Diagrams showing (a) Common midpoint gather, and (b) NMO correction applied on the CMP gathers. From left to right, they are CMP gather, NMO corrected gather and stacked trace. Figure modified from *Duo* [2011].

In this study, seismic reflection (Chapters 4 and 6) and refraction techniques (Chapter 5) are used to construct images of the near-surface structural architecture. As shown by the examples of the first Chapter, the seismic reflection method has been recognized as a useful tool to detect the buried structures in the impact studies. Diagnostic features such as a circular depression, rim faults and an annular trough can be clearly observed on high-resolution seismic reflection profiles [*Mazur et al.*, 2000; *Osinski and Lee*, 2005; *Pilkington and Grieve*, 1992; *Westbroek*, 1997].

## 4.2 Data Overview

A series of 2D seismic profiles were donated by petroleum operators to aid in delineating the buried structural patterns. Reprocessing techniques and interpretations were applied to capture the structural anomalies. Figure 4.4 shows the locations of these seismic profiles and the relevant acquisition parameters are summarized in Table 4.1. It is important to note that these legacy lines were acquired for much deeper exploration. As such, the acquisition parameters were not optimal for imaging the shallow features of the structure. Despite this, they were invaluable to the initial reconnaissance aspects of our study as we were able to extract useful evidence that is consistent with an impact origin for the structure. A 3D seismic cube located in the southern edge of the studied structure was also donated to the project. However, due to the fact that it was acquired far away from the structure's centre and was aimed for the deeper targets, it did not provide any new additional insight and is not included in our analysis.

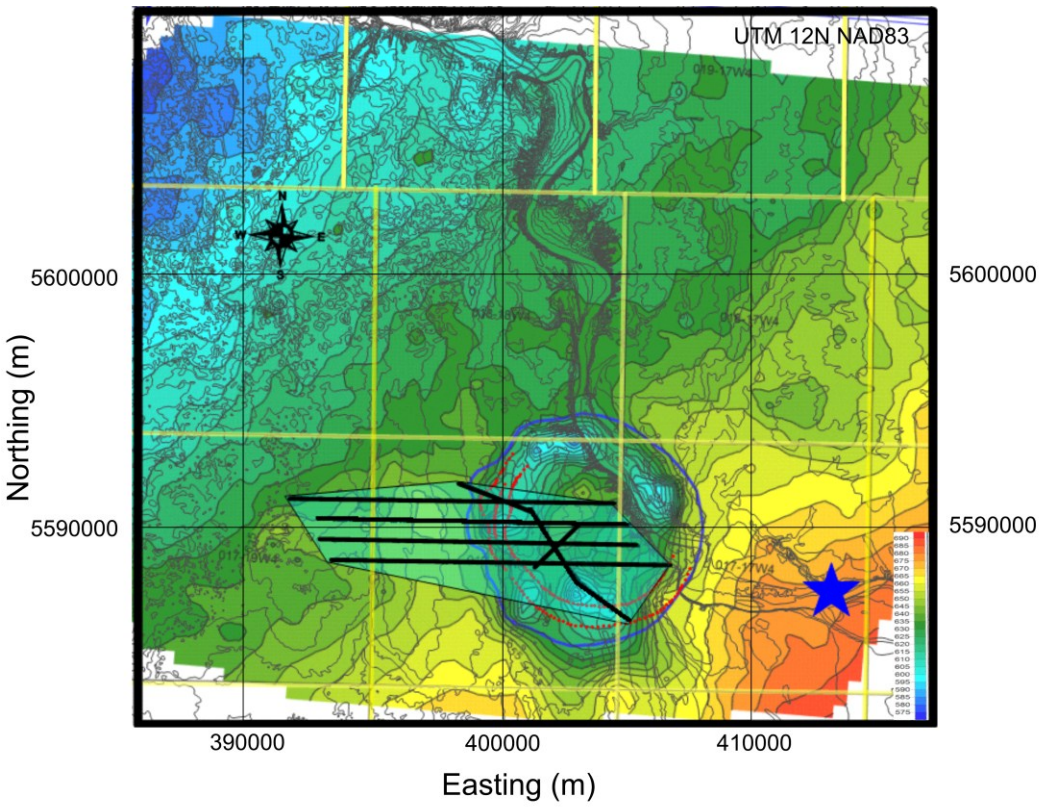


Figure 4.4 Location map showing the legacy seismic profiles utilized in this study. The colored contour map of the Oldman Formation top displays the local dipping direction towards the northwest. Thick black lines indicate the 2D seismic data. Red and blue curves represent the estimated faults patterns and the structure outline from seismic and well log data, respectively. The location of Bow city is represented by the blue star. Yellow grids show the township boundaries. Figure is modified from *Schmitt et al.* [2013] and *Glombick et al.* [2010].

Table 4.1 Summary of the acquisition parameters of the legacy seismic profiles.

| Line | Year | Source | Length (km) | Fold | Group/Source Spacing (m) | Group Configuration |
|---|---|---|---|---|---|---|
| ZCX-019 | 1979 | Dynamite | 8.21 | 4 | 33.5/134.1 | 9 over 34.1 m |
| 86-249 | 1986 | Dynamite | 13.24 | 12 | 20/100 | 9 over 20 m |
| 86-250 | 1986 | Dynamite | 11.97 | 12 | 20/100 | 9 over 20 m |
| 86-251 | 1986 | Dynamite | 11.61 | 12 | 20/100 | 9 over 20 m |
| 86-252 | 1986 | Dynamite | 12.67 | 12 | 20/100 | 9 over 20 m |
| EME001 | 1987 | Vibe 10-90 Hz | 2.48 | 15 | 20/80 | 12 over 20 m |
| EME004 | 1987 | Vibe 10-90 Hz | 5.5 | 15 | 20/80 | 12 over 20 m |
| EYE | 1994 | Dynamite | 3 | 20 | 10/60 | 9 over 20 m |

Survey ZCX-019 was acquired in the late 1970's and is the oldest seismic line we obtained for this study. This short profile was collected along Township Road 17-4 in the west bank of the Bow River. Due to the low fold and the large spacing of the source and receiver, the data quality, particularly the shallow portion is poor and useful information cannot be observed. Moreover, seismic Profile 86251 from Survey 86 was acquired along the same road in 1986. Therefore, Survey ZCX-019 was not included in the primary dataset for analysis.

Survey 86 was the second dataset donated to this project to carry out this seismic reflection interpretation. In terms of all the seismic data, Survey 86 provided the most completed and comprehensive evidence that verifies the structural irregularities. Serendipitously, these four 12 km parallel seismic profiles spaced 800 m apart approximately cover the entire west half of the structure as delineated

by the geological surface top mapping. In these surveys, the geophone groups were planted every 20 m and the dynamite source was fired every 100 m. The closer shot/receiver spacing and higher fold (compared with the older ZCX-019) provide significant improvements to the near-surface imaging.

Survey EME from 1987 is the only dataset acquired using seismic vibrators. This survey consisted of two intersecting profiles. Compared with the dynamite source, this vibrator source provides adequate energy to image the shallow reflectors of interest but much less useful seismic energy in the deep sections (below 1500 ms). Since the interval of interest in this study is in the close subsurface above 500 ms, distinctive structural features on the central disturbed zone were partially imaged. Profile EME 004 tied (i.e crossed) the three southerly profiles of Survey 86 and greatly assisted in the integration of the whole data set.

Survey EYE is the latest legacy seismic data, which has a total length of only 3 km. Due to the close group/source spacing and the spread out of 240 channels, this line achieves the highest fold and strongest energy. It covers the 'ring-like' blocky area and ties-in Profile 86-252 which helps the data systematic discussion.

With carefully applied reprocessing workflows (detailed processing flow will be discussed in Chapter 6) and comprehensive analysis, I discovered a series of distinctive features that support a hypervelocity impact origin for this structure. Although structural anomalies were discovered in these seismic profiles, it is important to note that utilizing these data sets to reveal the shallow subsurface targets in detail was quite difficult and complicated because the donated legacy data was not collected to image the shallow section.

## 4.3 Seismic Reflection Characteristics in Time Scale

In this section, the seismic data analysis is conducted on the donated poststack time-migrated seismic profiles. Synthetic seismograms are generated to assist in identifying numerous Cretaceous horizons. Thus, supplementary observations are noticed to reinforce the structural anomalies within the structure. Geological horizon topographic maps created from the travel times of the interpreted units display distinctive disruptive zones and the annular trough in the near-surface strata. Such detailed analysis not only provides important clues that verify the impact origin, but also yields significant hints for the subsequent seismic data acquisition and refraction inversion studies in the following chapters.

### 4.3.1. Synthetic Seismograms

Synthetic seismograms *tie*, or calibrate, the seismic horizons from two-way travel time to depth by correlating the borehole geophysical logs to the seismic profiles. Essentially, a synthetic seismogram is calculated from sonic log (DT) and density log (RHO) data to provide the normal incidence acoustic impedance Z with depth. Using Equation 4.4, one then can calculate the reflection coefficient R as a function of depth (RC). Integration of the sonic log transit times allows for these depths to then be converted to two-way travel times and transforms the function of the reflectivity RC in depth to one of RC in time. With some knowledge of the character of the seismic wavelet, usually 'extracted' from the observed seismic data itself using methods of deconvolution [*Yilmaz*, 2001], one then obtains a theoretical seismogram by convolving it with the reflectivity (RC). This synthetic seismogram can then be directly compared to the observed seismograms to distinguish the various geological horizons. Thus, the seismic reflectors can be precisely tied to the geological lithology units in depth domain.

Despite there being over 1000 available boreholes in the area, a search of the well log data base (Accumap® provided to the U of Alberta courtesy of IHS Inc.) showed only 78 wells had both sonic and density logs. In fact, there are limited data sets of the sonic and density logs of interest due to the fact that our target layers are in the shallow subsurface above 500 m, particular the top 300 m. This zone is not of economic interest as it is the ground water protection zone from which hydrocarbon production is not allowed. As such, there is little incentive for producers to obtain log information here. Regardless, we were still able to find 13 log sets in the periphery of the seismic lines from which we generated the synthetic seismograms for further interpretation (Table 4.2). Of these we chose the synthetics from Wellbore 00/08-28-17-18/0 and Wellbore 00/05-25-17-19/0 near the seismic Line 86252 to display the relationship between the geological intervals and seismic reflectors (Figures 4.5 and 4.6). Detailed synthetic seismic traces were created using Petrel® software supplied to the University of Alberta by Schlumberger. In order to ascertain the quality and accuracy of the seismograms, despiking was first applied on the sonic logs to remove the spurious spikes and artifacts. The time window of the seismic wavelet was picked for each well to make the best extraction. Good correlations between the synthetic seismogram and seismic data were obtained.

Table 4.2 List of the wellbore information utilized to generate the synthetic seismograms.

| Wellbore Name | Type | Kelly Bushing level (m) | Measured Depth (m) | Surface X | Surface Y | Seismic survey tie | Top interpreted well top | Bottom interpreted well top |
|---|---|---|---|---|---|---|---|---|
| 00/22-10-17-18/0 | GAS | 837.2 | 1215 | 399243.4 | 5588667 | 86249 | Taber Coal | Paleozoic |
| 00/03-24-17-19/0 | OIL | 857.5 | 1280 | 394159 | 5588949 | 86249 | Foremost | Paleozoic |
| 00/04-19-17-18/0 | DRY | 851.8 | 1290 | 395221.4 | 5589145 | 86249 | Oldman | Paleozoic |
| 00/16-13-17-19/0 | CONW IW | 852.2 | 1273 | 394841.6 | 5588584 | 86249 | Oldman | Glauconitic |
| 00/08-20-17-18/0 | AOIL | 841.2 | 1240 | 398001.3 | 5589231 | 86250 | Taber Coal | Glauconitic |
| 00/14/21-17-18/0 | DRY | 837.9 | 1265 | 398716.2 | 5590199 | 86251 | Oldman | Paleozoic |
| 00/16-23-17-19/0 | DRY | 869.7 | 1310 | 393334.5 | 5590310 | 86251 | Oldman | Paleozoic |
| 00/05-25-17-19/0 | DRY | 871.5 | 1322 | 393786.3 | 5591119 | 86252 | Oldman | Paleozoic |
| 00/05-30-17-18/0 | DRY | 864.8 | 1277 | 395354.5 | 5590760 | 86252 | Foremost | Paleozoic |
| 00/16-25-17-18/0 | SUSG AS | 807.1 | 607 | 404526 | 5591411 | 86252/EYE | Belly River | Medcine Hat |
| 00/07-30-17-18/0 | GAS | 857.8 | 1260 | 395906 | 5590988 | 86252 | Belly River | Paleozoic |
| 00/08-28-17-18/0 | GAS | 831.5 | 633 | 399869 | 5590851 | 86252 | Belly River | Medcine Hat |
| 00/16-14-17-18/0 | DRY | 820.3 | 1218 | 402794 | 5588245 | EME 004 | Taber Coal | Paleozoic |

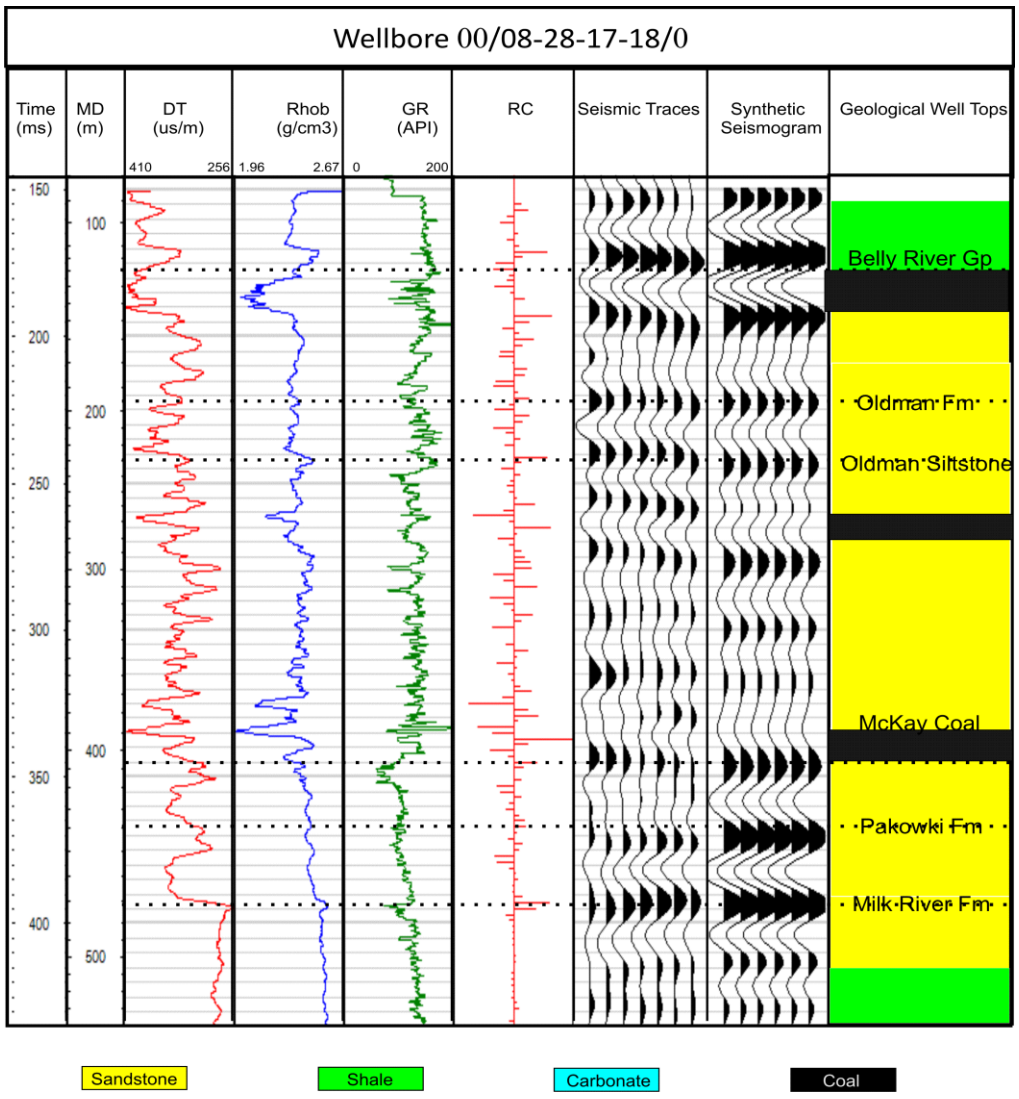


Figure 4.5 Illustration of the synthetic seismogram extracted from Wellbore 00/08-28-17-18/0 located in the vicinity of seismic Profile 86252. From left to right, logs are sonic ($us/m$), density ($g/cm^3$), gamma ray ($API$). The associated calculated reflect coefficient (RC) time series, a set of seimsic traces centred on CMP 467 from 86252, and the corresponding synthetic traces are shown. This well was employed to tie with the shallow Cretaceous horizons.

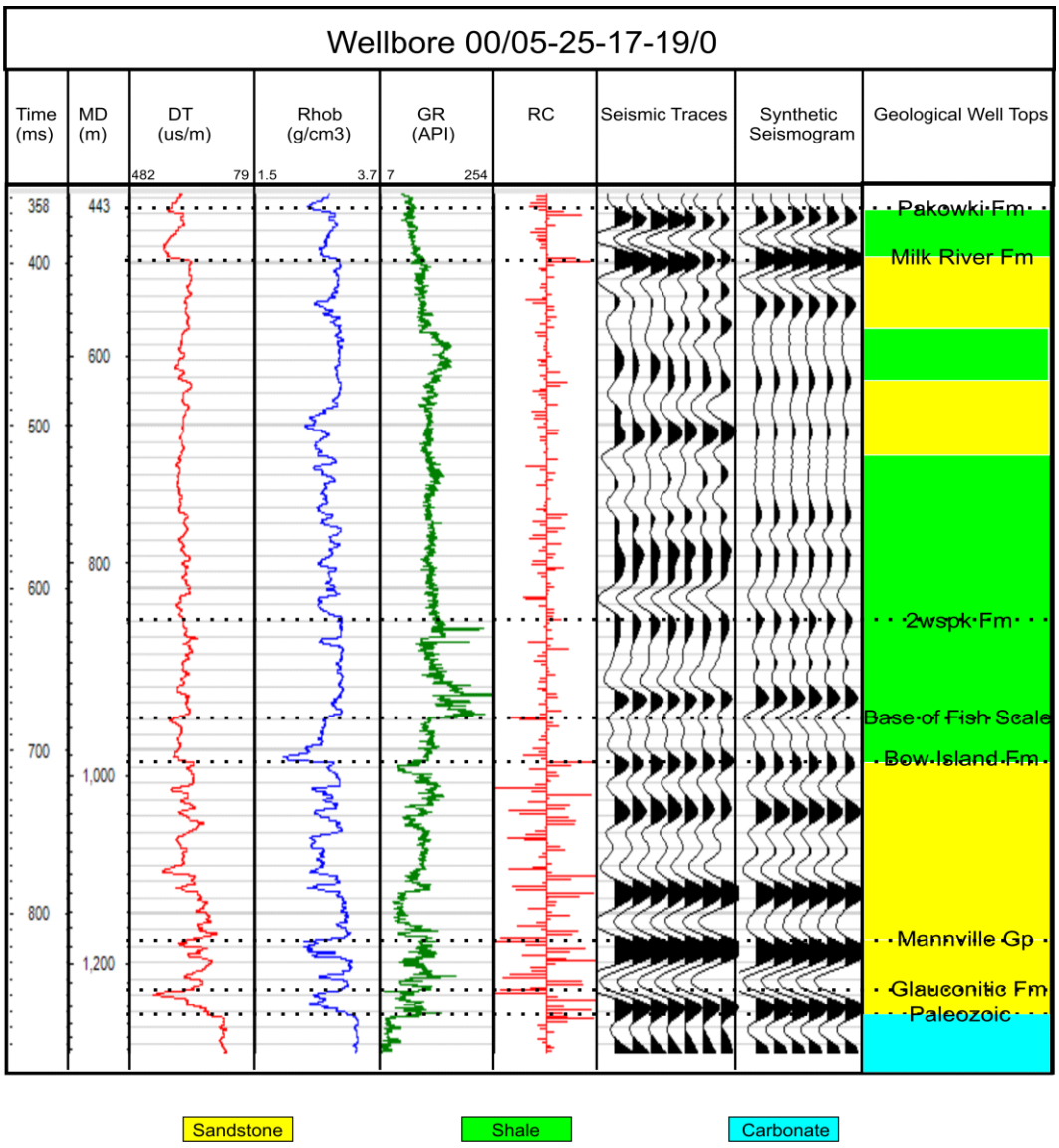


Figure 4.6 Illustration of the synthetic seismogram extracted from the Wellbore 00/05-25-17-19/0 located in the vicinity of seismic Profile 86252. From left to right, logs are sonic ($us/m$), density ($g/cm^3$), gamma ray ($API$). The associated reflect coefficient (RC) time series, the seismic traces centred at CMP 1073 from 86252, and the corresponding synthetic traces are followed**.** This well was used to tie with the deeper horizons.

### 4.3.2. Interpretations of Seismic Horizons

As just mentioned, synthetic seismograms were utilized to associate the seismic reflectors with the Upper Cretaceous geological units. Before these could be compared to the donated seismic sections, the series of legacy surveys were adjusted to the same elevation datum level. This is necessary for the different surveys to all be properly compared to each other without introducing artifacts to the interpretation. A seismic reference datum of 900 m was selected since the seismic profiles were aligned to 900 m during the data processing. In addition, it is important to note that a datum that is higher than the highest survey stations (869 m) can keep more shallow signals which are quite essential to this study. Furthermore, quality check (QC) and minor adjustments were applied to make sure that all the seismic horizons were aligned in all of the surveys.

#### 4.3.2.1. Survey 86

Survey 86 is located in the west bank of the Bow River and is comprised of four parallel 2D lines. 12 wells located in the vicinity of the seismic surveys were employed to interpret the shallow horizons. Of this set, Profile 86249 (Figure 4.7) is chosen to highlight the simple regional geology due to the fact that this survey was acquired away from the estimated center of the structure; thus the regional structural patterns can be seen.

A number of notable features can be observed in seismic Profile 86249 (Figure 4.8). Generally, the morphology of the Cretaceous horizons is flat and continuous with a slightly westward dipping. A monotonous layered structure with flat-lying horizons appears in the deeper sections below the Milk River reflector. However, an evident chaotic zone (highlighted in the red box I) is apparent to the east of CMP 650 and it becomes most significant in the intervals between the top of Belly River Group and the Milk River horizon. These dim and discontinuous

reflections indeed add more difficulties in tracking the near-surface horizons. Moving eastward, the seismic energy turns into consistent and uniform and the reflectors are continuously parallel to each other from CMP 500. However, the broken strata detected to the east of CMP 140 (highlighted by red box II) prominently interrupt this coherence. The disturbed Belly River Group reflector, which is significantly tilting to the east, in turn, is somewhat symmetric with the west disruptive zone around CMP 650. In fact, a circular shape is presented on the horizon maps that will be discussed later.

Moving northward, structural patterns with evident broken layers can be detected within the other three profiles (86250, 86251, and 86252). These supplementary seismic images in Figures 4.9, 4.10 and 4.11 are discussed as followed to provide a comprehensive interpretation of the Bow City structure.

One of the most pronounced features that consisting showing on the profiles is the highly disruptive zone (highlighted by yellow shading). The reflections in this area are scattered and there are little or no continuous events. Analogous to the 'what' in acknowledged impact craters discussed in Chapter 2, this seismic 'transparent zone' is the interrupted region resulting from the large amount of energy released shortly from the hypothesized hypervelocity event. From the seismic perspective, the appearance of these discontinuous events is due to the incoherently energy scattering results from small disruptive pieces within the structure. In contrast, it is important to notice that the reflectors in Profile 86249 are more coherent and less disturbed with a flat central area.

Immediately looking beneath this chaotic zone, three reflectors, the top of McKay Coal (drawn by green line), the Pakowki (drawn by purple line), and the Milk River (drawn by blue lines), exhibit more continuous, but still displaced features with small perturbations. Moving away from this region, the discontinuous events are tracked into the coherently flat-lying horizons. From the two profiles locating

in the northern area (86251 and 86252), significant raised and disruptive horizons are visible below the yellow transparent zone. The southerly line 86250 (Figure 4.9), in turn, displays less broken and more consistent characters. An apparent anticline centered near CMP 280 appeared right beneath the highly interrupted area. It is interesting to note that the reflectors in Profile 86249 (Figure 4.8) remain flat and continuous and no seismic transparent area is observed. Nevertheless, the morphology showing in these seismic profiles, particularly the three northerly images, indicates the existence of a central uplift in this potential disruptively eroded complex crater.

Further evidence verifying the appearance of the central uplift is the curved reflectors observed in Profile 86251 (Figure 4.10). Although this anticlinal feature becomes less apparent with increasing, there is still notable elevation contrast in the three lower layers between 300 ms to 400 ms. Such a central summit pattern with bending reflectors suggests the fact that the uplift of the central core was formed and developed during the modification stage of a meteorite impact activity. The resulting impact structure with the diagnostic central crest is, in turn, characterized as a complex impact crater.

Another blocky terrace interrupted by listric normal faults is interpreted in the outer rim blocky depression. Looking from west to east on Profile 86252, the flat-lying Belly River reflector in the shallow subsurface is significantly dropped down at CMP 540 (highlighted by the box in Figure 4.11). Seismic reflections between 200 ms to 350 ms are sliding downwards with upward rotation towards the structure center. This blocky structural pattern appears to be continuing as moving into the center core and three normal faults (drawn by blue, cyan, and green in red box) are delineated to display the same disturbed and slumping aspects. Indeed, a smaller fault (drawn by pink curve in the red box) is also likely seen near CMP 420, which might extend this blocky texture of the structure floor further into the centre. On Profiles 86250 and 86251, the same slumping strata

and listric faults pattern are observed and more detailed structure is displayed on the inner side of these faults. In fact, these slumped blocks are interpreted as defining the outline of the ring-shape moat as discussed in the geological mapping (Chapter 3) and the outermost fault indicates the edge of the structure. A possible explanation of the formation of these complex faults patterns is that the hanging walls were severely rotating and sliding downwards along the fault plane due to the impact energy projected during modification stage. Besides, a minor faulted region is described near CMP 550 with a significant downward depression in Profile 86249 (highlighted by red box in Figure 4.8), it dips towards the central core but has a directed outward thrust vergence. The detection of this reverse fault further increases the complexity of this study structure.

Whether such normal faults pattern can be integrated among these profiles and the reverse fault is existing or not is still an open question due to the limit of the data quality and resolution. Regardless, the discovery of the central peak and rim faults on the seismic profiles has pointed out that this structure is complex and unique in this area, which supports the hypothesis of an impact origin.

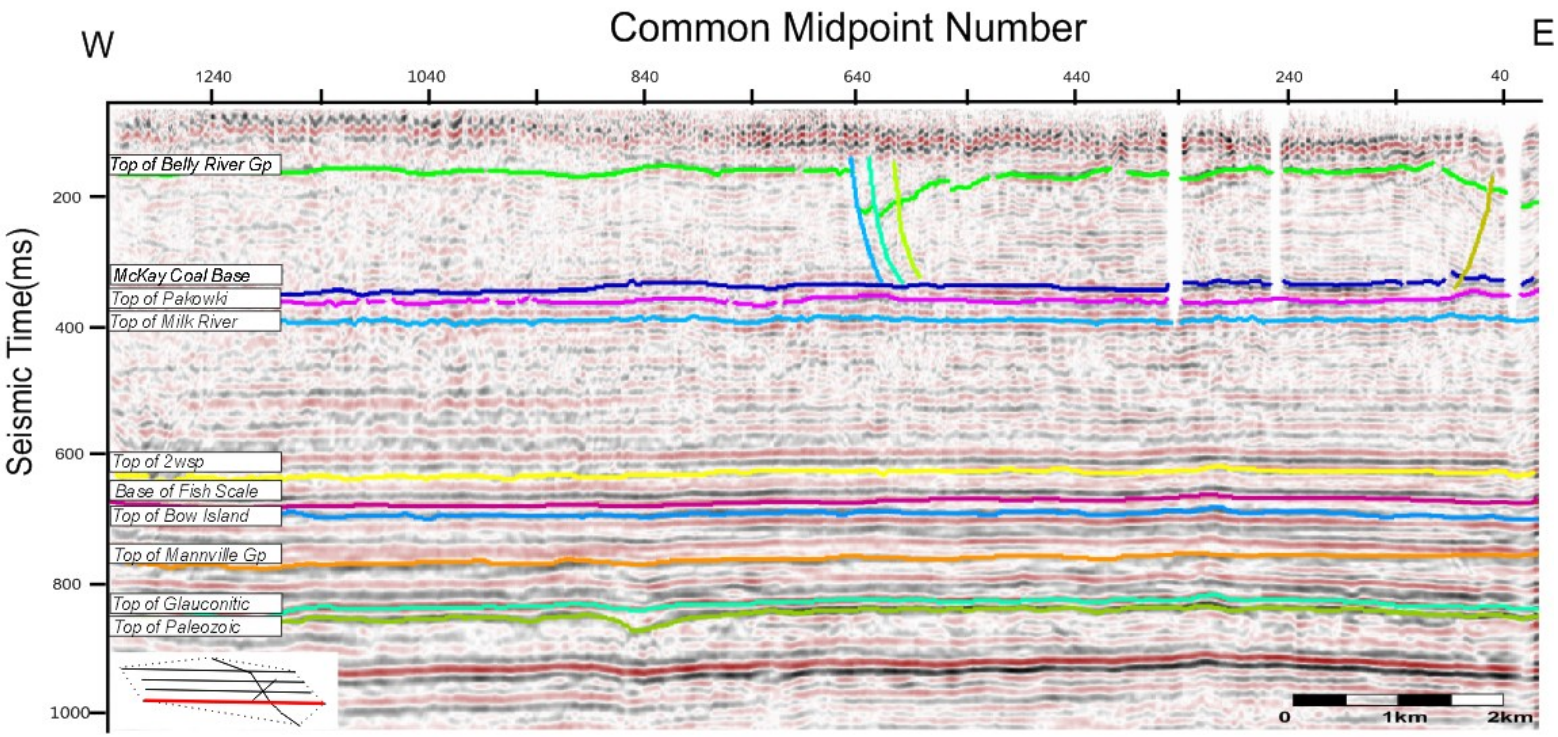


Figure 4.7 Seismic profile 86249 with interpreted reflectors. Common midpoint interval is 10 m and the bottom image represents the location of the line by red.

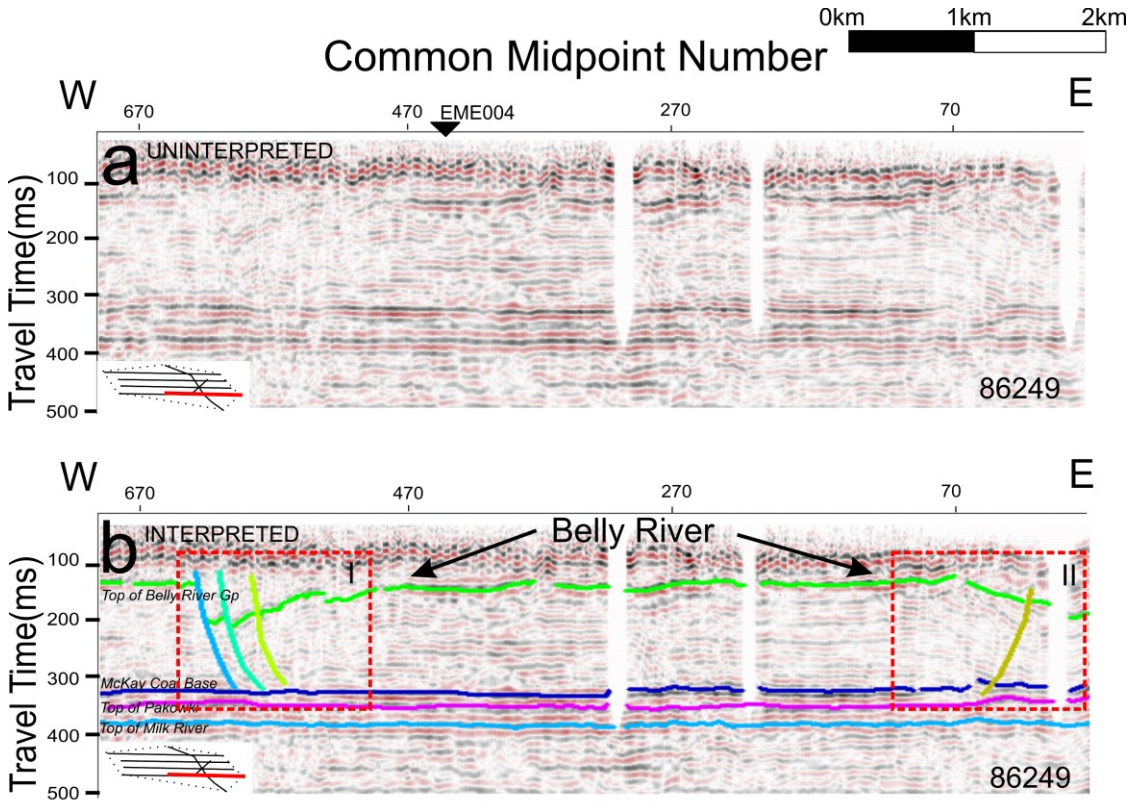


Figure 4.8 Seismic profiles of 86249. a) Uninterpreted profile. b) Interpreted seismic profile. Box I and II emphasize the disturbed structural patterns. Colored lines show the interpreted shallow horizons. Diagnostic faults patterns are presented by the colored curves.

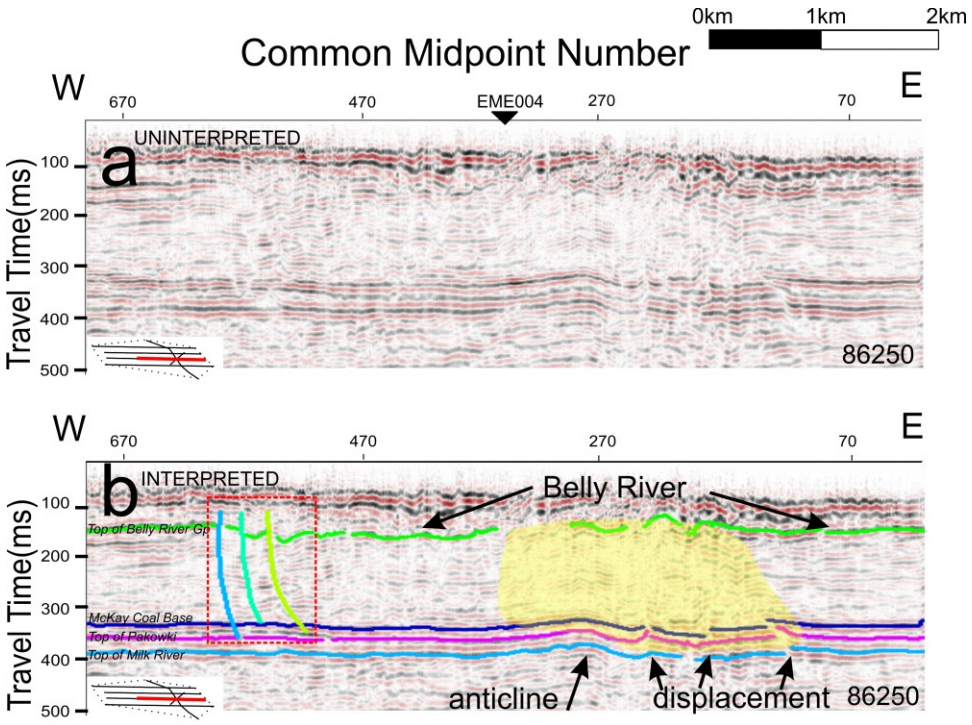


Figure 4.9 Seismic profiles of 86250. a) Uninterpreted profile. b) Interpreted seismic profile. Dashline red box emphasizes the disturbed structural patterns. Colored lines show the interpreted shallow horizons. Yellow shading highlights the interrupted shallow horizons. Diagnostic faults patterns are presented by the colored curves. The black triangle in a) represents the location that intercepts with EME004.

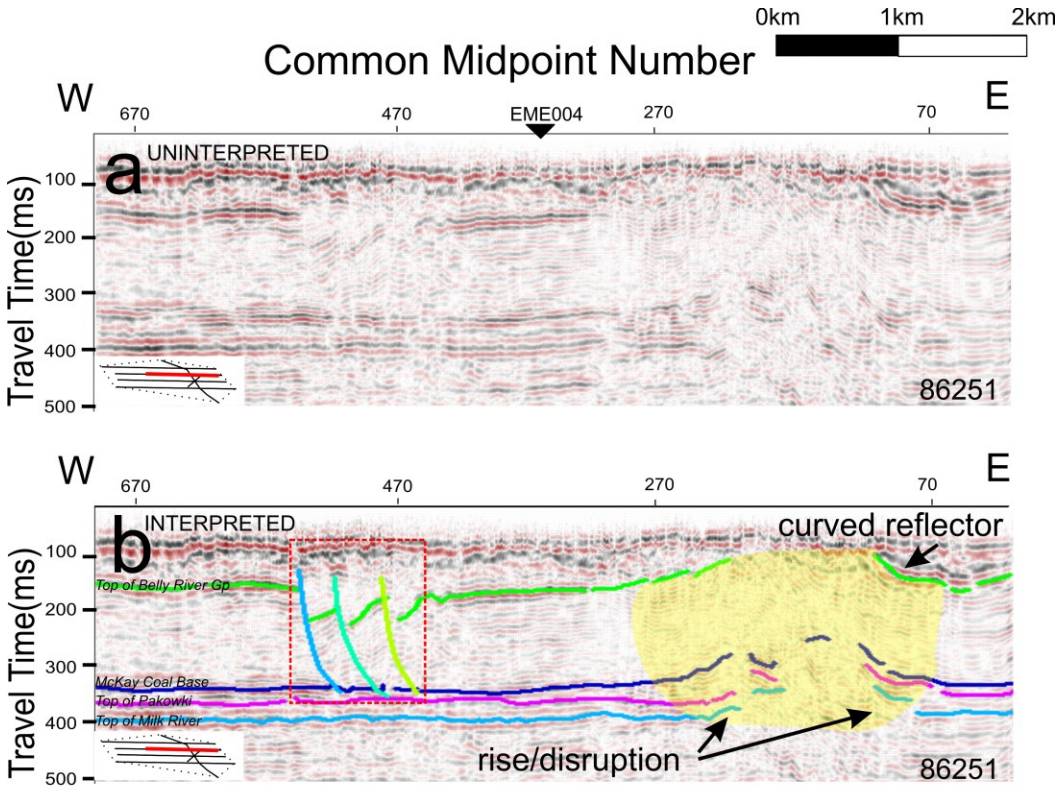


Figure 4.10 Seismic profiles of 86251. a) Uninterpreted profile. b) Interpreted seismic profile. Dashline red box emphasizes the faulted structural patterns. Colored lines show the interpreted shallow horizons. Yellow shading shows the interpreted shallow horizons. The black triangle in a) shows the location that intercepts with EME004.

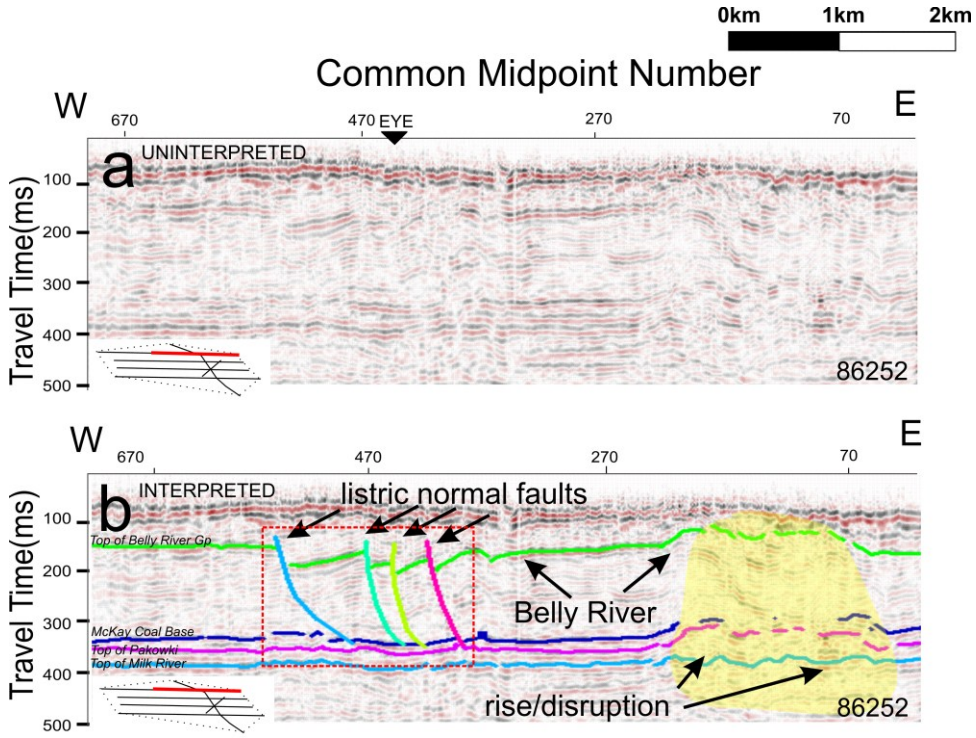


Figure 4.11 Seismic profiles of 86252. a) Uninterpreted profile. b) Interpreted seismic profile. Dashline red box emphasizes the faulted structural patterns. Colored lines show the interpreted shallow horizons. Yellow shading highlights the interrupted shallow horizons. The black triangle in a) shows the location that intercepts with profile EYE.

### 4.3.2.2 Survey EME

Survey EME includes two seismic profiles that run from the south edge of the rim through the central uplift zone. Profile EME 004 runs through the area of interest from south to north and, importantly, it intersects with the three southern profiles of Survey 86. Thus, it plays a key role in tying these multiple profiles together. Indeed, the existence of this line greatly improves the confidence of the data analysis over the entire collection of seismic data sets and the subsequent structural interpretation. However, the second profile, EME 001, is of significantly lower quality and does not show interesting structural patterns. In addition, to our knowledge, this profile is located in the central disturbed area, which is quite damaged and complex. Therefore, only limited information is provided to exhibit the displacements (Figure 4.12).

In profile EME 004, the shallow horizons above 400 ms (Figure 4.10) are significantly disrupted. The uppermost reflector, top of the Belly River Group (highlighted by green), is clearly discontinuous with numerous faults and large displacements. Moving north into the structure from the south side, a significant downward sliding of the Belly River unit with an inward rotation is first observed at CMP 15. The anticlinal uplift centered at CMP 110 is clearly visible in the damaged zone as continuing moving northward. The signal continuity improves between CMP 188 to CMP 300, which might be consistent with the annular terrace zone. Indeed, this coherent transition displays a similar seismic architecture to the southernmost profile (86249) in Survey 86. Another deformed region with gently folding and blocky morphology is seen near CMP 340. This region adds more complexity to the inner side of the crater. As continuing into the deeper structure, the three interpreted horizons (McKay Coal Base, Pakowki, and Milk River) are more uniform except for small interruptions near CMP 360. No resolvable displacement is detected below 400 ms, and all of the reflectors show flat-lying and monotonous layered characteristics. This does not mean that

displacements do not exist in situ, rather it means that these are below our capabilities to resolve them. Using the standard ¼ wavelength Rayleigh criterion, we estimate the vertical resolution to be no better than 20 m. This notable texture contrast between the upper and lower successions yields distinct evidence for the existence of the destroy event in the simple flat layers during Cretaceous.

In addition, a series of normal faults tilting towards different directions are discovered in the near surface. Externally, at least two pronounced normal faults locating in the southern edge of annular depression are revealed near CMP 20 and CMP 100 (highlighted in the red box III). A bilateral symmetric faulted pattern is also detected in the northern edge near CMP 330, CMP 360 and, CMP 370 (highlighted in the red box I). Compared with the rose-pedal fault pattern in Survey 86, the analogous faulted features between these two profiles include inward verging, slumping hanging wall and, 'pop-up' central uplift. However, Profile EME 004 displays more coherent and continuous structural patterns with less depression. This might result if the fact that this profile mostly obliquely crosses a proximate structural terrace, which has fewer disruptions. Regardless, the blocky strata in the ring-like moat are interpreted as a similar fault pattern to the listric normal faults in Survey 86. It provides the information that constrains the size of the structure and the shape of the outer rims. Further towards the centre, two apparently normal faults appear near CMP 130 and CMP 200 (highlighted in the red box II). These two faults in the inner rim of the annular trough are gently tilting towards the center core with nearly vertical dip angles. This might arise from the angle at which the seismic profile intersects the fault.

To conclude, more seismically distinctive features in the southern area have been pointed out in Profile EME 004, including complex faults pattern and pronounced displacements observed within the inner structure. More importantly, Profile EME 004 ties a series of profiles in Survey 86 and assists in the joint interpretation and modeling.

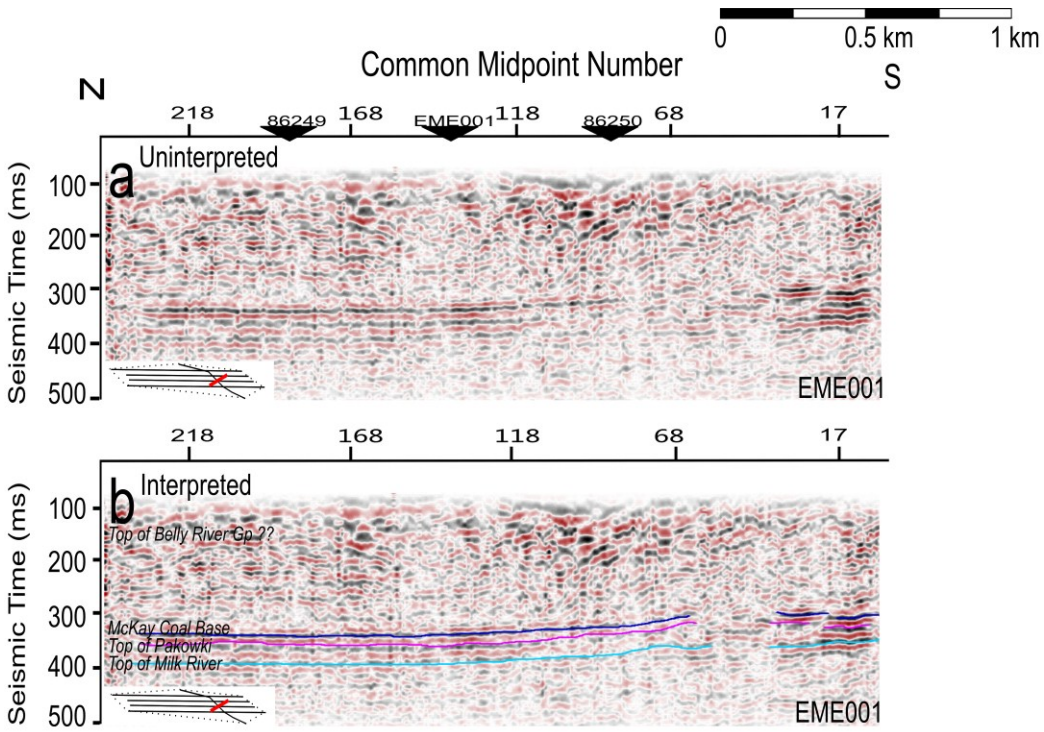


Figure 4.12 Seismic profile of survey EME 001. a) Uninterpreted profile b) Interpreted profile. The colored lines represent the interpreted horizons of the Mckay Coal, the Pakowki and the Milk River. The Belly River Group reflector is too discontinuous to interpret. The black triangles in a) show the intersection points with Profiles 86249, EME001, and 86250.

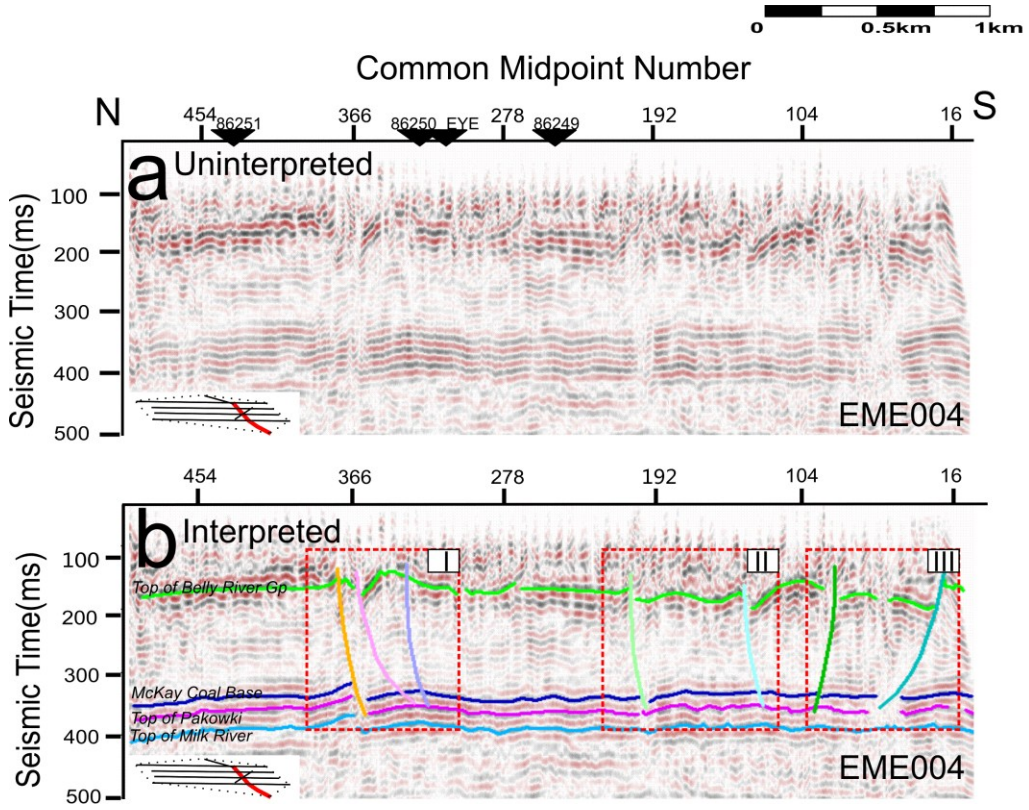


Figure 4.13 Seismic profile of survey EME 004. a) Uninterpreted profile b) Interpreted profile. The colored lines represent the interpreted horizons of Belly River Group, Mckay Coal, Pakowki and Milk River. Three red boxes emphasize the interpreted faults. The black triangles in a) show the intersection points with Profiles 86251, 86250, EYE and 86249.

### 4.3.2.3 Survey EYE

Survey EYE is located in the northern edge of the studied structure. It intersects with Profile 86252 and presents numerous key features in the annular depression zone.

In its interpreted profile (Figure 4.14), the shallow reflections above 300 ms are dim and broken between CMP 420 and CMP 130 (highlighted by the red box). Within the structure, the flat-lying Belly River reflector (highlighted by bright green lines) is evidently slumping downward and a pronounced folding pattern is visible near CMP 110. In the deeper section, the McKay Coal base (deep blue), Pakowki (purple) and Milk River (sky blue) horizons are tracked and less disruptions are observed; they exhibit a simple monotonous structures.

Similar blocky textures are visible on this profile, which verifies the impact generated-depression on the northern section (highlighted in the red box). Marked by the notable downward displacement near CMP 420, a normal fault verging towards the central uplift is interpreted as the margin of the structure. Another three similar features with downwards sliding are discovered near CMP 240 and CMP 150. Indeed, these normal fault patterns are possiblely be the extension of the listric faults displayed in Survey 86 and Survey EME due to the similar verging trend, analogous texture, and rose-petal shape. Regardless, such listric faults in Profile EME provides the proof of the disruptive and incoherent structural style of the northern edge of the structure.

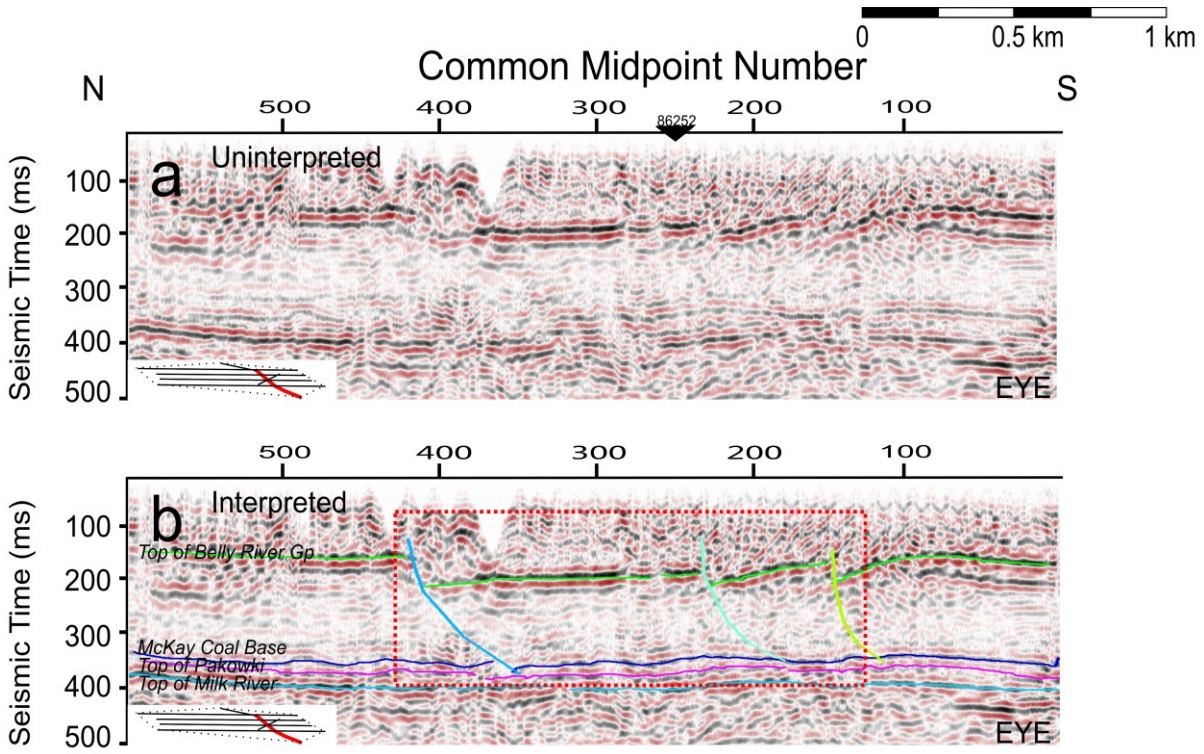


Figure 4.14 Seismic profile of survey EYE. a) Uninterpreted profile b) Interpreted profile. The colored lines represent the interpreted horizons of Belly River Group, Mckay Coal, Pakowki and Milk River. The red box emphasizes the interpreted faults. The black triangle in a) presents the interception with profile 86252.

### 4.3.3 Seismic horizon maps

The time topography maps (isochrones) of each horizon were generated from the travel time of the interpreted seismic horizon using Petrel® software. A geostatical algorithm called the convergent interpolation method [2] is selected to produce these contour maps. Figure 4.15 exhibits the contoured time maps for a number of the major reflecting horizons from the Belly River Group down to the Paleozoic Unconformity. Generally, to the west and outside of the structure, the horizons are mostly flat-lying and parallel to one another with only a gently westward dipping that is expected regionally. Compared with the geological structure maps created from picked well tops, similar structural architecture is presented.

The reader will notice that are a series of small bumps in the topography along the 2D seismic lines. In fact, these bumps are not real but are rather an artifact of the closely spaced time picks resulted from the noise and the imperfections of the processing techniques. Nevertheless, a number of characteristic structural features are observed in these time contour maps.

The substantial travel time contrast is one of the most significant aspects observed on the shallow surfaces. The uppermost Belly River Group reflector exhibits the most pronounced time perturbations, which indicate the fact that it was severely deformed (Figure 4.15a). Two evident structural variations in the semi-circular depressed moat and the central summit point out diagnostic clues for identifying the structural architecture. However, it should also be noted that the Belly River reflector is barely visible in the faulted terrace and the centre peak due to the degree of disruption.

[2] Convergent interpolation is a fast and general purpose algorithm with good extrapolation. It adapts to sparse or dense data distributions through converging iterations at successfully finer grid resolutions.

Therefore, more evidence from high-resolution seismic images and borehole drilling is necessary to prove that the Belly River group reflector still remains in the disruptive regions. While, the deeper seismic reflectors associated with the base of McKay Coal, top of the Pakowki and top of Milk River are more continuous and coherent; and their time topographies are much smoother. Such monotonous layered textures are clearly manifested on the contour maps.

Looking at details, gentle disruption of the McKay Coal reflector with folding and faulted patterns (Figure 4.15 b) is still visible beneath the central peak. At the rim edge, a slight subsidence is detected also on the McKay Coal time topography map. It is necessary to point out that the time disturbance at the central uplift continues to the Milk River surface but the semi-circular moat has almost gone.

At times beneath the Milk River horizon, the seismic reflections display increasingly less evidence of the structural deformations other than regional westwards dipping (Figure 4.15 c). On the Second White Specks map, smaller local bumps appearing under the central core are visible in Figure 4.12d. It is important to note that in this case where we see definite lateral variations in the structure, we may also expect velocity artifacts in the images such as the pull-ups or pull-downs. If the upper velocity is lower than the surrounding formations, a seismic 'pull-down' in the deeper structure would be observed; while if the velocity is higher, a 'pull-up' structure could be seen. Whether the observed uplifts seen in the deeper horizons beneath the central deformed uplift are formed as part of the hypothesized impact event or are merely seismic artifacts cannot be completely resolved. Evidence from other structures (and from our upcoming refraction tomographic analyses of Chapter 5) would suggest that the features are real as the wave speeds in the central peak should be lower than normal. Drilling of these features is considered as the best technique to test the true depths of these formations.

Continuing down to the Glauconitic and Paleozoic Unconformity reflector, the isochron maps mainly display a simple layered structure with a coherent and westwards dipping pattern (Figures 4.15e and f). Although there are still minor topographic highs existing on this surface, these travel time perturbations are smaller than 5 ms and are unlikely to be real features given that the sampling rate of the digital data is 2 ms.

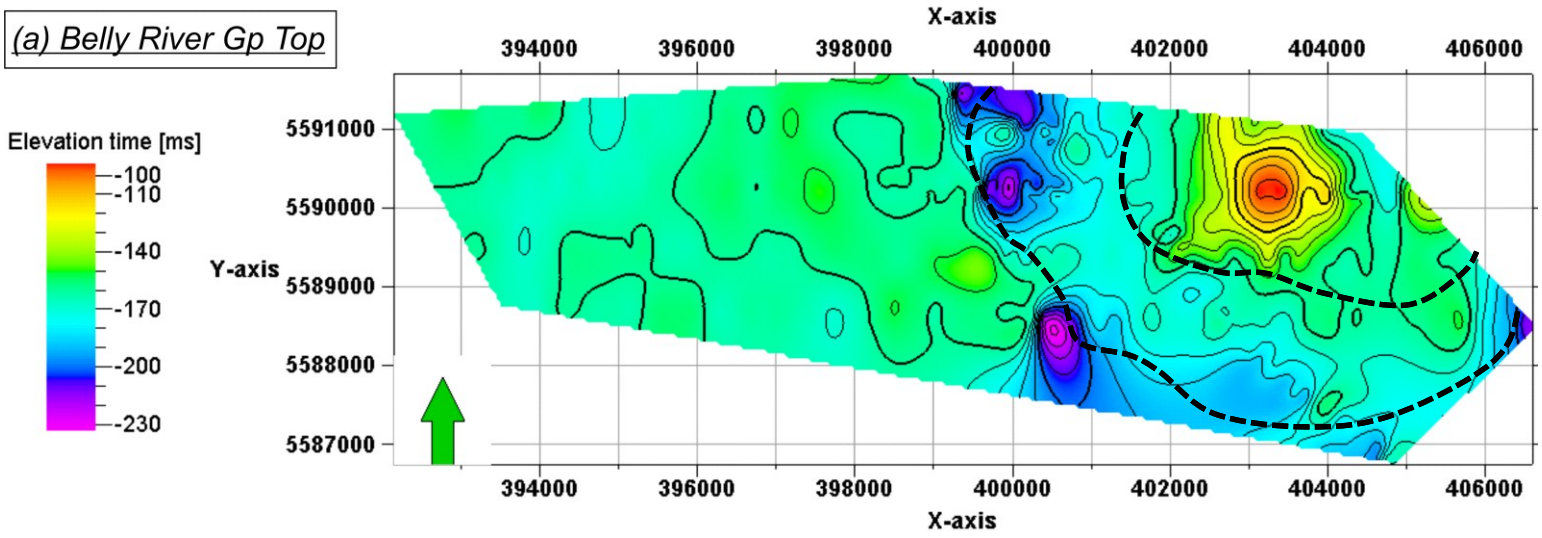


Figure 4.15 Topography time maps of different seismic reflectors. a) Top of Belly River Gp. b) McKay Coal Base. c) Milk River Top. d) Second White Speckled Top. e) Glauconitic Top. f) Paleozoic Unconformity. Time elevation scales are different for each panel. The thick dash lines represent the estimated structural outline and central peak. Green arrows point out the north direction. Coordinates are given in UTM 12N NAD 83.

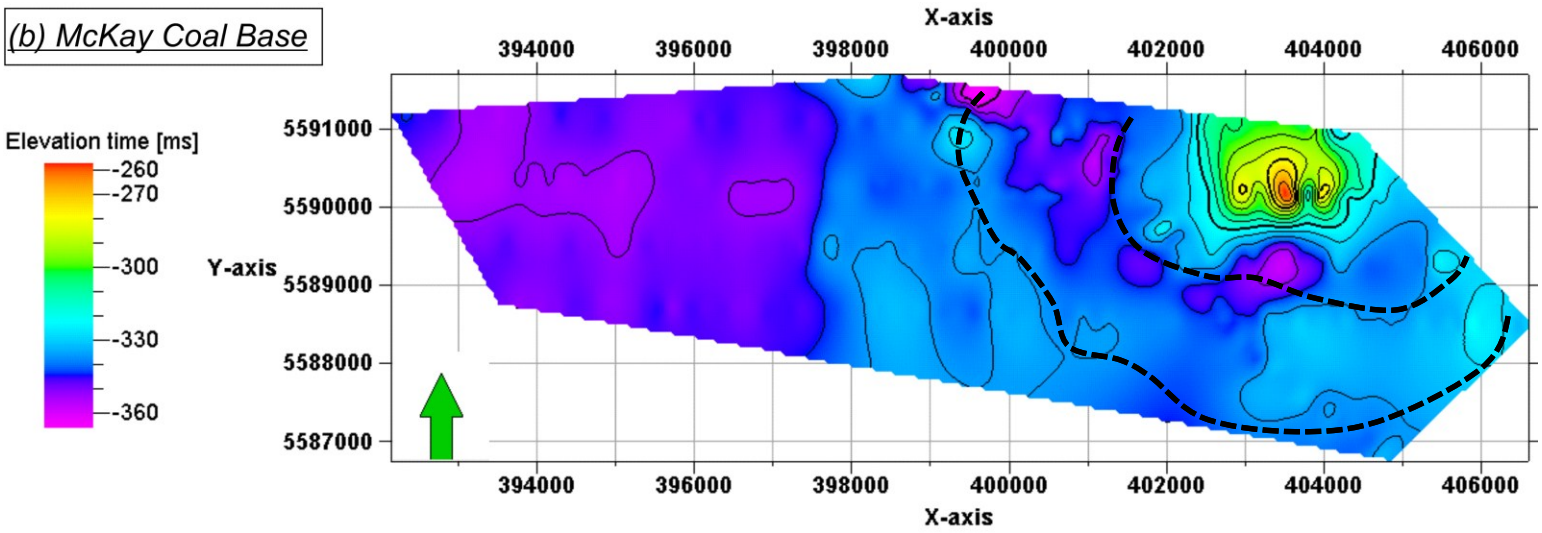
(b) McKay Coal Base
X-axis
394000
396000
398000
400000
402000
404000
406000
Elevation time [ms]
-260
-270
-300
-330
-360
Y-axis
5591000
5590000
5589000
5588000
5587000

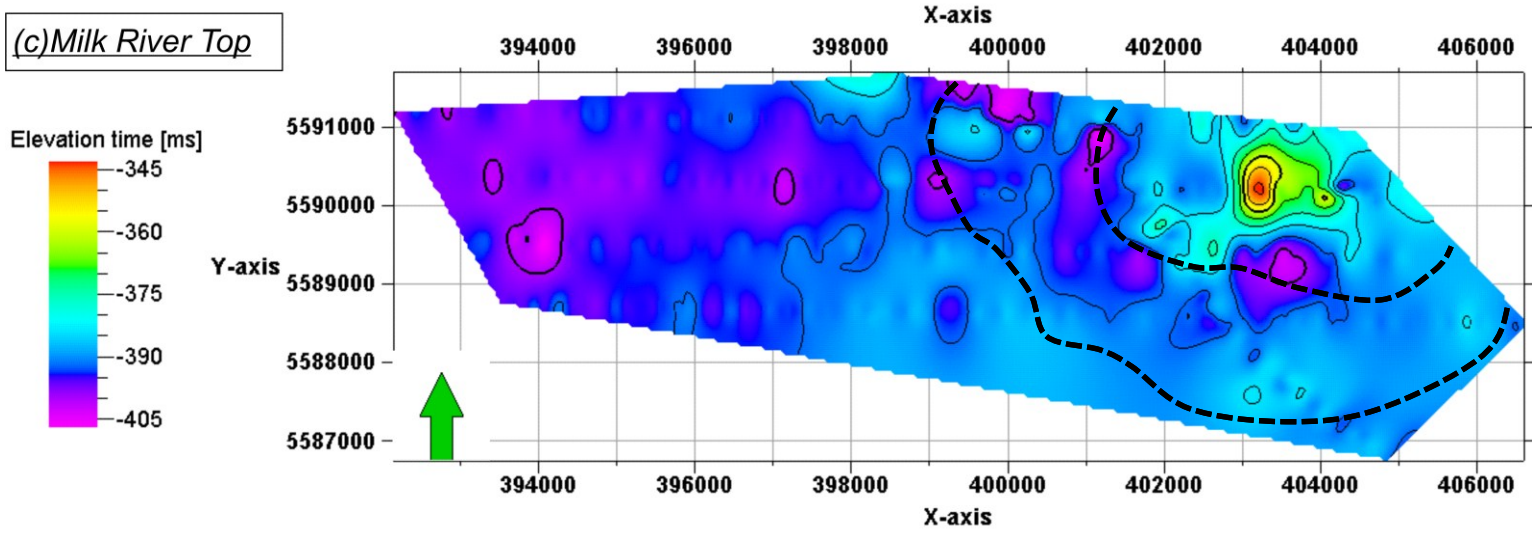
(c)Milk River Top
Elevation time [ms]
-345
-360
-375
-390
-405
X-axis
394000
396000
398000
400000
402000
404000
406000
Y-axis
5591000
5590000
5589000
5588000
5587000

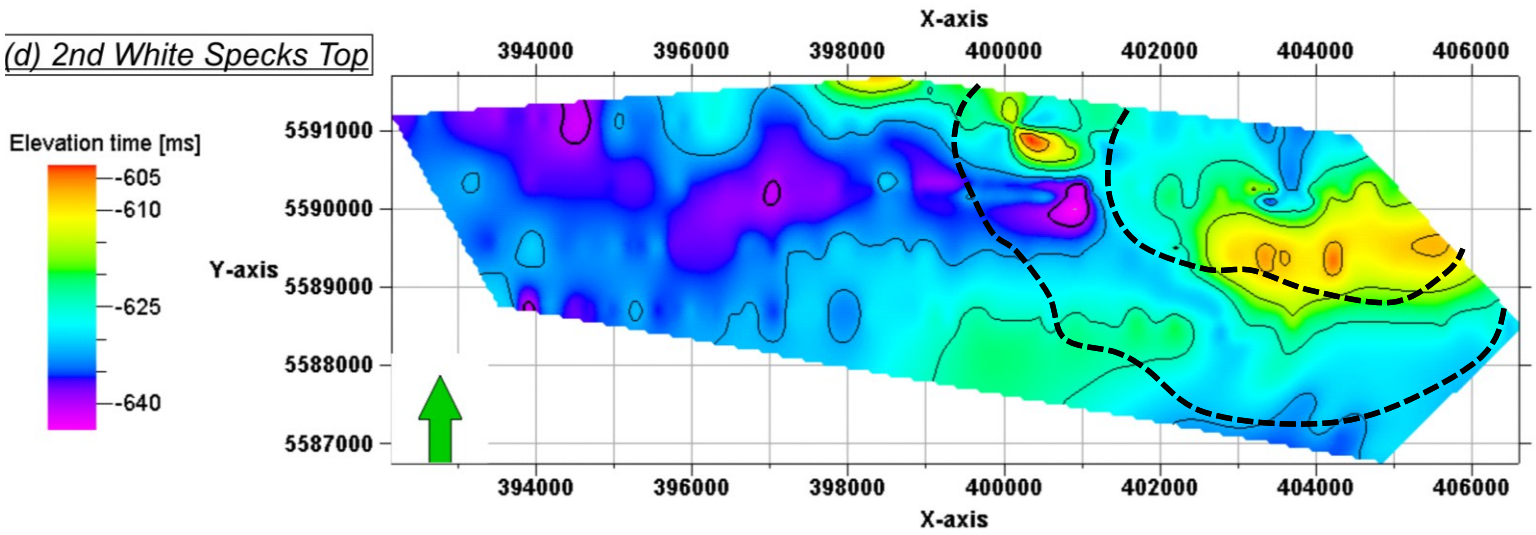
(d) 2nd White Specks Top
Elevation time [ms]
-605
-610
-625
-640
X-axis
394000
396000
398000
400000
402000
404000
406000
Y-axis
5591000
5590000
5589000
5588000
5587000

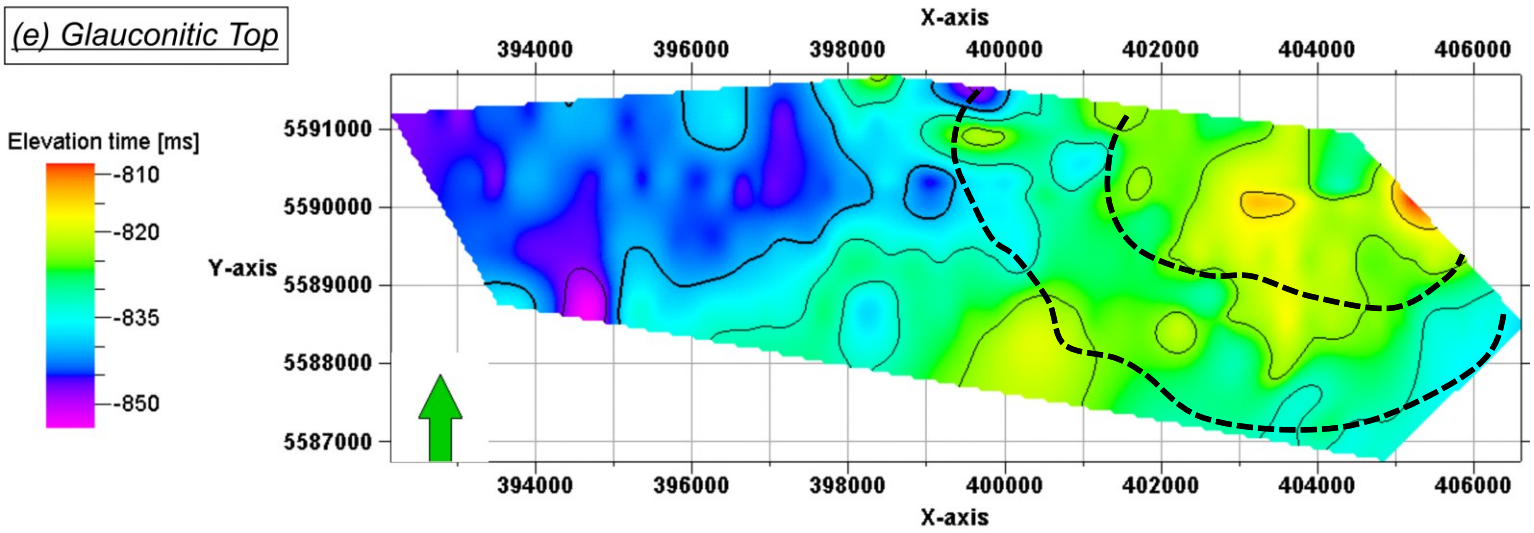
(e) Glauconitic Top
Elevation time [ms]
-810
-820
-835
-850
X-axis
394000
396000
398000
400000
402000
404000
406000
Y-axis
5591000
5590000
5589000
5588000
5587000

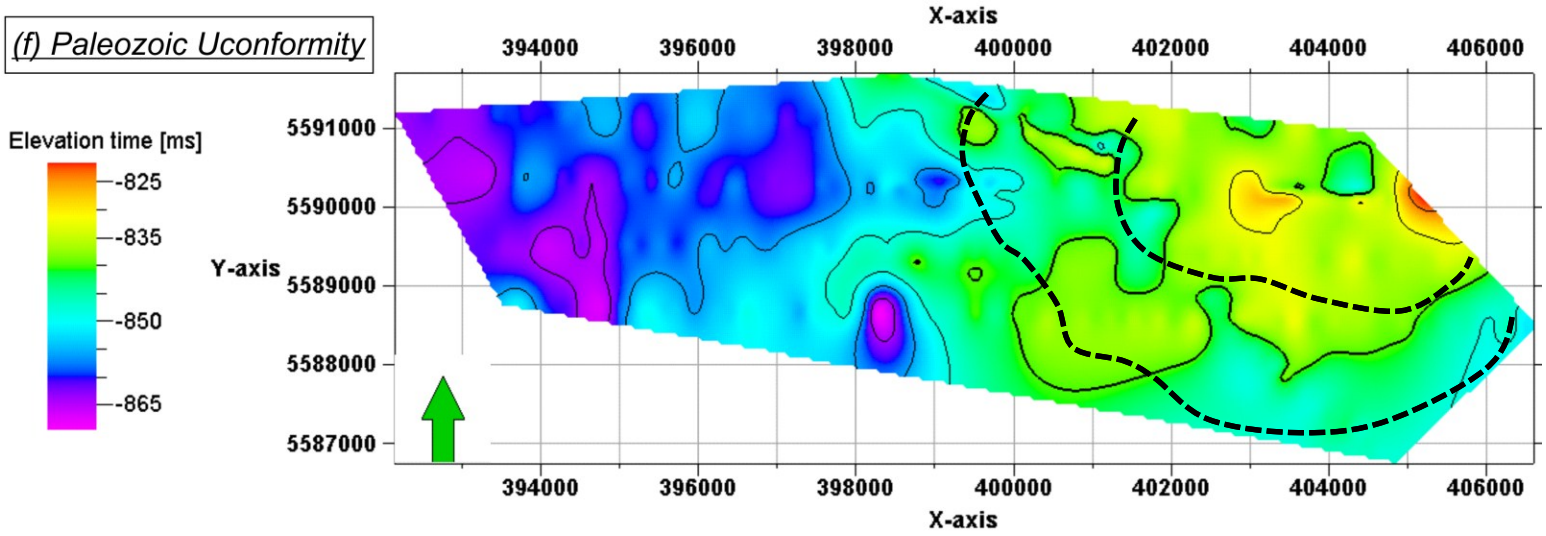
(f) Paleozoic Uconformity
Elevation time [ms]
-825
-835
-850
-865
X-axis
394000
396000
398000
400000
402000
404000
406000
Y-axis
5591000
5590000
5589000
5588000
5587000

## 4.4 Summary

In this chapter, the seismic reflection technique was applied to the donated legacy seismic profiles in order to assist in the characterization of the buried structure first detected by careful mapping of geological horizons by the Alberta Geological Survey [*Glombick et al.*, 2010]. The chapter began with a general introduction of the seismic reflection method that provided background knowledge of seismic reflection imaging. Followed by the overview of the data quality and data features of different surveys, such profiles were discussed with careful examinations.

Detailed interpretation was made on the stacked seismic profiles and their derivative contoured isochron time topography maps. It is worthwhile to point out that structural features diagnostic of an impact origin including listric faults, annular moat, and a central raised and highly disrupted zone can be interpreted. Deeper reflections display progressively less deformation suggesting that we are only seeing the roots of the structure in the uppermost 500 m.

The evidence shown in this Chapter supports additional details of the conclusions of our recently published contribution [Glombick et al, 2014]. That contribution did not include series EYE and EME explicitly, nor did it describe in any detail the processing or the isochron maps. By the detection of these distinctive structural patterns, particular the central uplift, this newly discovered structure was recognized as a candidate complex impact crater. Indeed, these structural patterns were in agreement with the geological mapping and were analogous to the structures presented in the previous impact craters.

Throughout this Chapter we reiterated the deficiencies of the legacy seismic data, particularly the fact that they were not collected to image the near surface. This

motivated the work in later Chapter 6 where we collected new and higher resolution seismic data obtain a more detailed image of keys parts of the structure.

# Chapter 5 Seismic Travel Time Inversion

Seismic inversion is recognized as a crucial process for highlighting velocity anomalies existing in the subsurface. In this chapter, a velocity model generated with the seismic refraction data from 2D seismic Line 86251 will be presented to describe the seismic velocity field associated with the Bow City structure. Detailed descriptions focused on the methodology of the RayInvr program, the application of the technique, and the analysis of the near-surface velocity structure will be conducted. Furthermore, a comparison of the seismic reflection profiles, the sonic logs, and the produced velocity model shows a good agreement.

## 5.1 Introduction

Seismic refraction surveys are widely employed in detecting irregular structural bodies buried under the surface, particularly as the existence of pronounced velocity contrast. Indeed, most of the seismic surveys associated with impact structures have employed less expensive refraction methods. The technique has been successfully applied in impact studies due to the effect of the shock-induced fracturing and brecciation, which can strongly affect the seismic wave speed [*Pilkington and Grieve*, 1992]. *Melosh* [1989] concluded that central uplifts are composed of highly fractured and deformed rocks that were originally located below the transit cavity. Therefore, a model of the structure, regardless of whether it is reconstructed from the direct lithologies or their associated seismic wave speeds, is expected to be quite complex. Indeed, the seismic velocity distribution might be disturbed throughout the entire impact crater including the central peak, the trough, the faulted rim, and annular terrace due to the significant comminution, disruption, melting and refilling [*Melosh*, 1989; *Pilkington and Grieve*, 1992]. Thus, it is worthwhile to review the refraction studies over confirmed impact structures.

In the early 1960's, seismic refraction studies were carried out to delineate the velocity distribution in the simple Brent Crater [*Millman and MacKenzie*, 1960; *Pilkington and Grieve*, 1992]. A lower velocity speed of 75% of the surrounding target materials was detected within the interruptive cavity. In Barringer crater, a severe velocity decrease around 50% in the central disturbed zone was discovered by the process of the shock-induced fracturing and sediments refilling [*Ackermann et al.*, 1975; *Pilkington and Grieve*, 1992]. The measured depth of the fractured zone was estimated to be 850 m based on the result of the detection of the low velocities.

In 2002, *Karp et al.* [2002] noticed that the velocity of the central uplift in the Lake Bosumtwi impact crater was significantly different from the surrounding materials. He also pointed out that the relatively low velocity discovered in the crater floor might result from the severe fracturing process during the excavation and modification stages. In addition, low wave speeds were confirmed in the central uplift by direct measurements using borehole seismic techniques [*Schmitt et al*, 2007]. However, the velocity within the impact crater is not always lower than the undeformed rock masses.

A higher velocity central peak was recognized in the center of the Vredefort structure by seismic refraction tomography modeling [*Green and Chetty*, 1990]. The existence of such high velocity contrast discovered in the central mounted area is due to the significant erosions that results in the presence of the lower strata. *Mazur et al.* [2002] claimed that the velocity structure of the Steen River impact crater, which was generated by the General Linearized Inversion (GLI) method, displayed a series of velocity anomalies such as a high central peak, a low rim moat, and the slumped blocks. *Niccoli et al.* [2004] later proved that these high velocity characteristics appeared in the central uplift and further pointed out the significant velocity anisotropy that resulted from the different fracturing system that occurred within the crater. Overall, the velocity field of the impact

crater is quite complex and variant and seismic refraction techniques have been proved to be an important tool in characterizing the velocity anomalies.

It is necessary to point out that numerous algorithms have been developed to create the velocity model such as the delay-time method [*Palmer*, 1986; 1991], the plus-minus method [*Hagedoorn*, 1959], and the generalized linear inversion method [*Hampson and Russell*, 1984; *Schneider and Kuo*, 1985].

In this study, a ray tracing method based on forward modelling of seismic travel-times and the least square inversion method was utilized. This is the RayInvr technique developed by Dr. Colin Zelt. First arrivals from seismic Profile 86251 were 'picked' as the input to produce the velocity structure of the shallow surface. Figure 5.1 exhibits the location of the seismic profile that was used to conduct the seismic tomography study.

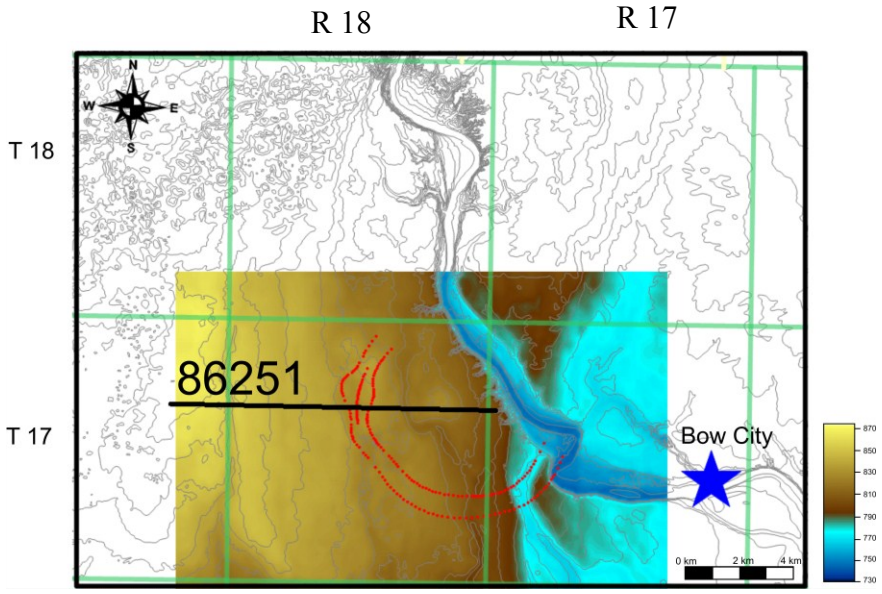


Figure 5.1 Location map of the seismic line 86251 conducted for velocity modelling. Color map is the surface topography map. Red curves show the rim faults interpreted on the seismic profile.

## 5.2 RayInvr Algorithm

RayInvr is a 2D ray tracing approach that involves both forward and inverse methods for generating a sparse 2D velocity model by minimizing the difference between the observed and modeled travel times [*Zelt and Ellis*, 1988; *Zelt and Smith*, 1992]. In this technique, the travel times of the refracted and reflected waves can be both considered as the data input.

The method is comprised of three major processes, which are model parameterization, forward ray tracing modeling, and inversion [*Zelt and Ellis*, 1988; *Zelt and Smith*, 1992]. The velocity model is first constructed assuming that the structure is comprised of multiple layers, which are defined by an arbitrary number of boundary nodes and velocity nodes. By linearly interpolating between the velocity nodes in both the vertical and the horizontal directions, each layer can be decomposed into a series of irregular trapezoids with different geometries and sizes. The layer boundaries can represent an interface that has either a continuous or discontinuous change in the velocity.

In this method, rays are propagated through the velocity model by solving the ray tracing equation with the zero-order asymptotic ray method [*Červený et al.*, 1977; *Zelt and Smith*, 1992]. This ray tracing system is comprised of a couple of first-order differential equations which can be expressed in two forms:

$$\frac{dz}{dx} = cot\theta, \quad \frac{d\theta}{dx} = \frac{(v_z - v_x cot\theta)}{v}, \tag{5.1}$$

$$\frac{dx}{dz} = tan\theta, \quad \frac{d\theta}{dz} = \frac{(v_z tan\theta - v_x)}{v}, \tag{5.2}$$

Where $\theta$ is the anle between the z axis and the tangent of the ray, v is the velocity of the seismic wave, and $v_x$ and $v_z$ are the partial derivatives of the velocity in

terms of the x and z axis, respectively. Of these two equations, Equation 5.1 is applied with z to solve the near-horizonal incidences, while Equation 5.2 deals with the near-vertical situation. Such equations are solved by an error controlled Runge-Kutta method that is used to solve the ordinary differential equation with control increased steps [*Sheriff and Geldart*, 1983]. At the predefined geological interfaces, Snell's law is applied to constrain the ray path direction (see Chapter 3). The turning or reflected points of the seismic waves that are located at the same layer are defined as the same ray group and the ray step length is dependent on the travel time errors and program efficiency. With assigning the proper ray steps and ray groups, the rapid forward modelling is carried out by an iterative ray shooting/bisection method (search mode) to find the appropriate take-off angles of the defined groups. In order to avoid the scattering and focusing induced by the model 'blockyness', boundary layer smoothing is applied, which subdividing the large boundary segments into smaller ones with a three-point averaging filter [*Averill*, 2007; *Zelt and Ellis*, 1988; *Zelt and Smith*, 1992].

The velocities control the ray path, and consequently the travel time inversion is considered to be a non-linear problem. A linearization technique is first applied to solve the problem by eliminating the higher order terms of the Taylor series expansion of the starting model. The linearized equation with these higher order terms neglected can be written as:

$$A\Delta m = \Delta t \tag{5.3}$$

where $A$ is the partial derivative matrix, $\Delta m$ is the model parameter adjustment vector (either a velocity node or boundary node), and $\Delta t$ is the travel time residual vector. In fact, $A$ is a factor in terms of $\partial t_i / \partial m_j$, where $t_i$ is the $i$th observed travel time and $m_j$ is the $j$th model parameter. Both parameters of $\Delta m$ and $\Delta t$ are obtained during the ray tracing.

In order to obtain $\Delta m$, a damped least square inversion technique is applied to solve the equation [*Aki and Richards*, 1980]. The partial derivatives of the boundary nodes are calculated by simple geometric considerations [*Spence et al.*, 1984] and the corresponding time difference between the observed and calculated travel times can be achieved.

It is necessary to assign a reasonable initial model and to iteratively adjust the model to minimize $\Delta t$. A good assessment of the uncertainty, resolution, and uniqueness of the model parameters are presented by the method as well. Indeed, a proper trade-off, which is defined as the damping factor, *D*, should be adjusted between the model resolution, the parameter adjustments, and the uncertainty [*Lutter et al.*, 1990; *Zelt and Smith*, 1992]. The velocity model is finalized by the travel-time residual, parameter resolution, and most importantly, the fact that most of the observed data points can be traced through the model.

## 5.3 Data preparation

The input to the inversion is the 'picked' refraction transit times from each of the common shot gathers. Some discussion of this procedure is required. Refracted waves are unavoidably acquired when one is carrying out a reflection seismic survey (and *vice versa*). The refractions are usually the first arriving waves and, as such they are usually most easily interpreted. Of all the seismic profiles obtained in this study, seismic Line 86251 from the legacy data set was selected to characterize the velocity structure. The reason to utilize this profile is that 1) as interpreted from the seismic reflection image, this line runs over the rim faulted blocks and central peak area; 2) the spacing of the shot and receiver is sampled uniformly and closely, which ensures the good resolution of the output model; 3) the locations of the shot point and field stations (receiver points) all fall along an almost straight line satisfying the RayInvr algorithm requirement; 4) the dynamite energy source produces high-quality data with good signal-to-noise ratios (S/N)

allowing the first arrivals to easily be identified; and 5) the proper offset range, particular the far-offset (~1200 m) that allows for seismic rays to sufficiently penetrate to the depths of interest.

Thus, this line was prioritized to perform the inversion technique. It will be interesting in future to carry out these analyses on the new, higher resolution, data sets also.

Detailed parameters of this profile are introduced as follows. The total length of the 11.8 km 2D seismic line, 86251, is acquired in the west bank of the Bow River. Explosive sources were placed in 18 m deep holes spaced every 100 m. The 14-Hz geophone groups (see Chapter 6) were planted every 20 m with a geophone spacing of 2.5 m. The digital seismic records were sampled at a 2 ms period over 120 channels in a symmetric split-spread recording geometry. A uniform range of source to receiver offsets from 20 m to 1200 m was achieved in most of the shot gathers.

Although both refracted and reflected data can be utilized in RayInvr program, only the first arriving refracted waves were used here as the input for model calculation. The refracted first breaks were identified manually by picking the earliest amplitude extremum using Vista® 2D/3D processing software. Only the unambiguous picks were made on the shot gather to assure the accuracy of the model; it is better not to include a time pick if it is known to be unreliable. An uncertainty of ±5 ms was estimated and assigned to all of the time picks. For each pick, the specific ray code (ray group) was determined to make sure that the corresponding ray path was reflected/refracted/turned in the assigned layer. It is important to note that accurately defining the ray group is an essential procedure to ensure model correctness. Figure 5.2 shows one of the raw shot gathers with picked first arrivals highlighted by green dashes. Three distinctive refraction groups showing different velocities are observed (highlighted by blue, yellow, and

green line, respectively). Significant deviations are seen between the east and west sides of the shot gather, these differences are suggestive of the existence of variations in the subsurface structure (and hence wave speeds). In total, 12995 clear first breaks were picked from the 114 shot gathers (Figure 5.3), and these were distributed between 3 ray groups. Due to the requirement of the two dimensional input, each pair of shot and receiver was re-projected into a straight line on the surface. Facilitated with the simple straight geometry of line 86251, the distance was calculated between each station and the easterly most station along the line. In this case, the longest offset acquired in this survey was 1.22 km.

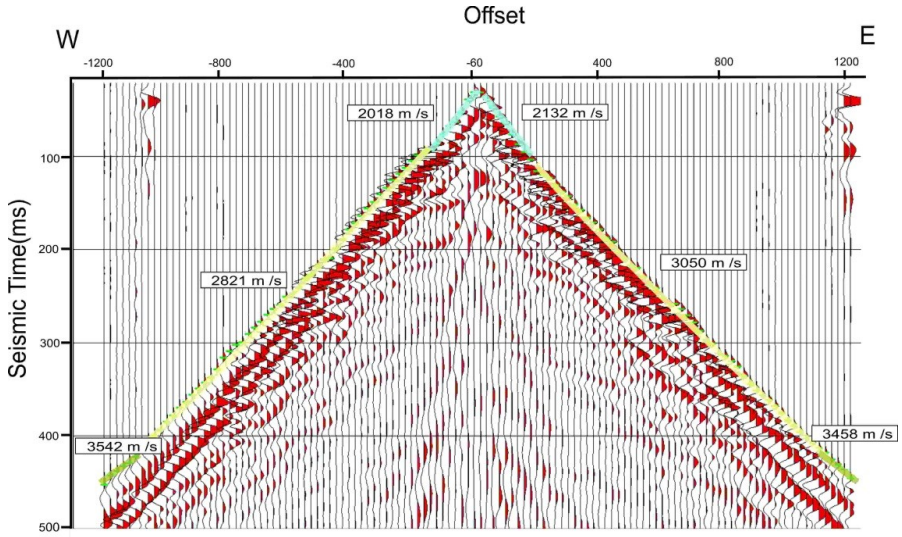


Figure 5.2 Example of the shot gather displaying the different refractions with significant different velocities. Three refraction are interpreted which are highlighted by blue, yellow, and green respectively.

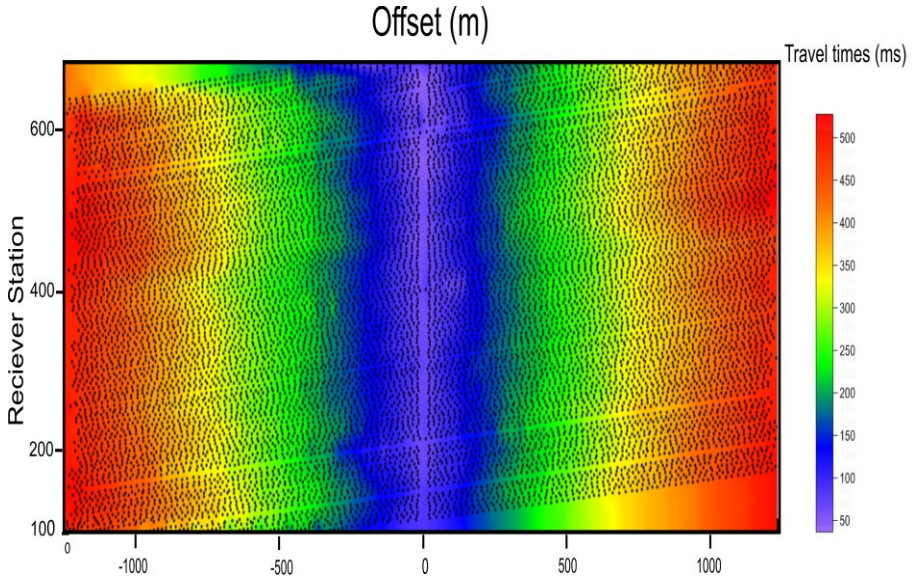


Figure 5.3 First arrivals picked from all of the common shot gathers of seismic line 86251. Totally, 12995 first breaks were picked on 114 shot gathers (marked by the black dots). Different color shows the picked travel times. Obvious deviations are observed at each offset.

## 5.4 Application of RayInvr program

A velocity model consisting of three horizontal layers was generated as the initial input for forward modelling calculation. This three-layer model was created with consideration of the observations from well logs, seismic reflection profiles and the three distinctive moveouts indicative of different refraction groups visible on the shot gather. The top low velocity layer might be suggestive of the overburden Quaternary fill and the topmost Cretaceous bedrock as compared with the higher velocity layer comprised of the Upper Cretaceous bedrocks. These low velocity features can be interpreted as the appearance of the numerous pore spaces in the weakly consolidated Quaternary glacial sediments and uppermost Cretaceous siliciclastics. The velocity zone in the middle might be comprised of the Cretaceous sandy bedrock, which has a velocity around ~2800 m/s. Another

velocity contrast around 400 m in depth provided evidence of the existence of the Milk River sandstone which has a distinctive higher velocity of ~3800 m/s. Due to the limitation of the data availability, the refraction data set only brought the upper 400 m information and indeed, this diagnostic velocity variation around the Milk River formation was not seen in all shot gathers due to the complex subsurface geology environments. It is important to note that the surface topography was included in the model to ensure the model accuracy.

The velocity model was tested with a layer-by-layer strategy by forward modelling and inversion techniques. Both of the interface nodes and velocity nodes were adjusted during the calculations and the final model was achieved after 8 iterations. As suggested by numerous numerical experiments [*Lutter et al.*, 1990; *Menke*, 1984; *Zelt and Ellis*, 1988; *Zelt*, 1999], the optimal value of damping factor ($D$) value is around 1 and for the uncertainty of the velocity nodes ($\sigma_v$) and the boundary nodes ($\sigma_z$) are 0.1 km/s and 0.1 – 1 $km$, respectively. Thus, a good trade-off was obtained between the model uncertainty and resolutions. It is important to notice that some nodes were held fixed during the inversion if the geologic rules were violated due to insufficient constraint yielded by the first arrivals alone.

## 5.5 Result and Discussion

The final model shown in figure 5.4 was selected according to the iteration stopping criteria described by Zelt [1992]. Such a criterion mainly involves four parts including (1) the number of rays traced; (2) the travel-time residual ($T_{RMS}$) and the norminal misfit parameter ($X^2$); (3) the parameter resolution; and (4) the parameter uncertainty.

The velocity model generated in this study was produced by tracing 10925 rays from the total picks of 12995 first arrivals. A good coverage of the entire model

was obtained by tracing more than 84 % of the rays. The final RMS residuals $T_{RMS}$ are limited to 12 ms and the nominal $X^2$ value is constrained to 5.925. Due to the imperfect straight geometry of the 2D line and the underparamerized nature of this methodology, the travel time residuals ($T_{RMS}$) and nominal misfit parameter ($X^2$) are not able to reach the ideal value of 0 ms and 1, respectively. However, this model has already yielded appropriate information to display the subsurface structures.

The resolution for the model nodes was also calculated by assessing the resolution matrix [*Zelt and Smith*, 1992]. The value of the diagonal element in this resolution matrix is a measurement of the averaging or linearizing variance of the true model during the inversion and a value higher than 0.5 means that the node is stable and well resolved. Of the total model parameters, nearly 80% of the boundary nodes and 50% of the velocity nodes have a resolution higher than 0.5. Particularly for the nodes at the second interface of the model, the best coverage and highest resolution were obtained due to the high-quality data picks and various angle apertures from different phases. Figure 5.5 exhibits the ray path and the corresponding resolution of velocity nodes and boundary nodes respectively. It is important to notice that the second layer was quite well resolved with high resolution both in boundary nodes and velocity nodes, which adds more credence to the velocity anomalies detected in the central disturbed area and faulted area. The deeper layer could not be well resolved because of the limitations and constraints from the scarcity of appropriate ray paths combined with low signal quality at the far offsets.

The absolute uncertainty of the model parameters was examined with the perturbation technique described by Zelt and Smith [1992]. It works by disturbing the selected node while keeping the rest of the parameters constant during the forward and inversed modeling and, repeatedly increasing the perturbations until the perturbed model cannot trace the rays as the original model or the nominal

misfit $X^2$ fail during the F-test [*Zelt and Smith*, 1992]. By this means, the model is estimated to have a velocity uncertainty of 70 m/s, 70 m/s, 200 m/s and boundary node uncertainty of 10m, 10m, 70 m for the layers from top to bottom, respectively.

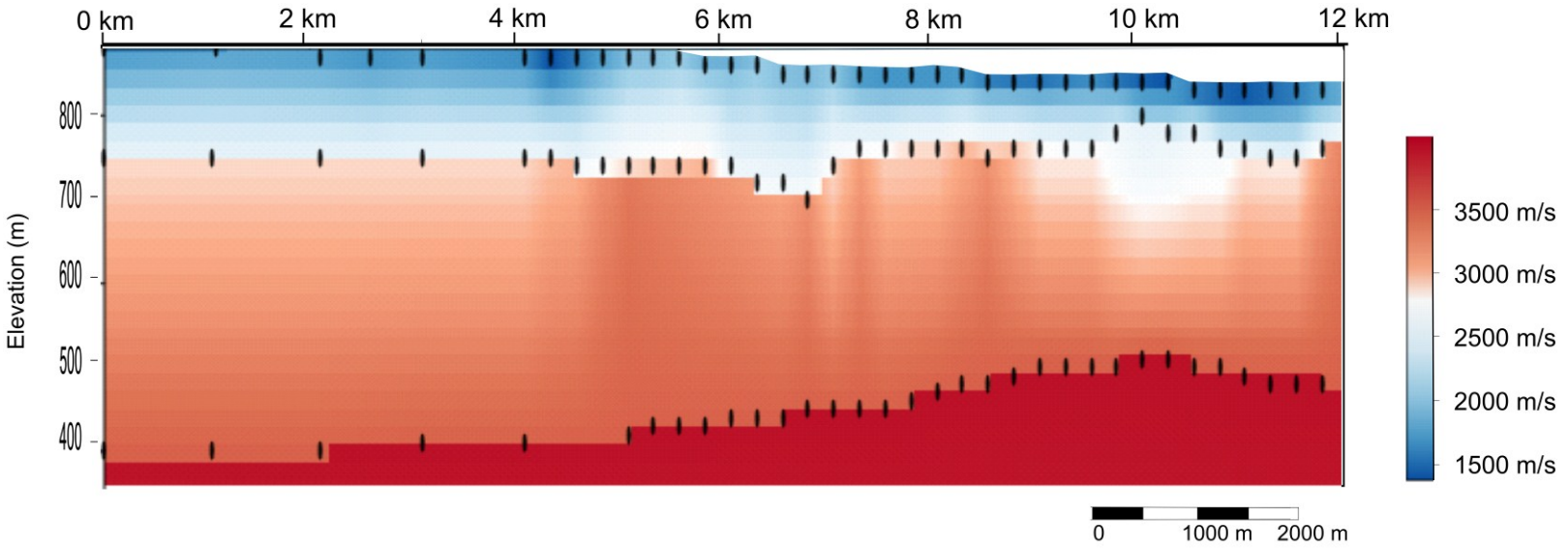


Figure 5.4 Final velocity model generated with first arrivals from seismic profile 86251. Black dots represent the model and velocity nodes utilized to constrain the calculations. A distinct low velocity zone can be seen near 6 km and 10 km around 700 m in depth. A high velocity anomaly is observed in the bottom of the second layer around 10 km. Vertical depth is exaggerated x8 for display.

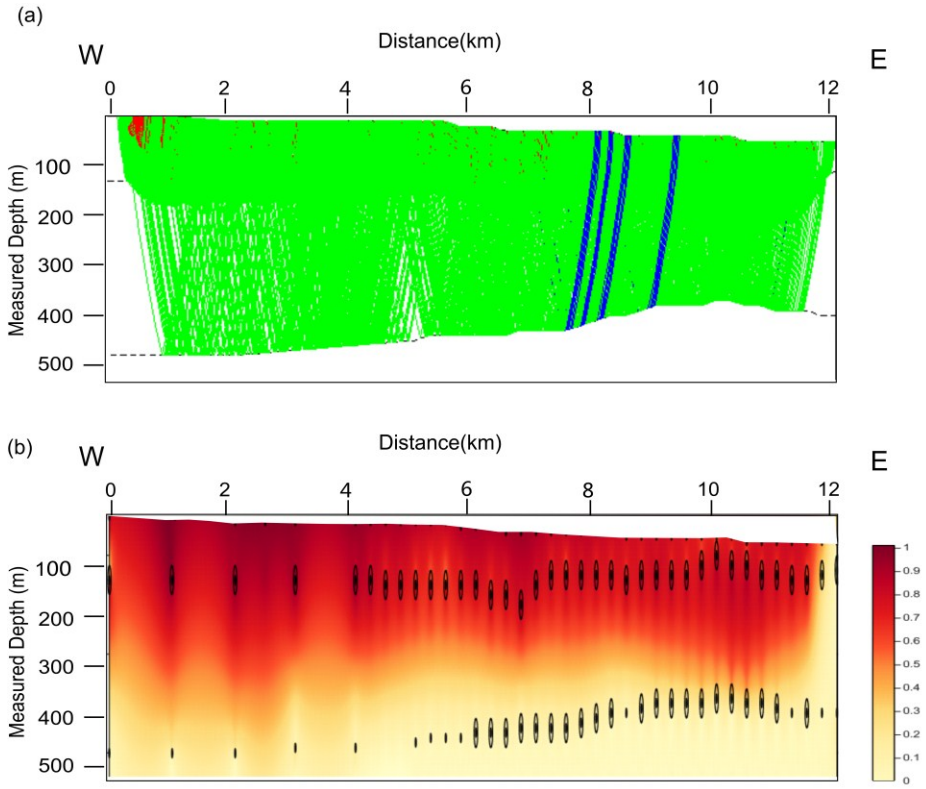


Figure 5.5 Diagrams showing (a) the ray paths traced through the velocity model and (b) the resolution parameter of the boundary and the P-wave velocity. The black dots represent the velocity nodes and boundary nodes. The validity of the velocity nodes are represented by the colors. And the boundary nodes that is well resolved (resolution >0.5) is highlighted by the ellipses. Vertical exaggeration is x8 for display.

## 5.6 Model Interpretation

Figure 5.6 shows the final model that comprised of three layers. In general, the velocity increases gradually from 1400 m/s to 4000 m/s with depth increases. Such a velocity trend ties well with the velocity information extracted from the Wellbore 00/05-30-17-18/0 and Wellbore 00/05-25-17-19/0. The characteristics of the three layers are:

1. The first layer has a velocity less than 2000 m/s; this is interpreted as the near-surface layer of the Quaternary deposits and the uppermost Cretaceous sediments. The refracted arrivals within the short offset were modeled to generate the velocity structure of the shallow surface and topography.

2. The second layer with a velocity approximately from 2400 m/s to 3400 m/s is recognized as the Late Cretaceous bedrocks. The refracted and head waves travelling through the sandy sequences are not uniform and consistent, which provide the evidence of the subsurface anomaly. Indeed, it is important to note that the lateral velocity variance around the second interface is quite complex with significant low velocity bodies between 6 km and 11 km (equal to CMP 100 to CMP 600 in figure 4.8) at 700 m elevation depth.

A clear low velocity zone at location of 10 km (equal to CMP 200 in figure 4.8) is visible on the top of this second layer. This raised area has a width of 2.5 km and a maximum vertical difference of 40 m with the undisturbed area. The average velocity of this layer ranges from 2400 m/s to 3400 m/s, but, the uplifted area exhibits a lower velocity between approximately 2000 m/s and 2600 m/s. This abnormal low velocity trend is possibly suggestive of a highly damaged and fractured rock mass and is similar to what has been seen in the central peak of the Lake Bosumtwi structure [*Karp et al.,*2002; *Schmitt et al.,*2007]. Another distinctive anomaly within the second interface is the low structural trough at 7

km. This area with a maximum of 40 m displays a lower velocity response than the surrounding area. Such a unique may arise from the shock induced fractures, but for definitive proof we would need to carry out logging, borehole seismic experiments, and testing on core samples to conduct detailed characterizations.

3. The bottom layer is defined as the sandy and shaly sequence of the Milk River sandstone, which has a significant high velocity of 3800 m/s. The inversion shows a strong contrast in the velocities in agreement with this. One interesting aspect is that beneath the central peak (10 km), the elevation of this high velocity zone is uplifted suggesting that these strata were pulled up at this location. It is curious that this pull-up feature is located beneath the low velocity zone; this may provide clues as to the degree of deformations of the various layers.

It is important to make a direct comparison between the travel-time inversion and the seismic reflection profile by superposing the inverted velocity structure on the reflection image directly, this is done in Figure 5.7 from which a number of good correlations are apparent that include:

1. The western portion of the seismic profile (Figure 5.7a), displays the uniform regional layered lithologies that are dipping gently westward; this suggests that one may not expect large lateral variations to the west of 6 km as is expected from mapping of the geological tops from the geophysical logs in Chapter 3. The inverted velocity structure (Figure 5.7b), too, shows relatively little variation over this zone and is in agreement with the expected flay-lying lithologies.

2. The seismic image is highly distorted to the east of 9 km and in this legacy profile appears to be seismically ‘transparent’. This lack of continuity of the seismic events in the reflection image was attributed to the severe disruption of this zone that we have interpreted to be the central uplift created during the impact

event. We expect the seismic velocity to be lower in this regime due to the disruption and this is confirmed in the velocity inversion model.

3. The broken strata on the faulted trough are another diagnostic structure visible on the profile (6-7 km). This fractured zone is estimated to have a low velocity feature due to the induced deformations and fracturing.

4. The high velocity uplifted below the low velocity disruptive zone at 10 km indeed correlates well with the uplifted Milk River strata interpreted on the reflected profile. Such a pull-up feature might be a good indicator of the rising of the deeper sediments during the modification stage of the formation of a complex impact crater.

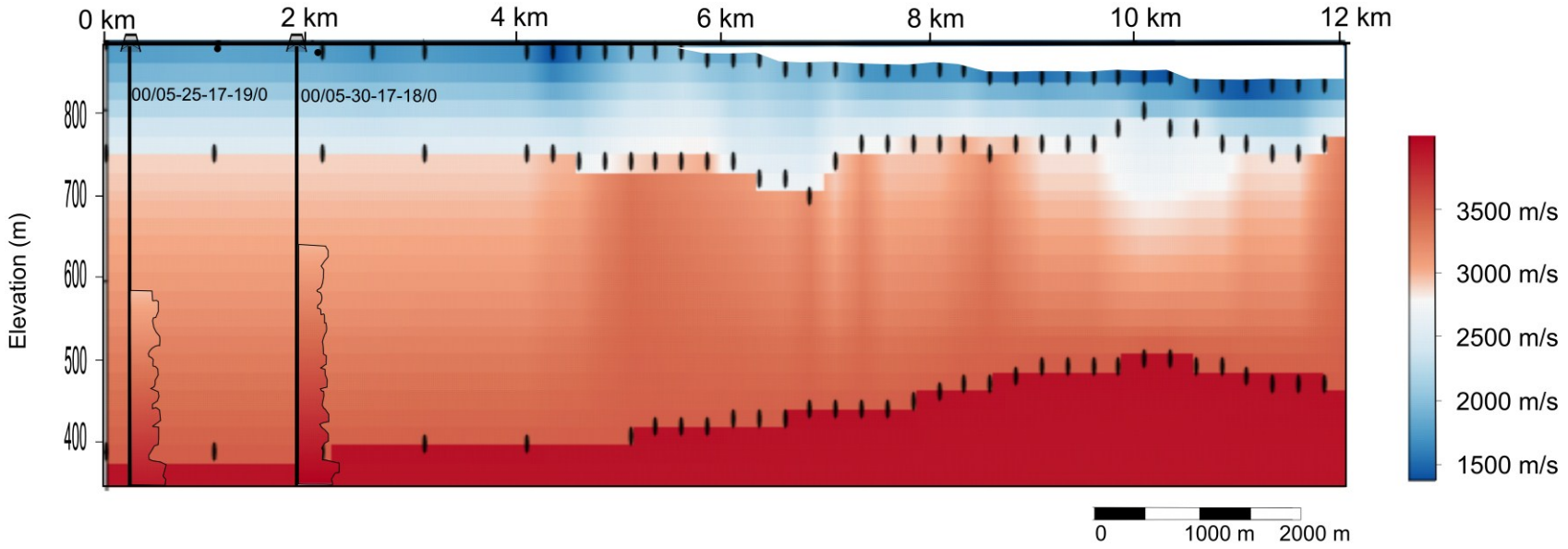


Figure 5.6 Velocity model correlated with sonic logs, also color mapped with the same code, from Wellbore 00/05-25-17-19/0 and Wellbore 00/05-30-17-18/0. Vertical depth is exaggerated x8 for display.

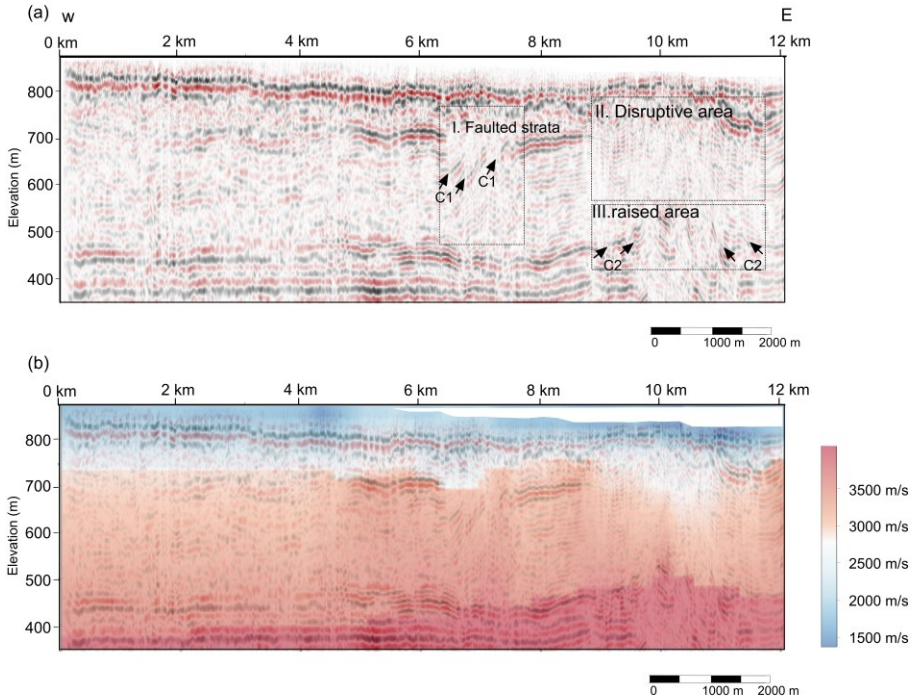


Figure 5.7 (a) Final post-stack time migrated seismic depth section of the Profile 86251. Disturbed and faulted areas are marked by dash line boxes. C1 is the faulted shallow Cretaceous unit, C2 is the uplifted deeper Cretaceous units. (b) As for (a), the velocity model was overlaid to correlate the anomaly features between velocity model and reflection profile. Vertical depth is exaggerated x8 for display.

## 5.7 Conclusion

A seismic travel time inversion study was carried out with the refracted arrivals from Survey 86251. By utilizing the RayInvr program provided by Zelt [1992], a three-layer velocity model with sufficient resolution was generated to display the subsurface structural features. Two significantly disrupted zones with pronounced low velocity characteristics were visible on the velocity model. These zones might result from the impact induced fracturing processes, which lowers the seismic wave speed. According to the deformation of the structural morphology and velocity discrepancy, these two zones were estimated to be the annular moat with faulted blocks and the highly disruptive central uplift, respectively. In fact, the raised area in the bottom of the central uplift area presents a velocity high pattern which might result from significant uplift of the lower strata. It is also important to note that this ray-traced model shows numerous similar velocity features with the structural patterns displayed on the reflection profile.

# Chapter 6 High-resolution Seismic Surveys

In order to improve our understanding of the structural features seen in the legacy 2D seismic profiles, we carried out a high-resolution seismic survey in the summer of 2013 along sections of Profile 86251. In this Chapter, I provide a comprehensive overview of these newly acquired seismic reflection profiles, beginning with the data acquisition, moving through the processing workflow, and ending with the interpretation of the stacked images. It is important to point out that the near-surface noise is the primary problem that influences the quality of the shallow subsurface signals. Thus, acquisition strategies and appropriate processing steps optimal for near-surface imaging were utilized, significantly enhancing the signal-to-noise ratio (S/N). These profiles provide additional evidence in support of the impact hypothesis for the structure, and may point the way towards a better understanding of the dynamics of the impact itself.

## 6.1 Seismic Data Acquisition

The high-resolution 2D seismic survey was carried out from west to east on the west bank of the Bow River. These new data were obtained at the same location as Profile 86251 in Survey 86 already discussed in Chapter 4. The total length of this straight seismic survey is ~4.7 km of two shorter lines strategically positioned to acquire data over the rim fault terrace and the central peak (Figure 6.1). The west profile is about ~2.9 km in length and was completed in three cable-spread length sections in 5 days. While the east line is ~1.8 km and was acquired in two cable-spread segments in 2 days.

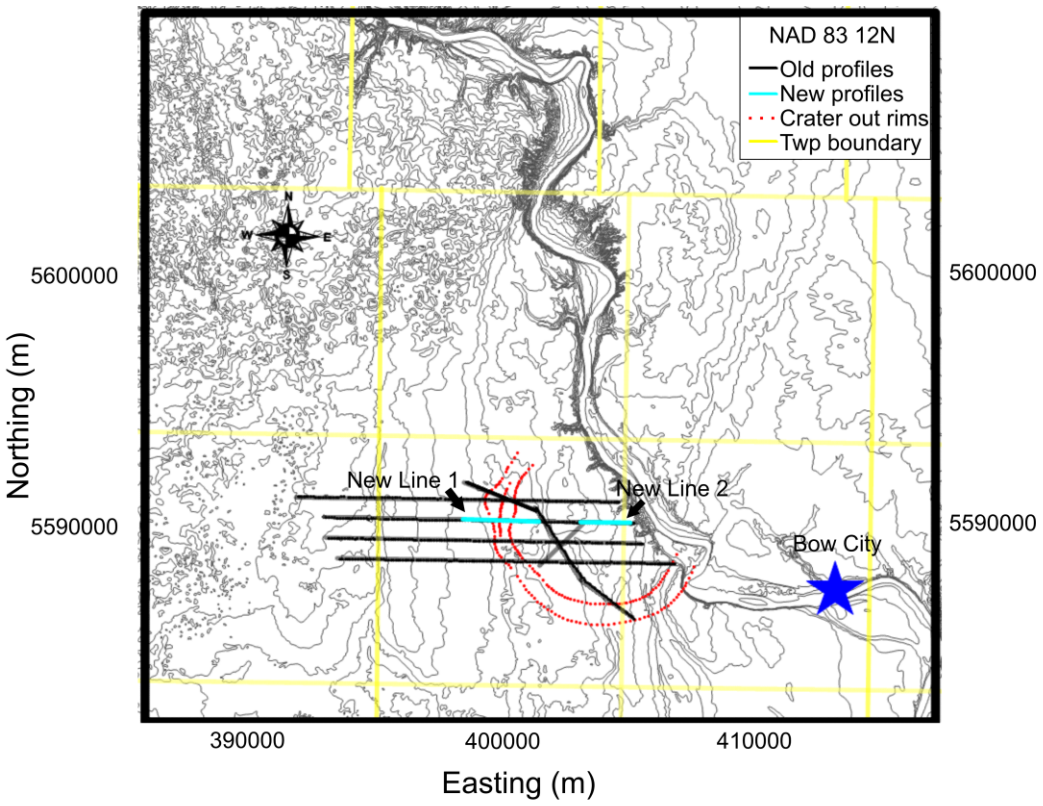


Figure 6.1 Location map of the new seismic surveys (cyan lines). The black lines are the locations of the donated 2D seismic profiles described in Chapter 4. The red curves represent the estimated faults patterns from seismic data. The yellow straight line shows the township boundaries. Data coordinates are in UTM 83 12 N zone. Figure is modified from *Schmitt et al.* [2013] and *Glombick et al.* [2010].

The University of Alberta Minivib$^{TM}$ (Industrial Vehicles International of Tulsa, Oklahoma) providing a linear sweep from 15 hz to 180 hz over 15 seconds, was utilized as the energy source. The 14-Hz geophones (for transferring mechanical signals to electric signals) were spaced every 4 m, creating a total 240-channel seismograph to record the seismic signals. The vibrator was activated at every field station (4 m spacing) with the 15 s linear sweep; a raw uncorrelated record was acquired at a 1 ms sampling period for 16.38 seconds such that the total length of the final correlated shot gather was about 1.38 s.

Increasing the quality of the seismic image is the key factor in designing this survey, and as such one must consider both the on-site conditions and the regional geological setting. One important consideration is the resolving power available. Seismic resolution is defined as the ability to identify two geologically distinct features from one another. The resolution may be classified as vertical and horizontal.

Vertical resolution describes the thinnest layer that can be clearly distinguished in the seismic records. It is mainly limited by the predominant wavelength λ and according to Rayleigh's quarter wavelength criteria is often assumed to be limited to approximately $\frac{\lambda}{4}$, although this may be pushed further under appropriate circumstances [*Widess*, 1973]. Thus, the shorter the wavelength, the better will be the vertical resolution. As there is an inverse proportional relationship between the wavelength ($\lambda$) and the frequency ($f$) with the velocity $v = \lambda f$, increasing the dominant frequency of the signal is one way to enhance the vertical resolution. The real situation is somewhat more complicated，and while one should strive to have the dominant frequency as high as possible the overall bandwidth (range of frequencies that contain useful data) should also be maximized.

One problem with real signals propagating into the earth is that there is significant attenuation of the higher frequency components of a signal with distance. Consequently, the deeper sections in fact, have much lower bandwidth and peak frequency than the shallow layers. In this study, the target units are in the upper 500 m and the thinnest geological unit is estimated to be 2 m [*Glombick et al.*, 2010]. Thus, a sweeping frequency of 180 Hz is selected and the data sampling rate is set at 1 ms to avoid the aliasing.

Table 6.1 Comparison of the acquisition parameters for the 2D seismic surveys.

| Parameter | Line1 | Line2 | 86251 Early line as comparison |
|---|---|---|---|
| Year of Acquisition | 2013 | 2013 | 1986 |
| Length of survey | 2.8 km | 1.8 km | 11.61 km |
| Line direction | W-E | W-E | W-E |
| Source | 6000-lb Minivib$^{TM}$ unit | 6000-lb Minivib$^{TM}$ unit | Dynamite |
| Sweep frequency | 15-180 Hz | 15-180 Hz | ~ |
| Sweep length | 16.383s | 16.383s | ~ |
| Shot interval | 4 m | 4 m | 100 m |
| Number of shots | 978 | 535 | 132 |
| Number of stations | 720 | 456 | 751 |
| Receivers | OYO 14-Hz | OYO 14-Hz | 14-Hz |
| Receiver spacing | 4 m | 4 m | 20 m |
| Group configuration | Single space | Single space | 9 over 20 m |
| Spread type | Split-spread | Split-spread | Symmetric split-spread |
| Number of Channels | 240 | 240 | 120 |
| Sampling interval | 1 ms | 1 ms | 2 ms |
| Record length | 1.38 s | 1.38 s | 3 s |
| Far offset distance | 2 km | 1.15 km | 12 km |
| Average nominal fold | 240 | 240 | 12 |

Lateral resolution is characterized as the ability to separate two close reflecting points in the horizontal direction. It is primarily dependent on the radius of the first Fresnel zone ($R_f$), which can be given as [*Sheriff*, 2002]:

$$R_f = \frac{v}{2}\sqrt{\frac{t}{f}} \tag{6.1}$$

where $v$ is the velocity of the seismic wave, $f$ is the frequency of the incident wavelet, and $t$ is the two-way travel time from source to the reflected medium. The essential meaning behind Equation 6.1 is that one should not be able to distinctly and independently distinguish two geological features if they are laterally separated by a distance of less than $2R_f$. As such, a commonly used tool to improve the horizontal resolution is increasing the dominant frequency of the seismic wavelet as much as possible. As with the vertical resolution, the fact that the deeper sections also are less clear is due to the higher frequency components being increasingly attenuated as the wave propagates. Thus, the dominant frequency shifts downwards and the Fresnel zone progressively increases.

The seismic data used in this project is entirely in a digital form, and as such we must consider some of the implications of this prior to designing our survey. In the case here, our geophones provide a continuous analog voltage, whose amplitude varies with time (i.e., the seismic signal). The values of such geophone voltages are sampled, or digitized, at a constant time increment of $\Delta t$. This time increment is very important because it controls the maximum frequency that the signal should contain. This is called the Nyquist frequency ($f_{Nq}$), expressed as:

$$f_{Nq} = \frac{1}{2\Delta t} \tag{6.2}$$

where $\Delta t$ is the sampling interval. If a signal contains frequencies above this limit, the energy within those components are inadequately sampled and said to be

aliased. The consequence of this is that the energy is not lost but is inappropriately shifted to lower frequencies, which can lead to artifacts in the data. As the maximum frequency utilized in this survey is 180 Hz, the corresponding largest sampling time interval would be 2.7 ms. Consequently, signals would not be affected by aliasing and distortion with applying 1 ms sampling time interval during the signals recording.

Another issue to consider is the lateral spatial sampling afforded by the geophones on the ground. Similarly, the space sampling interval can be constrained by the Nyquist wavenumber (in units of radians/m), which is defined as

$$K_{Nq} = \frac{\pi}{\Delta \mathrm{x}} \tag{6.3}$$

where $\Delta$ x is the spatial sampling interval (i.e. the spacing between the geophones or stations). Instead of using the wavenumber, one can just as readily employ the concept of the spatial Nyquist frequency $F_{Nq} = 1/2\Delta x$ with units of cycles/m, which may be more easily understood. This is tied to how fast a given seismic arrival 'moves out' laterally across an array. For purposes of illustration consider a snapshot in time of the amplitudes of a monofrequency seismic signal with time frequency $f$ propagating horizontally along the surface with an apparent speed $v'$; the apparent lateral wavelength of this signal will be $\lambda' = v'/f$ and its apparent lateral spatial frequency is then $f/v'$. Hence, to avoid spatial aliasing, $f/v' < F_{Nq}$ or $\Delta x < v'/2f$ needs to be satisfied. This means that signals that moveout at low apparent wave speeds across the array or those with sufficiently high temporal frequencies can be more easily aliased. Hence, larger receiver spacing would result in more frequency components being aliased. Unfortunately, it can be very difficult to avoid spatial aliasing even with the small $\Delta x$ = 4 m used in our surveys. However, we must realize that there is no perfect survey existing since the cost of the survey is another key factor that needs to be taken into account.

Undoubtedly, a seismic survey with higher signal-to-noise ratio (S/N) provides more useful information of the subsurface structures. Different strategies are used to maximize the signal. One would be to activate the seismic source repeatedly at the same location and then sum, or 'stack', all of the time records obtained at the same source-receiver combination. This is referred to as 'vertical stacking', and it can be problematic as this requires more time to acquire the data. Another, more important, strategy is the common midpoint stacking technique, which essentially allows one to sum together (after appropriate corrections described in detail later) a large number of records that are all ostensibly sampling the same reflection point in the earth. The more common midpoint (CMP) records that can be stacked, the better the signal to noise ratio is. In seismic data acquisition community jargon, the number of traces stacked is called the fold. Hence, here we employed a strategy of activating at every field station to obtain higher fold. Usually, increasing the number of 'live' geophones in a spread and more shot points in the survey lead to a higher fold and correspondingly stronger signal energy [*Duo*, 2011]. Indeed, far offset records also increase the fold of the seismic survey. However, separating the seismic refractions and reflections signals at the long offset usually adds more difficulties in the seismic reflection processing due to the similar frequencies and moveout velocities, particularly for the near surface reflectors [*Pelton*, 2005]. Other problems such as normal moveout (NMO) stretching and frequency distortion occurred inevitably in the shallow reflection imaging as well [*Yilmaz*, 2001]. Regardless, far-offset gathers were collected to yield more velocity information for the tomography modelling. By utilizing the layout of 240-channels and shooting at every receiver station, a favorable result of 240 nominal fold was achieved instead of the maximum of 20 obtained in the earlier legacy surveys discussed in the last Chapter. In our high spatial resolution surveys, reflections from the near surface reflectors are stronger and more consistent which build a solid base for the high-resolution seismic characterizations.

## 6.2 Seismic Data Processing

Data processing is an important step on the path to producing high quality interpretable seismic. By means of noise attenuation and signals correction, the reflected signals are clearly identified to display the final subsurface structures. Numerous procedures have been developed to remove various kinds of 'noise'. Generating high resolution profiles, too, requires both careful acquisition of the field data and the appropriate design of the processing procedures (or workflow). Severe artifacts can completely conceal the real structures which lead to the unexpected result.

In this project, seismic data processing was completed using VISTA® software package provided courtesy of GEDCO, Calgary. The following sections will discuss the detailed work flows employed during the data processing. These include noise attenuation, amplitude balancing, surface statics, deconvolution, velocity analysis, post-stack migration and filtering. Table 6-2 list the processing sequences applied in this study.

Table 6.2 Processing Work Flow

| Processing Step | Description |
|---|---|
| Geometry Input | |
| Trace editing | Kill and remove bad traces |
| First-break picking | Characterize low velocity zone for statics input |
| Amplitude gaining | Compensate for energy loses |
| Elevation/refraction statics | Remove lateral variations near the surface |
| Noises filtering and Muting | Attenuate noises |
| Predictive deconvolution | Eliminate multiples |
| Spiking deconvolution | Compress the wavelet into spike |
| CMP binning | |
| Initial velocity analysis | Determine stacking velocity |
| NMO correction | |
| Residual statics | Remove near-surface velocity variation |
| Surface consistent deconvolution | Improve surface variation |
| Velocity analysis (iterative) | |
| NMO correction | |
| CMP stacking | |
| Post-stacked deconvolution | Remove multiples |
| FX- 2D prediction | Attenuate incoherent noise |
| Migration | Correct dipping reflectors into true position |
| Time-to-depth conversion | Present data in depth domain |

### 6.2.1 Geometry set-up

The proper survey geometry assignment is essential before applying any work flow. It involves assigning the accurate location of each field station in *x* and *y* (i.e. easting and northing) and elevation of each shot and receiver point to the correct trace channel number. Improper geometry assignments can yield unexpected velocity and statics problems and eventually lead to the misinterpretation of the subsurface structures. Therefore, extreme care needs to be taken to control the quality of the geometry dataset.

This process of course begins in the field with a proper survey of the field stations. Usually, these geodetic data are collected separately as part of the seismic project with Global Positioning Satellites (GPS) or leveling data and are stored separately. During shooting of the seismic survey, detailed observer reports should also be recorded. According to these reports, the geometry of the shot and receiver points in each shot gather can be assigned with the field station number. Indeed, detailed notes on the survey records can help the processor gain better understandings of the situation of the acquisition such as weather disturbance, traffic noise, and electric pipeline influence.

### 6.2.2 Seismic vibrator correlation

A 6000 lb Minivib$^{TM}$ was utilized as the energy source, with a linear sweep of 15 s length with 0.5 s linear tapers generated. Due to the significant overlaps of the 15 s long wavelet, the raw shot records (Figure 6.2a) are not informative until they have been correlated with the seismic sweep (Figure 6.2b). The vibrator correlation process yields an output trace that is similar to that which would be produced by a simple source such as an explosion. Hence, the generated common-shot gather reveals the information of the subsurface reflectivity structure that, through the convolutional model, is related directly to the geological structure.

During the seismic survey, the source-generated sweeps and the corresponding geophone output signals are stored digitally to await further processing. The preliminary quality control is applied on the correlated shot gathers in the field computer and subsequent re-examination will be conducted for later processing.

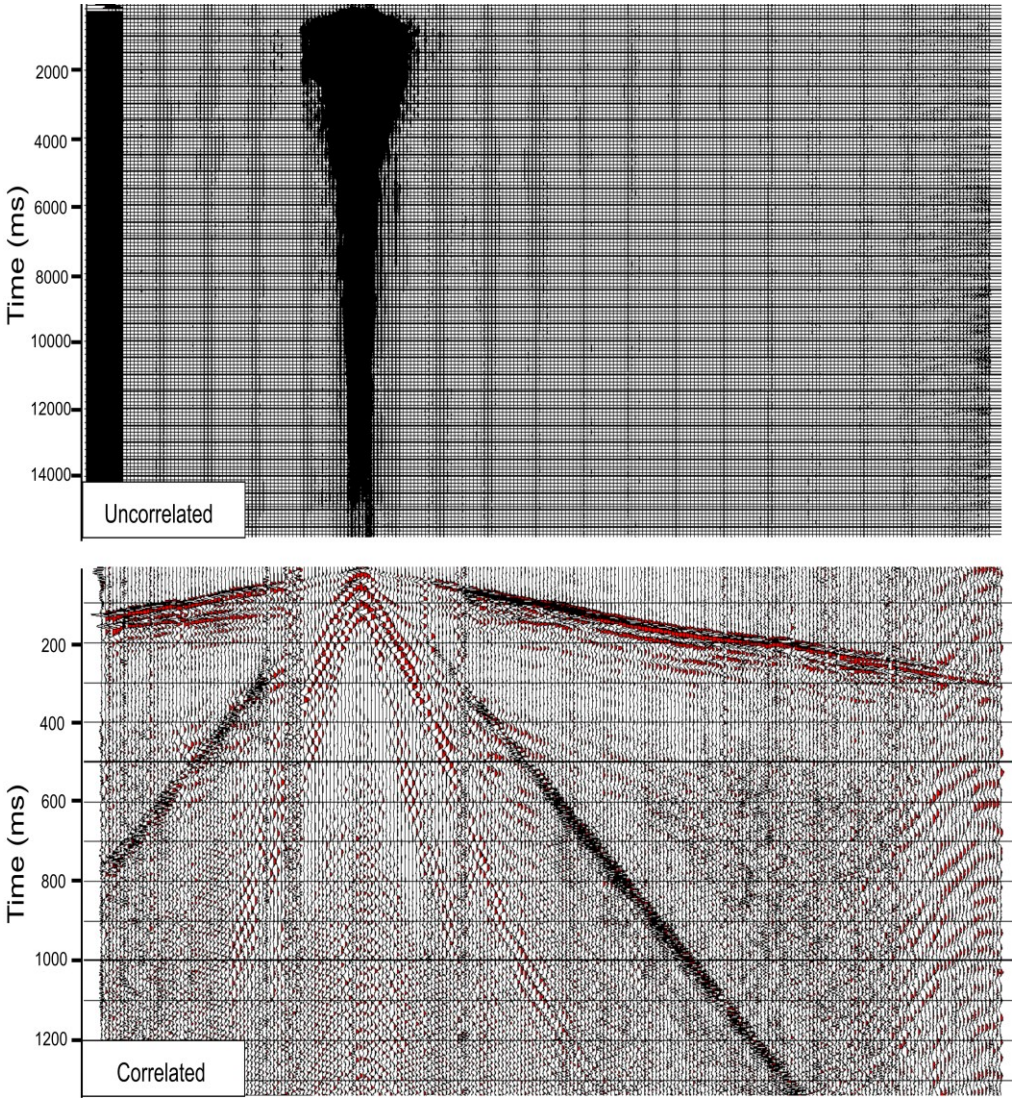


Figure 6.2 Examples of raw uncorrelated shot gather (top) and its corresponding correlated (bottom) shot gather. Automatic gain control (AGC) was employed for displaying the corrected shot gather. A 1.3 s correlated record was obtained from a 15 s vibrator sweep and the 16.3 s total record length.

### 6.2.3 Trace editing

Noise traces with anomalous amplitudes, equipment glitches and spurious frequencies can severely affect the signal-to-noise ratio (S/N) and are deleterious to the data quality. Therefore, special attentions need to be made during the Quality Control (QC) of the seismic records. Bad traces with distinctive amplitude and glitches can be detected easily by visual examination (Figure 6.3). Random noise might result from the temporary circumventing of equipment, the improperly planting of geophones, the traffic noise on the side ways or the extreme weather conditions such as heavily rain or wind. Killing or muting these significantly noise-contaminated traces is a necessary step ensures that this noise does not enter into the final data for processing.

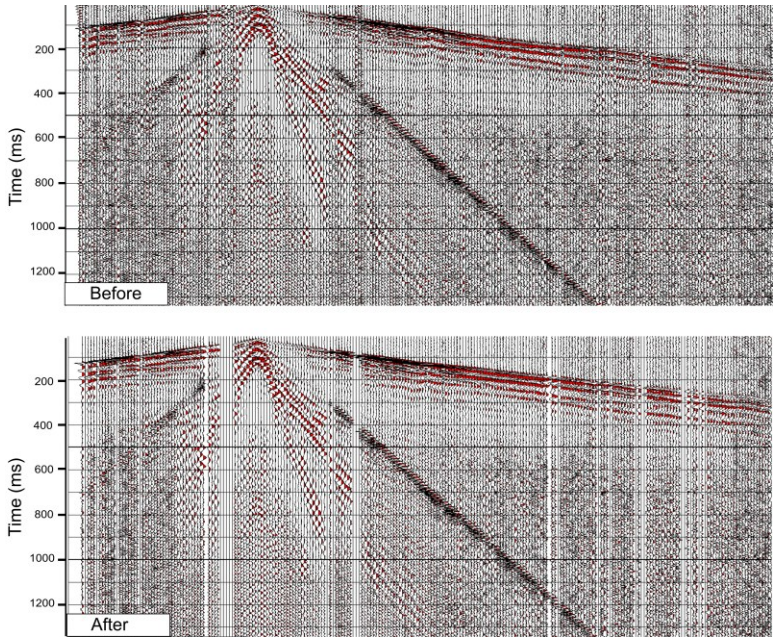


Figure 6.3 Example of the bad tracing which have anomalous amplitudes, transit glitches and spurious frequencies.

In addition, computing the energy and frequency attributes of the input seismic traces and cross plotting the corresponding statistics are other useful techniques to recognize the bad traces from large dataset. As the source-generated amplitudes decay geometrically with propagation offset distance, higher frequency can be reserved in the near surface that closes to the source. The extreme high or low frequency values performed on the cross-plotting graph can be rejected since these values are probably associated with strong noise traces. Monochromatic noise typified by a specific frequency (such as power line noise at 60 Hz) can be obviously observed and muted as well (Figure 6.4).

However, it is important to note that coherent noise including ground roll, surface waves, and air blast are not suggestive to be muted here due to the fact that such noises are usually considerably contaminated with the signals. Processing techniques that efficiently remove coherent noises will be discussed later in this chapter.

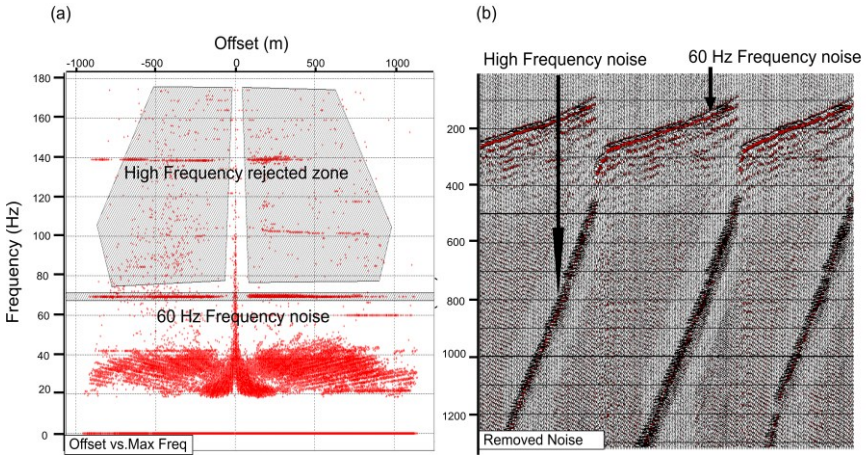


Figure 6.4 (a) Cross plot of source-receiver offset versus maximum frequency for seismic Line 2. (b) Display of the attenuated noise that within the rejected zone on (a).

### 6.2.4 First-break Picking

A ‘first break’ is geophysical jargon for the time that is chosen, or ‘picked’ from a seismogram of the arrival of a seismic wave. In the case here, they are the earliest signal detected as the seismic pulse initiated from the energy source and their travel time measurements are utilized to characterize the velocity distributions near the subsurface as was demonstrated in the last Chapter. Usually, the initial compression on each trace displays a down kick and the shape of locus of these refracted signals with increasing source-receiver offset primarily depends on the elevation variations of the sources and the receivers. The low velocity near surface zone, usually referred to as the weathering layer, is often characterized by the irregular and laterally varying velocity structures (Figure 6.5). Properly identifying such first arrivals on the common shot gather (CSG) can ensure the suitable statics corrections to remove the influence of the lateral variations and generate clear velocity image of the subsurface structures. Further, travel-time inversion algorithms applied to these first breaks can delineate the geological structures on the basis of the wave speeds of the differing lithologies (as shown in chapter 5).That aside, this additional velocity information which can be further employed in recognizing the velocity anomalies and the migration process.

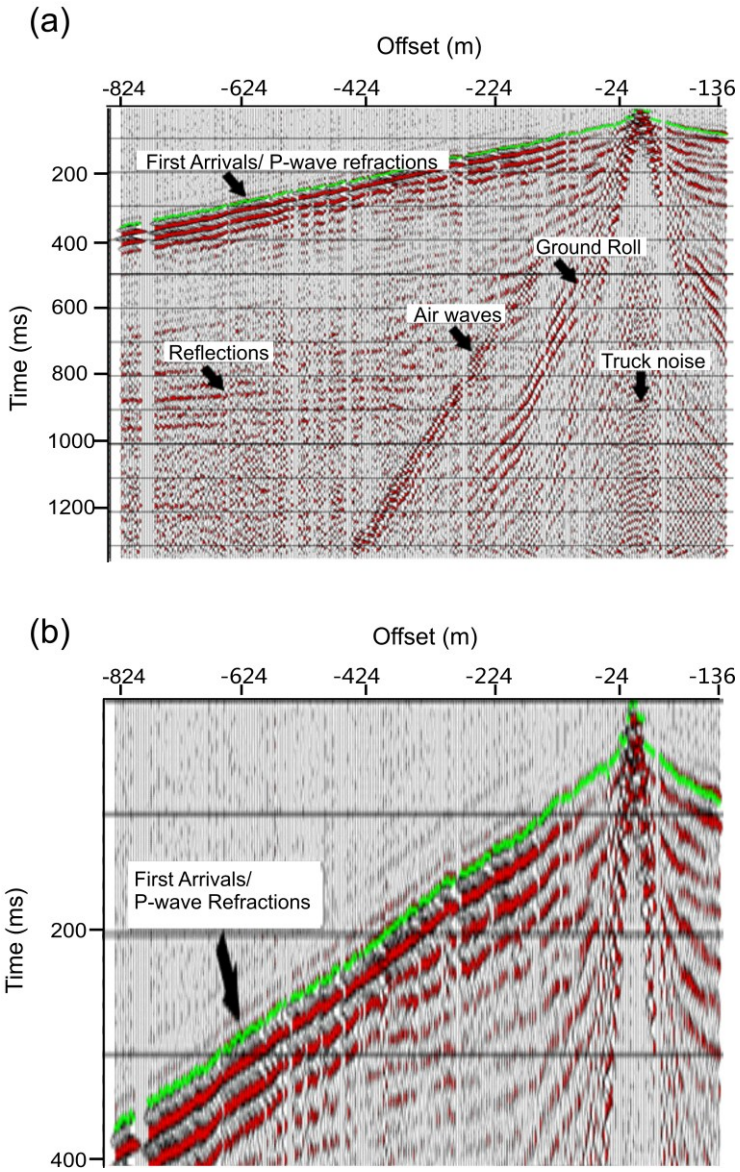


Figure 6.5 Shot gather showing the different types of seismic waves.

## 6.2.5 Energy compensation

In the seismic reflection method, the signal-to-noise ratio (S/N) is one of the crucial factors to influence the image quality and compensating energy (or more appropriately the amplitudes) of the reflections is key in this process. The basic

reason we must consider this is that the wave amplitudes decrease with distance from the source point. In a homogenous medium, the energy travelling outward from a seismic pulse develops a spherical wavefront because the speed is the same in all directions. In the simplest hypothetical case we assume that no energy is lost to the medium as the wave travels (i.e. there is no attenuation), that is, the energy of the wavefront remains constant. However, as the area of the wavefront grows with progressive movement outward, its energy intensity as measured in terms of Watts/m$^2$ must decay proportional to $1/r^2$, where $r$ is the radius of the wavefront at a given time. Energy (and hence intensity) is also proportional to the square of the amplitude of the wave; the amplitude decays according to $1/r$. In fact, the Earth's interior is quite complex with a variable velocity structure. This velocity structure also results in focusing and defocussing which controls the intensity at points over the surface of the wavefront. Finally, real rocks do absorb the wave energy during its propagation. As such, large portion of the energy loss is caused from the inelastic attenuation such as the frequency-based absorption and the wavefront scattering. All of these factors contribute to the decay of the seismic intensity, hence, amplitudes with distance from the source. While in principle, one could account for all of these deterministically, actually obtaining the proper information to do this is not practical and usually more empirical or experienced based approaches are taken to correct for the decline in the wave amplitude. In this study, a number of techniques have been applied to compensate the energy losses empirically and statistically (Figure 6.6).

Automatic gain control (AGC) is one of the most commonly applied methods which utilizes the technique of the automatic volume control in electronic audio system [*Gadallah and Fisher*, 2005]. The amplifier in each AGC window is determined by the ratio between the mean value of all of the amplitudes in the time gate and the average value in the entire trace. The critical parameter of this method is the length of the time gate. A long time gate can result in too many variations, while a short time gate can lead to the loss of the signals due to too

much equalization. In our study, a relative small window size of 400 ms was selected to amplify the shallow target layer (Figure 6.6b).

Another method performed in the study was exponential gaining which primarily focuses on the correction of geometrical spreading [*Claerbout*, 1986]. This technique is based on the reality of the exponential seismic energy losses with time and distance and recovering the energy by multiplying an appropriate exponential curve ($i.e., t * e^{nt}$). A selection of $n =$ 0.8 was utilized after a series of trials (Figure 6.6c).

In addition, the frequency spectrum of the seismic data is compensated by the effective technique of time-variant spectrum balancing which decomposed into components over different frequency bands, an individual gain is then separately applied to each component and then all of the components are superposed back together to reform the now-gain trace. This has the result of increasing the high frequencies in the signal with an added bonus that much of lower frequency surface wave energy is weakened. It is important to note that the good determinations of the band-pass range and the AGC window need to be reached to ensure the good output (Figure 6.6d).

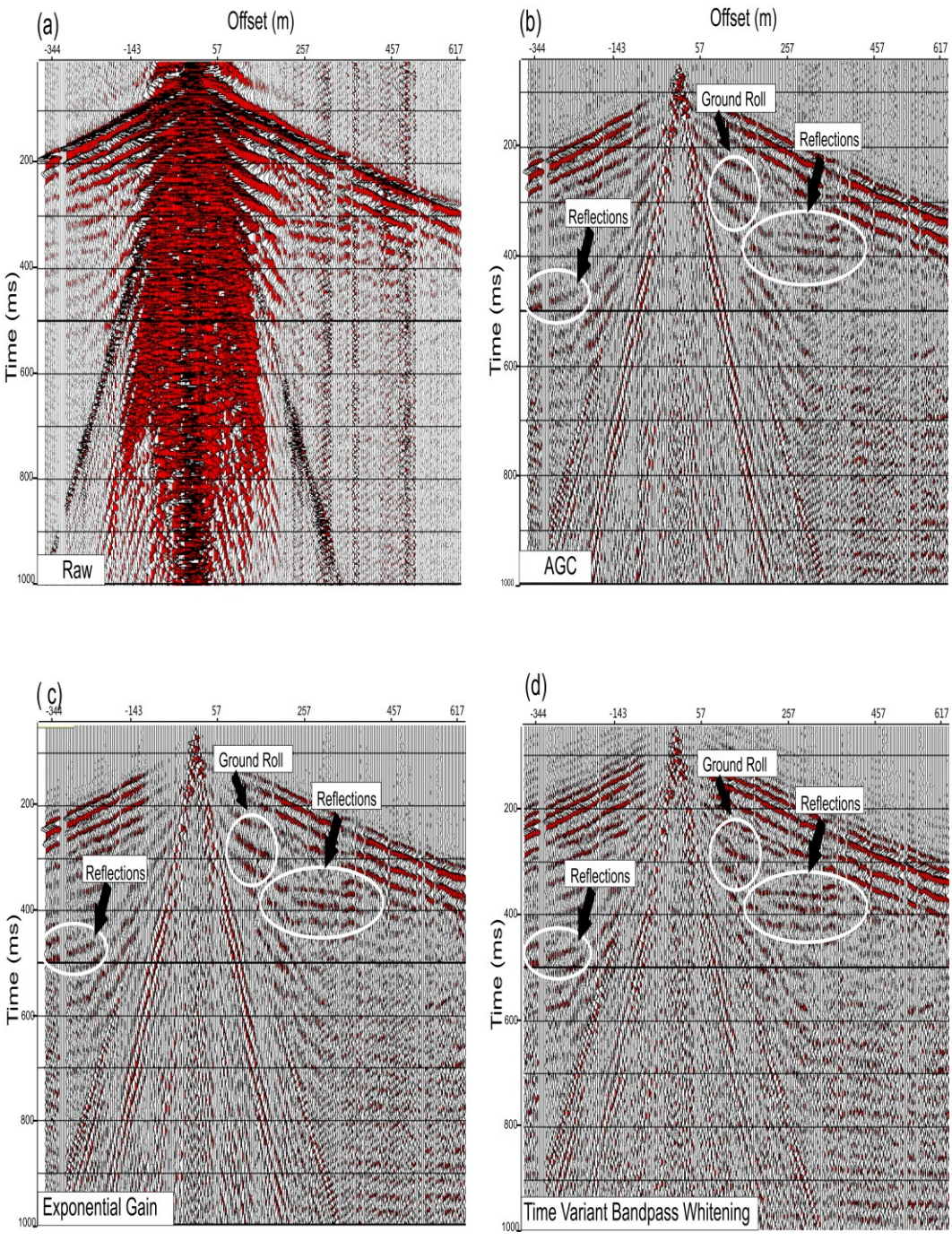


Figure 6.6 Illustration of different amplitude compensation methods utilized in the study. a) Raw shot gather. b) As for (a), applied AGC. c) As for (b), applied exponential gaining. d) As for (c), employed time variant bandpass whitening.

### 6.2.6 Elevation/Refraction Statics Corrections

It is widely known that the times of the seismic reflections are strongly affected by the heterogeneous near-surface velocity conditions, particularly when the surface topography and the shallow subsurface structures are complicated and irregular. The unconsolidated layer beneath the surface, which is named as weathering or low velocity zone, is characterized with pronounced low velocity speed and severe absorption of the high frequency components [*Yilmaz*, 2001]. The transit times of the reflected seismic waves traveling through this heterogeneous unit are shifted up or down in time relative to that expected due to the variance of ray paths and speed. In this case, the pattern of the seismic reflected waves can be significantly distorted. Consequently, if these near surface problems are not accounted for properly, a poor-quality image with artificial geologic structures might be produced. The time shifts required to attenuate this problem are referred to as 'static time shifts' or 'static corrections'.

Elevation static correction is a widely used technique to remove the effect of the topographic variations on seismic reflection records. It requires that a constant datum elevation be chosen and then it seeks to correct for the topographic highs and lows relative to this datum by shifting the seismic traces up or down in time as needed. The reader may recall in the last Chapters that the datums of all of the legacy seismic surveys differed, and before these data sets could be properly integrated they all needed to be shifted to the same datum plane. Method variation on this theme is called the refraction static correction that aims to reduce time shifts introduced by variable thicknesses and velocities of the low velocity layer. This is accomplished using algorithms such as Hagedoorn's plus-minus technique, the reciprocal method, and least-square inversion [*Chan*, 2013; *Yilmaz*, 2001]. Here, the plus-minus technique with utilizing the first breaks was utilized to build the model of the near surface.

In conducting the elevation/refraction static corrections, properly estimation of the shifted time is the key factor to ensure a good outcome. In fact, this problem can be well resolved by good knowledge of the selected elevation of the fixed datum, the velocity of the weathering layer, and the corresponding replacement velocity. The velocity of the weathering layer can be estimated from the velocity of the direct waves on the shot gather and further corrected with the geological surficial information. The fixed datum is usually placed slightly below the unconsolidated layer, and the replacement velocity between the weathering layer and the fixed datum is calculated by the velocity of the first refractions on seismic record [*Gadallah and Fisher*, 2005]. However, if the target interval is shallow and significant elevation variations exist on the surface, placing the fixed datum at an elevation above the highest surface point might be a better choice because it avoids the potential loss of some near-surface data. In this case, a reasonable replacement velocity needs to be assigned by combining the regional geological environments and the seismic events. A number of near-surface seismic reflection studies [*Ogunsuyi and Schmitt*, 2010; *Stucchi and Mazzotti*, 2009] have pointed out that the replacement velocity could be considered as the velocity of the first refractions when the fix datum was chosen as the elevation of the highest point.

Due to the shallow target units, a datum with an elevation above any point on the surface was employed. For the legacy seismic datasets described in the Chapter 4, a datum of 900 m was selected. For these new lines acquired in 2013, a datum of 840 m was applied since the highest elevation of the 2013 field stations was much lower. The same weathering velocity of 650 m/s was utilized and the replacement velocities were recognized from the travel speed of the first refractions. Therefore, significant improvements can be observed in figure 6.7 that the apparent bumps were removed after corrections. Detailed elevation and refraction statics of new Line 1 were displayed in figure 6.8.

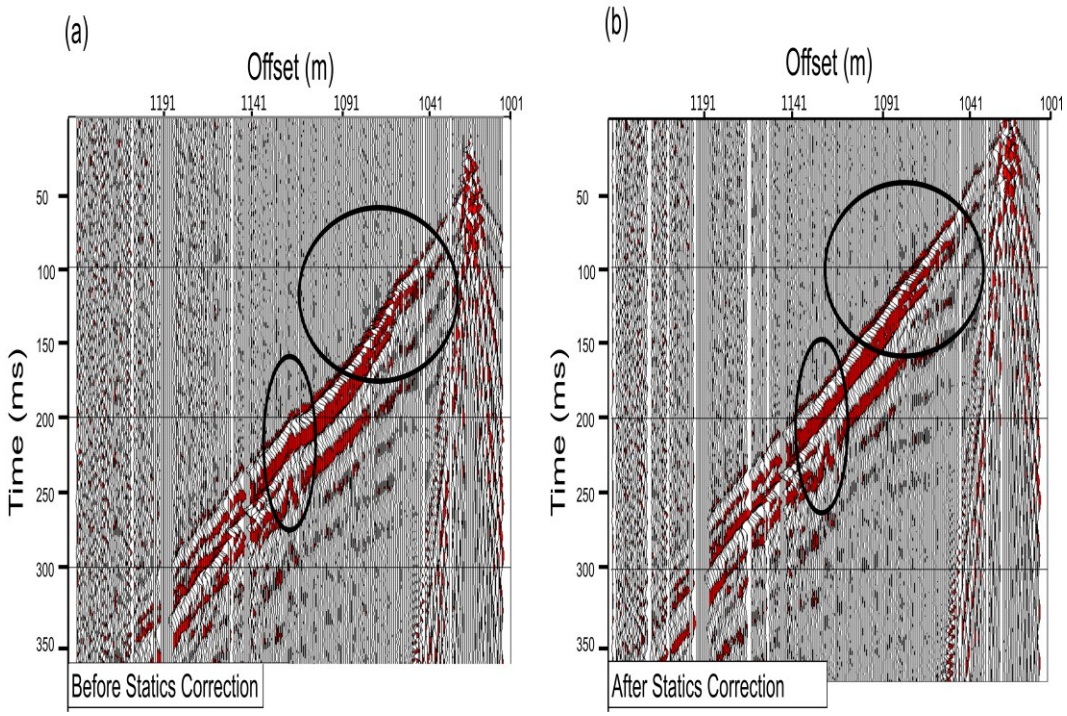


Figure 6.7 Examples of the same shot gather in line 1 showing the improvements of statics corrections. a) Before applying statics corrections. b) After applying statics corrections.

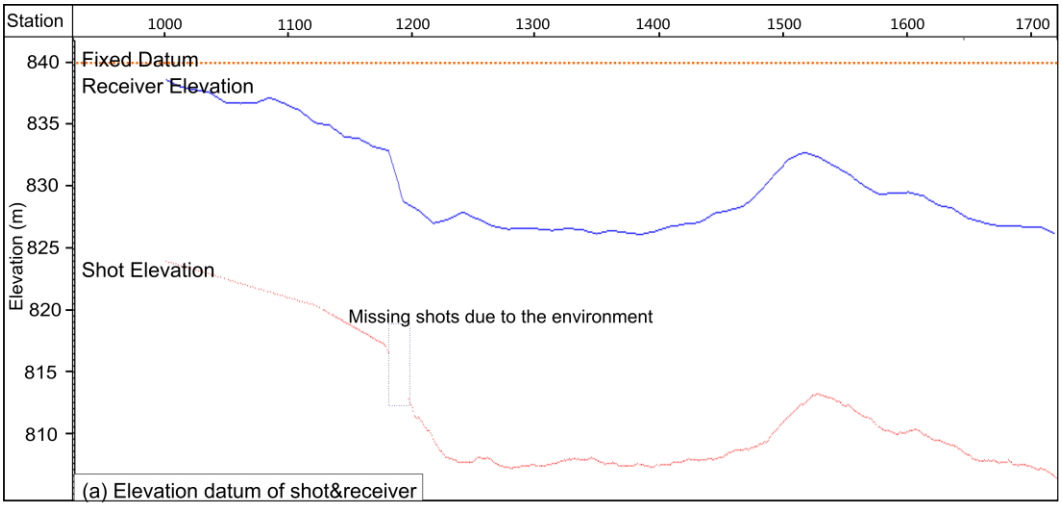


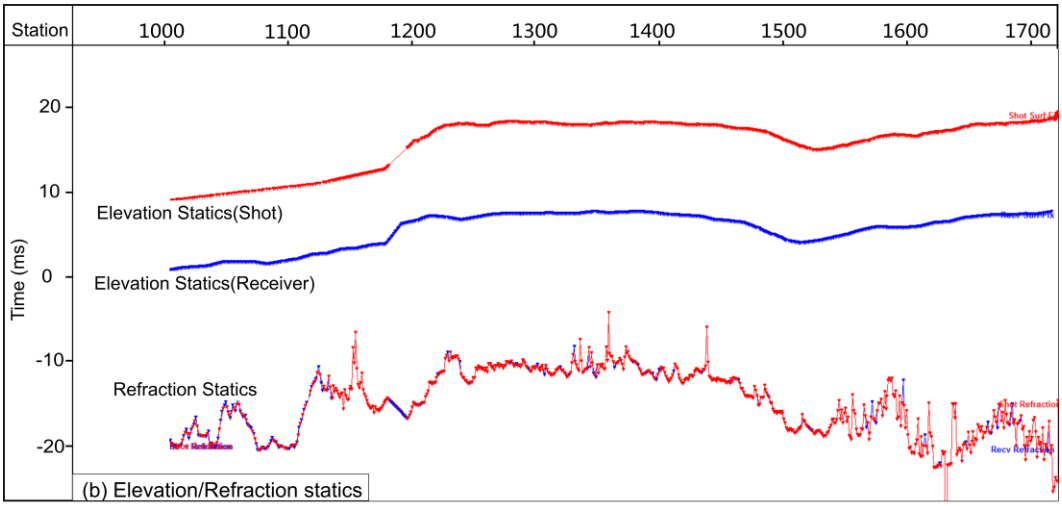


Figure 6.8 (a) Elevation of the shots and receivers with showing the fixed datum of new Line 1. (b) Elevation and refraction statics calculated in Vista® using the fixed datum in (a). Red lines represent the shot and blue lines represent the receivers.

## 6.2.7 Frequency Analysis

As discussed earlier, the continuous analog seismic signals output by the geophones are sampled at a selected constant time interval to create a time series

trace. Time series have specific amplitude at certain time and these digital signals can be decomposed using the Fourier transform into a number of sinusoids with unique frequency, amplitude and phase-lag. The Fourier transform is also another way to represent the data but in the frequency domain instead of the time domain. The sinusoids can be characterized by unique amplitude and phase at certain frequency and the amplitudes and their phase shifts can be plotted as functions of frequency.


Figure 6.9 Flow chart displaying the Fourier Transform and data analysis.

Fourier analysis is a powerful tool in seismic data processing because the signals in frequency domain allow the processor to apply numerous techniques to analyze the data set. In practice, the Fourier transform is affected on the digital data using the Fast Fourier Transform (FFT) algorithm (Figure 6.9). In order to better recognize the signals in frequency component, different frequency panels from 0 to 90 Hz were generated to extract the corresponding signals in time domain. This frequency spectrum analysis provides a solid base for the latter procedures of noise attenuation and deconvolution that performed on frequency domain.

## 6.2.8 Noise Attenuation

The quality of the seismic images strongly depends on the signal-to-noise ratio (S/N). To enhance the data quality, boosting the signal amplitudes only emphasizes the visualization of the seismic reflections of interest. Indeed, effectively attenuating the seismic noise is another essential process. Seismic noise can be classified as being either coherent or random. Usually, random noise

such as ringy traces and spurious signals are detected visually and muted manually when QC the traces (as mentioned in section 6.2.2). Coherent noise can be generated by the energy source or by other factors such as electrical power line noise. These require special attention because the energy in these modes can overlap with the desired reflected signals both in the time and frequency domains. In this study, numerous techniques were employed to remove the coherent noise such as the time variant band-pass filter, the F-K filter, and the RT filter.

### 6.2.8.1 Time variant band-pass filter

Band-pass filtering in the frequency domain is an effective process that can attenuate or even eliminate energy in the signal at the low and high frequency limits. The most common application in seismic data processing is called the 'trapezoidal' filter, where the trapezoid is taken to be the shape of the function in the frequency domain that modulates (i.e. multiplies) the Fourier transform of the trace. Based on the frequency analysis discussed in section 6.2.7, the dominant frequency of the seismic signals is determined as well as the boundaries of where it is thought useful signal resides. The trapezoidal shaped function is then defined by selecting four frequencies at which the corner points of the trapezoid can be selected. Only the data falling within this bandwidth can be passed through the filter, while the components of the signal at frequencies outside the trapezoid are 'stopped' (i.e. removed).

This kind of filter is easily applied but it does have some disadvantages. One is that the frequency content of the seismic data and its unavoidable noise is usually time and space-dependent. For example, compared with seismic signals at later times, the shallower portions in a seismic have more energy at higher frequency as recently noted above. As well, low frequency noise such as head waves and refractions also exist in the seismic data and this overlaps in time the actual desired reflections [*Yilmaz*, 2001]. Therefore, different trapezoidal band-pass

filters chosen over different time ranges were utilized to better attenuate the noise, and as such these are called time-variant band pass filters. It is important to notice that such time variant band pass filter only solves a complex problem in a simplistic method. Regardless, good improvement could be observed in the corrected shot gather (Figure 6.10). Additionally, it is necessary to apply the time variant band-pass filter several times after later processes such as deconvolution, f-k filtering and migration due to the fact that these processes can inadvertently increase the noise again.

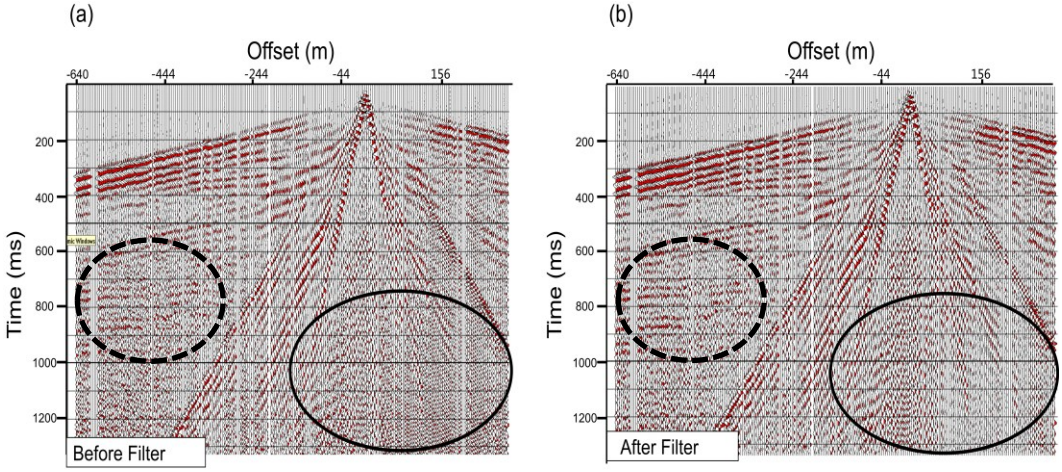


Figure 6.10 Selected shot gather from new Line 1 showing the effect of the noise attenuation by time variant bandpass filter. a) Raw shot gather before filtering. b) Same shot gather after noise eliminations (0-400 ms: 20/25 Hz - 60/70 Hz, 400-1200 ms: 15/25 Hz - 55/60 Hz). High frequency noise in the lower sections (highlighted by black circle) is significantly removed. The reflection signals (highlighted by the dot circle) are more evident in the filter profile.

### 6.2.8.2 Frequency - Wavenumber (*f-k*) Filter

Frequency-Wavenumber (*f-k*) filtering is proficient at attenuating coherent noise, such as ground roll or air waves, that moveout with a particularly velocity or dip in the image of the seismic data in the 2D space-time (*x-t*) domain. The *f-k* filter is carried out in the frequency versus wavenumber domain [*Yilmaz*, 2001] after application of the 2D Fourier Transform to the data. The moveout velocity ($v$) of the seismic waves across the *x-t* domain image can be found in the f-k domain

$$v = \frac{2\pi f}{k}, \tag{6.4}$$

where *f* and *k* are the frequency and wavenumber (reciprocal of the wavelength) of the seismic waves, respectively. According to such relationship, a seismic phase that has a constant velocity is displayed as a linear event with constant slope in the f-k domain. Thus, coherent noise with distinctive low velocity including ground roll, surface waves, air waves, and refractions can be separated from the reflections and further attenuated by the design of the rejected zone (Figure 6.11 (a)). In fact, the advantage of *f-k* domain filtering is that it avoids removing the signals that overlapped in the *x-t* domain. However, narrow rejected bands should be avoided as they can produce ringy traces due to the Gibb's phenomenon. Too wide filtered area should be paid attention as well because of the unexpected induced impact of wavelet distortion and over smoothing.

In our study, the *f-k* filter was applied to reduce the surface waves and ground roll that significantly concealed the reflection signals at near-offsets. However, seismic refractions were not eliminated to avoid attenuating the shallow seismic reflections. Figure 6.11 represents the f-k filter applied on shot gather in new Line 1. The rejected area was selected based on the velocity lower than the speed of air wave (350 m/s). On the f-k domain, these low velocity events can be easily

recognized by the small slope and the high energy. The pie-sliced rejected zones were designed in both positive and negative wavenumber panels since the data in the positive wavenumber panel was transformed from the negative offset and the other half was from positive offset signals. As a result, the ground roll and air waves existed in the shot gather were obviously attenuated.

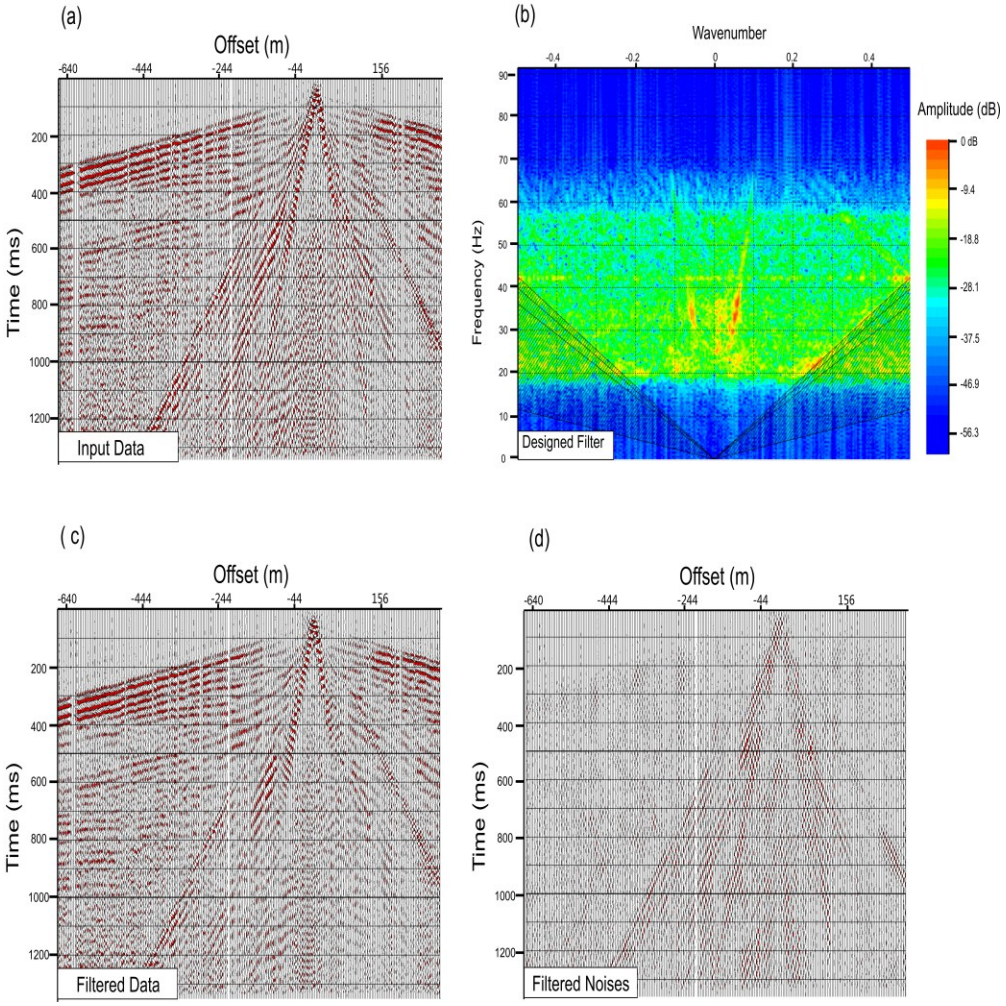


Figure 6.11 Examples of frequency-wavenumber (*f-k*) attenuations to remove the ground rolls and air waves. (a) Shot gather before *f-k* filter. (b) Design of the pie-sliced zone to reject the low velocity events. (c) Input shot gather after *f-k* filtering. (d) Display of the removed noises.

### 6.2.8.3 Radial-Trace Transform Filtering

The radial-trace transform further filters coherent noise by remapping the seismic traces from *x*-*t* domain into the time-apparent velocity (*t*-*r*) domain. Followed by a low pass filter, guided waves and surface waves can be successfully reduced [*Henley*, 2000; 2003; *Ogunsuyi and Schmitt*, 2010]. The working theory behind this process is that the linear events with constant velocity in *x*-*t* domain are re-projected as radial traces with a common moveout angle. When shifted into the time-apparent velocity (*t*-*r*) domain, a lower apparent frequency is produced due to the time stretching of the wavelet (ideally zero) [*Henley*, 2003]. Therefore, application of a standard bandpass filter to each radial trace removes the linear noise and produces a cleaner image upon transformation back to the *x*-*t* domain. It is important to note that a small apparent velocity interval (Δv) should be chosen during this remapping of the data to ensure sufficient sampling.

## 6.2.9 Deconvolution

The earth is comprised of different types of rock masses and materials with distinctive physical properties and lithologies [*Yilmaz*, 2001]. Ideally, the seismic traces could be considered as the convolution of the seismic pulse and the reflectivity sequence between different interfaces. However, the recorded seismic traces are affected by numerous elements such as source generated waves, earth reflectivity, and recording noise. Indeed, the earth reflectivity trace: a series of spikes with time each of which corresponds to the reflectivity of the geological interfaces in depth as already discussed in Chapters 3 and 4 during calculation of the synthetic seismograms, would be provide the best data possible for interpretation. The real seismic trace is a considerably ‘smeared’ representation of this ideal trace. The goal of deconvolution is to reduce this smearing as much as possible in order to improve the temporal resolution of the seismic image. In the time domain within the convolutional model, a seismic trace can be expressed as

$$x(t) = w(t) * e(t) + n(t)\,, \tag{6.5}$$

where $x(t)$ is the seismic recorded trace (i.e. seismogram), $w(t)$ is the source wavelet, $e(t)$ is the earth reflectivity, and $n(t)$ is random ambient noise. Therefore, the recorded trace series is undesirably contaminated with random noise, reverberations and multiples. Indeed, such coherent noises play a key role in affecting the image resolution by lowering the signal-to-noise ratio (S/N) and narrowing the bandwidth.

Deconvolution aims at boosting the vertical resolution of the seismic records and is widely employed to 'collapse' (i.e. shorten in time) the wavelet and to correct for the reverberations and multiples. It obtains the earth reflectivity $e(t)$ from the seismic record $x(t)$ by first finding an estimate of the source wavelet $w(t)$. In an ideal circumstance, the inverse filter should be a spike at each earth's reflectivity with summing up the reflected energy [*Yilmaz*, 2001]. However, the perfect result can never be completed due to the limitation of the assumptions in this method which includes (1) the recorded seismogram obeys the convolution model described as (6-4); (2) the seismic wavelet $w(t)$ is in minimum phase; (3) the noise and seismic reflectivities are 'white' (i.e. contain all frequencies). In fact, in this study the input wavelet utilized in the correlated vibrator seismic traces is a zero-phase Klauder wavelet which breaches the minimum phase assumption. Regardless, significant improvements can be observed on the records after applying predictive deconvolution and spiking deconvolution.

Predictive deconvolution can evidently remove the reverberations and multiples that initially generated from the repeated reflections near the sedimentary boundaries. Such multiples greatly conceal the weaker but more important real reflectors and lead to the production of the false structures that inevitably influence the judgment of the interpreter [*Gadallah and Fisher*, 2005]. In the Bow City study attenuating the multiples, particularly near the surface, is one of the

most challenging tasks. Predictive deconvolution is an integrated technique that involves spiking deconvolution, but it also assumes that the periodic multiples are predicted. By applying a predictive filter, the time-advanced input series of the multiples is estimated and subsequently subtracted from the original trace. Thus, a new trace free of multiples would be acquired by means of subtracting the estimated series with the input trace. It is necessary to point out that the estimated lag length and the operator length are the key parameters in this method. Relying on the autocorrelation result of the input wavelet, the length of the predictive lag is estimated. Empirically, the length of the second zero crossing is recognized as an optimal predictive lag, but several trials are still required to be tested to select the best value [*Gadallah and Fisher*, 2005]. In addition, the operator length should be in an optimal length to include sufficient information of the seismic traces and the spurious spikes should be avoided. In this study, two operations of predictive deconvolutions were employed on the pre-stacked data and post stacked data, respectively. A length of 80ms operator with 20ms lag was employed after several tests on new line 1. Compared with the raw shot gather (Figure 6.12a), evident suppressions of the multiples close to the primary reflections are seen in the processed data (Figure 6.12b).

Spiking deconvonlution was applied after removing the multiples noise to boost the vertical resolution. It works by compressing the wavelet into a spike and therefore, broadening the frequency bandwidth. Indeed, spiking deconvolution is a special case of the predictive deconvolution with zero predictive lag [*Yilmaz*, 2001]. Figure 6.12c shows a shot gather with utilizing a 60 ms spiking operator with 1% whitening. The reflections were much narrower and continuous on the shot gather after performing spiking deconvolution. However, some attention should be made since spiking deconvolution would inevitably exaggerate the spurious signals and frequency noise in the records.

Surface consistent deconvolution improves the resolution of the reflections by applying the inverse filter to source, receiver, offset and common midpoint separately. This method assumes that the source wavelet is primarily dependent on the locations of source and receiver. Through decomposing the seismic traces into source, receiver, offset and midpoint components, the corresponding amplitude spectrum for each component is obtained with Gauss-Seidel algorithm [*Yilmaz*, 2001]. Thus, the earth reflectivity can be effectively recovered through applying the individual inverse filter. This method was used after the residual statics to restore the seismic reflections energy (Figure 6.12d).

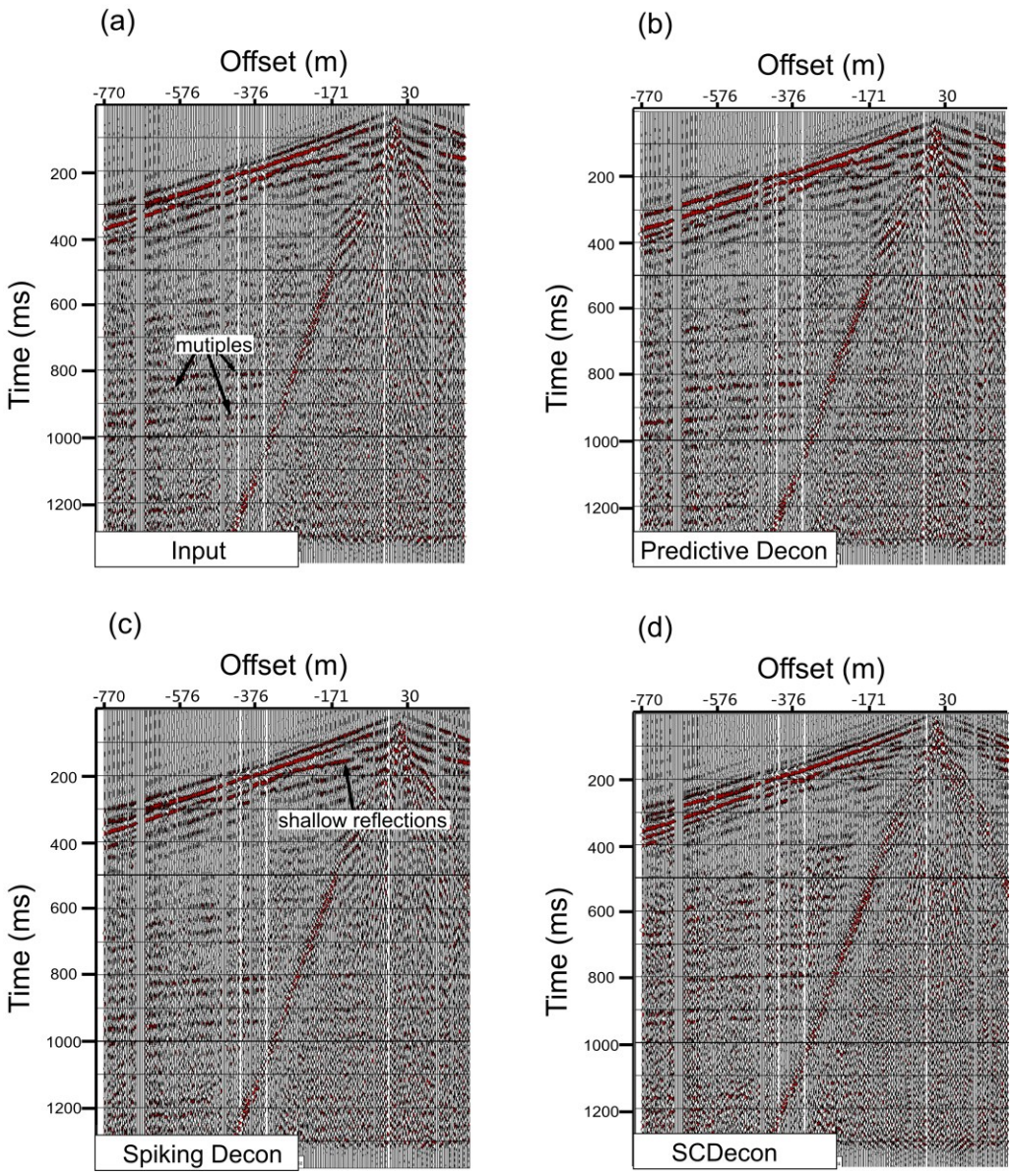


Figure 6.12 (a) A shot gather from new line 1 after energy compensation and noise attenuation. (b) As for (a), predictive deconvolution was applied to remove the multiples. (c) As for (b), spiking deconvolution was employed to boost the vertical resolution. (d) As for (c), surface consistent deconvolution was utilized to recover the reflections energy.

### 6.2.10 CMP Binning

During seismic data processing, the seismic field records are primarily organized into what are referred to as common shot gathers (CSG). However, the standard processing techniques used here require that the seismic traces be organized according to the geometric midpoint positions between the sources and the receivers. This midpoint-time domain is the other conventional geometry employed to produce the high-resolution subsurface images. In sorting the seismic traces that must be acquired in the original shot-receiver (CSG) into common midpoint (CMP) gathers, the seismic traces can be assigned into the same midpoint with different offsets, the traces within a single CMP gather are said to be within the same 'bin' [*Yilmaz*, 2001] (Figure 6.13). The nominal fold, is a measure of the number of the seismic traces from the same bin; the fold is highly related with the final data quality and resolution. Usually, the higher the fold is, the better the signal-to-noise ratio (S/N) will be. Therefore, CMP binning can greatly boost the signal-to-noise ratio (S/N) and further provide the velocity information from the hyperbolic seismic reflections by velocity analysis. Figure 6.14 shows the nominal fold of the new seismic Line 1 compared against that for the legacy Line 86251, respectively. Compared these two lines, a much higher maximum fold of 240 was obtained for the new line (Figure 6.14a). This high fold amount plays an important role in ensuring the high resolution imaging for these new profiles.

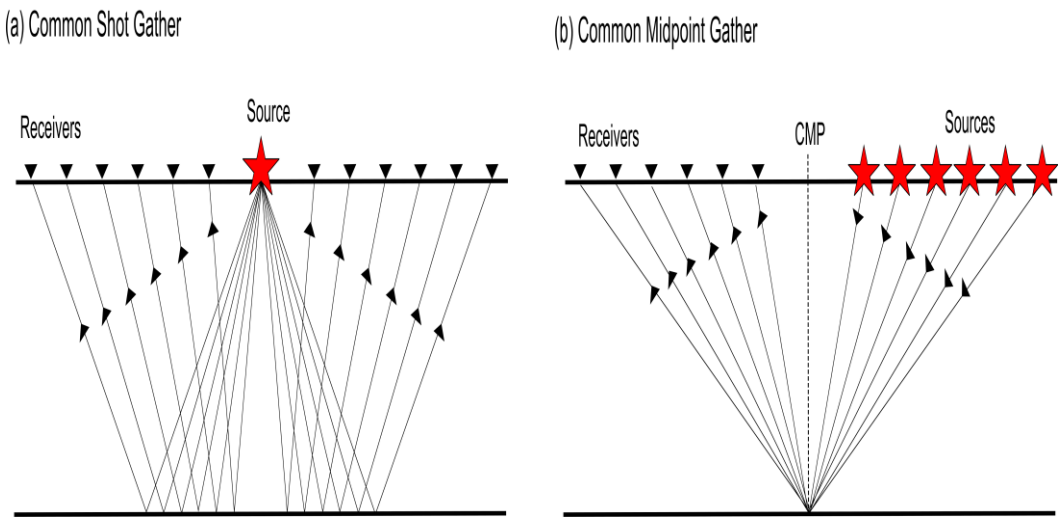


Figure 6.13 Diagrams showing the (a) common shot gather and (b) common midpoint gather.

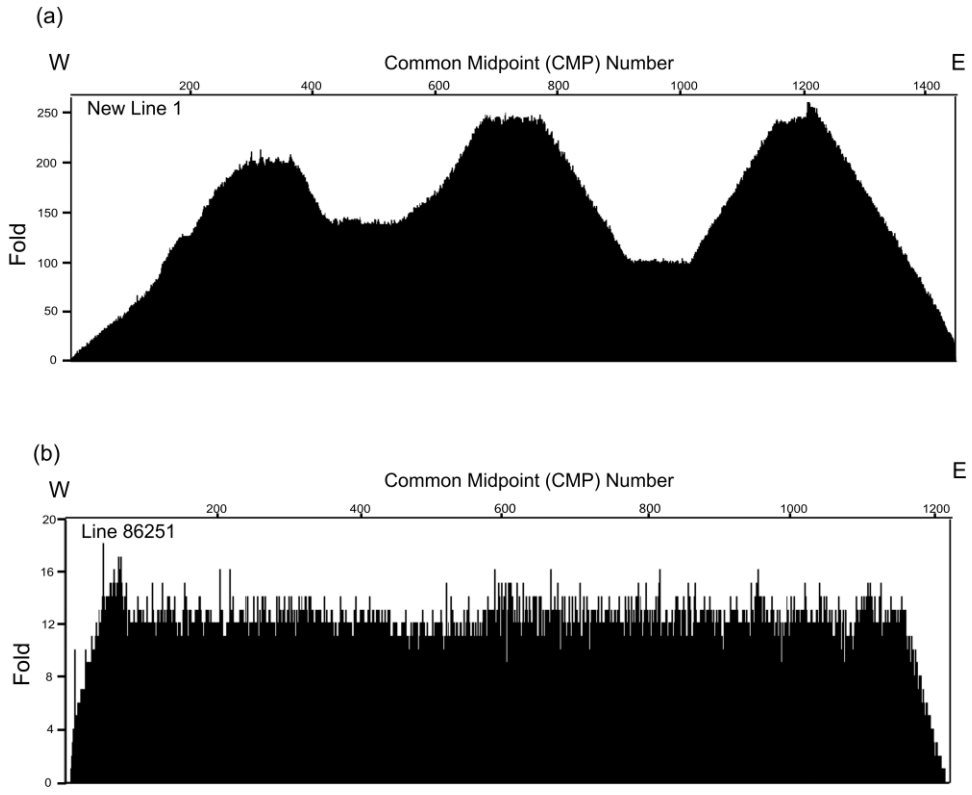


Figure 6.14 Subsurface fold for (a) new Line 1 and (b) earlier profile 86249 .

### 6.2.11 Velocity analysis and NMO

Velocity analysis refers to the procedure of extracting information about the correction factors (i.e. the stacking velocities) needed to process the data from the data itself. The best set of 'stacking velocities' is necessary to carry out the 'flattening' of the seismic reflectors in order to prepare them for stacking. As will be seen, 'stacking velocities' are real correction factors that account for hyperbolic curvature of the *x-t* travel time locus of a given reflection point, a stacking velocity has units of m/s but it must not be confused with the real lithology dependent velocities or the rocks. Therefore, the rms velocity is pointed out to build up the relationship between the stacking velocity and the interval velocity. The rms velocity can be defined as

$$v_{rms}{}^2 = \frac{1}{t_0}\sum_{i=1}^{N} v_i^2\,\Delta t_i\,, \qquad (6.6)$$

where $v_{rms}$ is the rms velocity, $t_0$ is the travel time at zero-offset, $v_i$ is the interval velocity of the $i$th layer and $\Delta t_i$ is the travel time in the $i$th layer at zero offset. When the layer is flat or dipping within a small angle, rms velocity is equivalent to the stacking velocity. While if the layer is significantly dipping, a smaller rms velocity is obtained than the stacking velocity by a factor of $cos\theta$. The RMS velocity that flattens the hyperbolic horizons, in fact, usually referred as the normal moveout (NMO) correction and it is the key step in the formation of a final seismic image. The stacking velocity function is first generated from the velocity of every picks and the entire stacking velocity field can be obtained by appropriate interpolation and extrapolation [*Gadallah and Fisher*, 2005].

In seismic reflection data processing, two methods are commonly used to build the stacking velocity field: these are the semblance and the constant velocity stack (CVS). Semblance is a technique that measures the energy coherence along the

hyperbolic reflections in CMP gathers. The plot is dependent on the velocity, two-way travel time and the offset between source and receiver. Mathematically, the relationship between these parameters can be approximately described as

$$t^2 = {t_0}^2 + \frac{x^2}{v^2} \quad , \tag{6.7}$$

where $t$ is the two way travel time, $t_0$ is the travel time at the zero-offset, $x$ is the offset between source and receiver and $v$ is the stacking velocity. The brightest spot on the semblance plot where represents the biggest coherent energy is recognized as the best estimation of the stacking velocity (Figure 6.15a).

Constant velocity stack (CVS) is a measurement of the velocity trend by applying NMO-correction with a range of constant velocities and tentatively stacking the closely spaced corrected CMP gathers (Figure 6.15b and c). The criterion of examining these velocity samples is the stacking response of the trace amplitude and the continuity of the reflection events. A velocity profile can be produced with careful adjustments of the velocity picks.

In fact, in practice the velocity analysis is usually employs a combination of these two methods together, and an appropriate stacking velocity which best fits the hyperbolic reflection events to produce the best flattening after application of the NMO correction.

Utilizing the information provided by stacking velocity function, the time shift of the NMO correction, defined as the time difference between zero-offset and the measured offset *x* can be calculated by

$$\Delta t_{NMO} = t - t_0 = t_0 \left[ \sqrt{1 + \left( \frac{x}{v_{NMO} t_0} \right)^2} - 1 \right], \tag{6.8}$$

where $t$ is the two-way travel time at offset $x$, $t_0$ is the two-way travel time at zero-offset, $v_{NMO}$ is the estimated NMO velocity and $x$ is the offset between the source and the receiver. Consequently, the true subsurface reflectors are imaged after shifting each trace to $t_0$.

However, special attention must be made during NMO correction due to the effect of the NMO stretch which is most evident in the early time and far offset. Such distorted seismic signals should be muted to avoid smearing of the reflection signals (Figure 6.15b). It is also important to notice that muting could reduce the folds especially at shallow subsurface. Thus, a reasonable compromise should be made between minimizing the influence of the signal distortions and reserving the most energy of the signals. In the end, a reasonable velocity model was generated to display the real velocity structure of the subsurface and provide the necessary information to apply for the NMO corrections (Figure 6.16).

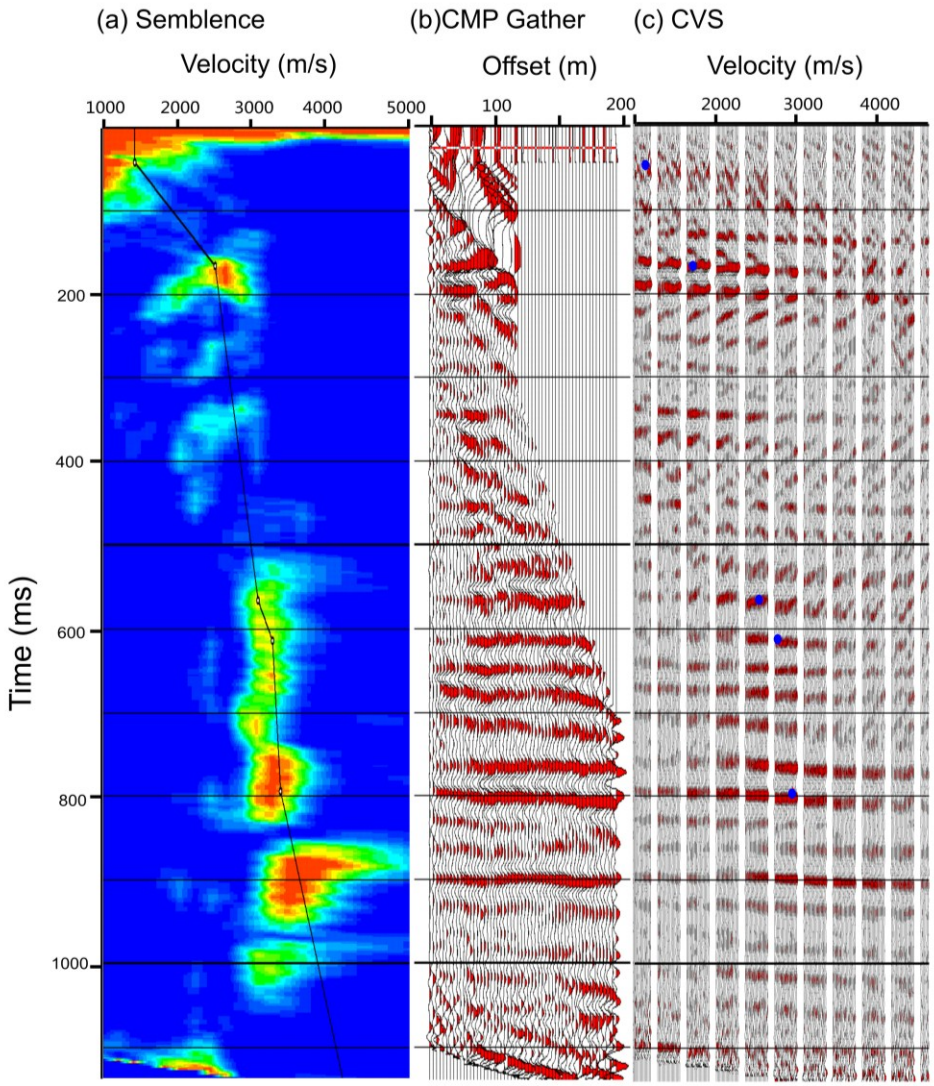


Figure 6.15 Interactive velocity analysis using (a) semblance plot displaying velocity picks, (b) tentatively corrected CMP gathers with picked velocity trend and (c) CVS plots with selected velocity samples.

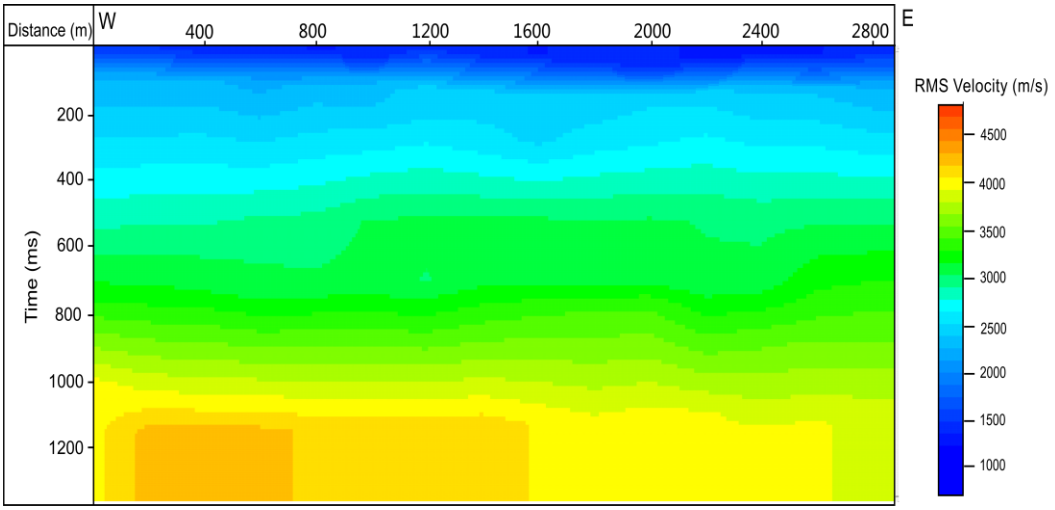


Figure 6.16 RMS velocity model of new Line 1 generated from final velocity analysis.

## 6.2.12 Residual Statics

Although elevation and refraction statics obviously attenuate the effects of the irregular topography and the low velocity zone, the reflected signals on the CMP gathers are still not lined up after the NMO correction. Such time deviations are primarily ascribed to the irregular conditions in the near-surface and the velocity errors generated from the velocity analysis [*Gadallah and Fisher*, 2005]. As a result, stacked image in poor quality could be produced with narrow frequency bandwidth and low reflected amplitudes. In order to eliminate the time deviations associated with the subsurface structures, residual statics are applied on the seismic records. Complementing the elevation and refraction statics, the reflected signals can be ideally aligned. However, several iterations of both residual statics and velocity analysis are often required to ensure the best result.

In this study, surface consistent residual statics utilizing the stack power optimization algorithm is employed to account for the anomalous travel time

effects of the near surface [*Ronen and Claerbout*, 1985]. It works by minimizing the time difference between the modeled trace and the individual NMO corrected trace on the CMP gather. The time difference is detected by cross-correlating each input trace with the modeled trace [*Gadallah and Fisher*, 2005]. Accordingly, a shot gather which provides more continuous reflection events and sharped reflectors is obtained after the statics correction. During this process, it is important to set up the appropriate parameters including correlation windows, maximum shifted time and NMO correction. The window should be selected within the area that has a good signal-to-noise ratio (S/N) to avoid the influence of noise. The maximum allowable time shift defining the largest time variations within the cross-correlation shifting should be reasonable as well. The value should be picked to allow the correction of the large time difference, while avoiding cycle skipping [*Nickerson*, 2007]. NMO correction should be applied with a proper velocity range, a suitable mute gate and reliable velocity picks [*Yilmaz*, 2001].

### 6.2.13 CMP Stacking

After application of the final residual statics with appropriate velocity analysis and NMO correction, the seismic traces within the same CMP gather are ready to be stacked together into a single trace that will ostensibly represent the normal incidence seismic reflection response of the earth at the map location of the CMP. This step is conducted by summing up all the NMO corrected traces in the CMP gather, and normalizing the energy by dividing the amount of the live traces. It is important to note that such a mechanism can greatly enhance the signal-to-noise ratio (S/N) since the coherent reflected energy is significantly boosted while the random noises is suppressed [*Gadallah and Fisher*, 2005]. Figure 6.17a shows the stacked section of the new line 1. Reflectors in the shallow sections are clearly visible.

### 6.2.14 Post-stack processing

Although a series of techniques have been applied on the seismic shot gathers to attenuate the noise and enhance the reflected signals, unwanted noise can still exist on the stacked profiles. Thus, post-stack processing becomes a necessary and worthwhile step to boost the signal-to-noise ratio (S/N) and improve the resolution of the stacked profiles. Migration, predictive deonvolution, time variant bandpass filter, spiking deconvolution and *FX* prediction were subsequently carried out on the stacked images.

#### 6.2.14.1 *FX* Decon

On the stacked sections, undesirable random noises were inevitably produced which significantly lower the frequency bandwidth and data resolution. The *FX* decon method utilizing the uncorrelated feature of the random noises was performed in the frequency domain to eliminate the incoherent noise. By applying the individual predictive deconvolution filter to each frequency in the assigned range, the output should mostly contain the predicted coherent signals [*Canales*, 1984; *Gadallah and Fisher*, 2005]. After transforming back into the *t-x* domain, an enhanced section that is ideally free of random noise is produced [*Yilmaz*, 2001]. Significant difference between figure 6.17a and figure 6.17b are seen on the shallow reflectors.

#### 6.2.14.2 Migration

The objective of migration is to eliminate the diffraction patterns and 'migrate' dipping reflectors in the seismic section into their real-earth positions. Since the assumption of the CMP stack is that the subsurface units are flat and horizontal, but in fact, they are complex and variable with pronounced dipping, interrupted

reflectors, and synclinal and anticlinal structures. As such, the actual subsurface reflection is not at the midpoint between the source and the receiver. This is problematic because in the final plotting of the seismic section, this seismic event is still placed at this midpoint; and consequently it is not in the correct location. Therefore, inaccurate analysis that generates the false structures will be presented if the correction is not employed. Currently, there are numerous migration algorithms which can be basically divided into two main styles: Kirchhoff or downward continuation. The Kirchhoff method was selected to correct the reflectors with a consideration of the diverse geologic situations, time cost and data quality.

Kirchhoff migration is a widely utilized method based on the assumption that all seismic events seen in a section are generated by diffraction of the seismic energy at the reflecting point in the earth. The essential idea is similar to that proposed by Huygens as described in Chapter 2. It sums up the seismic energy along each hypothetical diffraction hyperbola at each point in the seismic section and relocates it at the apex as the source of such dispersive energy. For each hyperbolic event, the velocity function is typically determined using the $V_{NMO}$ function at the apex in the hyperbola [*Yilmaz*, 2001]. Thus, the subsurface true position moves 'updip' along the dipping reflector. However, the drawback of the Kirchoff method is that it can only handle the time-variant velocity. It does not work well when the velocities vary laterally. In addition, it is also computationally expensive. Regardless, significant improvements are observed in the migrated profile (Figure 6.17 c)

However, it is import to point out that migration can generate the high frequency alias particularly for the highly dipping event and further reduce the resolution of the seismic profile. In order to generate a clean and high-quality profile, the optimal diffraction patterns and wide bandwidth need to be taken into account as

well as the correct velocity model. Figure 6.17c shows the stacked image with applying migrations.

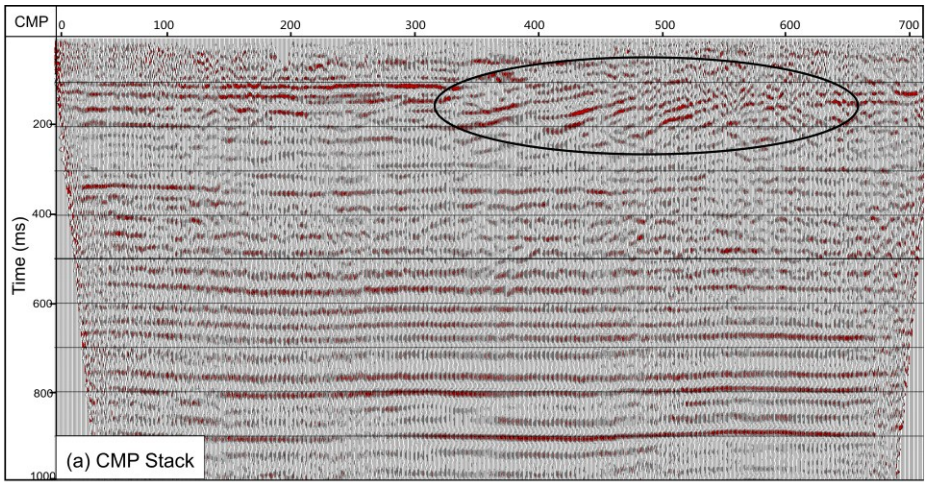
CMP
0
100
200
300
400
500
600
700
Time (ms)
200
400
600
800
1000
(a) CMP Stack

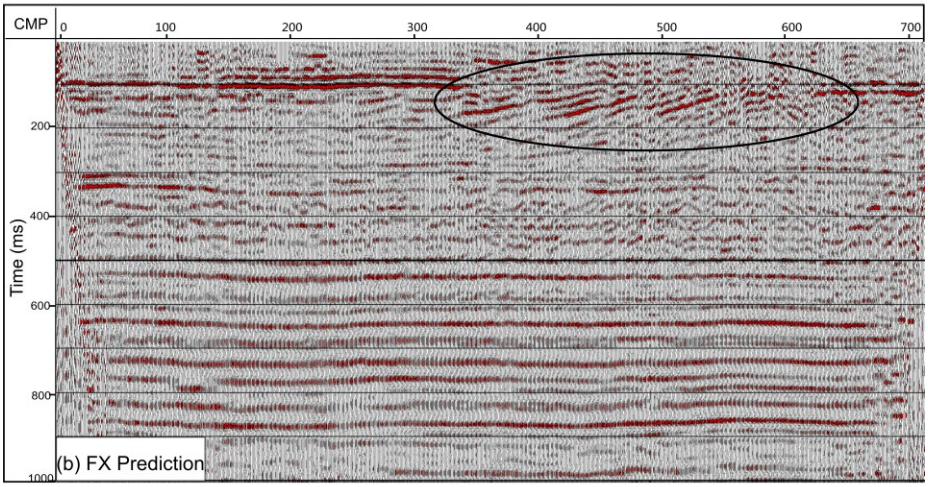
CMP
0
100
200
300
400
500
600
700
Time (ms)
200
400
600
800
1000
(b) FX Prediction

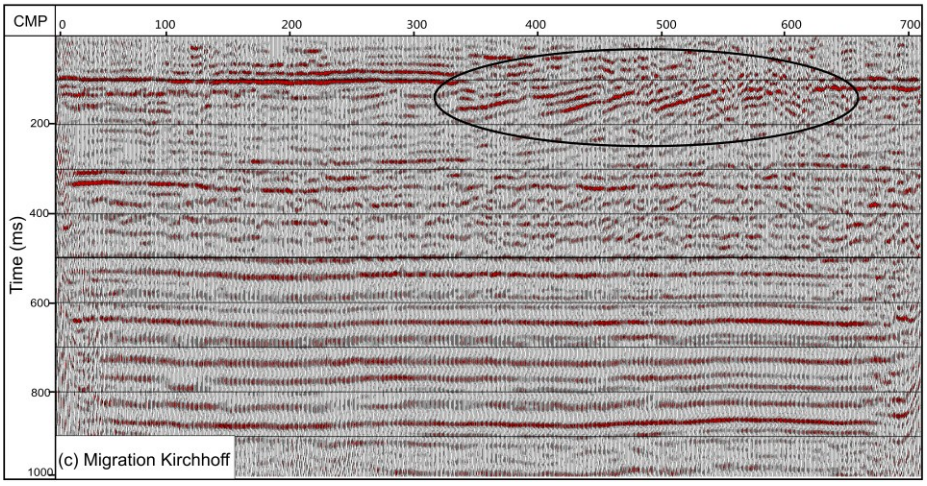
CMP
0
100
200
300
400
500
600
700
Time (ms)
200
400
600
800
1000
(c) Migration Kirchhoff

Figure 6.17 Examples of the effect of the post-stack processing of new Line 1. (a) Initial CMP stacked profile. (b) As for (a), *FX* prediction was applied to remove the incoherent noises. (c) As for (b), Kirchhoff migration was performed.

## 6.3 Data Analysis

To this point, high-resolution seismic profiles have been produced by applying detailed processing workflows that focus on the elimination of the near-surface noise and multiples. Seismic interpretation was subsequently conducted aided by synthetic seismograms calculated from nearby sonic and density logs. The new profiles refine the images of the original legacy data sets of Chapter 4 and support the interpretations of a central peak uplift and slumping blocks at the outer rim. This section primarily focusses on an initial interpretation and horizon analysis of the high-resolution profiles acquired in 2013. The entire seismic joint interpretation with legacy survey will be discussed in Chapter 7.

### 6.3.1 Seismic well tie

To interpret the new seismic profiles, synthetic seismic traces were generated with the density and sonic logs from wellbore 00/14-21-17-18/0. This well is located in the west portion of the new line 1 and the well logs were measured from 210 m to 1249 m in depth. Regrettably, the uppermost lithologies of the most interest here were not logged again because they were not economic targets. With properly calculating the acoustic impedance (AI) response, the seismic reflection coefficient (RC) was extracted and the geologic well tops from the Foremost unit to Paleozoic unconformity were appropriately tied with the seismic horizons (Figure 6.18). Due to the limit of the data availability, only one well locating on the seismic profile was deemed suitable for examination. As noted, the depth limitations on this geophysical log do not allow the shallower units to be tied to

the geology. However, the interpretations can be greatly assisted with seismic line 86251 since they were acquired in the same location.

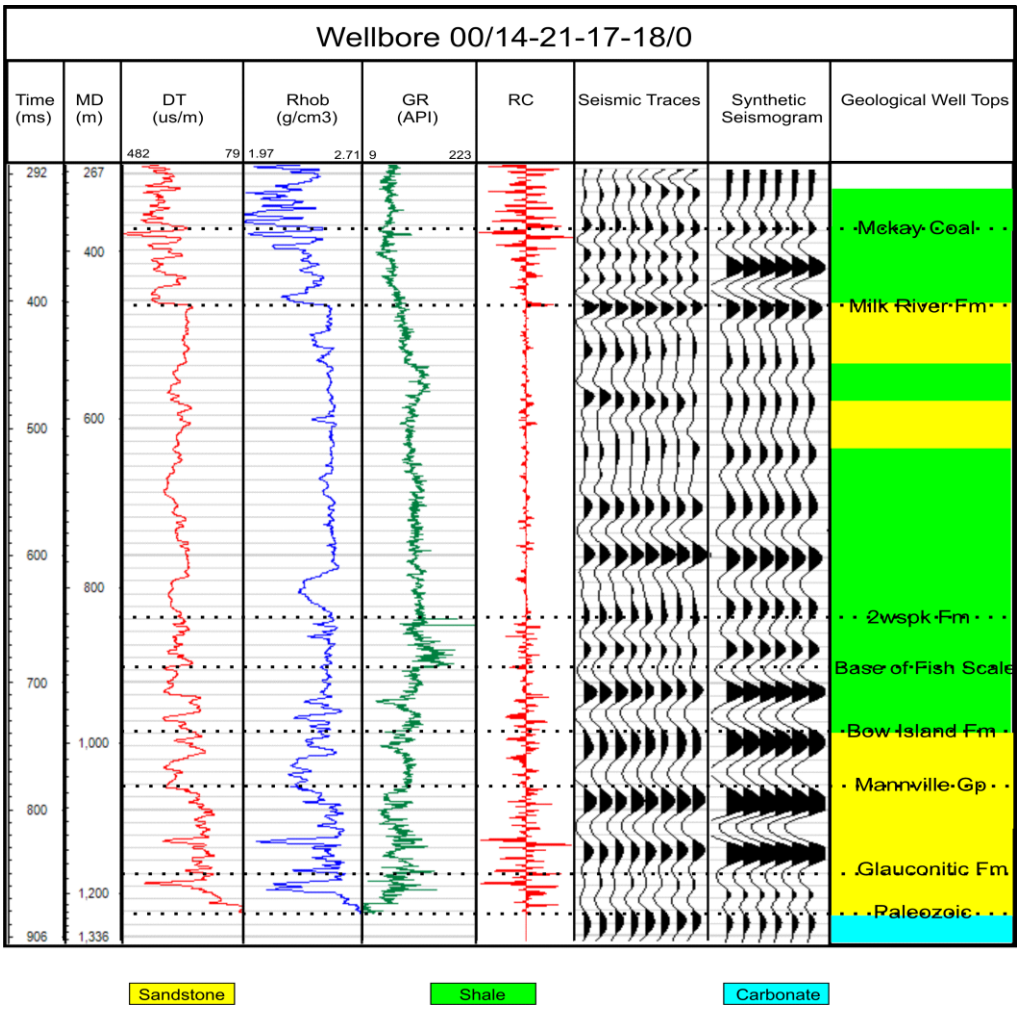


Figure 6.18 Synthetic seismogram extracted from Wellbore 00/14-21-17-18/0 to tie with seismic horizons in profile new Line 1. From left to right, logs are sonic ($us/m$), density ($g/cm^3$) and gamma ray ($API$). The associated reflect coefficient (RC), seimsic traces at CMP 188 from Line1 and synthetic traces are displayed as followed.

### 6.3.2 Horizon analysis

With the guidance of the synthetic seismogram and the earlier interpretation carried out in seismic profile 86249, shallow subsurface seismic horizons in the Upper Cretaceous were tracked in the new profiles. Figures 6.19 and 6.20 present the uninterpreted and interpreted sections of new Line 1 and Line 2. A number of distinctive characteristics can be seen in these images.

The new seismic Line 1 (Figure 6.19) focuses on the apparent disturbed zone consisting of a series of fault-bounded blocks of the shallow units to the east of CMP 125. The Belly River Group reflector (highlighted by blue) is flat-lying west of this point, but it becomes blocky and discontinuous, dropping from 160 ms to 200 ms at CMP 330. This point in fact might delineate the western rim of this structure. Continuously moving east into the structure, this horizon is progressively interrupted, and three listric faults (draw by green, grass green and light blue) are seen with similar counter-clockwise (in this view) rotations. These patterns correlate well with the interpretations made on legacy seismic profile 86251 in Chapter 4. However, these new images display the faults more clearly.

These new images of Figure 6.19 also allow more details to be seen. For example, at least one normal fault (highlighted with indigo line), with a westward apparent dip is captured around CMP 626. The detection of this fault adds more complexity of this possible impact crater.

Interestingly, to the east of this fault, the seismic reflectivity is more regular with the seismic units are lying more uniformly on each. This may be suggestive of a terrace region. We have earlier interpreted the strong reflector at ~150 m as the top of the Belly River Group on the basis of ties to nearby log observations. A less probably, but not impossible, interpretation is that this flat reflector could be

related to fall-back breccia or melt, but this cannot be resolved at the present time without drilling.

Looking into the deeper parts, the seismic events below the McKay Coal reflector are more continuous although small deformations appear immediately beneath the listric faults. This might be the bottom of the structure; and if so a direct measurement can be conducted to estimate the final existed structural depth which is at 400 m.

The other profile, Line 2, is located in the central uplift zone and also adds additional details to the interpretation of profile 86251. A distinct damaged area (highlighted by yellow shading in figure 6.20), to the west of the CMP 250, is one of the most pronounced structural patterns. Although continuous reflectors are barely detected in this area due to the significantly scattered seismic energy, severely dipping reflectors with uplifted thrust faults (highlighted by arrows) are still visible. Dominated by the raised up deeper strata, this bending feature provides the evidence of the central peak which is one of the diagnostic structures in the complex crater. Such information provides more details on the formation of this abnormal structure and further verifies that it might be the deep root of a complex impact crater. A more interesting feature of the curved Belly River reflector (light blue) is characterized between CMP 250 and CMP 375. This anticlinal behavior is seen in the lower horizons as well, but with less pronounced curvature. As mentioned in section 4.2, this uplift behavior indicates a complex structure with impact origin.

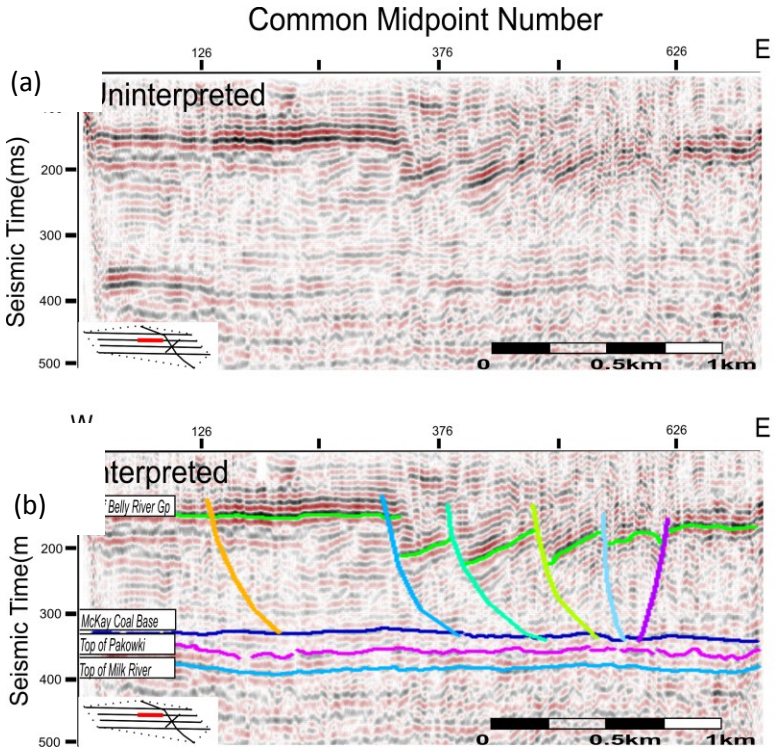


Figure 6.19 Seismic profiles of new Line 1 (a) uninterpreted section and (b) interpreted section. Diagnostic disruptive structures such as listric normal faults and bending reflectors are visible.

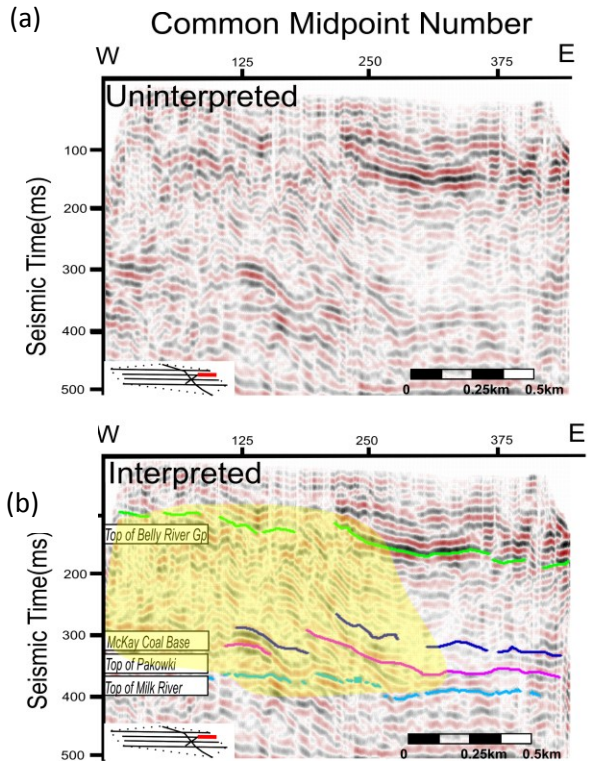


Figure 6.20 Seismic profiles of Line 2 (a) uninterpreted and (b) interpreted sections. Diagnostic disruptive structures are highlighted by the yellow shading.

## 6.4. Summary

A high-resolution seismic reflection study was carried out to allow for more detailed examination of the structures first described in Chapter 4 and Chapter 5. The processing of the seismic data produced two, short, but detailed profiles over zones containing what were interpreted to be rim faults (Line 1) and the central uplift (Line 2). Compared with the legacy data set which was acquired for the deeper petroleum targets, the new profiles provide clear images of the rim faulted blocks and central chaotic zone caped by the curved reflectors. Such abnormal features reinforce the impact origin of this buried structure. However, as looking into the deeper part, the energy is more coherent and the geologic units are more continuous and uniform which displays the regional geologic nature. In order to detailed characterize this unique structure, joint modeling and interpretation will be conducted in the next chapter.

# Chapter 7 Joint modeling and discussion

How the Bow City structure developed and when it formed are two of the most important questions in this study. To provide additional information to assist in solving these interesting questions, detailed characterizations with geo-modeling techniques are carried out here. This Chapter starts with a presentation of the time-depth convention of the interpreted seismic profiles, and isopach maps are generated to display the thickness features of the different layers. Followed by the careful examinations of a detailed 3D model, systematic discussions will be conducted to analyze the origin, the shape, and the age of this irregular bowl-shape body.

## 7.1 Time-to-depth conversion

The seismic data produced in *x-t* domain were carefully analyzed in Chapters 4 and 6, and a number of distinctive features were observed on the profiles. These profiles were analyzed with 'depth' represented by the 'two-way-travel-time' of the seismic waves; this is how the seismic data must actually be recorded. However, a final interpretation of this data after converting it to the *x-z* (i.e. spatial depth) domain allows for the construction of a structural model that is closer to the true subsurface structures in real *x-y-z* coordinates. As such, all the time migrated seismic profiles (see Chapters 4 and 6, Figures 4.7 - 4.14, 6.19, 6.20) were converted into *x-z* depth sections in the Petrel® software to get a better understanding of this irregular geobody. Converting the profiles from the *x-t* time domain to the *x-z* depth domain, requires a reliable velocity model, i.e., a proper mapping of the two-way travel times to depth. Indeed, velocity modelling is the critical process in imaging the subsurface structures, and it is recognized as the bridge to connect between time and depth. Thus, achieving an accurate velocity model is a critical step to produce a credible transform.

The velocity modelling employed in this study was generated by the layer cake technique. It requires velocity functions that characterize the velocity field within each layer. Consequently, with applying appropriate interpolations and accurate quality control with sonic well log data, the entire velocity model is created. A model with 5 discrete depth intervals was generated as directed by the seismic stratigraphy analyzed in the *x-t* time profiles in combination with the calibrated sonic logs. These interpreted seismic surfaces used to build the model intervals were first smoothed and despiked to avoid introducing artifacts. The velocity information derived from the calibrated sonic logs of 13 hydrocarbon exploration wells close to seismic profiles were utilized to produce the velocity trend for each layer. Such analytical velocity curves were determined by best fitting the cross plot of average velocity and travel time sampled from the sonic logs data. Figure 7.1 displays the velocity relationship of the sampled data between the two-way travel time (TWT) and elevation depth (z).

However, building a velocity model is only the preliminary process for the model conversion. Undoubtedly, appropriate quality control (QC) and output verification are the essential steps needed to assure the reliable result. Depth information picked from the well tops was accessed to correct the generated surface, and reasonable modifications were carried out to remove the artifacts. Figure 7.2 presents the produced velocity profile for seismic Profile 86251. Utilizing the velocity model discussed above, the seismic profiles in time sections are successfully converted into the depth sections. Distinctive slumped terraces with listric faulting are displayed. Figures 7.3, 7.4 and 7.5 show the depth sections of 86251, new Line 1 and Line 2, which will be using for the modeling in the later sections.

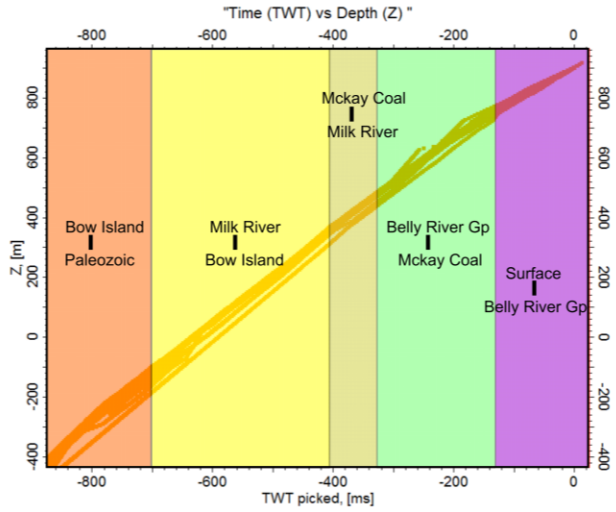


Figure 7.1 Diagram showing the velocity information. Orange data points are the sampled data extracted from the sonic logs of 13 wells showing the relationship between the two way travel time (ms) and the elevation depth (m).

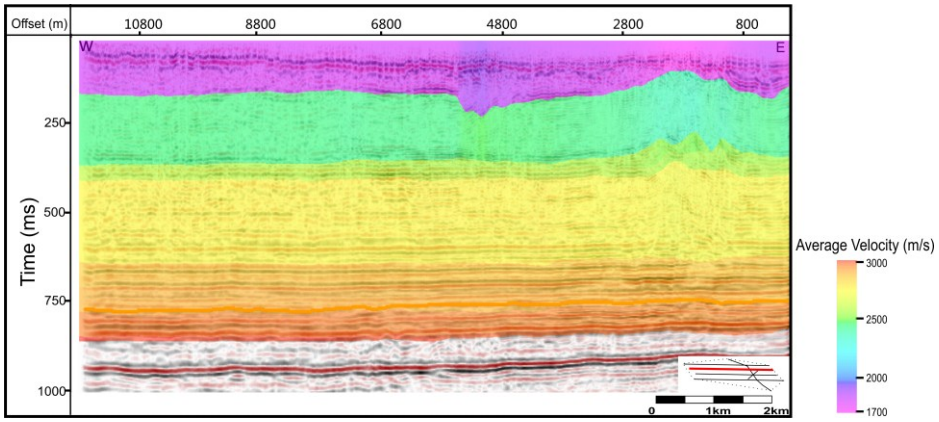


Figure 7.2 2D average velocity profile of seismic line 86251 extracted from the velocity information in Figure 7.1.

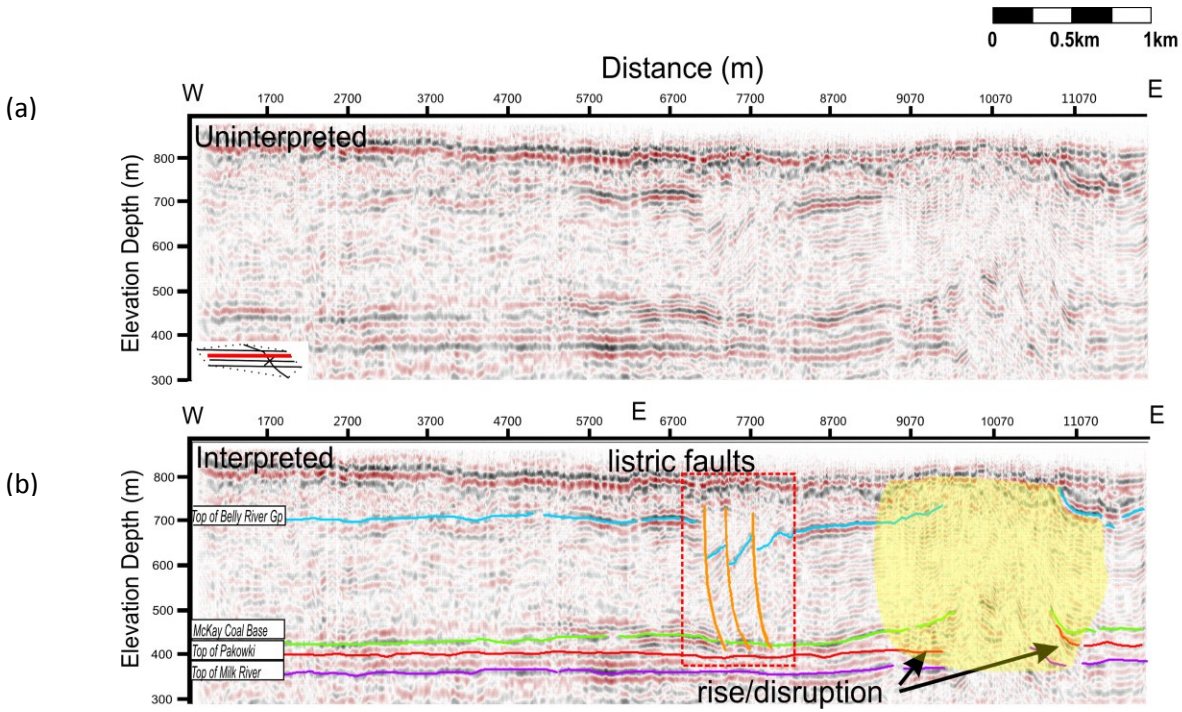


Figure 7.3 Seismic profiles of 86251 in depth scale. (a) Uninterpreted profile. (b) Interpreted profile. Colored lines show the interpreted shallow horizons. Dashline box emphasizes the diagnostic faults patterns represented by orange lines. Yellow shading displays the disturbed structural patterns. Vertical exaggeration is x5.

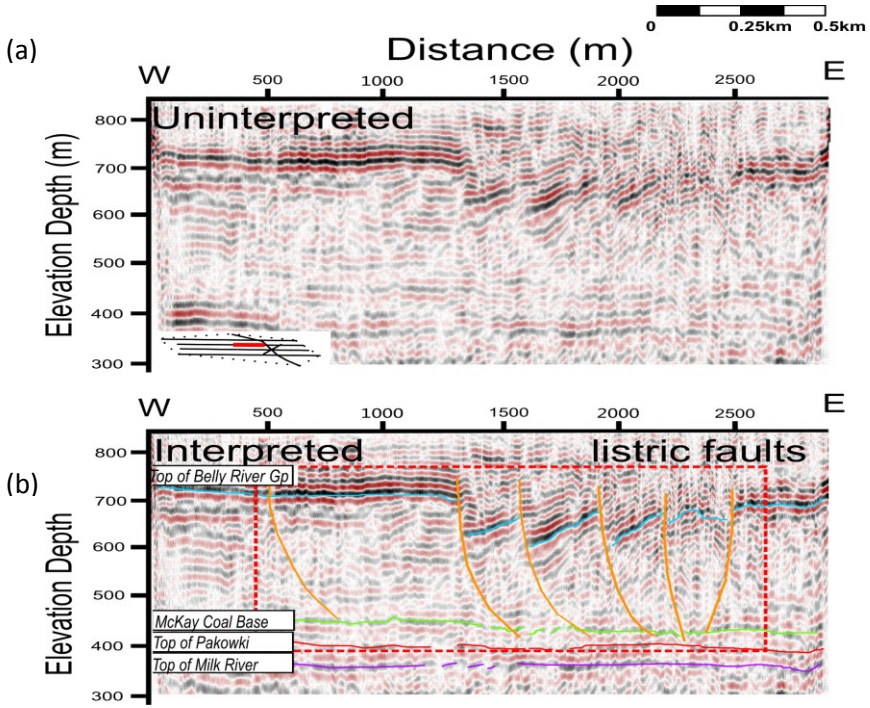


Figure 7.4 Seismic profiles of new Line 1 in depth scale. (a) Uninterpreted profile. (b) Interpreted profile. Colored lines show the interpreted shallow horizons. Dashline box emphasizes the diagnostic faults patterns that exhibits more structural details. Vertical exaggeration is x2.

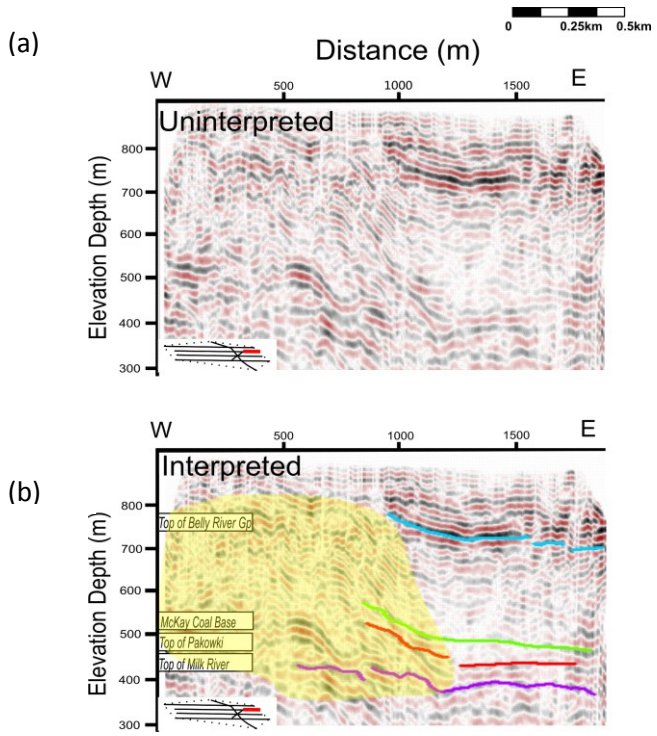


Figure 7.5 Seismic profiles of new Line 2 in depth scale. (a) Uninterpreted profile. (b) Interpreted profile. Colored lines show the interpreted shallow horizons. Yellow shading represents the disturbed structural pattern and central uplift with thrusting faults. Vertical exaggeration is x2.

## 7.2 Isopach Map

An isopach is essentially a map on a line beneath which the thickness of a given rock stratum of interest is constant. An isopach map is then just a contour map of the thickness of the said layer. In this section, we examine the structure in terms of the layer thicknesses using a combination of the seismic and well log data. In contrast, an isochron outlines a horizon that is inferred to have been produced at the same time. Usually, we take a given geological formation top to be isochronal and so an isochron map would provide the depth to a given formation top.

The depths to each of the isochrons is determined by transforming the observed seismic two way times to depth as just discussed above. This allows first the construction of a 3D geological model (Figure 7.6), with each of the layers separated by isochrons. Isopachs of the different layers are generated by simply taking the depth differences between the desired isochrons and a number of these are shown in Figure 7.7. The deformed morphology of the Bow City structure is quite significant in the near surface such as the Belly River Group, the Mckay Coal, the Lea Park, and the Milk River sandstone. In contrast, the structural elements in the deeper sessions show little variation in thickness, which indicates a return at greater depths to the relative simple geologic environment of the region as discussed in Chapter 3.

The isopach (Figure 7.7a) from the assigned datum (900 m a.s.l) through the Belly River Group unit is the topmost map examined and it exhibits a series of notable structural patterns that are similarly found in acknowledged impact craters. The most prominent feature that shows on the isopach is the ring-like thickening strata that is located around the central thinning. Although this thickness change is noticed to be not perfectly continuous and uniform, it correlates well with the blocky depressions displayed on the seismic reflection profiles and the velocity anomalies in the travel-time inversion model. Indeed, this annular shape structure

can be used to constrain the size of the potential impact crater, which is around 8 km rim-to-rim diameter.

The underlying structural element from the Belly River Group to the Mckay Coal base (Figure 7.7b) continuously reveals this spectacular structural style with some unique features. Clear evidence that displays a maximum elevation contrast of 80 m is exhibited between the regional datum and the annular thinning strata. Although distinctive circular thickening is no longer reserved in the centre and the thickening rock masses are not as consistent and concentrated as the upper layer, the inner structure is still thickened and several diagnostic thick spots located inside the circular outline are observed. Such structural geometry exhibits similar morphologic features to the generic model of the complex crater [*French*, 1998; *Melosh*, 1989; *Osinski and Lee*, 2005].

Deeper in the structure, the thickness between the Mckay Coal base and the Milk River formation (Figure 7.7c) becomes more uniform, aside from a noticeable central thickening. A localized trend that thins from east to west is clearly manifested. Although there is no evidence that markedly defines the circular geometry, some gentle thinning of 25 m can be still noted surrounding the central thickening. This structural pattern, in fact, indicates that the slumping textures at the out rim were minimally, or not at all, affected in the deeper strata.

The isopach map from the Mckay coal to the Mannville formation was mapped with less disruptions and elevation contrasts. Indeed, similar characteristics without showing the crater geometry can be noticed in the lower strata between the Mannville and Paleozoic formations. The apparently undeformed structural patterns detected in the deep layers demonstrate that the upper Cretaceous bowl-shaped morphology in fact can not have resulted from deeper then upward collapsing mechanism (e.g., salt tectonics, volcanic eruptions, and dolines). Instead, impact is recognized as the one of the few processes that leads to the

formation of the surface disruption with a reservation of the original deep layers [*Melosh and Ivanov*, 1999; *O'Keefe and Ahrens*, 1999]

A 3D model displaying the lateral elevation variations of the Belly River surfaces was created (Figure 7.8a). Diagnostic structural aspects with annular moat, central uplift, and circular outline are clearly visible on the otherwise monotonous regional geologic setting. It is important to point out that if the assumption of the connected concentric faults pattern detected at the ring-like depression in the seismic profiles is valid, the outer zone of the structure, therefore, can be described as a development of the progressive collapse of the footwall existed in the actively slumping fault terrace (Figure 7.8b). Such observations further assist in understanding the structure and characterizing the structure's genesis.

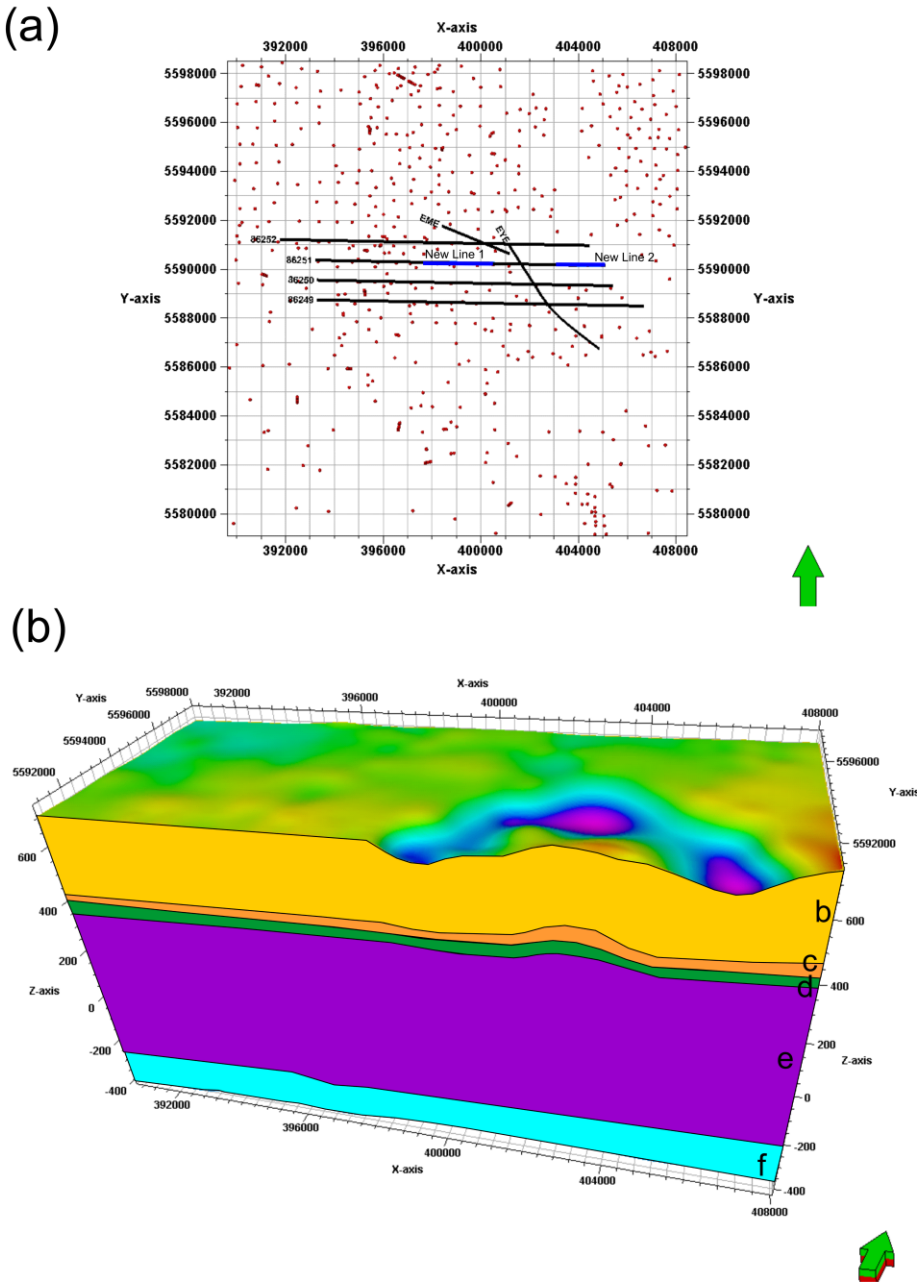


Figure 7.6 (a) Map showing the seismic profiles (line) and well data set (dots) utilized to generate the isochron surfaces and 3D model. (b) 3D model displaying the zones that used to create the isochron maps in figure 7.7. The surface is covered by the topography map of the Belly River Group.

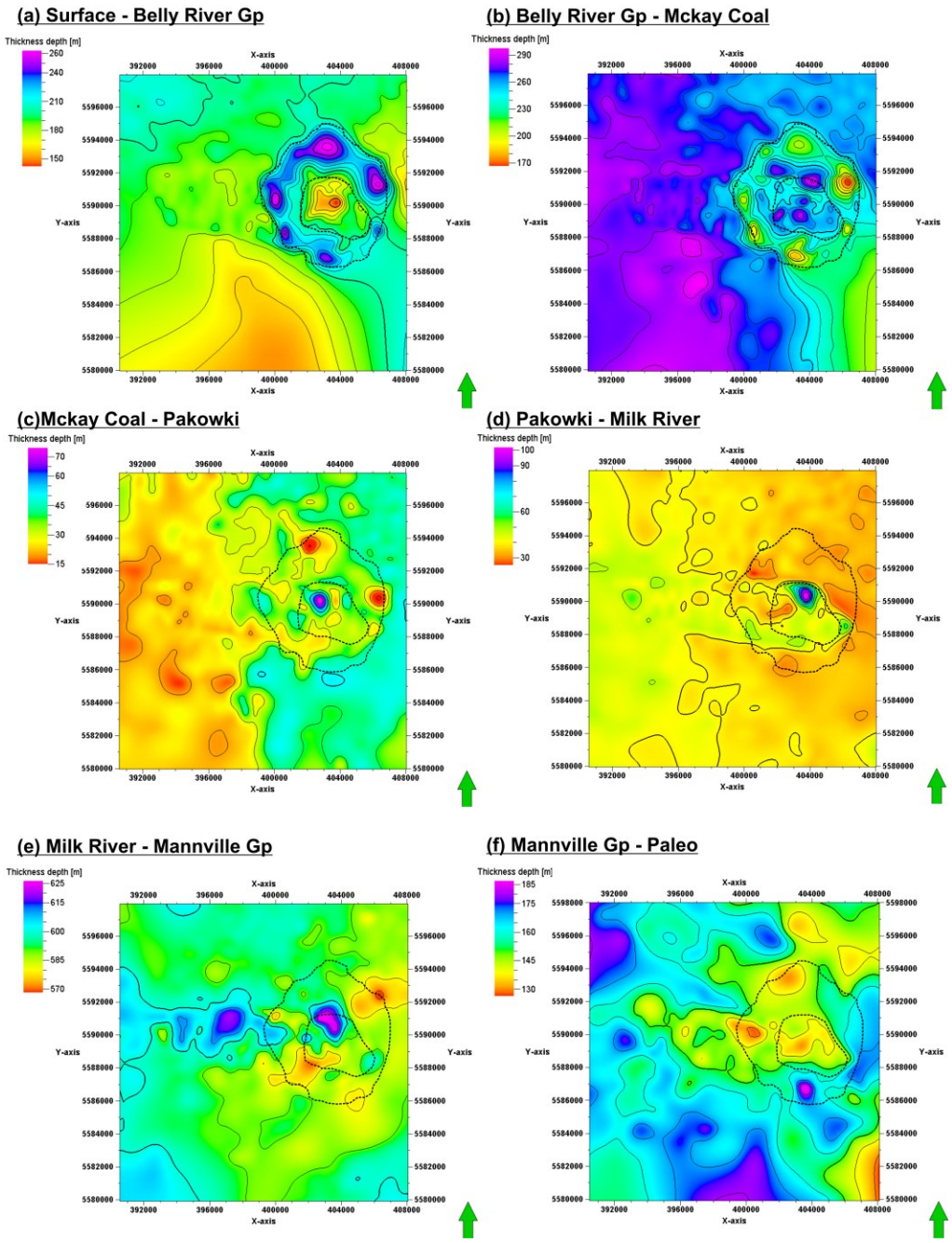


Figure 7.7 Isopach maps exhibiting the thickness of different stratigraphic intervals. Maps are produced with the seismic interpretations and well tops shown in figure 7.6 (a). Representative zones are highlighted by different colors and letters in figure 7.6 (b). The black dotted curve is the estimated structure outrim and central high region.

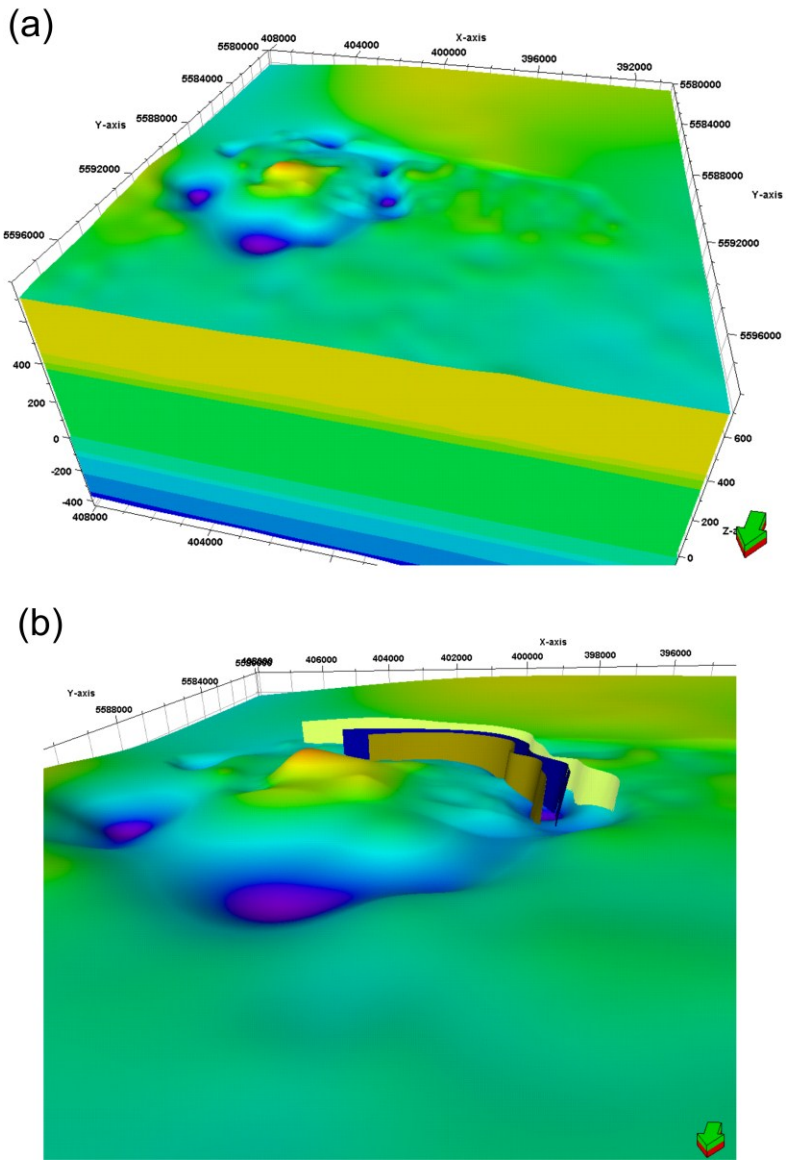


Figure 7.8 3D models presenting the distinctive structural patterns. (a) Oblique view of the Belly River Group from northeast showing circular depression with central uplift. (b) Oblique view of the Belly River Group surface revealing the distinctive faults patterns in the outer zone. Colored blocks display the three listric faults patterns interpreted in seismic profiles. Vertical exaggeration is 1:7.

## 7.3 Discussion

A number of distinctive irregular patterns of the impact craters are observed in the structural elements of the Bow City structure. These most particularly include an annular moat, a central peak, and the tiled fault patterns indicated from the seismic and well logs data. The complex outcrop faulting provides additional evidence, particularly given that there are no known tectonics, volcanics, karsting, or salt dissolution in the area. A final tantalizing piece of information is the anomalies in the velocity structure across the structure, especially the low velocity zone corresponding to the uplift but with a higher velocity pulled up beneath it. All of this is strongly suggestive of a hypervelocity impact, but unfortunately we still do not have the final conclusive evidence of shock metamorphism.

Since evidence of shock metamorphism has not yet been discovered yet, it is necessary to critically examine the alternative possible nonimpact scenarios that might produce the same abnormal structural aspects. The discussion here follows our earlier presentations in Glombick et al [2014]. Moreover, detailed descriptions of the morphology, the formation, and the estimated age are conducted to further deduct the development of this possible eroded impact crater.

### 7.3.1 Structure origin

Large endogenous geological events such as volcanic eruption, doline (karst) collapse, and salt tectonics can yield similar structural patterns as the impact craters with slumping rim terrace and even central peaks. In fact, the only evidence that can be unambiguously employed to confirm the impact genesis of the abnormal structure is the shock-metamorphic features such as planar deformations (PDFs), shatter cores and shock metamorphism [*French and Koeberl*, 2010; *Melosh*, 1989]. Thus, the other potential explanations of volcanic eruption, doline formation, and salt tectonics are discussed as followed.

A volcanic caldera is a steep, bowl-shaped cavity that formed from the volcano collapse as the molten material leaves the magma chamber. Calderas can have enormous diameters of 1-100 km and distinctive magmatic mineral are usually observed. Ring dikes also develop radially around the central vent and the slumping rim collapses gradually. In the vicinity of the Montana-Alberta border, there is clear evidence showing the existence of Eocene (~50 Ma) igneous intrusions discovered 100 km south of the Sweet Grass Hills [*Glombick et al.*, 2014]. Evidence from both the lab results and the geophysical imaging techniques have been discovered to verify this Eocene igneous complex [*Rukhlov and Pawlowicz*, 2012]. However, there is no proof indicating any magmatism or volcanism in the periphery of Bow City. No volcanic or igneous deposits are observed in the vicinity and more importantly, the deeper sedimentary units beneath the Bow City structural are quite consistent and uniform without severe disruptions. Thus, possible volcanic genesis can be excluded due to the lack of the volcanic deposits and the deeper damage of the rock beds.

Dolines (sinkholes produced during karsting), one of the representative collapsed Karst surfaces, is developed due to the dissolution of evaporates or carbonates. A doline is usually a circular topographic depression with diameters from a few to several hundred meters. These could be misinterpreted as a potential impact crater. In fact, solution-collapsing geomorphologies are not uncommon in the subsurface of parts of Alberta and Saskatchewan since the Devonian (~360 Ma) carbonates and evaporates are easily dissolved. For example, Bown [2012] and Arkadani et al [2014] have recently described the geophysical studies of buried karst terraces in NE Alberta at the top of the Devonian carbonates immediately beneath the early Cretaceous siliciclastic foreland basin deposits. Despite this, it is not likely that a solution-collapsing mechanism can account for the development of the Bow City structure due to the unique morphology and simple regional geologic settings. It is important to notice that the size of circular sinkholes is much smaller than 8 km. Dolines do not have central uplift structures as they are collapse features driven

by gravity. Most convincingly, however, is the fact that there is a thick (~750 m) layer of insoluble siliciclastic sandstones and shales uniformly deposited between the bottom of the Bow City structure and the top of the Paleozoic carbonates. No disruption of the layering is apparent as shown in the seismic sections. Finally, as mentioned in the formation of caldera, the significant disruptions of the deeper rocks masses are one of the prerequisite for the process.

The extensional circular structure created by halokinesis could be considered to be another candidate that explains the genesis of the Bow City structure. Halokinesis is a type of salt tectonics and it takes place when highly soluble evaporite rich rock salt exists within the stratigraphic intervals. A circular compensatory subsidence of the overlying rocks masses surrounded by the salt flowage could be observed due to the fact that the salt cannot be compacted as the depth changes. In WCSB, there are several significant localized salt deposits primarily detected in the Devonian Elk Point Group [*Drees et al.*, 1994; *Grobe*, 2000; *Wright et al.*, 1994]. However, there is no salt diapir recorded in the vicinity of the Bow City structures and no evidence is observed from the well cutting [*Glombick et al.*, 2014]. Besides, a lack of evidence displaying the morphological patterns of the salt bodies and imaging of the disrupted seismic reflectors in the deeper Cretaceous units ruled out the salt halokinesis scenario.

### 7.3.2 Structure morphology

Due to the relative inaccessibility of finding a similar crater (aside from perhaps Lake Bosumtwi) and the impossibility of conducting a real impact experiment at the scale of the Bow City structure, there is no simple and direct method known to exactly relate the energy (mass and speed) of the impactor and the size of the final impact crater. Thus, in order to better understand the dimensions and physical change, a series of scaling laws have been summarized based on the experimental tests using exploration source in the impact study. Examinations of these

relationships can greatly help us constrain the morphology of the Bow City structure and further understand the formation of this possible impact crater. These scaling equations are primarily concluded by Melosh [2011] on basis of the numerical calculations, geological mapping of existing craters, and the results of large nuclear explosions from testing during the Cold War. These data have been compiled by various authors to form scaling relationships.

For a complex impact crater, the final rim-to-rim diameter D with regards to the transient crater $D_t$ can be expressed as:

$$D = 1.17 \frac{D_t^{1.13}}{D_{s-c}^{0.13}}, \tag{7.1}$$

where $D_{s-c}$ is an empirical constant diameter at the transition between the simple to complex crater which is usually about 3.2 km on the Earth. It is important to notice that all the length units are in kilometers.

For the central uplifted amount $h_{su}$ pushed upwards from deeper materials, the relationship in terms of the final diameter D can be described as:

$$h_{su} = 0.06 D^{1.1} \tag{7.2}$$

Due to the rapid developments of the impact experiment techniques, more and more precise scaling rules have been pointed out by the researchers. The diameter of the transient crater $D_{tc}$ at the ground surface level can be deducted from:

$$D_{tc} = 1.161 \left(\frac{\rho_p}{\rho_t}\right)^{1/3} L^{0.78} v_i^{0.44} g^{-0.22} (\sin\theta)^{1/3} \tag{7.3}$$

where $\rho_p$ and $\rho_t$ are the densities of the projectile and the target, respectively, $L$ is the diameter of the project body, $v_i$ is the velocity of the projectile and $\theta$ is the incident angle.

As impactor velocities reach 12 km/s, melting can be produced by the impact. The rock masses that melt from the shock impact $M_m$ as the projectile mass $M_p$ can be described as:

$$M_m = 0.25 M_p \frac{v_i^2}{\epsilon_m} \sin\theta \qquad (7.4)$$

where $\varepsilon_m$ is the individual internal energy that is around 5.2 *MJ/kg* for granite.

Given that we have little else to go on, it is a useful exercise to characterize the Bow City structure in detail by applying such scaling laws. For a complex crater that has a rim-to-rim diameter of 8 km, an initial transit cavity between 6.3 km and 7 km is estimated to form and the amount of the uplift in the central peak is supposed to be around 590 m and 670 m.

In fact, it is quite difficult to precisely define the development of the impact crater due to the fact that a number of factors strongly affect the formation of the crater such as density, projectile size, gravitational acceleration, and the impact angle. However, briefly speculations on the formation of the Bow City structure are necessary to bring up some potential scenarios.

Stony projectiles are the most common meteorites discovered in impact studies [*French*, 1998]. A chronditic meteorite is one type of stony meteorites, which usually have a density around 3000 to 3750 kg/m$^3$. We will assume that the projectile is chronditic with a density around 3500 kg/m$^3$ and that it is striking vertically into the target surface with a density of 2500 kg/m$^3$ to form a crater that

has the similar size to the Bow City. The relationship (Equation 7.3) in terms of the projectile size and project velocity can be obtained as shown in Figure 7.9 and this suggests that 800 m diameter body is required if the projectile velocity is at 20 km/s.

Based on what we discussed above, a carton model showing the development of Bow City structure is illustrated (Figure 7.10). A 800 m stony projectile (3500 kg/m$^3$) travelling at 20 km/s was assumed to strike on the target surface, which has a density of 2500 kg/m$^3$ (Figure 7.9). In the end of the excavation stage, the diameter of the transit crater was calculated according to Equation 7.1 with considered that the final rim-to-to diameter is 8 km. In the modification stage, a structural uplift around 600 m in the centre was obtained with applying the scaling relationship in Equation 7.2. In the end, the final crater was buried and highly eroded. The structural features in the final crater were defined according to the seismic reflection profiles, particularly the depth section that exhibit in seismic Profiles 7.3, 7.4 and 7.5.

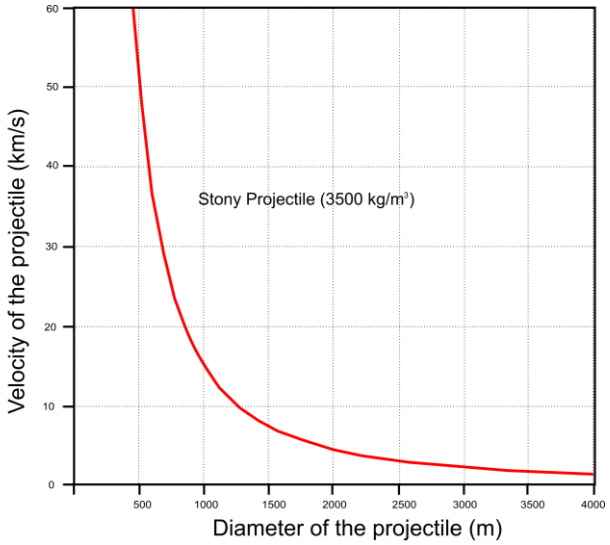


Figure 7.9 Diagram showing a vertically incoming stony meteorite projectile (density = 3500 kg/m$^3$) in terms of the incoming velocity and its diameter to create a transit impact crater of 6.3 km in diameter.

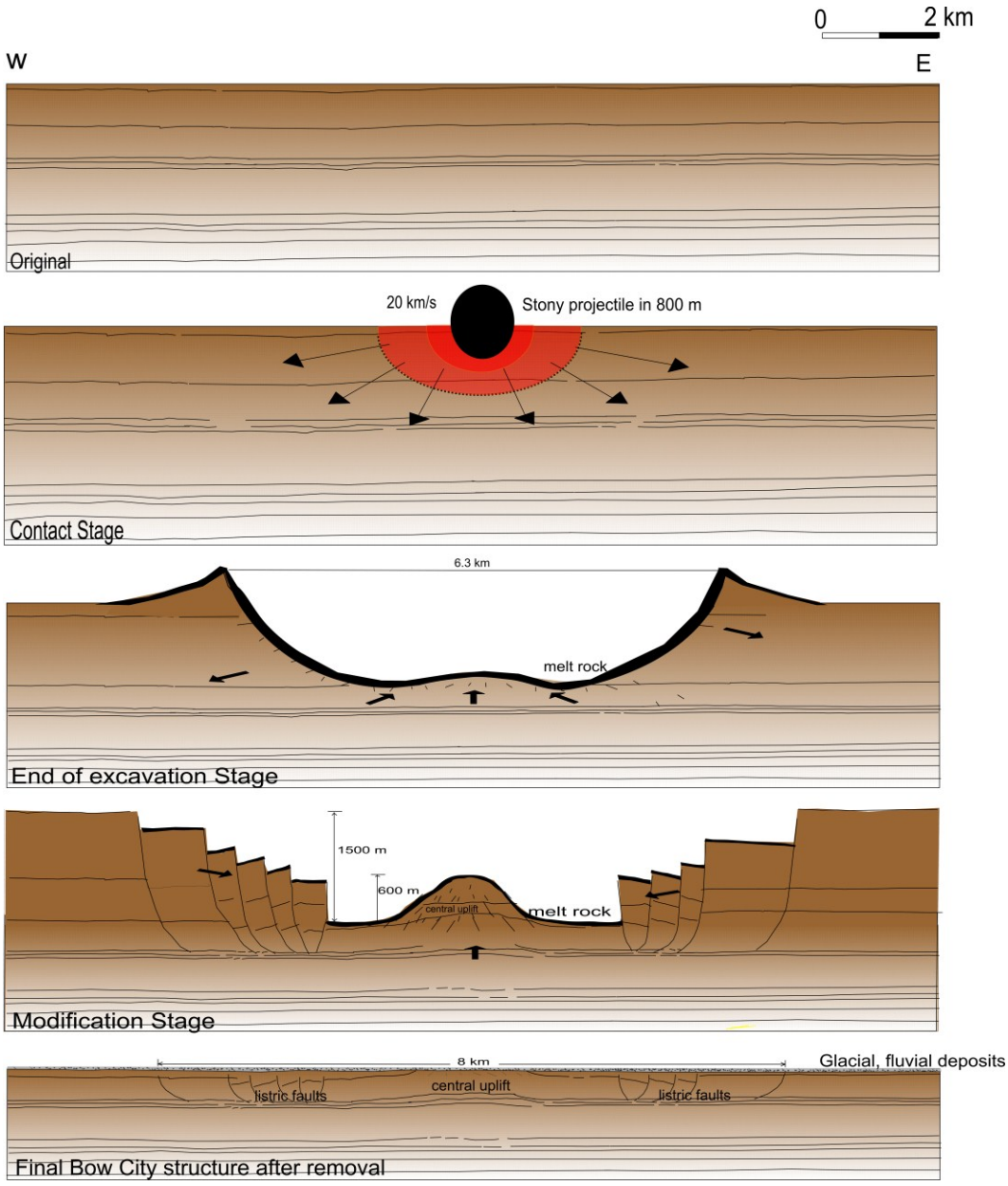


Figure 7.10 Schematic models showing the formation of the Bow City structure. Structural morphology is calculated with the relationships summarized in *Melosh* [2011].

### 7.3.3 Age

Currently, due to the highly erosion feature, there is no clear evidence to for precisely evaluating the age of Bow City structure. However, appropriate suggestions could be pointed out with the evidence from seismic images and field reconnaissance. In the seismic profiles, severe disruptions on the top of the Belly River sedimentary rocks were discovered. In addition, minor folding and gentle damage observed in the deeper units of the Mckay Coal formation and Milk River formation indicate more continuous and coherent architectures. Thus, this impact activity had to have occurred after the deposition of the Belly River Group units with an upper limit of 75 Ma. Exposed fault patterns observed from the field outcrop provides detailed information to verify and confine this assessment. The Horseshoe Canyon Formation that is found in the annular depression is recognized as the youngest interruptive units. It is necessary to notice that there is a time-transgressive at the contact of Bear Paw and Horseshoe Canyon units. The easterly Strathmore Member has an older age that the westerly Drumheller Member. Thus, it suggests that the earliest time that the catastrophic event could have occurred was around 73 Ma.

## 7.4 Summary

A series of diagnostic features such as blocky strata in the annular moat, highly disrupted patterns at the central uplift area and the bowl-shaped structural geometry were observed on the 2D isopach maps and 3D model produced from the seismic and well logs data. I integrating the evidence discovered from various techniques, a better understanding of this possible impact crater was achieved. The creation of the structure by volcanic, karst, or halokinesis mechanisms are rejected due to the observations of the uniform structural patterns in the deeper sections, the significant uplifted strata in the central area, and the historical records of the regional geological settings. Also, the structure is considered to

have a rim-to-rim diameter of 8 km and the central uplift was estimated to have been initially 600 m on the scaling laws. Although the age of the structure is still not determined yet due to severe erosion, a maximum age of 73 Ma is estimated based on the age of the youngest sediments deformed.

# Chapter 8 Conclusion and Future work

## 8.1 Conclusion

Currently, meteorite impact cratering has been recognized as one of the most important processes affecting the biological and morphological history of the Earth. In fact, such omnipresent events that significantly shape the target surface are discovered in numerous planets. On Earth, more than 185 (Earth Impact Data Base at the University of New Brunswick [*Spray and Ellis*, 2013]) impact craters have been confirmed, with 14 craters found in the Western Canada Sedimentary Basin (WCSB). This relatively large concentration in the WCSB arise from the existence of extensive sets of seismic data that have allowed us to 'see' many of these features that are otherwise invisible to us at the surface. Indeed, it is likely that the majority of impact craters on Earth is still buried under the surface, and they are awaiting detection. Under this circumstance, the Bow City structure was first noticed by staff in Alberta Geological Survey (AGS) during detailed near-surface structure mapping [*Glombick*, 2010]. Anomalous faulting and bending of strata were noticed in a region of otherwise monotonous and gently dipping geological layers. On the structural maps generated from the geologic markers interpreted on well logs, a semi-circular outline was discovered. The motivation of this study is to examine the genesis of a newly discovered possible impact crater near Bow City. The uniqueness of this structure is that it was highly eroded and buried, and what we are looking at are the remaining deep roots. Distinctive details of the disturbed structural patterns are expected to be observed by the geological and geophysical subsurface imaging techniques. Such characterizations can be utilized to further constrain the origin of this unique structure and provide invaluable information to the impact study.

Seismic reflection, refraction, and geo-modeling techniques integrated with the well logs were employed to conduct this study. The preliminary analysis was made on a series of legacy 2D seismic profiles donated from the oil and gas companies. After carefully reprocessing the data, detailed interpretations were presented a number of diagnostic structure features. An inversion method utilizing the travel time of the first arrivals in seismic Profile 86251 was examined to produce the velocity model of subsurface structures. Further, in 2013, a seismic 2D survey optimized for imaging the shallow subsurface was carried out on site to reveal more detailed information. Clear images exhibiting the structural patterns of the shallow earth interior was obtained. In addition, a 3D model that integrates the information of seismic and geological structure mapping was finalized to display the image of the Bow City structure.

A number of legacy 2D seismic profiles, located in the vicinity of the structures, were first obtained to perform the preliminary analysis of this impact structure. Seven profiles running through the western portion of the structure were utilized. Although such datasets were originally collected for the deeper petroleferous targets, several distinctive structures could still be observed in the upper 500 m. A number of Cretaceous horizons, calibrated from well log data, were carefully tracked on these seismic reflection profiles, and the architecture of the geologic units in the shallow ground was displayed.

The refraction data of Profile 86251 (from Survey 86) was also used to conduct a velocity inversion technique. The RayInvr method produced by Dr. Colin Zelt was utilized to quickly highlight the velocity anomalies that appeared in the subsurface. The P-wave first arrivals were picked in the reflection profile and considered as the input of this algorithm. By iterative forward and inverse modeling, a final velocity model with optimal resolution and travel time residuals was successfully achieved. In this model, velocity anomalies were detected, which correlated well with the structure patterns displayed in the reflection image.

In addition, a high-resolution 2D seismic survey that consists of 2 short profiles was conducted to improve the understanding of the structural features detected in the early legacy dataset. These two profiles were acquired along the Profile 86251, which covered the rim faulted zone and the central uplift, respectively. After applying the processing technique designed for the shallow geologic targets, both the vertical and horizontal resolutions were greatly improved. One of the greatest concerns during the processing is to effectively remove the near-surface noise, which masks the shallow reflection signals in this study. Numerous trials and tests were applied to optimize the parameters and work flows. Thus, cleaner and higher-resolution images were finally obtained, providing more detailed information on the faulted slumped blocks and central raised zone.

All the seismic profiles (time scale) were converted to depth images with the contribution of the velocity information extracted from the sonic logs. Converting these seismic profiles to depth images indeed brings more geological meaning and intuitive thinking to the style of the structure. The isopach maps created with the interpreted seismic horizons provide more constraints on the change of the thickness layers as well. In addition, utilizing the result from the geological mapping, seismic imaging and velocity inversion, a final 3D structural model was created at the end of this study. This model, showing the elevation variation of the uppermost Belly River reflector, pointed out the structure architecture directly and visually. A final discussion was conducted to point out the scenarios of the origin and the development of this possible impact crater.

To conclude, various lines of evidence supporting an impact origin for the Bow City structure is summarized as follows:

- A ring-like structure displayed in the structure maps generated with the geologic markers.

- A series of faults and steeply dipping units were observed during the geologic reconnaissance.
- Slumping blocks are interpreted as listric faulted patterns and the central disruptive uplift with a bending reflector in the seismic reflection profiles. On the isochron maps, a semi-circular morphology and elevation variations are presented to estimate the architecture of the structure.
- Velocity anomalies were discovered in the faulted rims and the central peak by means of a seismic travel time inversion technique.
- The circular outline and the central uplift observed on the 3D model points out the size and unique structure patterns directly.

Based on the proof mentioned above, Bow City structure is considered as the remaining deep roots of a complex impact crater. Other endogenic geological origins are not supported by the regional geological history and the present evidence. Currently, the size of the final crater is estimated to be ~8 km in rim-to-rim diameter and its age is younger than ~73 Ma.

## 8.2 Future work

Although a number of lines of evidence has been provided by this study that suggest that the Bow City structure is an impact crater, further studies to verify the impact genesis are still necessary. Such studies include:

- Finding evidence of shock metamorphism. Currently, existence of the shocked rocks is the prerequisite criteria to confirm the impact origin. Detailed sampling in the periphery area will be the necessary step. Based on the shatter cores and PDFs discovered in other impact studies, such rocks might be buried within the structure. Careful diamond coring of a variety of sites around the structure would provide fresh material for study, as well as allow access for logging and borehole seismic

experiments to confirm the existence of the anomalous velocity structure. However, there also remains the possibility that such evidence may never be found as the shock levels may never have been sufficiently high at this depth to leave shock artifacts.

- Geological outcrop mapping. Although distinctive faults and dipping beds have been seen in the west side of the structure area, observations from the east of the Bow River area are still missing. A more detailed geological investigation of this area is warranted.

- Other geo-techniques such as gravity, magnetic, and electrical resistivity surveying. Gravity mapping is emphasized to be one of the useful tools to identify impact anomalies due to the fact that fracturing and disturbance processes in the hypervelocity impact can obviously change the gravity distribution of the target zone. Moreover, magnetic and electrical resistivity tomography (ERT) could highlight the possible contrasts in magnetic and resistivity of the damaged rock masses within the crater, respectively.

- High-resolution seismic profiles. Undoubtedly, seismic techniques produce the highest resolution images for visualzing the subsurface structural styles. The new dataset acquired in 2013 prominently marked more details, however, more such lines are needed to conduct a comprehensive seismic characterization. Shooting a survey that runs through the central area between new Line 1 and Line 2 would be necessary to detect the currently ‘transparent’ central area. In addtion, acquiring data to the east of Bow River can compensate the ‘blank’ on the east portion of this structure. Corresponding lines along a N-S axis through the inferred centre of the structure would also be of value.

- Tomographic velocity characterization. Velocity detection can be utilized to distinguish the velocity anomalies generated by the impact damage. More modeling is expected to be conducted to the show the velocity distributions, especially with new Line 1 and line 2. The test of the validity of the inversed model such as ray density test and stability test is expected to be conducted as well.

# Bibliography


Ackermann, H., R. Godson, and J. Watkins (1975), A seismic refraction technique used for subsurface investigations at Meteor Crater, Arizona, Journal of Geophysical Research, 80(5), 765-775.

Ahrens, T. J., and J. D. O'Keefe (1987), Impact on the Earth, ocean and atmosphere, International journal of impact engineering, 5(1), 13-32.

Aki, K., and P. G. Richards (1980), Quantitative seismology: Theory and methods, 1, I: WH Freeman and Co.

Aki, K., and P. G. Richards (2002), Quantitative seismology, University Science Books.

Averill, M. G. (2007), A lithospheric investigation of the southern Rio Grande rift, The university of Texas at El Paso, Texas.

Banerjee, I. (1989), Tidal sandsheet origin of the transgressive Basal Colorado Sandstone (Albian): a subsurface study of the Cessford, southern Alberta, Bulletin of Canadian Petroleum Geology, 37, 1-17.

Barton, R., K. Bird, J. G. Hernández, J. M. Grajales-Nishimura, G. Murillo-Muñetón, B. Herber, P. Weimer, C. Koeberl, M. Neumaier, and O. Schenk (2009), High-impact reservoirs, Oilfield Review, 2010(21), 4.

Beaty, K. S., and D. R. Schmitt (2003), Repeatability of multimode Rayleigh-wave dispersion studies, Geophysics, 68(3), 782-790.

Boslough, M. B. (1990), A thermochemical model for shock-induced reactions (heat detonations) in solids, The Journal of chemical physics, 92(3), 1839-1848.

Braman, D. R., and L. V. Hills (1990), Overview of Campanian to Paleocene stratigraphy, southern Alberta foothills. In: Field guide to uppermost Cretaceous-Tertiary strata in southern Saskatchewan and Alberta. D.R. Braman and A.R. Sweet (eds.). in Canadian Society of Petroleum Geologists 1990 Annual Convention, edited, pp. 53-57, Calgary, Alberta.

Brenan, R., B. Peterson, and H. Smith (1975), Origin of Red Wing Creek structure: McKenzie County, North Dakota, Earth Sci. Bull.;(United States), 8(3).

Buchwald, V. F. (1975), Handbook of iron meteorites: Their history, distribution, composition and structure, University of California Press Berkeley.

Bustin, R. M. (1992), Organic maturation of the Western Canadian Sedimentary Basin, International Journal of Coal Geology, 19, 319-358.

Caldwell, W. G. E., B. R. North, Stelck, C.R., and J. H. Wall (1978), A foraminiferal zonal scheme for the Cretaceous System in the interior plains of Canada. In: Western and Arctic Canadian Biostratigraphy., Geological Association of Canada, Special Paper 18, 495-575.

Canales, L. L. (1984), Random noise reduction, paper presented at 1984 SEG Annual Meeting, Society of Exploration Geophysicists.

Cant, D. J., and G. S. Stockmal (1989), The Alberta foreland basin: relationship between stratigraphy and Cordilleran terrane-accretion events, Canadian Journal of Earth Sciences, 26(1964-1975).

CANVEC (2007), CanVec, Canada, edited by G. o. C. Centre for Topographic Information, Natural Resources Canada, Earth Sciences Sector, Centre for Topographic Information.

Catuneanu, O., and A. R. Sweet (1999), Maastrichtian-Paleocene foreland-basin stratigraphies, western Canada: a reciprocal sequence architecture, Canadian Journal of Earth Sciences, 36(5), 685-703.

Cervenf, V., I. Molotkov, and PSenCik (1977), Ray Method in Seismology, University of Karlova, Prague, Czechoslovakia.

Červený, V., I. A. e. Molotkov, I. A. e. Molotkov, and I. Pšenčík (1977), Ray method in seismology, Univerzita Karlova.

Chan, J. S. (2013), Subsurface geophysical characterization of the crustalline canadian shield in Northeastern Alberta: Implications for Geothermal Development, University of Alberta, Edmonton, Alberta.

Christopher, J. E. (1974), The Upper Jurassic Vanguard and Lower Cretaceous Mannville groups of southwestern SaskatchewanRep., 349 pp, Saskatchewan Department of Mineral Resources.

Christopher, J. E. (1984), Depositional patterns and oil field trends in the lower Mesozoic of the northern Canada Williston Basin, Canada. In: Williston Basin, Anatomy of a Cratonic Oil Province, Rocky Mountain Association of Geologists., 223-243.

Claerbout, J. (1986), Imaging the Earth's interior, Geophysical Journal of the Royal Astronomical Society, 86(1), 217-217.

Clement, J., and T. Mayhew (1979), Newporte discovery opens new pay, Oil and Gas Journal, 77(27), 165-172.

Collins, G. S., H. J. Melosh, and G. R. Osinski (2012), The impact-cratering process, Elements, 8(1), 25-30.

Danuor, S., A. Aning, J. Pohl, T. Karp, and H. Berckhemer (2013), GEOPHYSICAL CHARACTERISTICS OF THE BOSUMTWI IMPACT CRATER FROM SEISMIC, GRAVITY AND MAGNETIC MEASUREMENTS, European Scientific Journal, 9(15).

Dawson, F. M., C. G. Evans, R. Marsh, and R. Richardson (1994), Uppermost Cretaceous and Tertiary Strata of the Western Canada Sedimentary Basin: Geological Atlas of the Western Canada Sedimentary Basin, Canadian Society of Petroleum Geologists and Alberta Research Council, Chapter 24.

DeMille, G. (1960), The Elbow Structure of South-Central Saskatchewan, Bulletin of Canadian Petroleum Geology, 8(5), 154-162.

Donofrio, R. R. (1981), Impact craters: implications for basement hydrocarbon production, Journal of Petroleum Geology, 3(3), 279-302.

Drees, N., G. Mossop, and I. Shetsen (1994), Devonian Elk Point Group of the Western Canada Sedimentary Basin, Geological Atlas of the Western Canada Sedimentary Basin, Canadian Society of Petroleum Geologists and Alberta Research Council, Special Report, 4.

Duo, X. (2011), Surface and borehole seismic images at the International Continental Drilling program Outokumpu borehole: implications for reflectivity of the crystalline crust, in Masters Abstracts International, edited.

Duo, X. (2011), Surface and borehole seismic images at the international continental drilling program Outokumpu borehole: Implications for reflectivity of the crystalline crust, University of Alberta, Edmonton, Alberta.

Energy, I. (2011), Accumap database, edited, IHS Energy, IHS Energy.

England, T. D., and R. Bustin (1986), Thermal Maturation of the western Canadian sedimentary basin south of the Red Deer River: I) Alberta Plains, Bulletin of Canadian Petroleum Geology, 34(1), 71-90.

Farshori, M. Z. (1983), Glauconitic sandstone Countess "H" Pool. In:. McLean, J.R and Reinson, G.E. (Eds.) Sedimentology of selected Mesozoic clastic sequences, Corexpo '83., Canadian Society of Petroleum Geologists, 27-411.

Fessenden, R. A. (1917), Method and Apparatus For Locating Ore-Bodies, U.S. Patent 1240328, September 18, 1917.

Fitzgerald-Moore, P., and J. A. Podruski (1988), Conventional oil resources of Western Canada : light and medium, xi, 149 p. pp., Geological Survey Canada, Ottawa.

Forsman, N. F., T. R. Gerlach, and N. L. Anderson (1996), Impact origin of the Newporte structure, Williston basin, North Dakota, AAPG bulletin, 80(5), 721-730.

French, B. M. (1998), Traces of catastrophe: A handbook of shock-metamorphic effects in terrestrial meteorite impact structures, Technical Report, LPI-Contrib-954, 1.

French, B. M., and C. Koeberl (2010), The convincing identification of terrestrial meteorite impact structures: What works, what doesn't, and why, Earth-Science Reviews, 98(1), 123-170.

Gadallah, M. R., and R. L. Fisher (2005), Applied seismology: A comprehensive guide to seismic theory and application, PennWell Books.

Gent, M., L. Kreis, and D. Gendzwill (1992), The Maple Creek structure, southwestern Saskatchewan, Summary of Investigations, 92-94.

Gerlach, T. R. (1994), Evaluation of a possible subsurface impact crater: The Newporte structure, northwestern Renville County, North Dakota, University of North Dakota.

Glaister, R. P. (1959), Lower Cretaceous of southern Alberta and adjacent areas, American Association of Petroleum Geologists, Bulletin, 43, 590-640.

Glombick, P., B. Hathway, S. Mei, C. Banks, and D. Hay (2010), Mapping the Belly River Group in Alberta.

Glombick, P., D. R. Schmitt, W. Xie, T. Bown, B. Hathway, and C. Banks (2014), The Bow City structure, southern Alberta, Canada: The deep roots of a complex impact structure?, Meteoritics & Planetary Science.

Glombick, P. M. (2010), Top of the Belly River Group in the Alberta Plains: Subsurface Stratigraphic Picks and Modelled Surface Open FIle Report 2010-10.

Green, R., and P. Chetty (1990), Seismic refraction studies in the basement of the Vredefort structure, Tectonophysics, 171(1), 105-113.

Grieve, R., K. Kreis, A. Therriault, and P. Robertson (1998), Impact structures in the Williston Basin, Meteoritics and Planetary Science Supplement, 33, 63.

Grieve, R. A., F. Langenhorst, and D. Stöffler (1996), Shock metamorphism of quartz in nature and experiment: II. Significance in geoscience*, Meteoritics & Planetary Science, 31(1), 6-35.

Grobe, M. (2000), Distribution and Thickness of Salt within the Devonian Elk Point Group, Western Canada Sedimentary Basin, Earth Sciences Report, 02.

Habib, A. G. E. (1981), Geology of the Bearpaw Formation in south-central Alberta, University of Alberta, Edmonton.

Hagedoorn, J. G. (1959), The plus-minus method of interpreting seismic refraction sections Geophys. Prosp, 7, 158-182.

Haites, T., and H. Van Hees (1962), The origin of some anomalies in the Plains of western Canada, Bulletin of Canadian Petroleum Geology, 10(9), 511-533.

Hajnal, Z., D. Scott, and P. Robertson (1988), Reflection study of the Haughton impact crater, Journal of Geophysical Research: Solid Earth (1978–2012), 93(B10), 11930-11942.

Hamblin, A. P. (1997), Stratigraphic architecture of the Oldman Formation, Belly River Group, surface and subsurface of southern Alberta, Bulletin of Canadian Petroleum Geology, 45(2), 155-177.

Hampson, D., and B. Russell (1984), First-break interpretation using generalized linear inversion, J. Can. Soc. Expl. Geophys, 20, 40-50.

Hanova, J., D. Lawton, J. Visser, A. Hildebrand, and L. Ferriere (2005), 3D Structural Interpretation of the Eagle Butte Impact Structure, Alberta, Canada, paper presented at 36th Annual Lunar and Planetary Science Conference.

Hayes, B. J. R., J. E. Christopher, and l. Rosenthal (1994), Cretaceous Mannville Group of the Western Canada Sedimentary Basin; Geological Atlas of the Western Canada

Sedimentary Basin, Canadian Society of Petroleum Geologists and Alberta Research Council, Chapter 19.

Henley, D. C. (2000), Wavefield separation in the radial trace domain, Geo-Canada 2000, Expanded Abstract(131).

Henley, D. C. (2003), Coherent noise attenuation in the radial trace domain, Geophysics, 68(4), 1408-1416.

Herber, B. D. (2010), 3D Seismic Interpretation of a Meteorite Impact, Red Wing Creek Field, Williston Basin, western North Dakota, UNIVERSITY OF COLORADO AT BOULDER.

Hopkins, J. C. (1987), Contemporaneous subsidence and fluvial channel sedimentation: Upper Mannville C Pool, Berry Field, Lower Cretaceous of Alberta, Bulletin of American Association of Petroleum Geologists, 71(3), 334-345.

Hopkins, J. C., S. W. Hermanson, and D. C. Lawton (1982), Morphology of channels and channel sand bodies in the Glauconitic sandstone member (Upper Mannville), Little Bow area, Alberta, Bulletin of Canadian Petroleum Geology, 30, 274-285.

Isaac, J. H., and R. Stewart (1993), 3-D seismic expression of a cryptoexplosion structure, Can. J. Expl. Geophys, 29(2), 429-439.

Jerzykiewicz, T. (1985), Stratigraphy of the Saunders Group in the central Alberta Foothills - a progress report. In: Current Research, Part B, Geological Survey of Canada(Paper 85-1B), 247-258.

Karp, T., B. Milkereit, P. Janle, S. K. Danuor, J. Pohl, H. Berckhemer, and C. A. Scholz (2002), Seismic investigation of the Lake Bosumtwi impact crater: Preliminary results, Planetary and Space Science, 50(7), 735-743.

Kent, D. M. (1987), Paleotectonic controls on sedimentation in the Northern Williston Basin, Saskatchewan. In: Williston Basin: Anatomy of a Cratonic Oil Province, Rocky Mountain Association of Geologists.

Khidir, A., and O. Catuneanu (2009), Basin-scale distribution of authigenic clay minerals in the Late Maastrichtian–Early Paleocene fluvial strata of the Alberta foredeep: implications for burial depth, Bulletin of Canadian petroleum geology, 57(3), 251-274.

Kiefer, W. S. (2003), Impact Craters in the Solar System, Space Science Reference Guide, Second Edition, on CD-ROM, Lunar and Planetary Institute.

Koeberl, C., and W. U. Reimold (1995), The Newporte impact structure, North Dakota, USA, Geochimica et Cosmochimica Acta, 59(22), 4747-4767.

Koeberl, C., W. U. Reimold, and D. Brandi (1996), Red Wing Creek structure, North Dakota: Petrographical and geochemical studies, and confirmation of impact origin, Meteoritics & Planetary Science, 31(3), 335-342.

Koster, E. H. (1984), Sedimentology of a for, Sedimentology of a foreland coastal plain: Upper Cretaceous Judith River Formation at Dinosaur Provincial Park, In: Field Trip Guidebook, Canadian Society of Petroleum Geologists, 115.

Leckie, D. A. (1985), The Lower Cretaceous Notikewin Member (Fort St. John Group), northeastern British Columbia: a progradational barrier island system, Bulletin of Canadian Petroleum Geology, 33, 39-51.

Leckie, D. A., J. P. Bhattacharya, and J. Bloch (1994), Cretaceous Colorado/Alberta Group of the Western Canada Sedimentary Basin: Geological Atlas of the Western Canada Sedimentary Basin, Canadian Society of Petroleum Geologists and Alberta Research Council, Chapter 20.

Lutter, W., R. Nowack, and L. Braile (1990), Seismic imaging of upper crustal structure using travel times from the PASSCAL Ouachita experiment, Journal of Geophysical Research: Solid Earth (1978–2012), 95(B4), 4621-4631.

Macdonald, D. E., T. C. Ross, P. J. McCabe, and A. Bosman (1987), An evaluation of the coal resources of the Belly River Group, to a depth of 400 m in the Alberta Plains, Alberta Research Council, Open File Report 1987-1988, 76.

Mazur, M., A. Hildebrand, D. Hladiuk, A. Schafer, and M. Pilkington (2002), The Steen River crater seismic refraction project, paper presented at Lunar and Planetary Institute Science Conference Abstracts.

Mazur, M., R. R. Stewart, and A. Hildebrand (2000), The seismic signature of meteorite craters, in Recorder, Canadian Society of Exploration Geophyscists Calgary, 10-16.

McLean, J. R. (1971), Stratigraphy of the Upper Cretaceous Judith River Formation in the Canadian Great Plains, Stratigraphy of the Upper Cretaceous Judith River Formation in the Canadian Great Plains, Report 11, 96.

McNeil, D. H., and W. G. E. Caldwell (1981), Cretaceous rocks and their foraminifera in the Manitoba Escarpment, Geological Association of Canada Special Paper, 21, 439.

Mellon, G. B. (1967), Stratigraphy and petrology of the Lower Cretaceous Blairmore and Mannville groups, Alberta Foothills and Plains, Alberta Research Council, Bulletin 21, 269.

Melosh, H., and B. Ivanov (1999), Impact crater collapse, Annual Review of Earth and Planetary Sciences, 27(1), 385-415.

Melosh, H. J. (1989), Impact cratering: A geologic process, Research supported by NASA. New York, Oxford University Press (Oxford Monographs on Geology and Geophysics, No. 11), 1989, 253 p., 1.

Melosh, H. J. (2011), Planetary surface processes, Cambridge University Press.

Menke, W. (1984), Geophysical data analysis: discrete inverse theory, Academic press.

Millman, P. M., and P. MacKenzie (1960), The Brent Crater, Queen's Printer.

Milton, D., A. Glikson, and R. Brett (1996), Gosses Bluff-a latest Jurassic impact structure, central Australia. Part 1: geological structure, stratigraphy, and origin.

Niccoli, M., A. R. Hildebrand, and D. C. Lawton (2004), Seismic velocity investigation of the Steen River impact structure, northern Alberta, CREWES research report, 16.

Nickerson, B. (2007), Seismic Methods for Summer Students in Global Geosolutions Inc, edited, p. 210, Calgary, Alberta.

Nurkowski, J. R. (1984), Coal quality, coal rank variation and its relation to reconstructed overburden, Upper Cretaceous and Tertiary plains coals, Alberta, Canada, AAPG Bulletin, 68(3), 285-295.

O'Connell, S. C. (1994), Geological History of the Peace River Arch; in Geological Atlas of the Western Canada Sedimentary Basin, Canadian Society of Petroleum Geologists and Alberta Research Council, 28.

Offield, T., and H. Pohn (1977), Deformation at the Decaturville impact structure, Missouri, paper presented at Impact and Explosion Cratering: Planetary and Terrestrial Implications.

Ogunsuyi, F. O. (2010), Geophysicsal characterization of Peace river landslide University of Alberta, Edmonton, Alberta.

Ogunsuyi, F. O., and D. R. Schmitt (2010), Integrating Seismic-velocity Tomograms and Seismic Imaging: Application to the Study of a Buried Valley, Advances in Near-surface Seismology and Ground-penetrating Radar, 361.

O'Keefe, J. D., and T. J. Ahrens (1999), Complex craters: Relationship of stratigraphy and rings to impact conditions, Journal of Geophysical Research: Planets (1991–2012), 104(E11), 27091-27104.

Osinski, G. R. (2004), Hypervelocity impact into sedimentary targets: Processes and products, University of New Brunswick (Canada).

Osinski, G. R., and P. Lee (2005), Intra-crater sedimentary deposits at the Haughton impact structure, Devon Island, Canadian High Arctic, Meteoritics & Planetary Science, 40(12), 1887-1899.

Osinski, G. R., P. Lee, J. G. Spray, J. Parnell, D. S. Lim, T. E. Bunch, C. S. Cockell, and B. Glass (2005), Geological overview and cratering model for the Haughton impact structure, Devon Island, Canadian High Arctic, Meteoritics & Planetary Science, 40(12), 1759-1776.

Osinski, G. R., and J. G. Spray (2005), Tectonics of complex crater formation as revealed by the Haughton impact structure, Devon Island, Canadian High Arctic, Meteoritics & Planetary Science, 40(12), 1813-1834.

Osinski, G. R., J. G. Spray, and P. Lee (2001), Impact-induced hydrothermal activity within the Haughton impact structure, arctic Canada: Generation of a transient, warm, wet oasis, Meteoritics & Planetary Science, 36(5), 731-745.

Palmer, D. (1986), The Generalized Reciprocal Method, Refraction Seismic, Geophisical Press.

Palmer, D. (1991), The resolution of narrow low-velocity zones with the generalized reciprocal method, Geophysical Prospecting, 39(8), 1031-1060.

Payenberg, H. D. T., M. D.A., and R. D. Braman (2001), Sequence Stratigraphy of the Milk River Formation in southern Alberta and Eagle Formation in northern Montana, in Canadian Soiety of Petroleum Geologists,, edited, p. 265, Calgary, Alberta.

Pelton, J. R. (2005), Near-surface seismology: Surface-based methods.

Pilkington, M., and R. Grieve (1992), The geophysical signature of terrestrial impact craters, Reviews of Geophysics, 30(2), 161-181.

Podruski, J. A. (1988), Constrasting Character of the Peace River and Sweetgrass Arches, Western Canada Sedimentary Basin, Geoscience Canada, 15(2), 94-97.

Porter, J. W. (1992), Oil and gas reserves of the Western Canada Foreland Basin. In: Foreland Basins and Fold Belts, R.W. Macqueen and D.A. Leckie, Memoir 55, 125-128.

Rampino, M. R., and C. Koeberl (2006), Comparison of Bosumtwi impact crater (Ghana) and Crater Lake volcanic caldera (Oregon, USA): Implications for biotic recovery after catastrophic events, in Biological processes associated with impact events, edited, pp. 101-120, Springer.

Robertson, P., and J. Sweeney (1983), Haughton impact structure: Structural and morphological aspects, Canadian Journal of Earth Sciences, 20(7), 1134-1151.

Ronen, J., and J. F. Claerbout (1985), Surface-consistent residual statics estimation by stack-power maximization, Geophysics, 50(12), 2759-2767.

Rosenthal, L., D. Lechie, G. Nadon, and Canadian Society of Petroleum Geologists (1984), Depositional cycles and facies relationships within the Upper Cretaceous Wapiabi and Belly River Formations of west central Alberta, v, 54 p. pp., Canadian Society of Petroleum Geologists, Calgary, AB.

Rosenthal, L., and R. G. Walker (1987), Lateral and vertical facies sequences in the Upper Cretaceous Chungo Member, Wapiabi Formation, southern Alberta, Canadian Journal of Earth Sciences, 24, 771-783.

Roy, S., and R. R. Stewart (2012), Near-surface Seismic Investigation of Barringer (Meteor) Crater, Arizona, Journal of Environmental and Engineering Geophysics, 17(3), 117-127.

Rudkin, R. A. (1964), Lower Cretaceous. In: Geological History of Western Canada, Alberta Society of Petroleum Geologists, 56-158.

Rukhlov, A., and J. Pawlowicz (2012), Eocene potassic magmatism of the Milk River Area, Southern Alberta (NTS 72E) and Sweet Grass Hills, Northern Montana: Overview and new data on mineralogy, geochemistry, petrology and economic potential, Alberta Geological Survey/Energy Resources Conservation Board, Open File Report, 1, 96.

Russell, L. S., and R. W. Landes (1940), Geology of the southern Alberta Plains, Geological Survey of Canada, Memmoir 221.

Safani, J., A. O'Neill, T. Matsuoka, and Y. Sanada (2005), Applications of Love wave dispersion for improved shear-wave velocity imaging, Journal of Environmental & Engineering Geophysics, 10(2), 135-150.

Sawatzky, H. (1972), Viewfield-a producing fossil crater, Canadian Soc. Exploration Geophysicists Jour, 8(1), 22-40.

Sawatzky, H. (1975), Astroblemes in Williston Basin, AAPG Bulletin, 59(4), 694-710.

Sawatzky, H. (1976), Two Probable Late Cretaceous Astroblemes in Western Canada-Eagle Butte, Alberta and Dumas, Saskatchewan, Geophysics, 41(6), 1261-1271.

Sawatzky, H. (1977), Buried impact craters in the Williston Basin and adjacent area, paper presented at Impact and Explosion Cratering: Planetary and Terrestrial Implications.

Schmitt, D., B. Milkereit, T. Karp, C. Scholz, S. Danuor, D. Meillieux, and M. Welz (2007), In situ seismic measurements in borehole LB-08A in the Bosumtwi impact structure, Ghana: Preliminary interpretation, Meteoritics & Planetary Science, 42(4-5), 755-768.

Schmitt, D. R., P. M. Glombick, W. Xie, and T. Bown (2013), The Bow City structure: Geological and Geophysical Evidence for an Impact Origin, AGS Report.

Schneider, W. A., and S. Kuo (1985), Refraction modeling for statics corrections, 55th Ann. Internat. Mtg., Soc. Expl. Geophys., , Expanded Abstracts, 295-299.

Scholz, C. A., T. Karp, K. M. Brooks, B. Milkereit, P. Y. Amoako, and J. A. Arko (2002), Pronounced central uplift identified in the Bosumtwi impact structure, Ghana, using multichannel seismic reflection data, Geology, 30(10), 939-942.

Scott, D., and Z. Hajnal (1988), Seismic signature of the Haughton structure, Meteoritics, 23(3), 239-247.

Sheriff, R., and L. Geldart (1983), Exploration seismology. Volume 1: History, theory, and data acquisition.

Sheriff, R. E. (2002), Encyclopedic Dictionary of Applied Geophysics.

Shoemaker, E. M., and E. C. Chao (1961), New evidence for the impact origin of the Ries Basin, Bavaria, Germany, Journal of Geophysical Research, 66(10), 3371-3378.

Singleton, A. C., G. R. Osinski, P. J. McCAUSLAND, and D. E. Moser (2011), Shock-induced changes in density and porosity in shock-metamorphosed crystalline rocks, Haughton impact structure, Canada, Meteoritics & Planetary Science, 46(11), 1774-1786.

Singleton, A. C., G. R. Osinski, P. J. A. McCausland, and D. E. Moser (2011), Shock-induced changes in density and porosity in shock-metamorphosed crystalline rocks, Haughton impact structure, Canada, Meteoritics & Planetary Science, 46(11), 1774-1786, doi:10.1111/j.1945-5100.2011.01290.x.

Smith, D. G. (1994), Paleogeographic Evomution of the Western Canada Foreland Basin; in Geological Atlas of the Western Canada Sedimentary Basin, Canadian Society of Petroleum Geologists and Alberta Research Council, Chapter 17.

Spence, G., K. Whittall, and R. Clowes (1984), Practical synthetic seismograms for laterally varying media calculated by asymptotic ray theory, Bulletin of the Seismological Society of America, 74(4), 1209-1223.

Spray, J. G., and B. Ellis (2013), Earth Impact Data Base, edited.

Stewart, J. S. (1943), Bassano Alberta, preliminary map, Geological Survey of Canada, Ottawa., Paper 42-8Rep., 4 p. and 1 map sheet pp.

Stewart, S. (2003), How will we recognize buried impact craters in terrestrial sedimentary basins?, Geology, 31(11), 929-932.

Stewart, S. (2011), Estimates of yet-to-find impact crater population on Earth, Journal of the Geological Society, 168(1), 1-14.

Stöffler, D., and R. Grieve (1994), Classification and nomenclature of impact metamorphic rocks: A proposal to the IUGS subcommission on the systematics of metamorphic rocks, paper presented at Lunar and Planetary Institute Science Conference Abstracts.

Stöffler, D., and R. Grieve (1996), IUGS classification and nomenclature of impact metamorphic rocks: Towards a final proposal, paper presented at International Symposium on the Role of Impact Processes in the Geological and Biological Evolution of Planet Earth, Postojna, Slovenia.

Stone, D. S. (1999), Cloud Creek: A possible impact structure on the Casper Arch, Wyoming, The Mountain Geologist.

Stone, D. S., and A. M. Therriault (2003), Cloud Creek structure, central Wyoming, USA: Impact origin confirmed, Meteoritics & Planetary Science, 38(3), 445-455.

Stucchi, E., and A. Mazzotti (2009), 2D seismic exploration of the Ancona landslide (Adriatic Coast, Italy), Geophysics, 74(5), B139-B151.

Sweet, A. R., and D. R. Braman (1990), Age and stratigraphic significance of the Wapiabi-Brazeau transition, south-central Alberta Foothills and Plains. In: Field guide to uppermost Cretaceous-Tertiary strata in southern Saskatchewan and Alberta., in Canadian Society of Petroleum Geologists Convention, edited, pp. 15-22, Calgary, Alberta.

Westbroek, H., and R. Stewart (1996), The formation, morphology, and economic potential of meteorite impact craters, CREWES research report, 8.

Westbroek, H.-H. (1997), Seismic interpretation of two possible meteorite impact craters: White Valley, Saskatchewan and Purple Springs, Alberta.

Whitaker, S. H. (1976), Geology and groudwater resources of the Cypress area, Sask. Resear. Counc, Geol. Div.,, Map 22.

Widess, M. (1973), How thin is a thin bed?, Geophysics, 38(6), 1176-1180.

Williams, G. D. (1963), The Mannville Group (Lower Cretaceous) of central Alberta, Bulletin of Canadian Petroleum Geology, 11, 350-368.

Williams, G. D., and C. F. Burk (1964), Upper Cretaceous. In: A Geological History of Western Canada, in Alberta Society of Petroleum Geologists, edited by a. R. P. G. R.G. McGrossan, pp. 169-189.

Wilshire, H., and K. A. Howard (1968), Structural pattern in central uplifts of cryptoexplosion structures as typified by Sierra Madera, Science, 162(3850), 258-261.

Wood, J. W., and J. C. Hopkins (1989), Reservoir sandstone bodies in estuarine valley fill: Lower Cretaceous Glauconitic Member, Little Bow Field, Alberta, Canada., American Association of Petroleum Geologists, Bulletin, 73, 1361-1382.

Wright, G., M. McMechan, and D. Potter (1994), Structure and architecture of the Western Canada sedimentary basin, Geological atlas of the Western Canada sedimentary basin, 25-40.

Wright, G. N., M. E. MeMechan, and D. E. G. Potter (1994), Structure and Architecture of Western Cnadana Sedimentary Basin ; in Geological Atlas of the Western Canada Sedimentary Basin, Canadian Society of Petroleum Geologists and Alberta Research council, Chapter 3.

Wu, P. (1991), Flexure of lithosphere beneath the Alberta Foreland Basin: evidence of an eastward stiffening continental lithosphere, Geophysical Research Letters, 18(3), 451-454.

Yilmaz, O. (2001), Seismic data analysis: Processing, inversion, and interpretation of seismic data: SEG, Investigations in geophysics(10), 81-90.

Yilmaz, Ö. (2001), Seismic data analysis, Society of Exploration Geophysicists Tulsa.

Zelt, C., and R. Ellis (1988), Practical and efficient ray tracing in two-dimensional media for rapid traveltime and amplitude forward modeling, Can. J. Explor. Geophys, 24(1), 16-31.

Zelt, C., and R. Smith (1992), Seismic traveltime inversion for 2-D crustal velocity structure, Geophysical journal international, 108(1), 16-34.

Zelt, C. A. (1999), Modelling strategies and model assessment for wide-angle seismic traveltime data, Geophysical Journal International, 139(1), 183-204.

# Appendix A Photo of the seismic vibrator


Figure A-1. Photo of the seismic vibrator utilized to acquire the high-resolution survey in 2013.


Figure A-2. Photo of the seismobile (left) that receives the signals originating from the energy source, the seismic vibrator (right).

# Appendix B Seismic profiles in depth scale

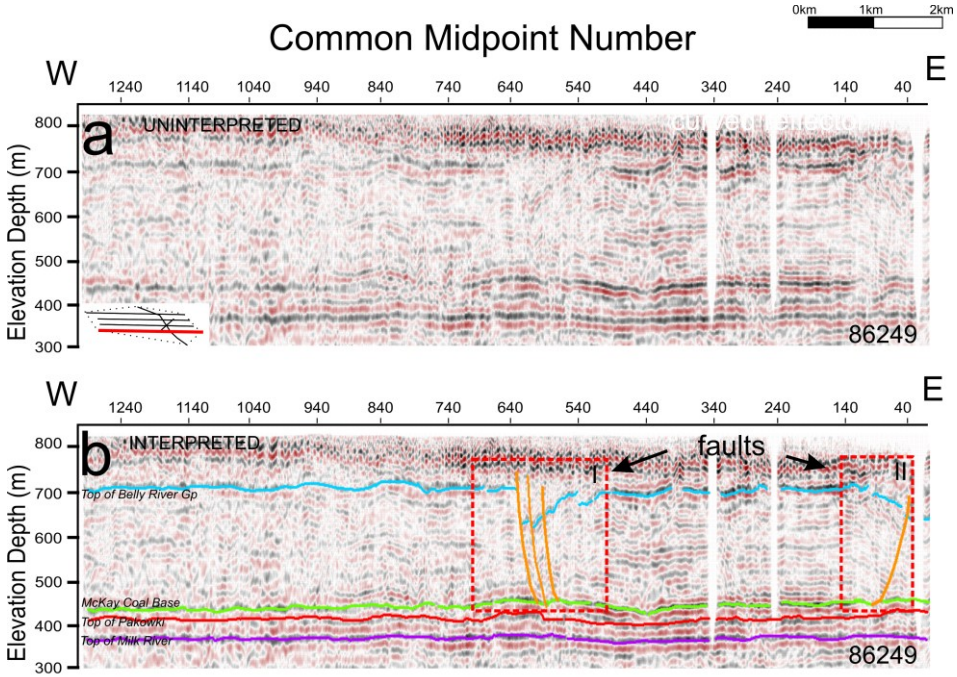


Figure B-1. Seismic Profiles of 86249 in depth scale. (a) Uninterpreted profile. (b) Interpreted profile. Colored lines show the interpreted shallow horizons. Dashline box emphasizes the diagnostic listric faults patterns.

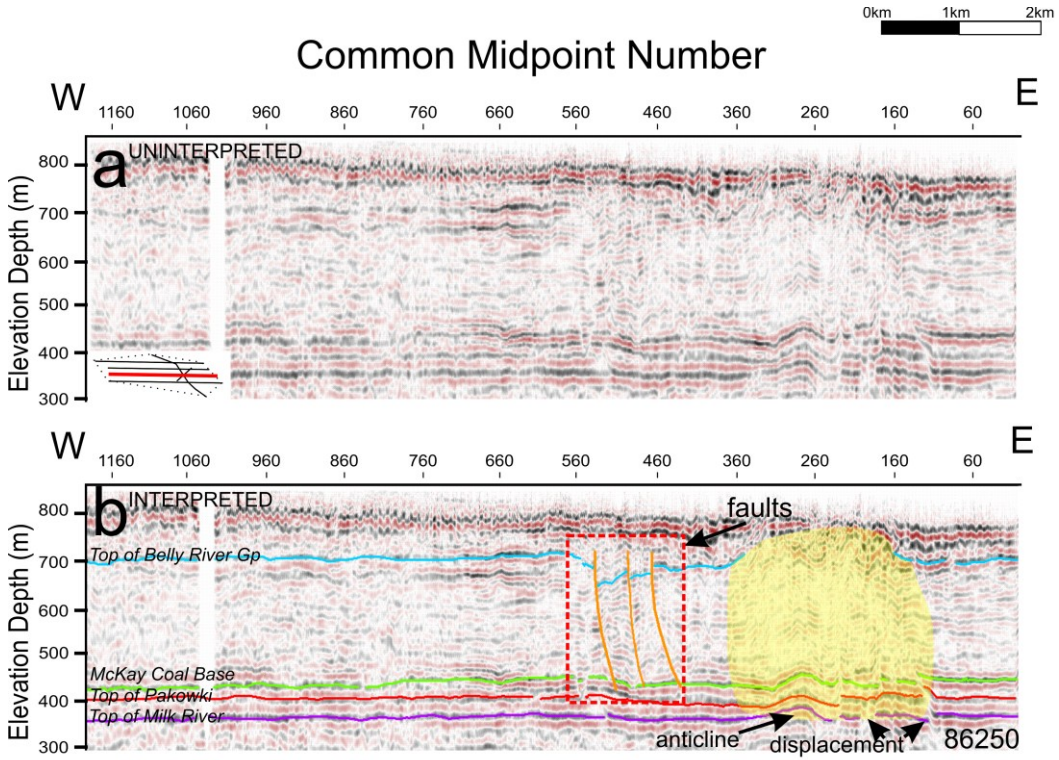


Figure B-2. Seismic Profiles of 86250 in depth scale. (a) Uninterpreted profile. (b) Interpreted profile. Colored lines show the interpreted shallow horizons. Dashline box emphasizes the diagnostic listric faults patterns. Yellow shading presents the anticlinal feature and the highly disturbed zone.

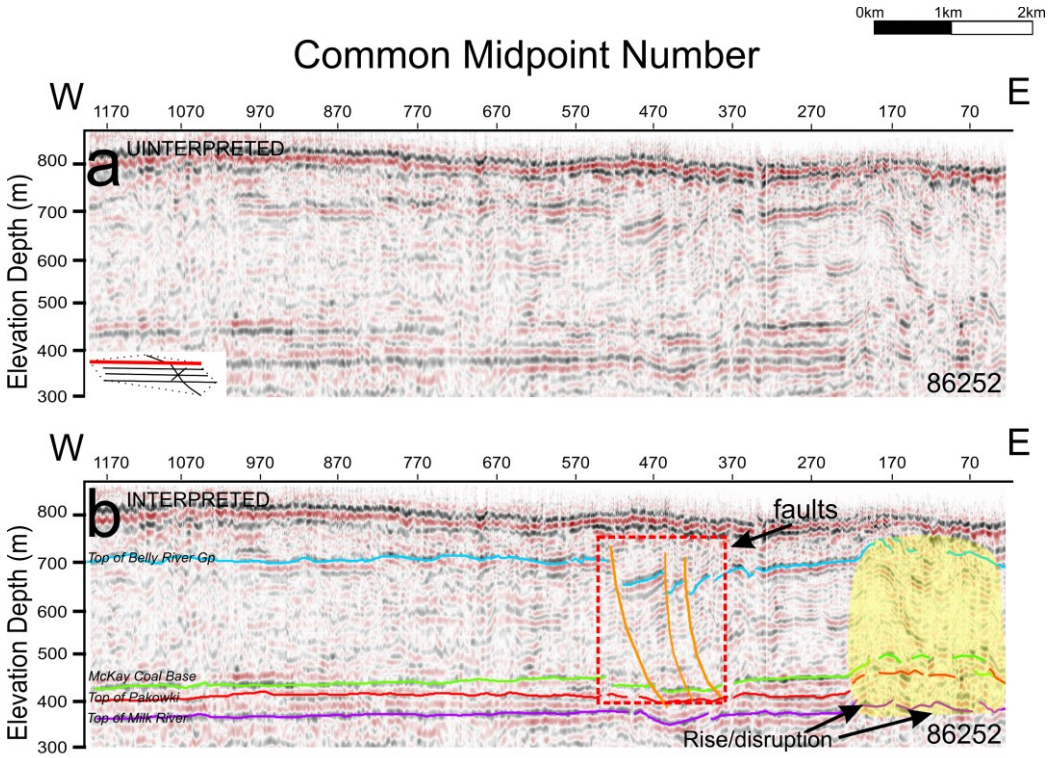


Figure B-3. Seismic Profiles of 86252 in depth scale. (a) Uninterpreted profile. (b) Interpreted profile. Colored lines show the interpreted shallow horizons. Dashline box emphasizes the diagnostic listric faults patterns. Yellow shading presents the raised highly disturbed zone.

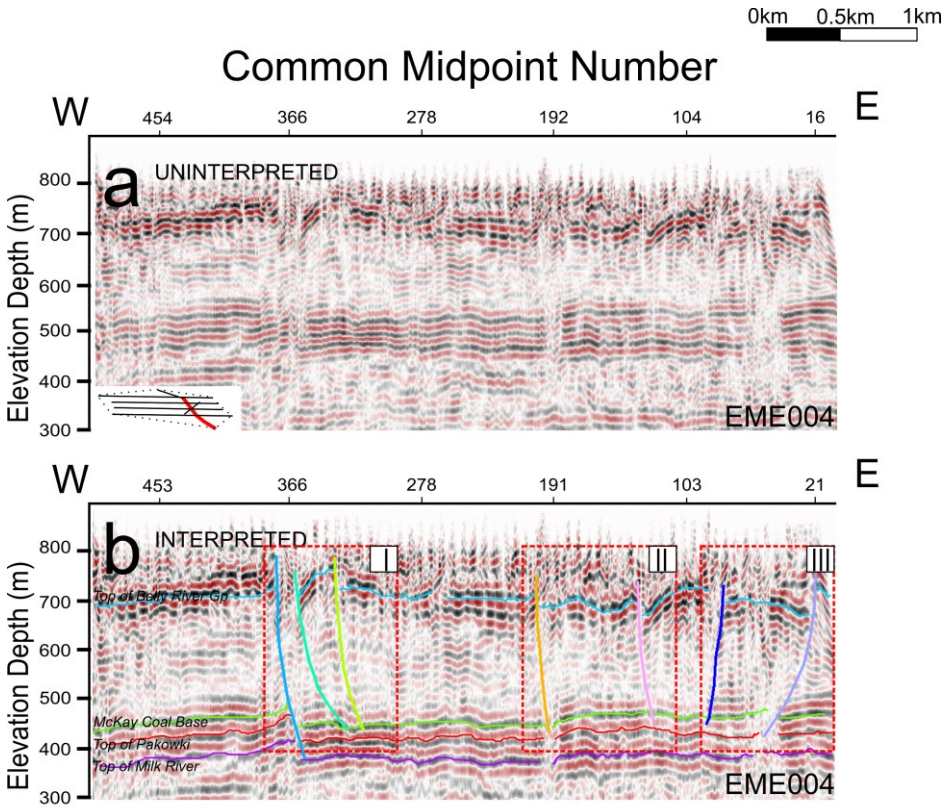


Figure B-4. Seismic Profiles of EME004 in depth scale. (a) Uninterpreted profile. (b) Interpreted profile. Colored lines show the interpreted shallow horizons. Dashline box emphasizes the diagnostic faults patterns.

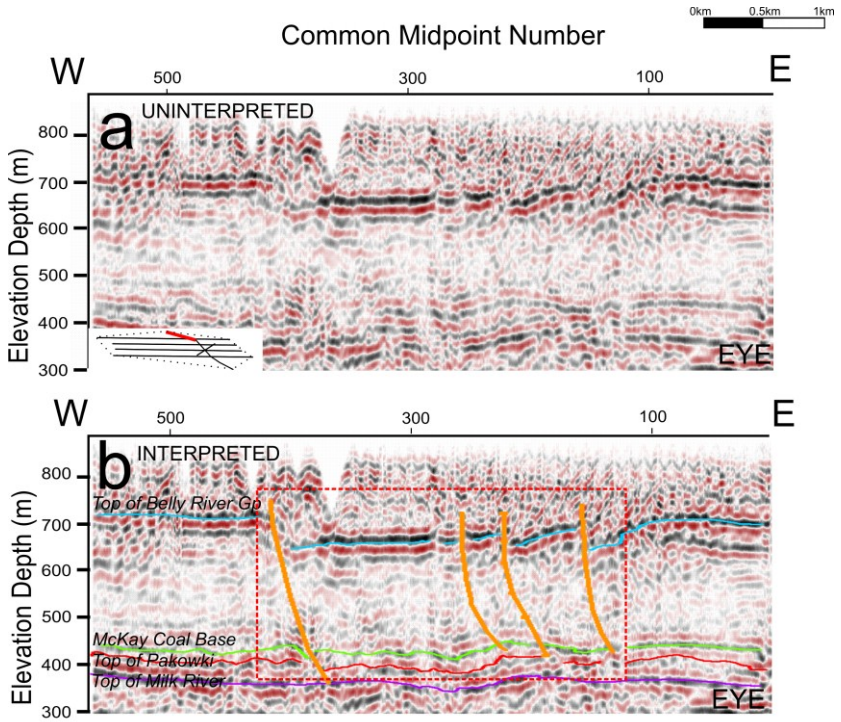


Figure B-5. Seismic Profiles of EYE in depth scale. (a) Uninterpreted profile. (b) Interpreted profile. Colored lines show the interpreted shallow horizons. Dashline box emphasizes the diagnostic listric faults patterns.